

DISS. ETH NR. 21638

A laser based mercury co-magnetometer for  
the neutron electric dipole moment search

ABHANDLUNG

zur Erlangung des Titels

DOKTOR DER WISSENSCHAFTEN

der

ETH ZÜRICH

vorgelegt von

Martin Christoph Fertl

Diplom-Physiker Univ., Technische Universität München

geboren am 01.02.1984

Deutschland

Angenommen auf Antrag von

Prof. Dr. Klaus Kirch

Prof. Dr. Antoine Weis

2013



# Abstract

This work introduces a laser-based  $^{199}\text{Hg}$  co-magnetometer into the experiment searching for a permanent neutron electric dipole moment (nEDM) at the Paul Scherrer Institute, Villigen, Switzerland.

The work discusses in detail the advantages of an ultraviolet (UV) laser light source for the  $^{199}\text{Hg}$  co-magnetometer in comparison to the  $^{204}\text{Hg}$  discharge bulbs used so far.

A UV laser system has been commissioned and frequency stabilized with the necessary accuracy. The Doppler- and frequency-modulation-free technique of *Sub-Doppler Dichroic Atomic Vapor Laser Lock* used to frequency stabilize the UV laser light and the experimental setup are described and discussed in detail.

The laser-based  $^{199}\text{Hg}$  co-magnetometer showed a more than five times increased signal-to-noise-ratio in a direct comparison measurement. The laser-based  $^{199}\text{Hg}$  co-magnetometer satisfies the sensitivity requirements for the next generation nEDM experiment (n2EDM).

Two models for the signal generation in the  $^{199}\text{Hg}$  co-magnetometer are developed to explain the increased magnetometry signal. These models are used to identify possibilities for increasing the magnetometer sensitivity even further.

A detailed model of the optical pumping process used to spin polarize the  $^{199}\text{Hg}$  atoms in the nEDM setup is presented. It turns out that the achievable spin polarization seems not to be limited by light-induced depolarization of  $^{199}\text{Hg}$  atoms.

The measurement of paramagnetic rotation as an alternative to light absorption to generate the  $^{199}\text{Hg}$  co-magnetometry signal in the nEDM geometry is discussed. Furthermore, possible benefits of using several even Hg isotopes on the magnetometry signal decay time are considered.





# Zusammenfassung

Die vorliegende Arbeit beschreibt die Realisierung eines laserbasierten  $^{199}\text{Hg}$  Komagnetometers für die Suche nach einem permanenten elektrischen Dipolmoment des Neutrons (nEDM) am Paul Scherrer Institut, Villigen, Schweiz.

Die Vorteile eines ultravioletten (UV) Lasers gegenüber den bisher als Lichtquelle verwendeten  $^{204}\text{Hg}$  Entladungslampen werden detailliert diskutiert.

Ein UV Lasersystem wurde in Betrieb genommen und dessen Lichtfrequenz mit der für das  $^{199}\text{Hg}$  Komagnetometer erforderlichen Genauigkeit stabilisiert. Die Frequenzstabilisierung erfolgt mit einer Doppler-freien Methode, ohne zusätzliche Frequenzmodulation des Lichts. Das Konzept und die experimentelle Umsetzung werden im Detail beschrieben und erklärt.

In einer ersten, direkten Vergleichsmessung zeigte das laserbasierte  $^{199}\text{Hg}$  Komagnetometer ein um mehr als das Fünffache höheres Signal-Rausch-Verhältnis. Es konnte gezeigt werden, dass das laserbasierte  $^{199}\text{Hg}$  Komagnetometer die Sensitivitätsanforderungen für ein nEDM Experiment der nächsten Generation (n2EDM) erfüllt.

Zwei Modelle der Signalentstehung im  $^{199}\text{Hg}$  Komagnetometer werden ausgearbeitet, um das vergrößerte Messsignal zu erklären. Aus diesen Modellen werden zusätzliche Möglichkeiten abgeleitet, um die Magnetometersensitivität in Zukunft weiter zu erhöhen.

Der Aufbau der Spinpolarisation der  $^{199}\text{Hg}$  Atome erfolgt durch optisches Pumpen. Der Vorgang wird für die Anordnung des nEDM Experiments modelliert. Dabei stellt sich heraus, dass die erreichbare Gleichgewichtspolarisation nicht durch lichtinduzierte Depolarisation beschränkt zu sein scheint.

Der Effekt der paramagnetischen Drehung wird als Alternative zur Messung von Lichtabsorption zur Erzeugung des Magnetometersignals diskutiert. Weiterhin wird die Möglichkeit diskutiert durch Zugabe von Hg Isotopen mit gerader Nukleonenzahl die charakteristische Signalzerfallszeit zu verlängern.



# Contents

<b>List of Symbols</b>	<b>13</b>
<b>List of Acronymes</b>	<b>15</b>
<b>1 Introduction</b>	<b>17</b>
1.1 Dipole moments and symmetries . . . . .	18
1.2 Sources of CP violation and nEDM predictions within the SM . . . . .	22
1.3 Sources of CP violation and nEDM predictions beyond the SM . . . . .	23
1.4 Current and prospective limits of EDM measurements . . . . .	25
1.5 Ultra-cold neutrons . . . . .	26
1.5.1 Neutron optical potential . . . . .	27
1.5.2 Electromagnetic interaction . . . . .	30
1.5.3 Gravity . . . . .	30
1.5.4 Weak interaction . . . . .	31
1.5.5 Production of ultra-cold neutrons and the PSI UCN source . . . . .	32
<b>2 The neutron electric dipole moment experiment</b>	<b>35</b>
2.1 Historical development of the nEDM experiment . . . . .	35
2.2 The experimental setup of the nEDM experiment at PSI . . . . .	38
2.3 Ramsey’s method and the nEDM . . . . .	39
2.4 Magnetometry requirements in the nEDM experiment . . . . .	44
2.5 Statistical sensitivity of the $^{199}\text{Hg}$ co-magnetometer . . . . .	45
<b>3 The components of the mercury co-magnetometer</b>	<b>51</b>
3.1 The element mercury . . . . .	51
3.2 Interaction of Hg atoms with electric and magnetic fields . . . . .	57
3.3 The $^{204}\text{Hg}$ discharge bulbs . . . . .	61
3.4 The UV laser system . . . . .	63
3.5 The laser frequency lock . . . . .	69
3.5.1 Light frequency accuracy requirements for nEDM/n2EDM . . . . .	69
3.5.2 The sub-Doppler dichroic atomic vapor laser lock . . . . .	70
3.6 UV grade optical fibers . . . . .	78

<b>4</b>	<b>The <math>^{199}\text{Hg}</math> co-magnetometer signal</b>	<b>87</b>
4.1	The interaction of $^{199}\text{Hg}$ atoms with a weak light beam . . . . .	87
4.1.1	Light absorption . . . . .	90
4.1.2	AC Light shifts . . . . .	93
4.1.3	Paramagnetic rotation . . . . .	95
4.2	An extended model for the absorptive signal . . . . .	100
4.2.1	Small signal model . . . . .	100
4.2.2	An extended model for the $^{199}\text{Hg}$ co-magnetometer signal . . . . .	102
<b>5</b>	<b>Comparison of <math>^{204}\text{Hg}</math> lamp and UV laser based <math>^{199}\text{Hg}</math> co-magnetometry</b>	<b>105</b>
5.1	Data analysis procedure . . . . .	105
5.2	AC signal comparison: UV laser vs. $^{204}\text{Hg}$ bulb . . . . .	107
5.3	Small amplitude model vs. extended model . . . . .	110
5.4	Signal to Noise comparison . . . . .	117
5.5	Laser-based $^{199}\text{Hg}$ co-magnetometer sensitivity . . . . .	118
5.6	Optical pumping process of $^{199}\text{Hg}$ atoms in the nEDM setup . . . . .	123
5.7	The depolarization of mercury in the precession chamber . . . . .	131
5.7.1	Depolarization in inhomogeneous magnetic fields . . . . .	131
5.7.2	Depolarization by light . . . . .	132
5.7.3	Depolarization by wall collisions . . . . .	135
<b>A</b>	<b>The Cramér Rao lower bound</b>	<b>143</b>
<b>B</b>	<b>The isotopes of mercury</b>	<b>147</b>
<b>C</b>	<b>The DAQ system of the <math>^{199}\text{Hg}</math> co-magnetometer</b>	<b>151</b>
<b>D</b>	<b>The FID signal after a band pass filter</b>	<b>155</b>
<b>E</b>	<b>Production of mercury spectroscopy cells</b>	<b>161</b>
<b>F</b>	<b>Properties of solarization-resistant UV fibers</b>	<b>167</b>
	<b>Bibliography</b>	<b>169</b>
	<b>Acknowledgments</b>	<b>183</b>

# List of Figures

1.1	The electromagnetic dipole interaction under T and P operation. . . . .	21
1.2	Strong penguin diagram contribution to the nEDM . . . . .	23
1.3	Possible sources of CP violation . . . . .	24
1.4	Feynman diagram of neutron $\beta^-$ decay. . . . .	31
1.5	Cut through the UCN source at PSI . . . . .	33
2.1	Pictorial scheme of the measurement configurations in the nEDM experiment	36
2.2	Scheme of the first nEDM experiment . . . . .	36
2.3	Historic development of the experimental upper limit for the nEDM. . . . .	37
2.4	Picture of the nEDM experimental setup . . . . .	40
2.5	Sketch of the nEDM experimental apparatus as used at PSI. . . . .	41
2.6	Pictorial representation of Ramsey's method of separated oscillatory fields.	42
2.7	Ramsey pattern for spin up neutrons . . . . .	43
2.8	The polarizing system of the $^{199}\text{Hg}$ co-magnetometer. . . . .	46
2.9	DC-coupled Hg co-magnetometer signal . . . . .	48
2.10	Hg co-magnetometer AC-coupled signal. . . . .	49
3.1	Lowest electronic states for the even and the $^{199}\text{Hg}$ isotopes. . . . .	53
3.2	Isotopic composition of $^{199}\text{Hg}$ enriched mercury used in nEDM . . . . .	56
3.3	Zeeman effect of the hyperfine structure of $^{199}\text{Hg}$ . . . . .	60
3.4	Photograph of a $^{204}\text{Hg}$ discharge bulb as used in the nEDM setup. . . . .	62
3.5	Monte-Carlo simulation of an Ar-Hg discharge tube . . . . .	64
3.6	Isotopic composition of the mercury in a $^{204}\text{Hg}$ discharge bulb. . . . .	65
3.7	Scheme of the light path inside the Toptica FHG pro system. . . . .	66
3.8	Photograph of the open FHG. . . . .	67
3.9	The basic signals of a DAVLL. . . . .	72
3.10	Sketch of the SD-DAVLL setup . . . . .	74
3.11	SD-DAVLL setup picture . . . . .	75
3.12	Magnetic field in SD-DAVLL setup . . . . .	77
3.13	SD-DAVLL slope at different pump beam powers. . . . .	78
3.14	Typical SD-DAVLL signal for $^{199}\text{Hg}$ . . . . .	79
3.15	Full-width-half-maximum of the $^{199}\text{Hg}$ $F = 1/2$ line. . . . .	80
3.16	SD-DAVLL signal from natural Hg 1 . . . . .	81

3.17	SD-DAVLL signal from natural Hg 2 . . . . .	82
3.18	SD-DAVLL signal for $^{199}\text{Hg}$ $F = 3/2$ line in strong field . . . . .	83
3.19	UV fiber mount at nEDM experiment . . . . .	85
3.20	UV light beam in the nEDM vacuum tank. . . . .	86
4.1	Setups for absorption or paramagnetic rotation measurement. . . . .	88
4.2	Light absorption cross-section of $^{199}\text{Hg}$ . . . . .	92
4.3	Volume-averaged vector light shift in nEDM. . . . .	96
4.4	Volume-averaged vector light shift in nEDM (frequency zoom) . . . . .	97
4.5	Frequency dependence of the paramagnetic rotation effect. . . . .	101
4.6	$^{199}\text{Hg}$ co-magnetometer signal: model comparison . . . . .	104
5.1	Power spectral density of nEDM Run 9494, cycle 123 . . . . .	108
5.2	AC signal contrast for different readout light configurations. . . . .	110
5.3	Atomic polarization according to the small amplitude model. . . . .	112
5.4	Direct comparison of small amplitude and extended model. . . . .	113
5.5	Optical pumping time 2 . . . . .	115
5.6	Corrected atomic polarization vs light absorption. . . . .	116
5.7	Achieved SNDR for $^{204}\text{Hg}$ bulb detection light . . . . .	118
5.8	Achieved SNDR for UV laser detection light . . . . .	119
5.9	Histogram SNDR lamp $40^\circ\text{C}$ . . . . .	120
5.10	Histogram SNDR laser . . . . .	121
5.11	Ambient air pressure at PSI for Feb 1 and Feb 2 2013. . . . .	121
5.12	Influence of $^{204}\text{Hg}$ bulb temperature . . . . .	122
5.13	Histogram SNDR lamp $30^\circ\text{C}$ . . . . .	123
5.14	Magnetic field uncertainty as function of measurement time . . . . .	124
5.15	Model for the optical pumping process in the polarization chamber vs. experimental data . . . . .	129
5.16	Model prediction of the atomic polarization chamber vs. experimental data . . . . .	130
5.17	Depolarization induced by light. . . . .	136
5.18	Effect of oxygen discharge cleaning . . . . .	137
5.19	Wall and light induced spin relaxation . . . . .	140
A.1	The correction factor $C$ as a function of the signal sampling rate. . . . .	146
A.2	The correction factor $C$ as a function of the dimensionless parameter $r$ . . . . .	146
B.1	Isotopic composition of the $^{199}\text{Hg}$ enriched mercury. . . . .	148
B.2	Isotopic composition of $^{199}\text{Hg}$ enriched HgO from Trace Sciences. . . . .	149
C.1	Electronic scheme of bandpass filter part 1 . . . . .	153
C.2	Electronic scheme of bandpass filter part 2 . . . . .	154
D.1	Comparison of the signal amplitude predicted by three different models. . . . .	158
D.2	Influence of FID signal amplitude on signal decay time . . . . .	159

E.1	Commercial spectroscopy cell. . . . .	162
E.2	Hg spectroscopy cell in oven. . . . .	163
E.3	Normalized transmission spectrum of 20 mm spectroscopy cell . . . . .	164
F.1	Wavelength dependent light attenuation coefficient of UV optical fibers . .	168

# List of Tables

1.1	Transformation behavior of electromagnetic fields and spin under discrete symmetries . . . . .	20
1.2	Overview of current EDM limits on different atomic and subatomic systems.	27
1.3	UCN related properties of materials used in the nEDM experiment . . . .	30
3.1	Physical properties of the element mercury. . . . .	52
3.2	Properties of the stable mercury isotopes. . . . .	52
3.3	Properties of the $6^1S_0 \rightarrow 6^3P_1$ intercombination line. . . . .	54
3.4	Isotope shift and hyperfine splitting of the $6^1S_0 \rightarrow 6^3P_1$ transition in mercury.	55
3.5	Linear Zeeman shift of the magnetic sub-levels of the $6^1S_0$ ground state in the odd mercury isotopes. . . . .	58
3.6	The g-factors of the magnetic sub-levels of the $6^3P_1$ excited state in mercury.	59



# List of Symbols

Symbol	Meaning	Value (CODATA2010) or units
$h$	Planck's constant	$6.626\,069\,57(29) \times 10^{-34} \text{ J s}$
$\hbar$	reduced Planck's constant	$4.135\,667\,516(91) \times 10^{-16} \text{ eV s}$ $1.054\,571\,726(47) \times 10^{-34} \text{ J s}$ $6.582\,119\,28(15) \times 10^{-16} \text{ eV s}$
$c_0$	speed of light in vacuum	$299\,792\,458 \text{ m s}^{-1}$ (exact)
$c$	speed of light in medium	$\text{m s}^{-1}$
$\mu_0$	permeability of the vacuum	$4\pi \times 10^{-7} \Omega$ (exact) $= 12.566\,370\,614 \dots \times 10^{-7} \text{ N A}^{-2}$
$\epsilon_0$	electric constant $\frac{1}{\mu_0 c^2}$	$= 8.854\,187\,817 \dots \times 10^{-12} \text{ F m}^{-1}$ (exact)
$e$	elementary charge	$1.602\,176\,565(35) \times 10^{-19} \text{ A s}$
$m_{\text{u}}$	atomic mass unit	$1.660\,538\,921(73) \times 10^{-27} \text{ kg}$
$k_{\text{B}}$	Boltzmann constant	$1.380\,648\,8(13) \times 10^{-23} \text{ J K}^{-1}$ $8.617\,332\,4(78) \times 10^{-5} \text{ eV K}^{-1}$
$m_{\text{e}}$	electron mass	$9.109\,382\,91(40) \times 10^{-31} \text{ kg}$ $5.485\,799\,094\,6(22) \times 10^{-4} \text{ u}$
$m_{\text{p}}$	proton mass	$1.672\,621\,777(74) \times 10^{-27} \text{ kg}$ $1.007\,276\,466\,812(90) \text{ u}$
$m_{\text{n}}$	neutron mass	$1.674\,927\,351(74) \times 10^{-27} \text{ kg}$ $1.008\,664\,916\,00(43) \text{ u}$
$\mu_{\text{N}}$	nuclear magneton $e\hbar/2m_{\text{p}}$	$5.050\,783\,53(11) \times 10^{-27} \text{ J T}^{-1}$ $3.152\,451\,260\,5(22) \times 10^{-8} \text{ eV T}^{-1}$
$\mu_{\text{B}}$	Bohr magneton $e\hbar/2m_{\text{e}}$	$927.400\,968(20) \times 10^{-26} \text{ J T}^{-1}$ $5.788\,381\,806\,6(38) \times 10^{-5} \text{ eV T}^{-1}$
$\alpha^{-1}$	inverse fine-structure constant $\frac{e^2}{(4\pi\epsilon_0\hbar c)}$	$137.035\,999\,074(44)$
$\mu_{\text{e}}$	electron magnetic dipole moment	$-928.476\,430(21) \times 10^{-26} \text{ J T}^{-1}$ $-1.001\,159\,652\,180\,76(27) \mu_{\text{B}}$
$g_{\text{e}}$	electron g-factor $2\mu_{\text{e}}/\mu_{\text{B}}$	$-2.002\,319\,304\,361\,53(53)$
$\mu_{\text{p}}$	proton magnetic dipole moment	$1.401\,060\,674\,3(33) \times 10^{-26} \text{ J T}^{-1}$
$g_{\text{p}}$	proton g-factor $2\mu_{\text{p}}/\mu_{\text{N}}$	$5.585\,694\,713(46)$
$\gamma_{\text{p}}$	proton gyro magnetic ratio $2\mu_{\text{p}}/\hbar$	$2.675\,222\,005(63) \times 10^8 \text{ s}^{-1} \text{ T}^{-1}$

$\mu'_p$	shielded proton magnetic dipole moment (H <sub>2</sub> O, sphere, 25 °C)	42.577 480 6(10) MHz s <sup>-1</sup> 1.410 570 499(35) × 10 <sup>-26</sup> J T <sup>-1</sup>
$\mu_n$	neutron magnetic dipole moment	-0.966 236 47(23) × 10 <sup>-26</sup> J T <sup>-1</sup> 60.307 740(15) neV T <sup>-1</sup>
$g_n$	neutron g-factor $2\mu_n/\mu_N$	-3.826 085 45(90)
$\gamma_n$	neutron gyro magnetic ratio $2\mu_n/\hbar$	-1.832 471 79(43) × 10 <sup>8</sup> s <sup>-1</sup> T <sup>-1</sup> 29.164 694 3(69) MHz s <sup>-1</sup>
$\omega$	angular frequency	s <sup>-1</sup>
$\nu$	frequency	Hz
$\omega_L$	Larmor frequency	s <sup>-1</sup>
$N$	number density	m <sup>-3</sup> or cm <sup>-3</sup>
$\rho$	mass density	kg m <sup>-3</sup> or g cm <sup>-3</sup>
$g_X$	g-factor of particle or atom in state X	1
$d_n$	neutron electric dipole moment	
<b>E</b>	electric field	V m <sup>-1</sup>
<b>B</b>	magnetic field	T
E	energy	V or J
V	potential energy	
U	voltage	V
T	temperature	K
<b>I</b>	nuclear spin vector	$\hbar$
<b>L, l</b>	orbital angular momentum	$\hbar$
<b>S, s</b>	single particle spin	$\hbar$
<b>J, j</b>	total electron angular momentum	$\hbar$
<b>F, f</b>	total atomic angular momentum	$\hbar$
<i>I</i>	nuclear spin	$\hbar$
<i>L, l</i>	orbital angular momentum	$\hbar$
<i>S, s</i>	single particle spin	$\hbar$
<i>J, j</i>	total electronic angular momentum	$\hbar$
<i>F, f</i>	total atomic angular momentum	$\hbar$
$\mu_X$	magnetic dipole moment of particle X	
$\sigma$	cross-section	cm <sup>2</sup> or b = 10 <sup>-24</sup> cm <sup>2</sup>
$\sigma^+$	left circular polarized light	
$\sigma^-$	right circular polarized light	
$\pi$	linear polarized light	
<i>Z</i>	nuclear charge number	

# List of Acronymes

<b>AC</b>	Alternating current
<b>AOM</b>	Acousto-optic modulator
<b>BAU</b>	Baryon asymmetry of the universe
<b>BS</b>	Beam splitter (cube)
<b>CERN</b>	European Organization for Nuclear Research
<b>CKM</b>	Cabibbo-Kobayashi-Maskawa (matrix)
<b>CP</b>	Combined operation of charge inversion and parity
<b>CPT</b>	Combined operation of charge inversion and parity and time-reversal
<b>CRLB</b>	Cramér Rao lower bound
<b>CMB</b>	Cosmic Microwave Background
<b>DAQ</b>	Data acquisition
<b>DAVLL</b>	Dichroic atomic vapor laser lock
<b>DC</b>	Direct current
<b>DPS</b>	Deuterated polystyrene
<b>EDM</b>	Permanent electric dipole moment
<b>EOM</b>	Electro-optic modulator
<b>FHG</b>	Fourth-harmonic generator
<b>FWHM</b>	Full width at half maximum
<b>Hg</b>	The element mercury
<b>HV</b>	High voltage
<b>ILL</b>	Institut Laue-Langevin
<b>LHC</b>	Large Hadron Collider
<b>nEDM</b>	Neutron electric dipole moment
<b>NDF</b>	Neutral density filter
<b>PBS</b>	Polarizing beam splitter (cube)
<b>PD</b>	Photodiode
<b>PMT</b>	Photomultiplier tube
<b>PRM</b>	Partially reflecting mirror
<b>PSI</b>	Paul Scherrer Institute
<b>QCD</b>	Quantum Chromodynamics
<b>RAL</b>	Rutherford Appleton Laboratory
<b>RF</b>	Radio frequency
<b>SCM</b>	Superconducting magnet

<b>SD-DAVLL</b>	Sub-Doppler Dichroic atomic vapor laser lock
<b>SFC</b>	Surrounding field compensation system
<b>SM</b>	Standard model
<b>SNDR</b>	Signal-to-noise-density ratio
<b>SATP</b>	Standard ambient temperature (298.15 K) and pressure (101.325 kPa)
<b>STP</b>	Standard temperature (273.15 K) and pressure (101.325 kPa)
<b>SUSY</b>	Supersymmetry
<b>UCN</b>	Ultracold neutron
<b>UVFS</b>	Ultraviolet grade fused silica
<b>UV</b>	Ultraviolet light

# Chapter 1

## Introduction

The search for a permanent electric dipole moment of the neutron (nEDM) is at the forefront of modern particle physics. With its long standing history it has served to test the modern quantum field theory formulation of the standard model (SM) of particle physics which is based on the concept of gauge fields and their symmetries. In 1950, E. Purcell and N. Ramsey were the first ones to point out that these symmetry assumptions must be tested experimentally [PR50]. They proposed to test the conservation of time reversal symmetry by the search for a permanent electric dipole moment (EDM) of the neutron and published a first experimental upper limit in 1957 together with J. Smith in Ref. [SPR57]. Since then searches for EDMs have been performed in many different molecular, atomic and subatomic systems but up to date no finite value has been found and only upper experimental limits have been set.

The importance of experimental tests of symmetries was demonstrated in the same year when the violation of parity (P) symmetry was observed in the weak interaction. First in nuclear beta decay by C. Wu *et al.* [WAH<sup>+</sup>57] and shortly after in the decay of charged  $\pi$  mesons by R. Garwin *et al.* [GLW57] and by J. Friedman and V. Teledgi [FT57]. The combined symmetry operation of charge conjugation and parity (CP) relates the matter and anti-matter particles observed in nature. The assumption that this could be a good (a conserved) symmetry of nature was disproven in 1964 by J. Christenson *et al.* [CCFT64]. They observed the decay of neutral K mesons into two and three pions. Furthermore, due to our own existence it appears obvious that during the evolution of the universe CP symmetry was broken as we live in a matter dominated universe. Calculations of the expected baryonic matter/anti-matter asymmetry of the universe (BAU) based on the CP violation found in the neutral meson systems fall short by about eight orders of magnitude relative to the BAU as extracted from the observation of the cosmic microwave background (CMB) [Rio98].

Besides the unexplained BAU there are two other long-standing puzzles in modern (astro-)particle physics. The first one was pointed out by F. Zwicky as early as 1933 [Zwi33, Zwi37]. Studies of the rotation curves of spiral galaxies revealed that these galaxies cannot be bound only by the gravitational interaction of their visible (i.e. electromagnetically interacting) matter. There has to be much more ‘dark matter’ than visible ordinary

matter in these galaxies to provide enough gravitational interaction to counterbalance the centrifugal forces. The second puzzle (a bit younger than the first one) comes from the studies of type Ia super novae. Their results have established that the universe is expanding at an accelerated rate while attractive gravity would decelerate the expansion [PAG<sup>+</sup>99, RFC<sup>+</sup>98]. The acceleration effect is attributed to the so-called ‘dark energy’ as the physical origin of this effect is yet unclear. The most recent observations of the CMB by the *Planck* satellite imply that ordinary matter as described in the SM makes up only about 4.9% of the energy content of the universe, while dark matter contributes about 26.5% and dark energy about 68.5% [AAAC<sup>+</sup>13].

Despite these shortcomings the SM has withstood a near endless list of high and low energy precision tests. The discovery of the long sought Higgs boson at the Large Hadron Collider (LHC) of CERN with a mass of about  $126 \text{ GeV}/c_0^2$  [Ac12, Cc12] is one of its most recent successes. Furthermore no proof for physics beyond the SM has been found within the energy range investigated by the LHC so far, suggesting that the SM is valid at least up to the TeV range. But despite its successes one has to conclude that the current version of the SM cannot be a complete description of the universe we see and that extensions have to be added to the SM to explain all observations. A large number of theoretical models have been developed to extend the SM seeking explanations for the yet unsolved problems like the BAU, dark matter, and dark energy. While offering solutions to the problems mentioned above many models predict EDMs orders of magnitude larger than in the SM. Since any EDM induced by the electroweak interaction in the SM is suppressed by many orders of magnitude below the experimental sensitivity accessible now or in the near future, searches for EDMs provide a probe for new physics beyond the SM free from electroweak background contributions. For CP violating effects in the strong interaction (QCD) part of the SM extremely stringent bounds are already provided by the current lowest upper limit on a nEDM.

The existing bound on the nEDM  $d_n \leq 2.9 \times 10^{-26} e\text{-cm}$  90% CL [BDG<sup>+</sup>06] restricts the so-called  $\bar{\theta}$ -term in QCD to as low as  $\approx 10^{-10}$ . A first solution to the question why the  $\bar{\theta}$ -term is so (surprisingly) small was proposed by R. Peccei and H. Quinn in 1977 in Ref. [PQ77]. A new hypothetical particle, the so-called *axion* around the energy scale of the electroweak interaction was postulated but is meanwhile ruled out by experiments. But axions or axion-like particles at different energy scales are still up for discovery in case they exist. Thus one can conclude that searches for EDMs at the low energy, but high intensity, edge of the SM are at the forefront of modern particle physics. Complementary to efforts of direct observation of new physics at the high energy frontier, low energy precision measurements continue to test theories of physics beyond the standard model of particle physics.

## 1.1 Dipole moments and symmetries

Symmetries are encountered very often in every day life, mostly in the geometrical context. While a triangle or a square have discrete symmetries (only rotations through certain

angles leave these objects unchanged), a circle is an object with continuous symmetry (an arbitrarily small or large rotation around the center leaves the circle unchanged). Also physical quantities can, in general, be characterized by their transformation behavior under certain discrete or continuous parameter transformations. A physical quantity is said to be symmetric under a certain operation if it remains unchanged. On the other hand a symmetry is said to be broken if the considered quantity changes and thus allows one to distinguish between the system's state before and after the symmetry operation.

The fundamental laws of energy, momentum or angular momentum conservation can be derived for a physical system that shows local continuous symmetry under time translation, spatial translation or angular rotation [Noe18]. The concept of symmetries has proven extremely useful for understanding the underlying structures of the SM. In the context of this work the most relevant discrete parameter transformations are the following:

- parity operation (P):  $\mathbf{x} \rightarrow -\mathbf{x}$ , inversion of all spatial coordinates (for an odd number of space dimensions)
- charge conjugation operation (C):  $q \rightarrow -q$ , inversion of all charges
- time reversal operation (T) :  $t \rightarrow -t$ , inversion of the direction of time.

In the SM the weak interaction is not invariant under the C operation. It only acts on left-handed particle or right-handed anti-particle states. The C operation transforms, e.g., left-handed particle into left-handed anti-particle states that are not observed in nature. Only the combined operation of  $CP$  relates the left-handed particle and right-handed anti-particle states which are observed.

To show the importance of the transformation behavior under the discrete parity and time reversal symmetry operations the electromagnetic interaction of a spin 1/2 particle  $f$  (charge  $Q_f e$ ) with a combination of electric  $\mathbf{E}$  and magnetic  $\mathbf{B}$  fields is presented according to the arguments of A. Czarnecki and W. Marciano in Ref. [RM10]. The matrix elements of the electromagnetic current  $J_\mu$  between the initial and the final state of a spin 1/2 particle (mass  $m_f$ ) with initial four-momentum  $p$  and final four-momentum  $p'$  are given by

$$\langle f(p') | J_\mu^{\text{em}} | f(p) \rangle = \bar{u}_f(p') \Gamma_\mu u(p) \quad (1.1)$$

where  $\bar{u}$  and  $u$  represent the Dirac spinors and  $\Gamma_\mu$  is given by

$$\Gamma_\mu(q) = F_1(q^2) \gamma_\mu + iF_2(q^2) \sigma_{\mu\nu} q^\nu - F_3(q^2) \sigma_{\mu\nu} q^\nu \gamma_5 + F_A(q^2) (\gamma_\mu q^2 - 2m_f q_\mu) \gamma_5 \quad (1.2)$$

where  $q = p' - p$  is the four-momentum transfer,  $\sigma_{\mu\nu} = \frac{i}{2} [\gamma_\mu, \gamma_\nu]$  and  $\gamma_5$  are combinations of the Dirac matrices and the form factors  $F_1$ ,  $F_2$ ,  $F_3$  and  $F_A$  describe the electric charge, the anomalous magnetic moment, the electric dipole moment and the anapole moment of the particle in the limit of  $q \rightarrow 0$ ,

$$F_1(0) = Q_f e, \quad (1.3)$$

$$F_2(0) = a_f Q_f \frac{e}{2m_f}, \quad (1.4)$$

$$F_3(0) = d_f Q_f. \quad (1.5)$$

	P	T	C
<b>B</b>	+	-	-
<b>s</b>	+	-	+
<b><math>\mu</math></b>	+	-	-
<b>E</b>	-	+	-

Table 1.1: Transformation behavior of the electric field **E**, the magnetic field **B** and the spin **s** under the discrete time reversal transformation T, the parity operation P and the charge conjugation operation C.

The effective dipole interaction Hamiltonian is given by

$$H_{\text{dipole}} = -\frac{1}{2} \left( iF_3 \bar{f} \sigma_{\mu\nu} \gamma_5 f + F_2 \bar{f} \sigma_{\mu\nu} f \right) F^{\mu\nu} \quad (1.6)$$

where  $F^{\mu\nu}$  is the electromagnetic field tensor. According to A. Czarnecki and W. Marciano this approach can be extended to neutral spin 1/2 particles like the neutron by replacing the charge  $Q_f$  with the charge of the particle's isospin partner. For the neutron the isospin partner is the proton, thus  $Q_n = +1$ .

In the 'non-relativistic' limit, the interaction Hamiltonian is given by

$$H_{\text{nonrel}} = -\mathbf{d}\mathbf{E} - \boldsymbol{\mu}\mathbf{B} = (-\mathbf{d}\mathbf{E} - \boldsymbol{\mu}\mathbf{B}) \frac{\mathbf{s}}{s} \quad (1.7)$$

where  $\mu$  is the magnetic dipole and  $d$  the electric dipole moment of the particle. The sign of  $d$  determines the relative orientation of the electric and magnetic dipole moment but is unknown as no finite EDM value has been detected to date. According to the Wigner-Eckart theorem the highest rank moment for a spin 1/2 particle are dipole moments proportional to the spin. The anapole moment vanishes in the case of a single nucleon. Thus the electromagnetic interaction is quantum mechanically fully described by (1.7). The two dipole moments have to be aligned parallel or anti-parallel to the spin **s** as this is the only well defined direction of the system without external fields. The transformation behavior of (1.7) can be derived from the transformation behavior of its single constituents as listed in Table 1.1 and depicted in Figure 1.1.

## Parity

As can be seen from Table 1.1 the parity operation changes (1.7) to

$$H_{\text{nonrel,P}} = -\mathbf{d}(-\mathbf{E}) - \boldsymbol{\mu}\mathbf{B} \neq H_{\text{nonrel}} \quad (1.8)$$

The part related to the electric dipole moment violates the symmetry while the part related to the magnetic dipole moment conserves the symmetry.



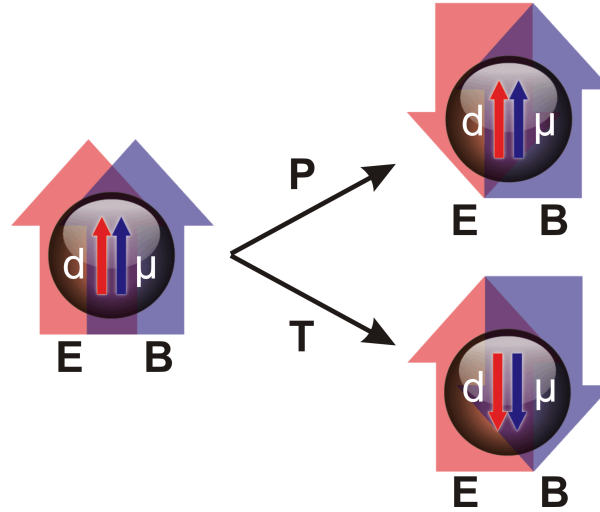


Figure 1.1: The electromagnetic dipole interaction with external fields under the time reversal T and parity P operation.

### Time reversal symmetry

In the same way it can be seen from Table 1.1 that the time reversal operator changes (1.7) to

$$H_{\text{nonrel},T} = -(-\mathbf{d})\mathbf{E} - (-\boldsymbol{\mu})(-\mathbf{B}) \neq H_{\text{nonrel}} \quad (1.9)$$

The part related to the electric dipole moment violates the symmetry while the part related to the magnetic dipole moment conserves the symmetry.

The interaction of the electric dipole moment with the electric field breaks the symmetry explicitly as the Hamiltonian/Lagrangian of the system is not invariant under the symmetry operation. If the Lagrangian of a system possesses the symmetry, but its energetic ground state does not then the symmetry is said to be spontaneously broken.

### CP and CPT violation

The CPT theorem [Lüd57, Bel55, Pau57] states that for any local Lorentz-covariant field theory of a point-like particle, the combined application of charge conjugation C, parity P and time reversal T operation has to leave the Hamiltonian in (1.7) unchanged. Thus the breaking of T symmetry by a permanent electric dipole moment implies the breaking of the CP symmetry as well, in case the CPT theorem applies. Furthermore EDM limits can be used to constrain CPT odd, but CP even effects [BPR08].

## 1.2 Sources of CP violation and nEDM predictions within the SM

Within the SM there are two sources of CP violation. The first one lies within the electroweak sector. As the mass eigenstates of the quarks (unprimed) are not identical to their weak interaction eigenstates (primed) the weakly interacting quark states are superpositions of the mass eigenstates. Both eigenstates are connected by the  $3 \times 3$  Cabibbo-Kobayashi-Maskawa matrix (CKM matrix,  $V_{\text{CKM}}$  [KM73]):

$$\begin{pmatrix} d' \\ s' \\ b' \end{pmatrix} = \begin{pmatrix} V_{ud} & V_{us} & V_{ub} \\ V_{cd} & V_{cs} & V_{cb} \\ V_{td} & V_{ts} & V_{tb} \end{pmatrix} \times \begin{pmatrix} d \\ s \\ b \end{pmatrix}. \quad (1.10)$$

One possible parameterization (including a global phase transformation of the quark states) of this matrix was proposed by L. Chau and W. Keung in Ref. [CK84]

$$V_{\text{CKM}} = \begin{pmatrix} c_{12}c_{13} & s_{12}c_{13} & s_{12}e^{-i\delta} \\ -s_{12}c_{23} - c_{12}s_{23}s_{13}e^{i\delta} & c_{12}c_{23} - s_{12}s_{23}s_{13}e^{i\delta} & s_{23}c_{13} \\ s_{12}s_{23} - c_{12}c_{23}s_{13}e^{i\delta} & -c_{12}s_{23}s_{13}e^{i\delta} & c_{23}c_{13} \end{pmatrix}, \quad (1.11)$$

where  $c_{ij} = \cos \theta_{ij}$ ,  $s_{ij} = \sin \theta_{ij}$  and  $\delta$  is a phase inducing all CP-violating effects observed, e.g., in the decay of neutral K mesons. The three angles and the phase parameter have the following experimental values [Gro12]:

$$\theta_{12} = (13.024 \pm 0.038)^\circ \quad (1.12)$$

$$\theta_{13} = (0.201_{-0.010}^{+0.019})^\circ \quad (1.13)$$

$$\theta_{23} = (2.360_{-0.021}^{+0.078})^\circ \quad (1.14)$$

$$\delta = 1.208_{-0.019}^{+0.053} \text{ rad} \quad (1.15)$$

The largest matrix element related to  $\delta$  is  $s_{12}e^{-i\delta} \approx 3.5 \times 10^{-3} e^{-i\delta}$  revealing that CP violation in the electroweak quark sector is a small effect. However, there is a finite contribution to the nEDM via a so-called *strong penguin diagram* shown in Figure 1.2. This contribution was calculated by M.B. Gavela *et al.* [GYO<sup>+</sup>84] and by I.B. Khriplovich *et al.* [KZ82] and was found to be

$$d_n \simeq 1 \times 10^{-32} e\text{-cm}. \quad (1.16)$$

The current best experimental upper limit  $d_n \leq 2.9 \times 10^{-26} e\text{-cm}$  CL 90% [BDG<sup>+</sup>06] lies about six orders of magnitude above the value of (1.16).

The second source of CP violation in the SM is related to the strong interaction described by quantum chromodynamics (QCD). Below 1 GeV the heavy particle degrees of freedom in the Lagrangian can be integrated out (replaced by effective field theory constants) to derive an effective Lagrangian for the low energy limit of the SM. The CP-odd

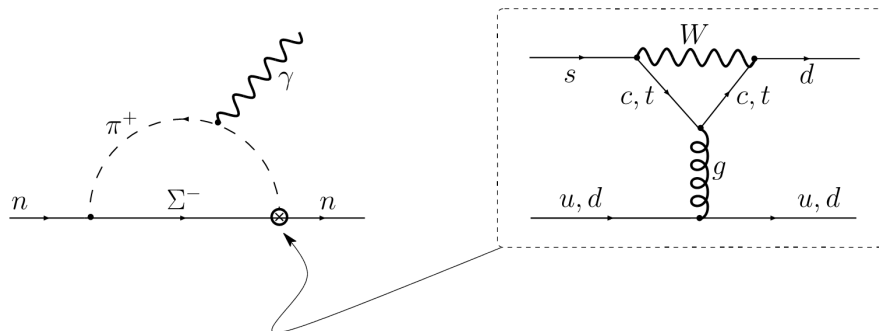


Figure 1.2: In the SM the largest electroweak contribution to a nEDM comes from the so-called *strong-penguin* diagram, that is enhanced via a chiral  $\pi^+$  loop. The picture is taken from Ref. [PR05].

terms can be ordered according to their dimension. The only CP-odd operator of dimension 4 is [PR05]

$$\mathcal{L}_{\text{dim}=4}^{\text{CP-odd}} = \frac{g_s^2}{32\pi^2} \bar{\theta} G_{\mu\nu}^a \tilde{G}^{\mu\nu,a}, \quad (1.17)$$

where  $g_s$  is the coupling constant of the strong interaction,  $\bar{\theta}$  a scalar and  $G_{\mu\nu}^a$  the gluon field tensor of QCD. This CP-odd operator induces a nEDM on the order of [PR05]

$$d_n \sim e \frac{\bar{\theta} m_*}{\Lambda_{\text{had}}^2} \sim \bar{\theta} \cdot 6 \times 10^{-17} \text{ e}\cdot\text{cm}, \quad (1.18)$$

where  $\Lambda_{\text{had}}$  is the cut-off scale of the effective field theory,  $m_* = m_u m_d / (m_u + m_d)$  is the reduced quark mass with the masses of the u(d) quarks  $m_u(m_d)$ . The current best upper limit [BDG<sup>+</sup>06] for  $d_n \leq 2.9 \times 10^{-26} \text{ e}\cdot\text{cm}$  CL 90 % restricts  $\bar{\theta}$  to a value  $\approx 10^{-10}$ . This is known as the strong CP problem. It is an open question why the value of  $\bar{\theta}$  is so small. In 1977 R. Peccei and H. Quinn [PQ77] proposed a new particle, the *axion*, to explain this puzzle. While the originally proposed axion at the electroweak energy scale is ruled out by experiment, axion-like particles still await their discovery in one of the various dedicated experiments, in case they exist [Gro12]. For a more detailed review of the relation between the strong CP problem and the axion the reader is referred to Ref. [KC10].

### 1.3 Sources of CP violation and nEDM predictions beyond the SM

Most extensions of the SM assume that the SM is only a low energy limit of a more fundamental high energy physics framework. High-energy effects can influence quantities, that are measurable in the low-energy limit, via virtual particles in quantum loops. As

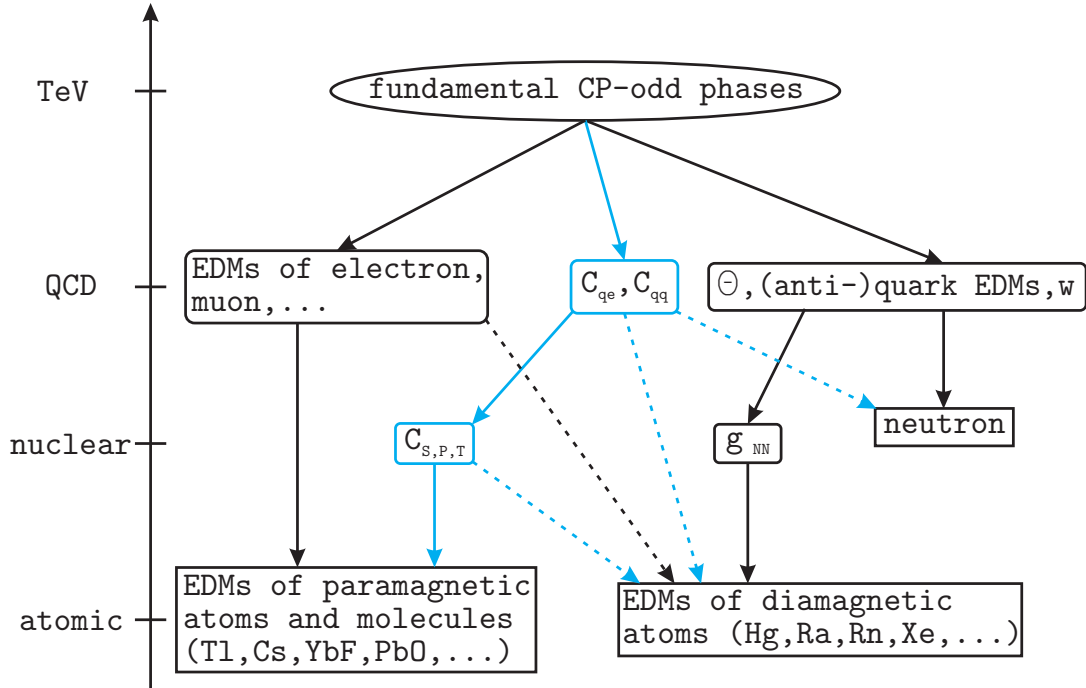


Figure 1.3: Overview of the possible different sources of CP violation beyond the SM in the systems accessible to direct measurements. Solid arrows indicate strong dependencies between a certain parameter and an EDM in the system, while dashed lines represent weaker dependencies. The scheme is taken from Ref. [PR05] with minor modification by the author.

shown in Figure 1.3 fundamental CP-odd parameters can be expected to propagate from an underlying high energy model ( $\approx TeV$ ) to the low energy limit that is probed by a variety of experiments. As pointed out in the previous section, EDMs are a manifestation of CP violation in case the CPT theorem is applicable. In [PR05] EDM searches in composite systems are grouped into three subsets

- the neutron
- paramagnetic atoms and molecules (Cs, Tl, YbF, PbO, ThO...)
- diamagnetic atoms (Hg, Ra, Rn, Xe, ...)

Searches for EDMs have also been performed in the leptonic sector of the SM. The only fundamental fermion for which a direct experimental EDM limit exists [BBB<sup>+</sup>09] is the muon, for the electron the limits are derived from measurements in composite (atomic or molecular) systems. Depending on the energy scale, different manifestations of the

fundamental CP-odd phases are probed, e.g., in terms of coupling constants or intrinsic fundamental fermion EDMs.

For systems with substructure a detailed theoretical understanding is needed on all energy levels involved in the system to relate the intrinsic parameters of the constituents to the measurable properties of the combined system. In general this is a very difficult task. For diamagnetic atoms like  $^{199}\text{Hg}$  a measurable EDM of the atom can be generated via the Schiff-mechanism [FG02] due to the finite size of the nucleus or via the interaction of the nuclear EDM with the hyperfine interaction within the atom [PGF11]. For a review on the state of the art of nuclear EDM calculations the reader is referred to Ref. [ERMvK13]. The effect of an intrinsic electron EDM on the diamagnetic atom is similarly difficult to calculate. The most recent calculations for the  $^{199}\text{Hg}$  atom, dating from the 1980's, agree in the order of magnitude, but not on the sign of the atomic EDM induced by an electron EDM [MPO87, FK85, FD12]. On the other hand a bare nucleon, e.g., a free neutron offers direct access to its electric dipole moment but is much more difficult to obtain for experimental investigations.

## 1.4 Current and prospective limits of EDM measurements

As motivated in Figure 1.3 one can expect to find EDMs in many fundamental and composite systems. Therefore EDM searches have been performed for nearly all the given systems over the past decades. Table 1.2 gives an overview on the current best upper limits for the EDMs of several particles and the systems in which they have been measured. The currently lowest experimental upper limit for the EDM of any particle is provided by the measurements on  $^{199}\text{Hg}$  [GSL<sup>+</sup>09]

$$d_{\text{Hg}} \leq 3.1 \times 10^{-29} \text{ e}\cdot\text{cm} \text{ (95 \% CL)}. \quad (1.19)$$

For the nEDM the currently lowest upper limit was published in 2006 [BDG<sup>+</sup>06]

$$d_{\text{n}} \leq 2.9 \times 10^{-26} \text{ e}\cdot\text{cm} \text{ (90 \% CL)}. \quad (1.20)$$

Since then several collaborations worldwide have set out on the journey to improve the nEDM limit.

The sensitivity scaling behavior of a typical Ramsey type nEDM experiment (as explained in detail in Section 2.3) is given by

$$\sigma(d_{\text{n}}) = \frac{\hbar}{2\alpha ET\sqrt{N_0}}. \quad (1.21)$$

Here  $\hbar$  is the reduced Planck constant,  $\alpha$  the contrast between the two neutron spin states,  $E$  the electric field strength felt by the neutron,  $T$  the interaction time and  $N_0$  the number of detected neutrons. A major improvement in sensitivity is expected from a larger number

of detected neutrons. Currently most approaches make use of storable, so-called ultra-cold neutrons (UCNs, see Section 1.5). These approaches can be roughly divided into two subgroups:

- **In-vacuum, room temperature experiments:** The UCNs are extracted from a UCN source into a vacuum chamber at room temperature. Spin precession experiments are performed in this vacuum chamber that consists of conducting electrodes (that can be charged to high voltage to provide the electric field) and an insulating spacer. The main advantage is to avoid any cryogenic environment in the experiment setup itself which allows, e.g., for short turn around times for component testing. But extraction losses from the source can significantly lower the number of available UCNs. Detailed descriptions of these experiments can be found in the literature, e.g., in Refs. [BBB<sup>+</sup>11, ABC<sup>+</sup>13, MAH<sup>+</sup>12, SBE<sup>+</sup>11]
- **Cryogenic experiments:** In cryogenic experiments UCNs are directly produced in superfluid helium by irradiation with a beam of cold neutrons. Thus one can avoid extraction losses for the UCN and make use of the higher electric field that can be applied across the superfluid helium. The long turn around times of large cryostats, in the case that modifications of the experiment are necessary, is a major disadvantage. Details on those experiments can be found, e.g., in Refs. [vdG09, Ito07].

Besides UCN experiments there is also an approach that makes use of the extremely large internal electric fields available in non-centrosymmetric crystals to enhance the sensitivity to a nEDM. In this case a beam of cold neutrons is passed through, e.g., a quartz crystal where the orientation of the electric field depends on the relative position to the nuclear planes [FJK<sup>+</sup>09].

On a longer time scale all UCN nEDM experiments aim for a sensitivity in the  $d_n \approx 1 \times 10^{-28} e \cdot \text{cm}$  range. The nEDM@PSI collaboration has chosen a two step approach. The sensitivity goal for the nEDM@PSI in a first phase is

$$d_n < 5 \times 10^{-27} e \cdot \text{cm} \text{ (95 \% CL)}. \quad (1.22)$$

For the second step with a new nEDM spectrometer, which is currently being designed, one aims at a sensitivity of

$$d_n < 5 \times 10^{-28} e \cdot \text{cm} \text{ (95 \% CL)}. \quad (1.23)$$

## 1.5 Ultra-cold neutrons

The nEDM@PSI as described in Chapter 2 is performed with so-called ultra-cold neutrons (UCN). Ultra-cold neutrons have very low kinetic energies such that they are reflected from a material surface under all angles of incidence. The following subsections summarize the most important properties of UCN relevant for the nEDM experiment. A short subsection is devoted to the production mechanism of UCN and the UCN source at PSI.

	Value / $e \cdot \text{cm}$	Reference	System
$d_e$	$\leq 1.05 \times 10^{-27}$ (90%CL)	[HKS <sup>+</sup> 11]	YbF
	$\leq 1.6 \times 10^{-27}$ (90%CL)	[RCSD02]	Tl
$d_\mu$	$\leq 1.0 \times 10^{-19}$ (95%CL)	[BBB <sup>+</sup> 09]	$\mu^\pm$
$d_n$	$\leq 2.9 \times 10^{-26}$ (90%CL)	[BDG <sup>+</sup> 06]	n
$d_p$	$\leq 7.9 \times 10^{-25}$ (95%CL)	[GSL <sup>+</sup> 09], theory: [DS03]	<sup>199</sup> Hg
$d_{\text{Hg}}$	$\leq 3.1 \times 10^{-29}$ (95%CL)	[GSL <sup>+</sup> 09]	<sup>199</sup> Hg

Table 1.2: Overview of current EDM limits on different molecular, atomic and subatomic systems.

### 1.5.1 Neutron optical potential

To explain the total reflection of low kinetic energy neutrons from material surfaces one has to consider the interaction of a slow neutron (vacuum wavelength  $\lambda$ ) with an atomic nucleus. The derivation of the neutron optical potential presented in this subsection follows mainly the presentation in Ref. [GRL91, Fer09].

In 'first order' Born approximation the interaction of a slow neutron with an atomic nucleus (mass number  $A$ ) can be described as the superposition of an incident plane wave and an outgoing scattered spherical wave

$$\psi = e^{i\mathbf{k}\cdot\mathbf{r}} + f(\theta) \frac{e^{ikr}}{r}. \quad (1.24)$$

Here  $\mathbf{k}$  is the wave vector of the incident neutron,  $\mathbf{r}$  is its position vector relative to the nucleus and  $f(\theta)$  is the so-called scattering amplitude. Since the interaction range  $R$  between the neutron and the nucleus is much shorter than the neutron wavelength ( $R \ll \lambda$ ) only isotropic S-wave scattering ( $l = 0$ ) can occur. Therefore  $f(\theta)$  is reduced to a constant neutron scattering length  $a$

$$f(\theta) = \text{const.} = -a. \quad (1.25)$$

In a simplified picture the scattering potential of a single nucleus can be approximated by a square well potential as pointed out in Ref. [FM47]. With the choice of a negative sign between scattering amplitude and scattering length, the far field wavefunction  $\psi \approx \frac{r-a}{r}$  vanishes at  $r = a$ . Thus  $a$  can be interpreted as the effective radius of the effective scattering potential.

According to Fermi's Golden Rule the differential scattering cross-section is given by

$$\frac{d\sigma}{d\Omega} = |f(\theta)|^2 = a^2, \quad (1.26)$$

where  $\Omega$  denotes the solid angle. Since  $R \ll \lambda$ , the physical interaction potential between the neutron and the nucleus can be represented by the so-called Fermi pseudo-potential  $V_F$

$$V_F = \frac{2\pi\hbar^2 a}{m_n} \delta^3(\mathbf{r} - \mathbf{R}), \quad (1.27)$$

where  $m_n$  is the mass of the neutron,  $\mathbf{R}$  the nucleus position vector and  $a$  the neutron scattering length.

In case of an ensemble of nuclei the scattered wave is a coherent superposition of the waves scattered by each single nucleus. The normalization constant is chosen such that in the far field the results for the real physical potential and the pseudo-potential coincide. Thus the scattering amplitude is given as

$$f(\theta) = \sum_k a_k e^{i\mathbf{Q}\cdot\mathbf{R}_k}, \quad (1.28)$$

where  $\mathbf{Q}$  is the wave vector transfer,  $a_k$  is the scattering length and  $\mathbf{R}_k$  the position vector of the  $k$ -th nucleus. In case of unpolarized neutrons one has to perform the sum over all spin states (and if applicable over all isotopic components)

$$\frac{d\sigma}{d\Omega} = \overline{|f(\theta)|^2} = \overline{\left| \sum_k a_k e^{i\mathbf{Q}\cdot\mathbf{R}_k} \right|^2} = \sum_{k,j} \overline{a_k^* a_j} e^{i\mathbf{Q}\cdot(\mathbf{R}_j - \mathbf{R}_k)}. \quad (1.29)$$

The correlation between the neutron scattering lengths  $a_k$  and  $a_j$  vanishes for a random distribution of the isotopes and spin states in the array of scattering centers and results in

$$\overline{a_k^* a_j} = \overline{a_k^*} \overline{a_j} = |\bar{a}|^2 \quad k \neq j \quad (1.30)$$

and

$$\overline{a_k^* a_j} = \overline{|a|^2} \quad k = j. \quad (1.31)$$

Equation 1.29 can be rewritten as

$$\frac{d\sigma}{d\Omega} = |\bar{a}|^2 \sum_{k \neq j} e^{i\mathbf{Q}\cdot(\mathbf{R}_j - \mathbf{R}_k)} + \sum_{k=1}^N \overline{|a|^2} \quad (1.32)$$

$$= |\bar{a}|^2 \left| \sum_k e^{i\mathbf{Q}\cdot\mathbf{R}_k} \right|^2 + N \overline{|a - \bar{a}|^2} \quad (1.33)$$

$$= a_{\text{coh}}^2 \left| \sum_k e^{i\mathbf{Q}\cdot\mathbf{R}_k} \right|^2 + N a_{\text{inc}}^2, \quad (1.34)$$

giving the definition of the coherent  $a_{\text{coh}}$  and the incoherent  $a_{\text{inc}}$  neutron scattering length. The first term in Eqn. 1.34 represents the diffraction of neutrons from nuclei (Bragg scattering). In spatial directions where the wave vector transfer  $\mathbf{Q}$  fulfills

$$\mathbf{Q} \cdot \mathbf{R}_k = 2\pi n \quad (n \in \mathbb{Z}) \quad (1.35)$$

the first term of Eqn. 1.34 is proportional to  $N^2$  where  $N$  is the number of scattering centers (Bragg peaks). The second term in Eqn. 1.34 vanishes for a mono-isotopic array of scattering centers as  $a = \bar{a}$ . Since the wavelength of UCN ( $> 500 \text{ \AA}$ ) is much larger than



the internuclear distance in any material ( $\leq 10 \text{ \AA}$ ) Eqn. 1.35 cannot hold true and there is no Bragg scattering of UCNs. In the large wavelength limit ( $> 500 \text{ \AA}$ ) the sum of Fermi pseudo-potentials (as given in Eqn. 1.27) can be replaced by a volume-average potential

$$V_F = \frac{2\pi\hbar^2}{m_n} [an(\mathbf{r})], \quad (1.36)$$

where  $n(\mathbf{r})$  is the number density of scattering centers.

This can be interpreted as a potential energy step at the surface of the material from which neutrons can be reflected. To determine the reflection behavior of a neutron from the wall one has to solve the Schrödinger equation in the different potential regions. In the region of the material wall the equation is given by

$$-\frac{\hbar^2}{2m_n} \nabla^2 \psi + \frac{2\pi\hbar^2}{m_n} [n(\mathbf{r})] \psi = \frac{\hbar^2 k_0^2}{2m_n} \psi, \quad (1.37)$$

where  $k_0 = \sqrt{2m_n E/\hbar^2}$  is the wave vector of the incident neutron in vacuum (with energy  $E$ ). This is equivalent to a wave equation in a material with refractive index

$$n_R(\mathbf{r}) = \sqrt{1 - \frac{4\pi [an(\mathbf{r})]}{k_0^2}}. \quad (1.38)$$

Since for most materials  $n_R < 1$ , total reflection on the vacuum-to-material interface can occur for neutrons of sufficiently low kinetic energy transverse to the interface. Ultra-cold neutrons can be reflected under all angles of incidence. Neutron reflectometry is a very sensitive method to investigate surface properties of samples. Note the reciprocity to the total reflection of light where vacuum is the less optically dense medium. The total reflection under all angles of incidence makes it possible to construct storage bottles for UCNs as well as UCN guides to transport UCNs from the source to the experiments. Good storage materials have Fermi potentials of up to 305 neV [SLB<sup>+</sup>10]. Absorption and up-scattering losses of UCN can be included in this picture by adding an imaginary part to the Fermi potential

$$V_F \rightarrow V - iW. \quad (1.39)$$

For  $W \ll V$  the wall loss per bounce probability can be expressed as

$$\mu(E, \theta) = 2 \frac{W}{V} \left( \frac{E \cos^2 \theta}{V - E \cos^2 \theta} \right)^{1/2} \quad (1.40)$$

where  $E$  is the total kinetic energy of the UCN and  $\theta$  the angle of incidence (relative to the normal on the surface). An overview of the UCN properties for different materials used in the nEDM experiment is given in Table 1.3.

Material	Number density / $(10 \times 10^{22} \text{ cm}^{-3})$	Fermi potential / $(\text{neV})$	Source
Al	6.02	54	[GRL91]
DLC (50 % $sp^3$ )	14.5	250	[Lau]
Ni <sub>85</sub> Mo <sub>15</sub>	8.54	232	[Lau]
Cu	8.93	168	[GRL91]
Ni	9.0	252	[GRL91]
dPS	-	$\approx 160$	[Kuz08, BDH <sup>+</sup> 08]

Table 1.3: UCN related properties of materials most frequently used in the nEDM experiment. Some materials have better storage properties in a specific chemical bond such as diamond-like carbon (DLC,  $sp^3$  hybrid) compared to graphite ( $sp^2$  hybrid). Hydrogen can be replaced by deuterium like in deuterated polystyrene (dPS).

### 1.5.2 Electromagnetic interaction

Unlike the proton the neutron has no electric charge but only a magnetic dipole moment. The interaction Hamiltonian with an external magnetic field has been introduced in Eqn. 1.9. The interaction energy of the two spin states is given by

$$E = -\boldsymbol{\mu}_n \cdot \mathbf{B} = \pm \mu_n |\mathbf{B}| \quad (1.41)$$

with  $\mu_n = 60.3 \text{ neV T}^{-1}$ . The magnetic dipole moment  $\boldsymbol{\mu}_n$  is related to the neutron spin  $\mathbf{s}$  via

$$\boldsymbol{\mu}_n = \gamma_n \mathbf{s}, \quad (1.42)$$

where  $\gamma_n = -1.832\,471\,79(43) \times 10^8 \text{ s}^{-1} \text{ T}^{-1}$  is the gyromagnetic moment of the neutron. Therefore the neutron spin and the neutron magnetic moment are anti-parallel. A 5 T magnetic field represents a  $\approx 302 \text{ neV}$  high potential barrier for a neutron whose magnetic moment is anti-parallel to the magnetic field. The interaction energy with such a magnetic field is on the order of the kinetic energy of the UCN (see Subsection 1.5.1). This is employed to polarize the UCNs in the nEDM experiment by guiding them through the 5 T field of a superconducting (SC) magnet. Those UCNs with parallel alignment of magnetic moment and magnetic field will be accelerated towards the center of the SC magnet and pass a thin aluminum vacuum window. Neutrons with the opposite spin direction will be reflected by the energy barrier. In this way one can produce a nearly 100% polarized beam of UCNs [SLF<sup>+</sup>05]. Furthermore UCNs can be spatially confined in magnetic field minima without any material wall interaction.

### 1.5.3 Gravity

Experiments with UCNs are one of the rare cases in particle physics where the gravitational interaction has significant influence on the flight trajectories of the particles under study

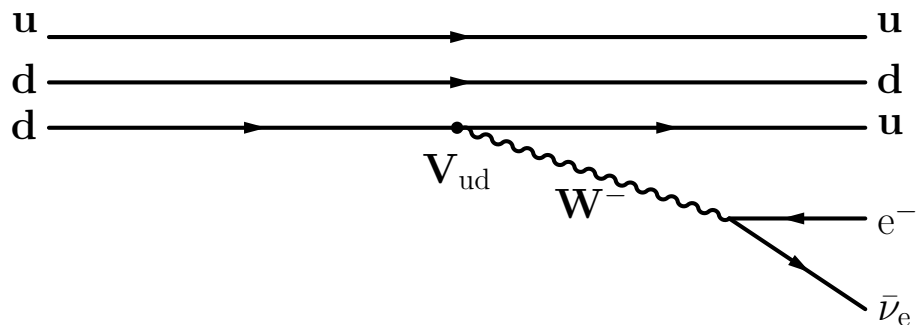


Figure 1.4: Valence quark level Feynman diagram for the  $\beta^-$  decay of a neutron into a proton. A d-quark converts into a u-quark via the weak interaction. The emitted  $W^-$  boson decays into an electron  $e^-$  and an anti-electron neutrino  $\bar{\nu}_e$ . The CKM matrix element  $V_{ud}$  scales the weak coupling at the vertex of the quarks.

and can be exploited to manipulate those. The potential energy difference is given by

$$E_{\text{pot}} = m_n g h, \quad (1.43)$$

where  $m_n$  is the mass of the neutron,  $g$  the Earth's local gravitational acceleration and  $h$  the height difference. For  $g = 9.81 \text{ m s}^{-2}$ ,  $E_{\text{pot}} = 102 \text{ neV m}^{-1}$ . Thus, a typical UCN with 300 neV energy will never rise higher than about three meters before falling back due to gravity. This allows the construction of UCN storage bottles that are open to vacuum at the top. On the other hand, gravity can also be used to accelerate UCNs to increase the transmission probability, e.g., through the window of a UCN detector.

### 1.5.4 Weak interaction

All free neutrons undergo nuclear beta decay via

$$n \rightarrow p + e^- + \bar{\nu}_e + 782 \text{ keV}. \quad (1.44)$$

Thus the neutron lifetime  $\tau_n$  sets the ultimate limit for the storage time in all UCN storage experiments. On the level of the valence quarks the beta decay can be described by the Feynman diagram given in Figure 1.4. A precise measurement of  $\tau_n$  offers in combination with decay correlation measurements, e.g., super allowed  $0^+ \rightarrow 0^+$  beta decays in heavier nuclei, a way to determine the CKM matrix element  $V_{ud}$  in (1.10). The amount of helium created in the primordial nucleosynthesis depends critically on  $\tau_n$ . The theoretical prediction is currently limited by the uncertainty of the neutron lifetime. Consequently the exact value of  $\tau_n$  is a field of intense research, in particular since some of the experimental results have shown significant disagreement [Gro12, WG11].

### 1.5.5 Production of ultra-cold neutrons and the PSI UCN source

As the nEDM experiment at PSI uses UCNs, a brief overview of the production techniques and the UCN source at PSI will be given. There are two main methods for the production of UCNs from a neutron source. The first principle makes use of Doppler-shifting a 'premoderated' beam of very cold neutrons into the UCN energy regime by reflection from receding neutron mirrors (turbine blades). For a detailed description the reader is referred to the excellent articles by A. Steyerl on the principles of the neutron-turbine [Ste75] as installed at PF2 at the Institute Laue-Langevin, Grenoble [SNS<sup>+</sup>86]. The second production scheme makes use of super-thermal down scattering of cold neutrons into the UCN energy regime ( $\leq 300$  neV) in a so-called UCN converter. This process was first proposed and worked out by M. Pendlebury and R. Golub in 1975 [GP75], the same year that A. Steyerl proposed the turbine technique [Ste75]. A first proof of principle of this idea with a UCN converter made out of superfluid  $^4\text{He}$  at  $\approx 1.2$  K was published in 1978 [AMGP78]. Since then this field has matured and new UCN sources of today use either super fluid helium at  $\approx 0.7$  K or solid ortho-deuterium at  $\approx 5$  K as converter material. The UCN converter material can be coupled to different sources of (cold) neutrons:

- A cold neutron guide delivers a (monochromatic) cold neutron beam to the UCN converter from a steady state nuclear reactor [ZPI11].
- The UCN converter is installed next to the core (in pile) of a steady state nuclear reactor, in pile of a pulsed nuclear reactor or in pile of a neutron spallation source. The different combinations are extensively discussed in various publications, e.g., in Refs. [MHJ<sup>+</sup>12, KSB<sup>+</sup>13, SBE<sup>+</sup>11].

A cut through the UCN source at PSI is shown in Figure 1.5. It makes use of the 590 MeV, 2.2 mA proton beam delivered by the PSI ring cyclotron. This proton beam can be kicked onto a dedicated spallation target, made out of lead-filled Zircalloy tubes to produce high energy neutrons [WH06]. These neutrons from the spallation reaction are thermalized in a  $2\text{ m}^3$  tank of heavy water ( $\text{D}_2\text{O}$ ) surrounding the spallation target before they diffuse into 30 l of solid ortho-deuterium (ortho  $\text{sD}_2$ ) at 5 K. In this crystal the neutrons are further thermalized to the cold neutron energy regime and can undergo down-scattering to the UCN energy regime by the excitation of single or multiple phonons. Because the UCN lifetime due to absorption is limited to several tens of milliseconds the UCN have to be separated from the (ortho  $\text{sD}_2$ ) UCN converter. Ultra-cold neutrons that leave the ortho  $\text{sD}_2$  vertically are guided towards a  $2\text{ m}^3$  intermediate storage volume. From this intermediate storage volume the UCN can be delivered to the experiments via UCN guides traversing the biological shielding of the spallation source. A more detailed description of the UCN source and its performance is given in Ref. [Göl12].

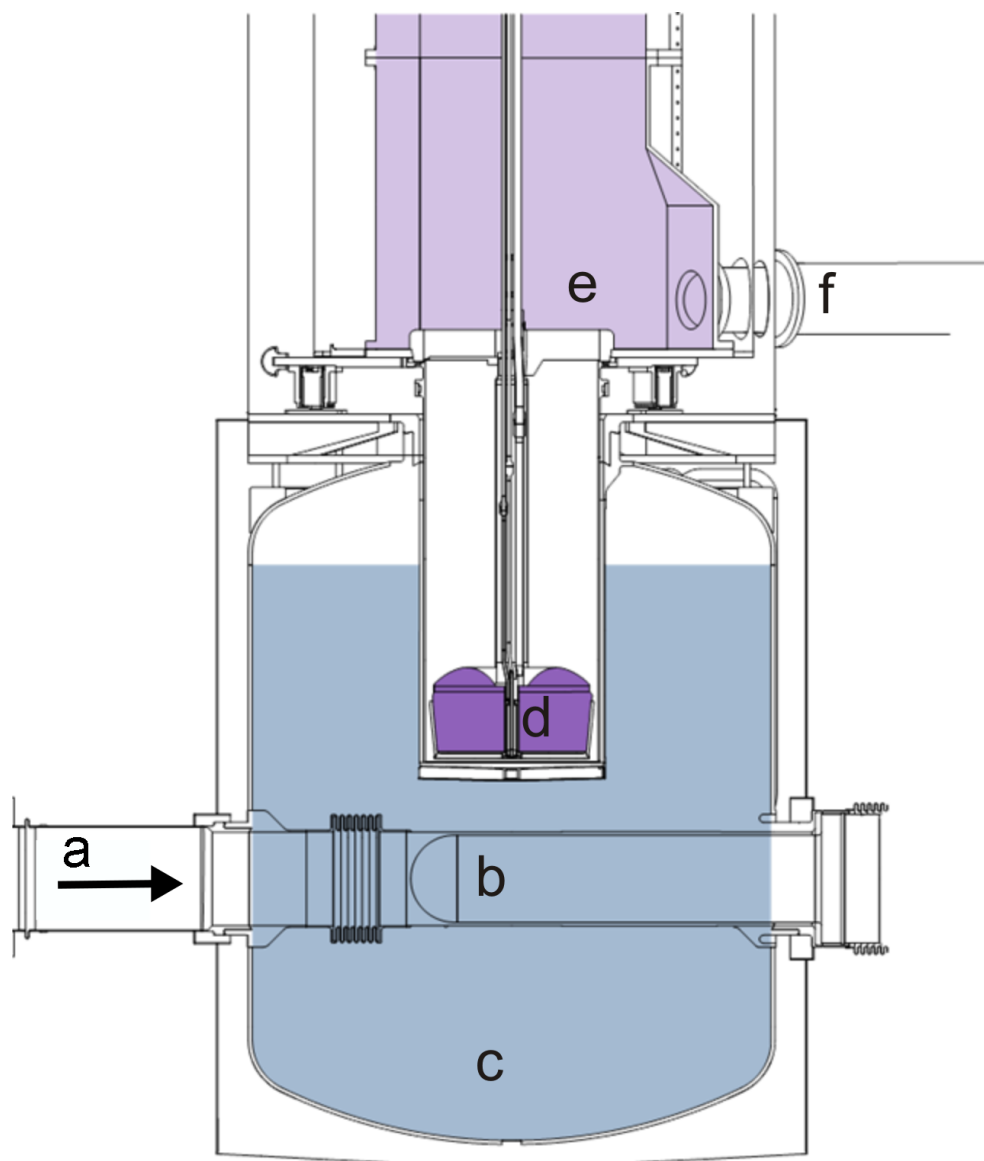


Figure 1.5: A cut through the UCN source at PSI. The 590 MeV proton beam (a) is kicked onto the spallation target (b) for up to 8 s. The spallation neutrons are thermalized in 2 m<sup>3</sup> of heavy water (c) surrounding the spallation target. The thermalized neutrons diffuse into 30 l of solid ortho-deuterium (d) at 5 K. The cold neutrons can be down-scattered into the UCN energy regime. The UCN can leave the ortho sD<sub>2</sub> vertically to reach a 2 m<sup>3</sup> storage volume (e) that can be valved off from the ortho sD<sub>2</sub> UCN converter. The UCN are delivered to the experiments with UCN guides (f) penetrating the biological shield of the UCN source.



# Chapter 2

## The neutron electric dipole moment experiment

This chapter will shortly discuss the history of the nEDM experiment and the experimental limits that have been established over more than 50 years of research. The experimental setup as installed at the Paul Scherrer Institute is presented and Ramsey's method of separated oscillating fields is introduced. The mercury co-magnetometer of the nEDM experiment is introduced and we derive the magnetic field sensitivity requirements for a successful operation in nEDM and n2EDM. Furthermore the statistical sensitivity of the Hg co-magnetometer is derived in terms of the initial signal-to-noise-density-ratio and the signal decay time from the Cramér-Rao lower bound.

### 2.1 Historical development of the nEDM experiment

The neutron electric dipole moment experiment of Ramsey, Purcell and Smith provided the first limit on any permanent electric dipole moment  $d_n < 5 \times 10^{-20} e \cdot \text{cm}$  (CL 95 %) [SPR57] in 1957. Ramsey's method of separated oscillating fields (developed in 1949/50 [Ram50a, Ram50b] and described in section 2.3) was employed to measure a possible difference of the Larmor precession frequency  $\omega_L$  of neutrons in a parallel and anti-parallel configuration of static electric  $\mathbf{E}$  and magnetic field  $\mathbf{B}$ . In the absence of an electric field the Larmor frequency is given by

$$\omega_L = \gamma B, \tag{2.1}$$

where  $B$  is the modulus of the magnetic field  $\mathbf{B}$  and  $\gamma$  is the gyromagnetic ratio. A comparison of the experimental situations is pictorially given in Figure 2.1. Their experimental setup used a cold neutron beam and is shown in Figure 2.2. From a Larmor frequency difference between the two measurement configurations one can extract the nEDM as

$$d_n = \frac{\hbar(\omega_{L\uparrow\downarrow} - \omega_{L\uparrow\uparrow}) - 2\mu_n(B_{\uparrow\downarrow} - B_{\uparrow\uparrow})}{2\hbar(E_{\uparrow\uparrow} + E_{\uparrow\downarrow})}, \tag{2.2}$$

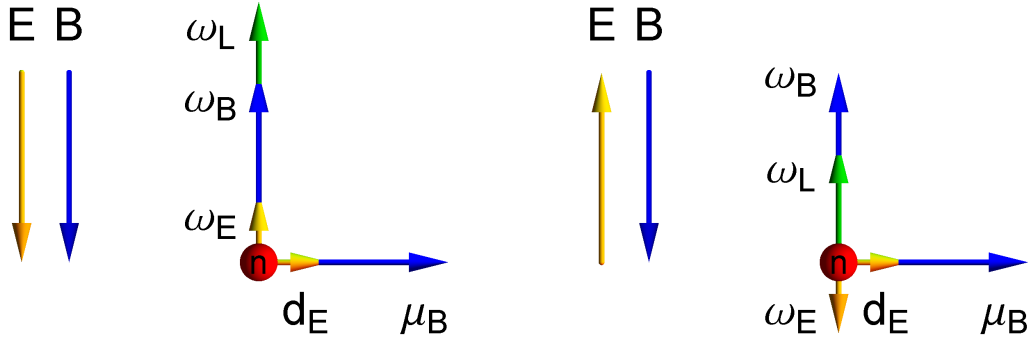


Figure 2.1: Pictorial scheme of the parallel and anti-parallel measurement configurations used in the nEDM experiment. The angular momentum vectors ( $\omega_B$ ,  $\omega_E$ ) related to the torque caused by the electric or magnetic dipole interaction are given in the same color as the corresponding fields ( $\mathbf{B}$ ,  $\mathbf{E}$ ) / dipole moments ( $\mu_n$ ,  $d_n$ ). The overall angular momentum vector related to the Larmor precession,  $\omega_L$ , is the vector sum of  $\omega_B$  and  $\omega_E$ . Here the electric dipole moment is assumed to be parallel with the magnetic dipole moment. In this case the Larmor frequency of the UCN would be increased in a parallel configuration of static electric and magnetic fields.

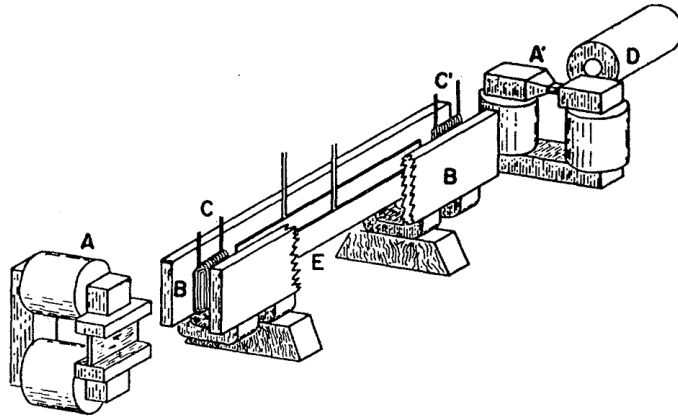


FIG. 1. Schematic diagram of the apparatus. *A*, the magnetized iron mirror polarizer. *A'*, the magnetized iron transmission analyzer. *B*, the pole faces of the homogeneous field magnet. Note the horseshoe-like magnets bolted along the bottom. *C*, *C'*, the coils for the radio-frequency magnetic field. *D*, the  $\text{BF}_3$  neutron counter. The magnetic fields in the polarizing magnet and the homogeneous field magnet are at right angles, and two twisted iron strips were used between them to rotate the neutron spins adiabatically.

Figure 2.2: Scheme of the first nEDM experiment in 1957 [SPR57].



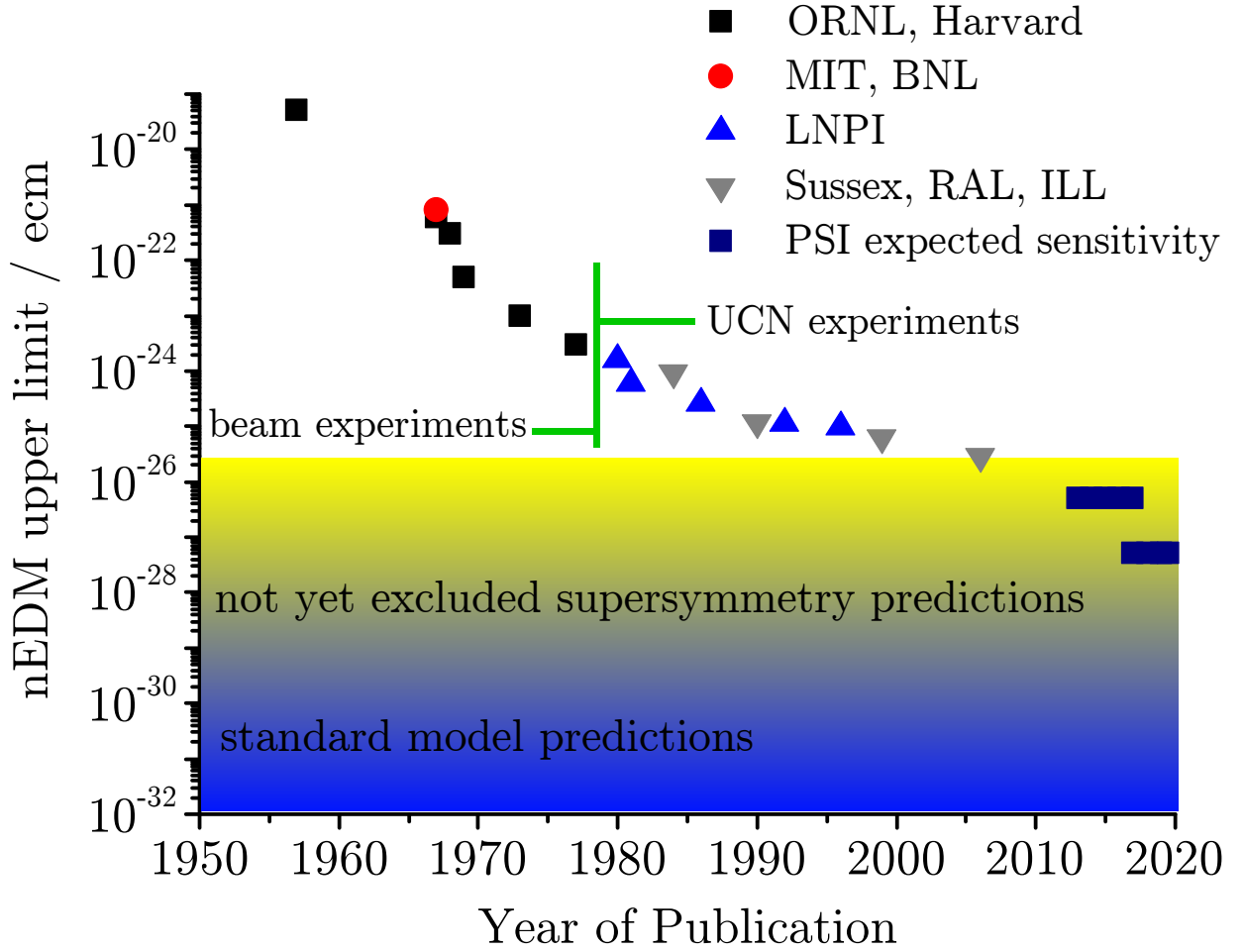


Figure 2.3: Historic development of the experimental upper limit for the nEDM. The green vertical line separates the results obtained with neutron beam experiments from those obtained with stored UCNs. The yellow area indicates the area of not yet excluded nEDM predictions from supersymmetric extensions of the standard model. The blue area marks the region of the nEDM prediction in the SM. In addition the projected sensitivity limits for the nEDM experiments at PSI (nEDM and n2EDM) are given. Figure provided by A. Knecht with minor modification by the author. (ORNL, Harvard:[SPR57, MDBR67, DBMR68, BMDR69, DMR73, DMP+77]; MIT, BNL: [SN67]; LNPI:[ABB+80, ABB+81, ABB+86, ABB+92, ABB+96],Sussex, RAL, ILL: [PSG+84, SCP+90, HBG+99, BDG+06])

$\omega_{L\uparrow\uparrow}(\omega_{L\uparrow\downarrow})$  represent the Larmor precession frequencies corrected for all systematic frequency shifts and  $\uparrow\uparrow$  ( $\uparrow\downarrow$ ) indicates the (anti-) parallel configuration of fields. The historical development of the experimental upper limits on the nEDM is shown in Figure 2.3. Over more than five decades the limit was reduced by more than six orders of magnitude. The exposure time of the neutrons to the electric and magnetic field configuration has been increased by five orders of magnitude by the ability to store neutrons (UCNs) in comparison to *in-beam* experiments (flight time in the experiment  $\approx$  milliseconds). At the

same time systematic effects related to the neutron motion in the electric field are strongly suppressed due to the much lower velocity of the UCNs compared to the cold neutrons in a beam experiment. On the other hand the number of available UCNs is orders of magnitude lower than in a typical cold beam. Recently a new in beam measurement of the nEDM has been proposed that makes use of the high peak flux of neutrons available from upcoming new neutron spallation sources, e.g., the European Spallation Source (ESS) in Lund, Sweden. The pulsed time structure of the neutron beam can be used to directly determine the motional magnetic field effect as a function of the velocity by a neutron time-of-flight measurement [Pie13].

## 2.2 The experimental setup of the nEDM experiment at PSI

A picture of the open vacuum tank of the nEDM experiment is shown in Figure 2.4. A schematic view of the nEDM setup at PSI is shown in Figure 2.5. Ultra-cold neutrons (UCNs) travel from the UCN source towards a superconducting magnet (SCM) which provides a 5 T longitudinal magnetic field along the beam line. Due to the magnetic dipole interaction only UCNs with anti-parallel spin relative to the magnetic field are accelerated in the magnetic field gradient and can pass the aluminum vacuum window of the beam line in the middle of the SCM. The transmitted UCN loose the gained kinetic energy by deceleration in the oppositely directed magnetic field gradient after the aluminum foil. The spin polarization of the UCNs after the SCM is close to 100 % [Pie11]. The spin direction can optionally be inverted with an adiabatic spin flipper in the fringe field of the SCM [GGH<sup>+</sup>09].

After the SCM the UCNs enter a *switch* which guides them in different directions, e.g., through a vertical UCN guide up into the precession chamber located in the vacuum tank. The precession chamber consists of two parallel electrodes made from aluminum which are coated with a layer of diamond-like carbon. An insulator ring with 470 mm inner diameter separates the high voltage (HV) electrodes by 120 mm, providing a volume of  $\approx 21$  l. This ring is made from polystyrene and coated on the inside with a layer of deuterated polystyrene [BDH<sup>+</sup>08]. The UCNs can be confined in the precession chamber by closing a mechanical shutter in the center of the lower electrode (UCN shutter).

The precession chamber is immersed in a static 1  $\mu$ T magnetic field  $\mathbf{B}_0$ . The main magnetic field is generated by a cosine-theta coil and trimmed by 33 trimcoils, all on the outside of the vacuum tank. Time-dependent magnetic fields  $\mathbf{B}_1$  transverse to  $\mathbf{B}_0$  can be generated in the volume of the UCN precession chamber with three additional coils on the outside of the vacuum tank. The top electrode of the precession chamber is normally charged up to about  $\pm 150$  kV, giving a typical electric field of  $\approx 12$  kV cm<sup>-1</sup> while the lower electrode is grounded. The entire vacuum tank is mounted inside a four-layer (high permeability) MuMetal shield to suppress magnetic field fluctuations from external sources and to provide a well defined magnetic field environment. To protect the MuMetal

shield from external magnetic field changes an active surrounding field compensation (SFC) system is employed. Details on the SFC system can be found in Ref. [Fra13].

After the Ramsey cycle (as described in detail in section 2.3) the UCN shutter is opened and the UCNs can leave the precession chamber towards the switch. During the time the UCNs spent in the precession chamber the switch has been rotated into a position connecting the vertical UCN guide to the neutron spin analyzer. This analyzer consists of a magnetized iron foil that transmits (due to the combination of magnetic and strong interaction) only UCNs with a certain spin projection on its magnetic field direction. These UCNs are detected after the iron foil in a high rate UCN detector [BBL<sup>+</sup>09]. The other spin component is stored above the spin analyzer foil until an adiabatic spin flipper is switched on to flip the UCNs spin component. Thus the UCNs that have been stored above the analyzer foil can be counted in the detector. To avoid systematic effects and UCN losses during the storage above the analyzer foil a double arm detector has been developed to count both UCN spin states simultaneously [Hel14].

In addition to the UCN related components there are two magnetometry systems installed in the vacuum tank. One is a double array of cesium magnetometers above and below the precession chamber electrodes. The magnetometers are installed inside the corona rings of the electrodes to protect them from possible HV discharges. They serve to survey the stability of the magnetic field at distinct points and to measure magnetic field gradients across the precession chamber. Details on the working principle and the performance of these magnetometers can be found in [GBS<sup>+</sup>06]. The second magnetometer is the <sup>199</sup>Hg co-magnetometer which allows one to measure the magnetic field in the same volume as the UCNs via optically detected nuclear magnetic resonance (ODNMR). This magnetometer, its mechanical setup, its working principle and its performance will be discussed in the rest of this thesis. A more detailed description of all the other subsystems of the nEDM experiment can be found, e.g., in Ref. [Zen13].

## 2.3 Ramsey's method and the nEDM

The nEDM experiment applies Ramsey's method of separated oscillating fields. This magnetic resonance technique is employed in many high precision frequency measurements, e.g., in atomic clocks and is a phase-sensitive detection scheme. In general a Ramsey-type measurement can be divided into five steps as depicted in Figure 2.6 for UCNs.

1. In the first step the particles are prepared in a spin polarized state. The quantization axis is given by the main magnetic field  $\mathbf{B}_0$  in the laboratory frame (LF). Here the magnetic moment  $\boldsymbol{\mu}$  of the UCNs is chosen to point anti-parallel to  $\mathbf{B}_0$  (spin up due to the negative gyromagnetic ratio of the neutron).
2. In the second step a sinusoidally oscillating magnetic field  $\mathbf{B}_1 = B_1 \hat{e}_{x \text{ or } y} \sin(\omega_{\text{RF}} t)$  is applied perpendicular to  $\mathbf{B}_0$  (measured in LF) in order to flip the magnetic moment. The linearly oscillating magnetic field can be decomposed in a component co-rotating and a component counter-rotating with the direction of the Larmor precession. In the

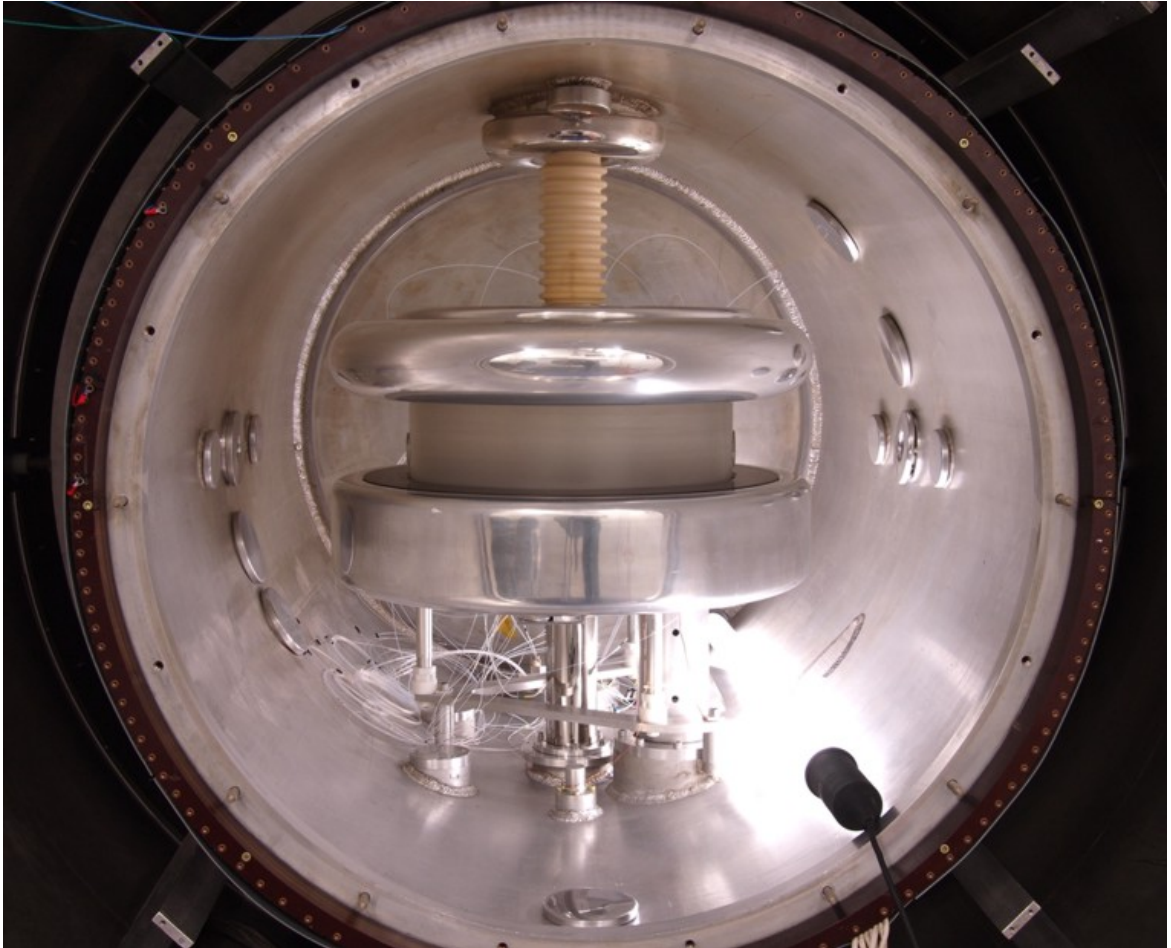


Figure 2.4: Inside the open vacuum tank of the nEDM experiment the UCN precession chamber is formed by two aluminum electrodes separated by 120 mm by an insulating polystyrene (PS) ring with inner diameter of 470 mm. The bottom electrode is on ground potential while the top electrode can be charged via the high-voltage feed-through up to  $\pm 200$  kV (maximum of power supply). The optical windows for the  $^{199}\text{Hg}$  co-magnetometer can be seen on the left and right side of the vacuum tank and well as in the insulator ring. The vertical aluminum tube at the right side below the bottom electrode contains the  $^{199}\text{Hg}$  polarization chamber.

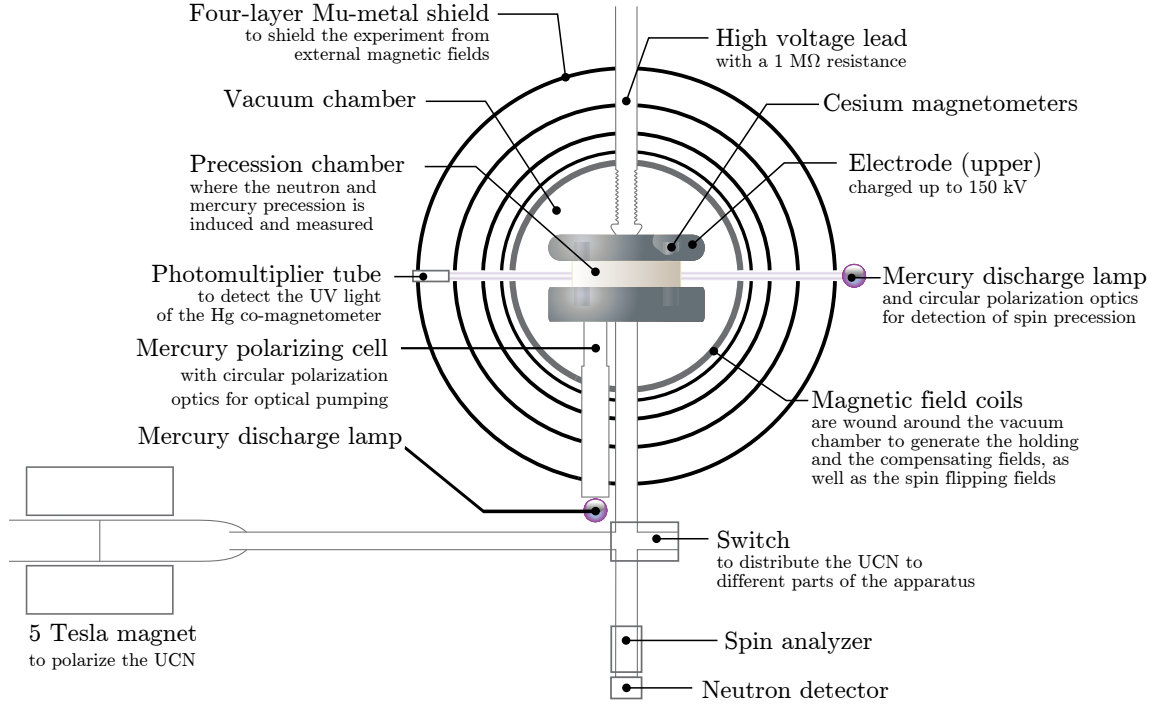


Figure 2.5: Sketch of the nEDM experimental apparatus as used at PSI. Details of the sub components are given in the text.

co-rotating frame  $\mathbf{B}_0$  vanishes and  $\mathbf{B}_1$  appears as a static magnetic field  $\mathbf{B}_1^*$  around which  $\boldsymbol{\mu}$  precesses. The duration  $T_{\text{RF}}$  and the amplitude of  $\mathbf{B}_1$  are adjusted such that  $\boldsymbol{\mu}$  is rotated by  $+\pi/2$  around  $\mathbf{B}_1^*$ . In the LF this corresponds to a rotation into the plane perpendicular to  $\mathbf{B}_0$  (1<sup>st</sup>  $\pi/2$  pulse). At the end of the pulse  $\mathbf{B}_1^*$  and  $\boldsymbol{\mu}$  have a relative phase shift of  $+\pi/2$  in the precession plane. The frequency of  $\mathbf{B}_1$  is chosen close to the Larmor frequency ( $\approx 30$  Hz for UCN in a  $1 \mu\text{T}$  magnetic field).

3. During the third step the magnetic moment of the particle precesses freely for a time  $T_{\text{free}}$  in the superposition of  $\mathbf{B}_0$  and the interaction under investigation. For the nEDM experiment this is the possible coupling of the neutron spin to the additional parallel or anti-parallel electric field  $\mathbf{E}$ . The signal generating the time-dependent  $\mathbf{B}_1$  field runs continuously but is not applied to the interaction region during the free precession time.
4. In the fourth step  $\mathbf{B}_1$  is turned on again for a duration  $\tau$  satisfying  $\omega_{\text{RF}}\tau = \pi/2$  (2<sup>nd</sup>  $\pi/2$  pulse), identical to the interaction in step 2. If  $\boldsymbol{\mu}$  was precessing with the same average frequency as the reference signal the relative phase shift between  $\mathbf{B}_1^*$  and  $\boldsymbol{\mu}$  will still be  $+\pi/2$  in the precession plane. Due to the second pulse the magnetic moment will be rotated by an additional angle of  $+\pi/2$  around  $\mathbf{B}_1^*$ . This corresponds to a  $\pi$  flip relative to  $\mathbf{B}_0$  in the LF and the UCN spin will point downwards at the end

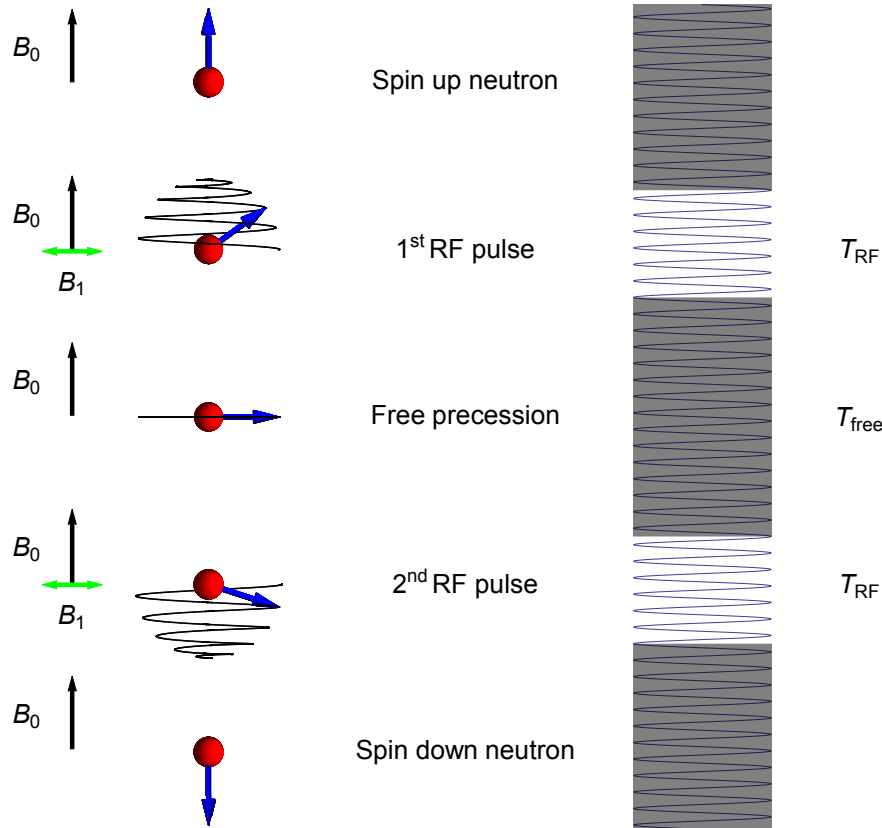


Figure 2.6: Pictorial representation of Ramsey's method of separated oscillatory fields. A detailed description of the single steps is given in the text.

of the pulse. For a relative phase shift of  $+3\pi/2$  between the magnetic moment and  $\mathbf{B}_1^*$  in the precession plane the magnetic moment is turned to its initial direction. The UCN spin will point upwards in the LF at the end of the pulse. For all other relative phase shifts the UCNs' spins will end up in a superposition of up and down states. For the case of zero relative phase shift between  $\mathbf{B}_1^*$  and  $\boldsymbol{\mu}$  there is no torque acting on  $\boldsymbol{\mu}$  in the co-rotating frame. Thus the final state will be a 50/50 superposition of up and down states.

5. In the last step the polarization state of the particles is detected. For the UCNs this happens after opening the UCN shutter to guide the UCN through the vertical guide and the switch to the spin analyzer and a UCN detector. The neutrons with spin projection up or down relative to the analyzer direction are counted separately. The result is a typical interference pattern as shown in Figure 2.7 for one spin component.

This measurement technique can also be looked at as a clock (oscillator) comparison experiment. The freely precessing magnetic moment of the UCN provides the first clock which is compared to the externally generated RF-signal, the second clock. In beam experiments the time separation of the RF pulses occurs along the particles' path through a region where the RF field is present, followed by a second region without RF and a third region

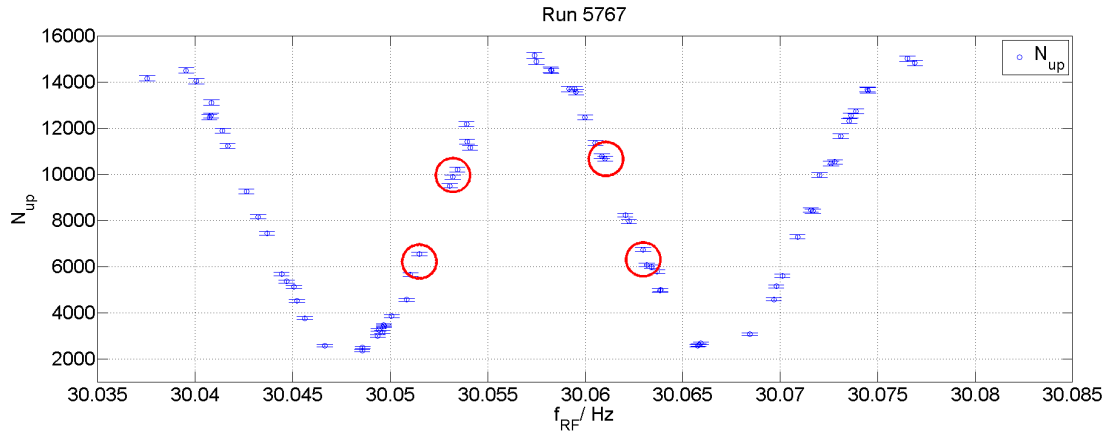


Figure 2.7: Ramsey pattern for spin up neutrons (nEDM Run 5767) after a storage time of 50 s. The number of spin up neutrons is counted as a function of the frequency of the applied transverse field  $\mathbf{B}_1$ .

in which the RF is present again. The exact shape of the fringe pattern was worked out by N. Ramsey in Ref. [Ram50b]. In the frequency region around the Larmor frequency of the UCN (as shown in Figure 2.7) the fringe pattern can be approximated by

$$N_{\text{up}}(\Delta\nu) = \frac{N_0}{2} \left[ 1 - \alpha \cos\left(\frac{2\pi \Delta\nu}{\delta\nu}\right) \right], \quad (2.3)$$

where  $N_0$  is the total number of particles (UCNs) counted (sum of both spin states),  $\Delta\nu = f_{\text{RF}} - \nu_L$  is the detuning of the RF signal  $f_{\text{RF}}$  relative to the particles' precession frequency  $\nu_L$ ,  $\alpha = \frac{N_{\uparrow,\text{max}} - N_{\downarrow,\text{min}}}{N_{\uparrow,\text{max}} + N_{\downarrow,\text{min}}}$  is the so-called visibility where  $N_{\text{min,max}}$  are counted on resonance. The full width at half maximum of the central Ramsey fringe is [May98, Pie09]

$$\delta\nu = \frac{1}{T_{\text{free}} \left( 1 + \frac{4T_{\text{RF}}}{\pi T_{\text{free}}} \right)}. \quad (2.4)$$

A change of the particles' precession frequency translates into a change of the count rates for the different spin states. As the slope is steepest at the detuning  $2\pi\Delta\nu = \pm\pi/2$  the RF frequencies in the experiment are chosen such as to have  $2\pi\Delta\nu \approx \pm\pi/2$  resulting in four so-called working points as indicated in Figure 2.7. With  $\delta\nu \approx \frac{1}{T_{\text{free}}}$  the statistical sensitivity for a nEDM is given by

$$\sigma(d_n) = \frac{\hbar}{2\alpha ET \sqrt{N_0}}, \quad (2.5)$$

where (2.2) was used under the assumption that the magnetic field variation ( $B_{\uparrow\downarrow} - B_{\uparrow\uparrow}$ ) vanishes or is known well enough that it can be corrected. This assumption will be reviewed in the next section. The scaling behavior of the statistical sensitivity can easily be justified.

The larger the applied electric field the larger the frequency shift due to a nEDM. And the longer the free precession time the larger the phase difference that can build up. The scaling with the square root of the number of detected particles is typical for a counting experiment such as the nEDM.

## 2.4 Magnetometry requirements in the nEDM experiment

To extract a nEDM according to (2.2) from a difference in the UCN Larmor precession frequency in parallel and anti-parallel electric and magnetic field configurations it is indispensable to suppress or measure changes of the magnetic field and magnetic field gradients configuration correlated with the relative direction of electric and magnetic fields. Such a correlated change can couple via different mechanisms to the neutron magnetic dipole moment and provide a false nEDM signal [PR12]. It is desirable to keep global magnetic field changes at a small level, to avoid the necessity of large corrections.

The major suppression of magnetic field changes is achieved by a four layer MuMetal shield around the vacuum tank that houses the UCN precession chamber. Furthermore an active stabilization of the magnetic field around the nEDM experimental setup, called the surrounding field compensation system, is in use [Fra13]. Residual magnetic field fluctuations are measured by the  $^{199}\text{Hg}$  co-magnetometer. The analysis approach for the nEDM search is to correct the Larmor frequency of the UCN for changes of the magnetic field relative to a mean magnetic field ( $\delta B$ ) of a measurement period (e.g., one night). The correction is given by

$$\nu_n^* = \nu_n + \frac{\gamma_n}{\gamma_{\text{Hg}}} \delta \nu_{\text{Hg}}, \quad (2.6)$$

where  $\nu_n^*$  represents the corrected and  $\nu_n$  the raw UCN frequency. The ratio of the gyromagnetic ratios  $\gamma_n/\gamma_{\text{Hg}}$  takes the different coupling strengths of the magnetic field into account. This approach is valid as long as the magnetic field drifts are larger than the additional error introduced by the  $^{199}\text{Hg}$  co-magnetometer.

The sensitivity requirement for the  $^{199}\text{Hg}$  co-magnetometer can be derived from (2.2) and (2.5). The uncertainty in a change of the Larmor frequency induced by magnetic field changes has to be smaller than the frequency change caused by a nEDM

$$\frac{4d_n E_0}{\hbar} \gg 2\mu_n \sigma (B_{\uparrow\downarrow} - B_{\uparrow\uparrow}), \quad (2.7)$$

where the symbols are explained after (2.2). To achieve the statistical sensitivity goal given in (1.22),  $d_n < 5 \times 10^{-27} e \cdot \text{cm}$  (95 % CL), the nEDM collaboration has planned to take data with an electric field of  $E_0 = 12 \text{ kV cm}^{-1}$ , a free precession time of  $T = 150 \text{ s}$ , a visibility  $\alpha = 0.75$  and  $N_0 = 350\,000$  detected UCN per single measurement cycle. This translates according to (2.5) into a sensitivity of

$$\sigma(d_n) = 4.1 \times 10^{-25} e \cdot \text{cm} \quad (2.8)$$



per cycle. Thus one has to perform about 20 000 measurement cycles to reach the sensitivity goal given in (1.22). To convert this into an effective duration of the experiment it is assumed that the PSI UCN source will deliver UCNs every 480 s. Then the goal can be reached within 100 days of data taking, not counting time reserved for studies of systematic effects. A detailed discussion of the nEDM spectrometer performance at the end of the year 2012 can be found in Ref. [Zen13].

The acceptable uncertainty on the magnetic field change per measurement cycle is

$$\sigma(\Delta B) \ll \frac{2E_0\sigma(d_n)}{\mu_n} = 160 \text{ fT} \quad (2.9)$$

Due to the correction procedure the  $^{199}\text{Hg}$  co-magnetometer adds its inherent noise onto the corrected UCN frequency  $\nu_n^*$ . According to (2.9) the required intrinsic magnetic field resolution of the UCN magnetometer is 160 fT for the measurement conditions assumed above. The additional noise contribution of the  $^{199}\text{Hg}$  co-magnetometer has to be small compared to the intrinsic statistical errors of the UCN frequency extraction. The relative uncertainty for the corrected UCN frequency is given by

$$\frac{\Delta\nu_n^*}{\nu_n^*} = \frac{1}{\nu_n + \frac{\gamma_n}{\gamma_{\text{Hg}}}\Delta\delta\nu_{\text{Hg}}} \sqrt{(\Delta\nu_n)^2 + \left(\frac{\gamma_n}{\gamma_{\text{Hg}}}\Delta\delta\nu_{\text{Hg}}\right)^2} \approx \sqrt{\left(\frac{\Delta\nu_n}{\nu_n}\right)^2 + \left(\frac{\Delta\delta\nu_{\text{Hg}}}{\nu_{\text{Hg}}}\right)^2} \quad (2.10)$$

$$\approx \sqrt{\left(\frac{\Delta\nu_n}{\nu_n}\right)^2 + \left(\frac{\Delta\delta B}{B_0}\right)^2}, \quad (2.11)$$

where the approximation  $\nu_n \gg \frac{\gamma_n}{\gamma_{\text{Hg}}}\Delta\delta\nu_{\text{Hg}}$  was made. A  $^{199}\text{Hg}$  co-magnetometer performing at twice the magnetic field sensitivity as the UCN magnetometer introduces additionally 12% statistical error. Thus a  $^{199}\text{Hg}$  co-magnetometer sensitivity of

$$\sigma(\Delta B) \leq 100 \text{ fT} \quad (2.12)$$

has to be achieved in 150 s for the nEDM measurement. For the ten times higher sensitivity goal in n2EDM, the sensitivity of the  $^{199}\text{Hg}$  co-magnetometer has to reach below 10 fT in 150 s.

## 2.5 Statistical sensitivity of the $^{199}\text{Hg}$ co-magnetometer

The mechanical setup of the  $^{199}\text{Hg}$  co-magnetometer inside the nEDM vacuum tank is shown in Figure 2.8. The  $^{199}\text{Hg}$  co-magnetometer can be divided in the  $^{199}\text{Hg}$  polarization part located below the grounded electrode of the UCN precession chamber and the measurement region inside the nEDM precession chamber where the magnetometry signal is generated. In the polarization part  $^{199}\text{Hg}$  atoms are continuously produced in the  $^{199}\text{Hg}$  source (a), either a temperature controlled droplet of metallic mercury or heated HgO that

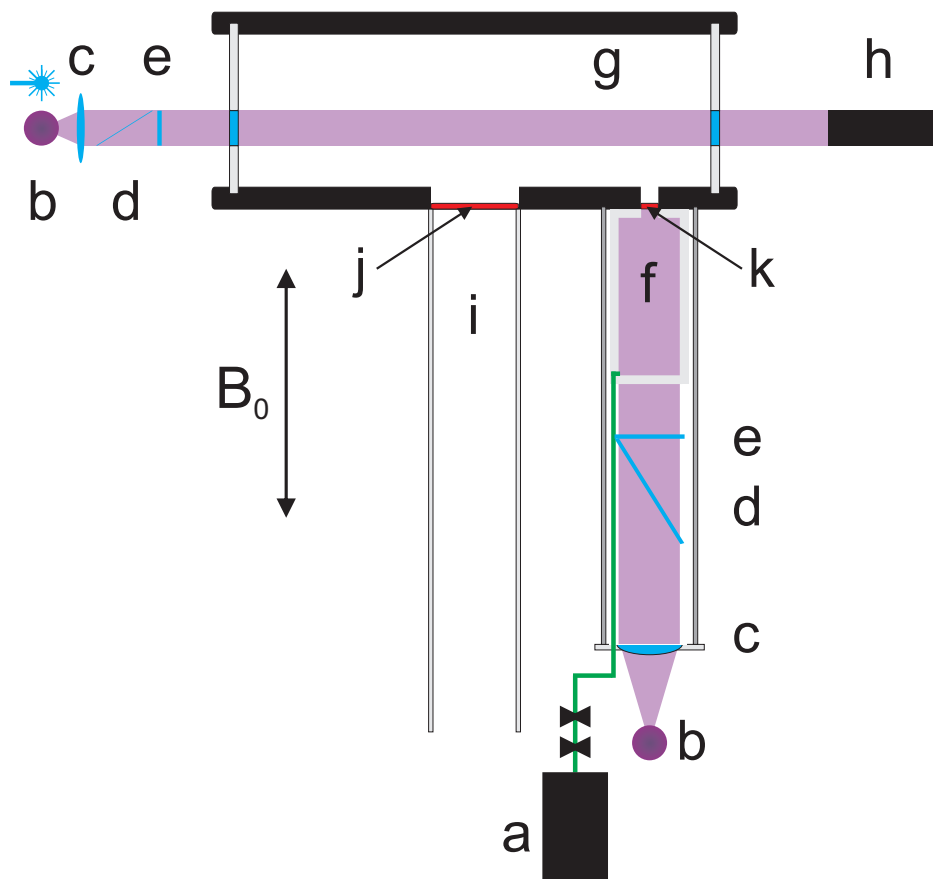


Figure 2.8: The polarizing system of the  $^{199}\text{Hg}$  co-magnetometer in combination with an absorptive detection scheme. The setup is described in detail in the text.

dissociates into Hg and O. The atoms travel via a capillary tube to the polarization chamber (f) where they are illuminated with circularly polarized light. The light is generated by a  $^{204}\text{Hg}$  discharge bulb (b) and passes a focusing lens ((c),  $f = 140$  mm), a linear polarizer (d) and a quarter wave plate (e) under  $45^\circ$ . The light is traveling (anti-)parallel to the main magnetic field and orients the spins of the  $^{199}\text{Hg}$  atoms along the magnetic field direction.

After typically 100 s to 350 s the polarized  $^{199}\text{Hg}$  vapor is released into the precession chamber (g) by opening the so-called Hg-shutter (k). A readout light beam generated by a second  $^{204}\text{Hg}$  discharge bulb (b) or a laser beam traverses the vacuum chamber and is detected on the photo-cathode of a photo multiplier tube or with a large area photo diode (h). For the absorptive measurement scheme (for details see Subsection 4.1.1) the light passes a linear polarizer (d) and a quarter wave plate (e) (with its axis under  $45^\circ$  relative to the plane of linear polarization) before it enters and leaves the precession chamber through two UV grade fused silica (UFVS) windows in the insulator ring. After a  $\pi/2$  pulse the polarized  $^{199}\text{Hg}$  atom spins precess around the magnetic field and modulate the light transmission through the precession chamber at their Larmor frequency. The UVFS windows are coated on the inner side with UV transparent dPE (deuterated polyethylene) to provide a sufficiently high neutron optical potential [BDH<sup>+</sup>08]. The  $^{199}\text{Hg}$  is pumped away after the measurement cycle when the UCN shutter (j) is opened in order to guide the surviving UCN to the detector.

A typical photomultiplier signal of the  $^{199}\text{Hg}$  co-magnetometer is shown in Figure 2.9. The signal level without Hg in the precession chamber is given by  $I_1$ . Shortly before  $t = 8$  s the Hg-shutter is opened for 2 s to release the polarized  $^{199}\text{Hg}$  atoms into the precession chamber. Due to the light absorption the PMT signal is reduced to level  $I_2$ . A 2 s long  $\frac{\pi}{2}$  pulse is applied to start the Larmor precession of the  $^{199}\text{Hg}$  atoms. The observation time  $T$  for the free induction decay (FID) starts at the end of the  $\frac{\pi}{2}$  pulse. After the band-pass filter of the nEDM data acquisition system (measured center frequency 7.8 Hz,  $Q \approx 5$ , for more details see App. C) the  $^{199}\text{Hg}$  co-magnetometer signal is approximately given by an exponentially decaying sinusoid as is shown in Figure 2.10. A detailed discussion of the signal shape is given in Subsection 4.2.2. To achieve the required magnetic field sensitivity with an exponentially decaying sine signal (start amplitude  $a_s$ ) a minimum signal-to-noise-density-ratio (SNDR) is needed which is given by the Cramér-Rao lower bound (CRLB) [GHK<sup>+</sup>10]

$$\delta B \geq \frac{\sqrt{12}}{\left(\frac{a_s}{\rho}\right) T^{3/2} \gamma_{\text{Hg}}} \sqrt{C}, \quad (2.13)$$

where  $\frac{a_s}{\rho}$  is the initial SNDR (normalized to unity bandwidth, see Section 5.1 for the determination of  $a_s$  and  $\rho$ ),  $T$  is the observation time and  $\gamma_{\text{Hg}}$  is the gyromagnetic ratio of the  $^{199}\text{Hg}$  atoms. In this calculation a white amplitude noise spectrum and a constant signal frequency is assumed. The factor  $\sqrt{C}$  takes into account the exponential decay of the signal with a characteristic decay time  $\tau$  as well as the overall number of data points

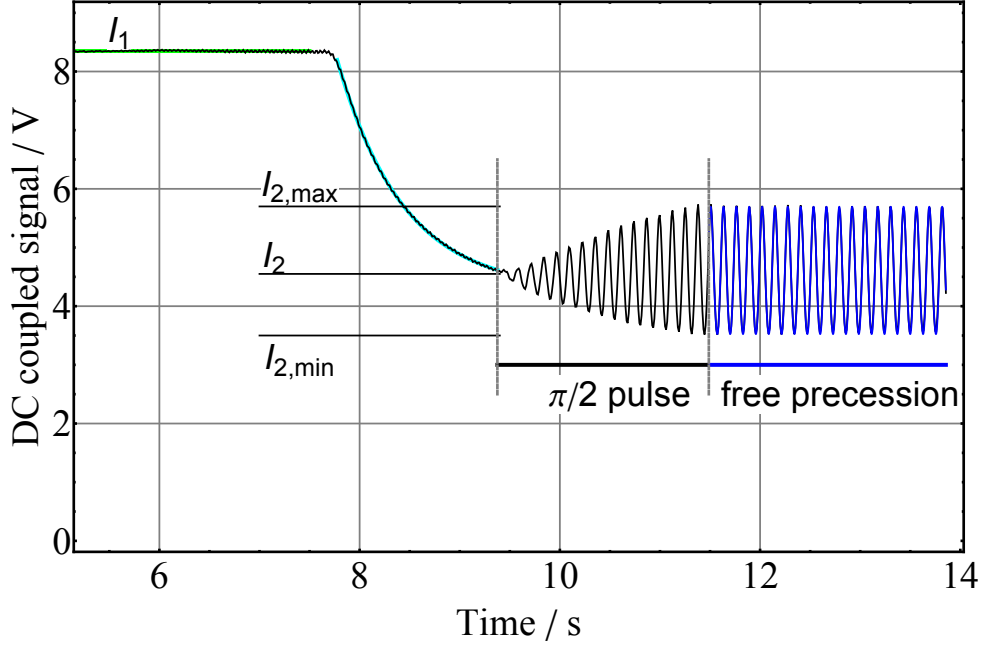


Figure 2.9: DC-coupled signal of the photo-multiplier in the  $^{199}\text{Hg}$  co-magnetometer. The  $I_1$  level is the PMT signal without Hg in the precession chamber. After the release of Hg atoms into the chamber the  $I_2$  signal level is measured. A  $\frac{\pi}{2}$  pulse is applied to start the Larmor precession of the  $^{199}\text{Hg}$  atoms in the magnetic field. The observation of free induction decay starts at the end of the  $\frac{\pi}{2}$  pulse .

[GHK<sup>+</sup>10]

$$C = \frac{N^3}{12} \frac{(1 - z^2)^3 (1 - z^{2N})}{z^2 (1 - z^{2N})^2 - N^2 z^{2N} (1 - z^2)^2}, \quad (2.14)$$

with  $z = e^{-\beta}$ ,  $\beta = 1/\tau$  the decay rate and  $N$  the number of signal samples recorded in total. For typical signal decay times of  $\tau \approx 100$  s, a signal sampling rate of 100 Hz and an observation time  $T = 150$  s the correction factor evaluates to  $\sqrt{C} \approx 2.17$ . A slightly alternative approach to [GHK<sup>+</sup>10] to derive the CRLB is given in appendix A.

To achieve the magnetic field sensitivity of 100 fT in  $T = 150$  s the  $^{199}\text{Hg}$  co-magnetometer has to reach an initial SNDR of

$$\frac{a_s}{\rho} \geq \frac{\sqrt{12C}}{\delta B_0 T^{3/2} \gamma_{\text{Hg}}} = 840. \quad (2.15)$$

For the ten times higher sensitivity requirements for n2EDM

$$\frac{a_s}{\rho} \geq \frac{\sqrt{12C}}{\delta B_0 T^{3/2} \gamma_{\text{Hg}}} = 8400 \quad (2.16)$$

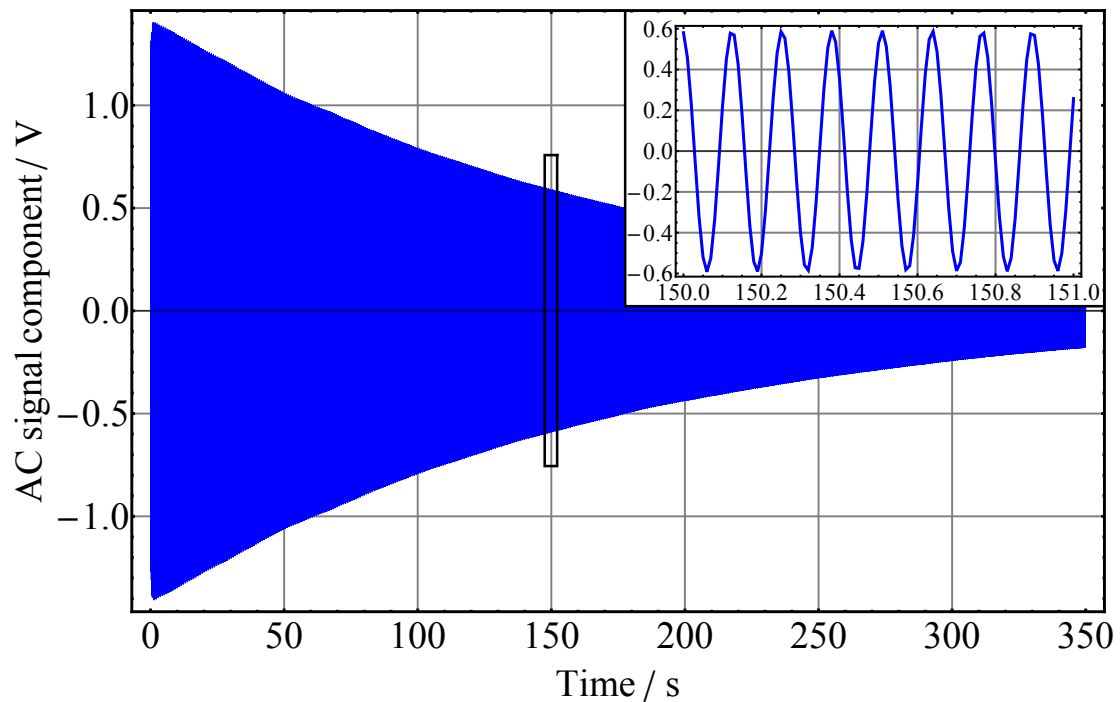


Figure 2.10: The AC component of the  $^{199}\text{Hg}$  co-magnetometer signal shows an exponential decay with the characteristic decay time  $\tau$ . As shown in the insert the signal is modulated at the Larmor frequency of the precessing  $^{199}\text{Hg}$  atoms. The axis labels apply to the insert, too.

will be needed. From (2.13) it is clear that the  $^{199}\text{Hg}$  co-magnetometer performance is improved by a large SNDR and a long signal decay time  $\tau$ . In Chapter 4 the signal generation in the  $^{199}\text{Hg}$  co-magnetometer and the important parameters necessary to achieve the best possible SNDR are discussed in detail. Furthermore possibilities to increase the signal decay time  $\tau$  are discussed.



# Chapter 3

## The components of the mercury co-magnetometer

This chapter will present the hardware of the  $^{199}\text{Hg}$  co-magnetometer as used in the nEDM experiment. First the important physical properties of the element mercury are summarized that make it suited to serve as a co-magnetometer in the nEDM experiment. Secondly the properties of the  $^{204}\text{Hg}$  discharge bulbs used as light sources so far are presented. The performance parameters of the new UV laser system are given and a new technique of laser frequency stabilization is introduced. Finally the properties of the multi-mode optical fibers used to transport the UV laser light to the nEDM experiment are discussed.

### 3.1 The element mercury

The physical and chemical properties of mercury ( $Z = 80$ ) are remarkably different from its neighbors in the periodic table of elements. Its special properties have rendered mercury an often used study object in atomic and particle physics since the end of the 19<sup>th</sup> century. Several Nobel prizes have been awarded for work directly related to the properties of mercury. In 1913 H. K. Onnes was awarded the Nobel prize “for his investigations on the properties of matter at low temperatures which led, inter alia, to the production of liquid helium” [Nob], after having liquefied helium-4 in 1908 and having discovered superconductivity of mercury in 1911. J. Franck and G. Hertz conducted experiments with mercury-filled electron tubes in 1914 and received the prize in 1925 “for their discovery of the laws governing the impact of an electron upon an atom” [Nob]. Some forty years later, the prize was awarded to A. Kastler in 1966 “for the discovery and development of optical methods for studying Hertzian resonances in atoms” [Nob], while developing and investigating the method of double resonance spectroscopy on mercury atoms.

More recently, mercury plays an important role in the development of more accurate atomic clocks based on a single  $^{199}\text{Hg}^+$  ion in a linear quadrupole trap [DUB<sup>+</sup>01]. Atomic clocks based on neutral  $^{199}\text{Hg}$  atoms in an optical lattice trap are also under development [MMM<sup>+</sup>12]. Mercury is the heaviest non-radioactive element that has been trapped in a

Property	Value
Nuclear charge number	80
Melting point	234.321 K
Boiling point	629.769 K
Saturated vapor pressure (SATP)	0.264 Pa
Atomic number density (SATP)	$6.414 \times 10^{13} \text{ cm}^{-3}$
$^{199}\text{Hg}$ $\sigma_{n,a}$	2150(48) b

Table 3.1: Important physical properties of the element mercury under standard ambient temperature and pressure conditions (SATP, 298.15 K, 101.325 kPa) [Hay14]. The neutron absorption cross-section  $\sigma_{n,a}$  for  $^{199}\text{Hg}$  is given for thermal neutrons ( $2200 \text{ m s}^{-1}$ ) [Sea92].

Isotope	$M/m_u$	$n/\%$	$I/\hbar$	$\mu_N/\mu_N$	$\mu_A/\mu_N$
$^{196}\text{Hg}$	195.965 807	0.15	0	...	...
$^{198}\text{Hg}$	197.966 743	10.1	0	...	...
$^{199}\text{Hg}$	198.968 254	17.0	1/2	0.505 885 5(9) [Sin07]	0.497 865(6) [Cag61] 0.497 869 78(8) <sup>1</sup>
$^{200}\text{Hg}$	199.968 300	23.1	0	...	...
$^{201}\text{Hg}$	200.970 277	13.2	3/2	-0.560 225 7(14) [Kon07]	-0.551 344(9) [Cag61] -0.551 349 2(25) <sup>1</sup>
$^{202}\text{Hg}$	201.970 617	29.65	0	...	...
$^{204}\text{Hg}$	203.973 467	6.85	0	...	...

Table 3.2: Properties of the seven stable mercury isotopes [Nat]. Besides the mass  $M$  in atomic mass units the isotopic abundance  $n$  in natural mercury is given. The nuclear spin  $I$  is given in units of  $\hbar$  and the magnetic moment of the nucleus  $\mu_N$  is given in units of the nuclear magneton  $\mu_N$ . The magnetic moment of the atom  $\mu_A$  is smaller than the nuclear magnetic moment  $\mu_N$  due to diamagnetic shielding.

magneto-optical trap, for the first time in 2008 [HMP<sup>+</sup>08]. Furthermore mercury is used as a nonlinear interaction medium in four-wave-mixing-technologies to produce the Lyman- $\alpha$  radiation needed to laser cool (anti-) hydrogen atoms [KSW12]. The  $^{199}\text{Hg}$  isotope is especially useful in magnetometry applications [GHI<sup>+</sup>98] and in the sensitive search for its permanent electric dipole moment [GSL<sup>+</sup>09]. The following discussion concentrates on the properties of mercury relevant for its use as a co-magnetometer in the nEDM experiment.

The most relevant physical properties of mercury concerning its use as a co-magnetometer in the nEDM experiment are summarized in Table 3.1. The position of mercury in the periodic table of elements is defined by its nuclear charge number  $Z = 80$ . Mercury is the only liquid metal at standard pressure and standard ambient temperature (SATP). The high saturated vapor pressure at SATP allows for high density vapors at room temperature without the need for heating and the concerns normally related to it (magnetic fields from currents, temperature gradients, ...).



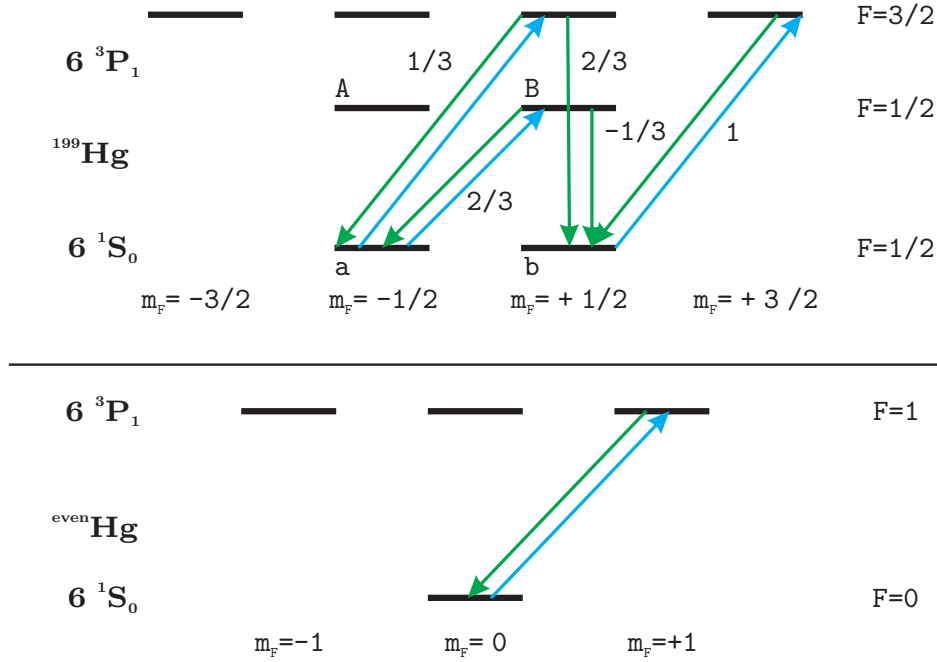


Figure 3.1: Lowest electronic states for the  $^{199}\text{Hg}$  isotope (top) and even isotopes (bottom). The wavelength of the transition  $6^1S_0 \rightarrow 6^3P_1$  is 253.7 nm. The  $^{199}\text{Hg}$  isotope shows hyperfine splitting in the first excited state due to its nuclear spin  $I = \frac{1}{2}$ . The even isotopes possess no nuclear spin and thus no hyperfine structure. The Clebsch-Gordan coefficient for each transition is given next to the transition arrow where the convention applies that e.g.  $-\frac{1}{3}$  means  $-\sqrt{\frac{1}{3}}$ .

Mercury consists of seven stable isotopes. Five isotopes have bosonic (integer spin, 0) and two have fermionic (half-integer spin,  $1/2$  or  $3/2$ ) character. Their natural abundances are given in Table 3.2. Only the mercury isotopes with odd nucleon number carry a nuclear spin  $\mathbf{I}$ . The electronic configuration of Hg is  $[Xe] 6s^2 4f^{14} 5d^{10}$  in which the two  $6s$  electrons are paired up in the electronic ground state term ( $6^1S_0$ ) to form a diamagnetic atom. Thus the nuclear spin  $\mathbf{I}$  forms the total angular momentum  $\mathbf{F}$  of the atom ( $^{199}\text{Hg}$   $F = 1/2$ ,  $^{201}\text{Hg}$   $F = 3/2$ ) in the ground state (Table 3.2). The nuclear magnetic moment  $\mu_N$  is responsible for the hyperfine splitting of the excited electronic energy levels in the odd isotopes. For the interaction of an atom with an external magnetic field the atomic magnetic moment  $\mu_A$  is relevant, which is reduced compared to the magnetic moment of the nucleus due to diamagnetic shielding by the electron shell.

The lowest electronic states for the even isotopes and the  $^{199}\text{Hg}$  isotope are given in Figure 3.1. The wavelength of the intercombination line between the spin singlet and the spin triplet state ( $6^1S_0 \rightarrow 6^3P_1$ ) is 253.7 nm. Detailed properties of the 253.7 nm line and

<sup>1</sup>In [Cag61]  $\frac{\gamma_{\text{Hg}}}{\gamma_{\text{H}}}$  was measured. Here  $\mu_{\text{Hg}}$  is re-calculated with  $\mu'_{\text{H}}$  (CODATA2012) = 2.792775598(30) and linear error propagation as in the original work [Cag61].

Property	Value
Wavelength	253.7 nm
Natural lifetime ${}^3P_1$	125 ns
Natural line width $\Gamma_0/2\pi$	1.27 MHz
Saturation intensity $I_{\text{sat}} = \frac{\pi hc\Gamma_0}{3\lambda^3}$	10.2 mW cm <sup>-2</sup>

Table 3.3: Important properties of the  $6^1S_0 \rightarrow 6^3P_1$  intercombination line. All values are stated for the even mercury isotopes i.e. no hyperfine splitting effects are taken into account.

the electronic states involved are given in Table 3.3. The odd isotopes of mercury ( ${}^{199}\text{Hg}$ ,  ${}^{201}\text{Hg}$ ) are two of the rare isotopes for which the nuclear polarization can be manipulated and probed by optical means (optically detected nuclear magnetic resonance, ODNMR). As shown in Fig 3.1 circularly polarized light can transfer angular momentum to the Hg atoms (e.g. transition  $a \rightarrow B \rightarrow b$  on the  $F=1/2$  line in  ${}^{199}\text{Hg}$ ) if the light emitted by the excited state has linear polarization. The transition probabilities are proportional to the Clebsch-Gordan coefficients which are also given in Fig 3.1. This mechanism is the basis of optical pumping used to spin polarize the Hg atoms and to derive a magnetometry signal as discussed in detail in Chapter 4 and 5.

For the use as a co-magnetometer in the nEDM experiment it is also important to consider the neutron absorption cross-section of mercury as the atoms are present in the same volume as the UCN (see Figure 2.5). For  ${}^{199}\text{Hg}$  the neutron absorption cross-section is  $\sigma_{\text{n,a}} = 2150(48)$  b for thermal neutrons ( $2200 \text{ m s}^{-1}$ ). All other isotopes either have neutron absorption cross-sections between 2 b and 60 b ( ${}^{198}\text{Hg}$ ,  ${}^{200}\text{Hg}$ ,  ${}^{201}\text{Hg}$ ,  ${}^{202}\text{Hg}$ ,  ${}^{204}\text{Hg}$ ) or have a tiny abundance ( ${}^{196}\text{Hg}$ ) and are thus irrelevant for the overall neutron absorption cross-section. This argument holds even more so as mercury enriched up to 91 % in  ${}^{199}\text{Hg}$  is usually used in the  ${}^{199}\text{Hg}$  co-magnetometer. For a typical  ${}^{199}\text{Hg}$  density  $n = 5 \times 10^{10} \text{ cm}^{-3}$  and an average relative velocity  $\bar{v} = 150 \text{ m s}^{-1}$  ( $v_{\text{UCN}} \approx 0$ ), the neutron absorption rate is  $R = n\bar{v}\sigma = 2 \times 10^{-5} \text{ s}^{-1}$ . This can be neglected compared to typical UCN storage times on the order of 180 s in the nEDM apparatus [Zen13].

A typical transmission spectrum of  ${}^{199}\text{Hg}$  enriched mercury as used in the nEDM experiment is shown in Figure 3.2. From this, one can determine the degree of enrichment in  ${}^{199}\text{Hg}$  by fitting the Doppler-broadened absorption profile at the line center position of each isotope. As the light absorption is not small for all of the peaks the following fit function was used

$$f_{\text{fit}}(x) = \exp \left[ - \sum_i (nL)_i s_i \sigma_D (f_i - x) \right], \quad (3.1)$$

where  $(nL)_i$  is the product of number density  $n$  and light path length  $L$  for the isotope  $i$ . The hyperfine splitting of the transition lines in the odd isotopes is taken into account by the factor  $s_i$  and the Doppler-broadened absorption cross-section  $\sigma_D (f_i - x)$  as a function

Isotope	Hyperfine component	$\Delta f_{198}$ / GHz
$^{199}\text{Hg}$	1/2	-15.409(13)
$^{204}\text{Hg}$	...	-15.313(13)
$^{201}\text{Hg}$	5/2	-14.6587(99)
$^{202}\text{Hg}$	...	-10.1018(45)
$^{200}\text{Hg}$	...	-4.8054(45)
$^{201}\text{Hg}$	3/2	-0.6763(27)
$^{198}\text{Hg}$	...	0
$^{199}\text{Hg}$	3/2	6.7273(69)
$^{201}\text{Hg}$	1/2	6.872(15)

Table 3.4: Isotope shift and hyperfine splitting of the  $6^1S_0 \rightarrow 6^3P_1$  transition in mercury. The frequency shift  $\Delta f_{198}$  is given relative to the line center of  $^{198}\text{Hg}$  [Sch63].

of the line resonance position  $f_i$  is given by

$$\sigma_D(f_i - x) = \frac{1}{\sqrt{2\pi}\Delta_{D,i}} e^{-\frac{(x-f_i)^2}{2\Delta_{D,i}^2}}, \quad (3.2)$$

where  $\Delta_{D,i}$  is the Doppler-width of the line for isotope  $i$ . All isotopes were included in the fit except  $^{201}\text{Hg}$  since two minority isotopes (besides  $^{204}\text{Hg}$ ) are very difficult to resolve within their overlapping transition line.

An enrichment of 85.5%  $^{199}\text{Hg}$  is found in this sample. The  $^{204}\text{Hg}$  content is  $\approx 4.9\%$  which causes an absorption background for the laser operated on the  $^{199}\text{Hg } 6^1S_0 \rightarrow 6^3P_1 F = 1/2$  line as the two lines overlap within their Doppler widths. The other even isotopes with abundances between 1.7% to 2.9% cause an absorption background for the light from the  $^{204}\text{Hg}$  lamps which is not isotopically pure as described in the next subsection. For a precise isotope ratio measurement a dedicated setup with sample and reference light beam should be used instead of a one-beam-only setup such as the nEDM apparatus to suppress, e.g., common mode intensity fluctuations. The manufacturer's isotopic specification is 83.80(20)%  $^{199}\text{Hg}$  and 3.60(5)%  $^{204}\text{Hg}$ <sup>2</sup> determined by ICP-MS<sup>3</sup>. For further calculations the manufacturer's specification will be used since ICP-MS is generally more precise (e.g., [Elm]) than atomic absorption spectroscopy and in this special case does not suffer from resolving three isotopes within the same absorption peak. Nevertheless a change of the isotopic composition, e.g., due to mass dependent diffusion on the way from the Hg source to the polarization chamber cannot be excluded.

<sup>2</sup>euriso-top, batch #J1851, see appendix B.

<sup>3</sup>Inductively Coupled Plasma Mass Spectroscopy

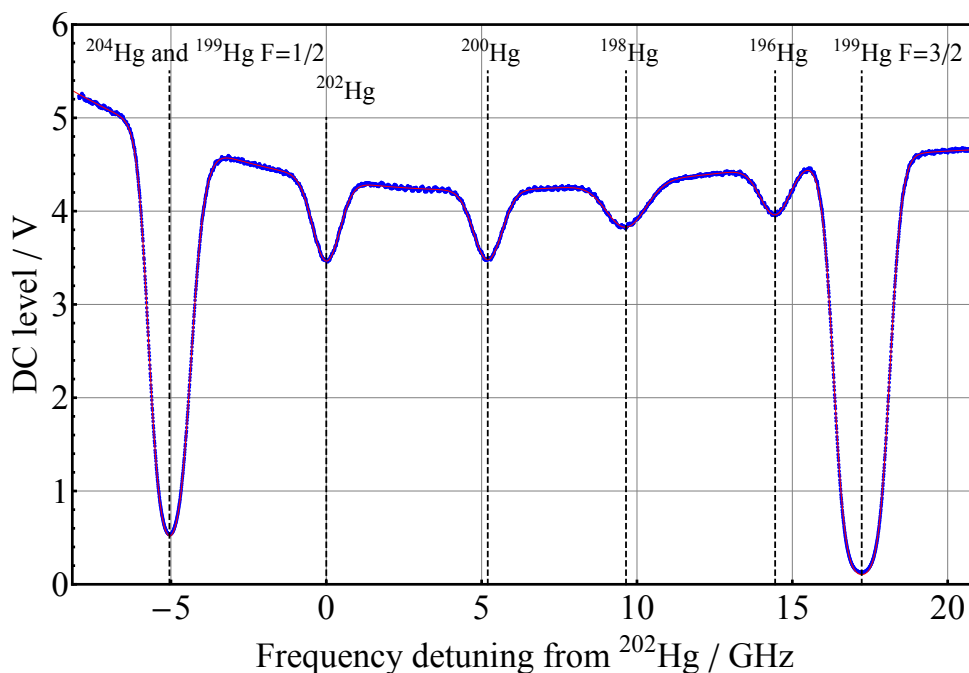


Figure 3.2: Transmission spectrum of the  $^{199}\text{Hg}$  enriched mercury vapor used in January 2013 in the Hg co-magnetometer. The measured data points are given in blue ( $\cdot$ ). A fit to the absorption lines is shown in red ( $—$ ). The degree of enrichment in  $^{199}\text{Hg}$  can be extracted to be about 85.5%. The  $^{204}\text{Hg}$  content is about 4.9% which causes an absorption background for the laser operated on the  $^{199}\text{Hg } 6^1S_0 \rightarrow 6^3P_1 F = 1/2$  line as the two lines overlap within their Doppler widths. The other even isotopes with abundances between 1.7% to 2.9% cause an absorption background for the light from the  $^{204}\text{Hg}$  lamps.

## 3.2 Interaction of Hg atoms with electric and magnetic fields

The nEDM experiment uses spin polarized  $^{199}\text{Hg}$  atoms in a combination of electric and magnetic fields. Here an estimation of the energy shift of the magnetic sub levels of the atomic ground and first excited state is given. The frequency shifts for the electronic transitions are given and compared to the unperturbed levels for the odd Hg isotopes. The influence of the magnetic field is described by the Zeeman effect, the influence of the electric field is given by the Stark effect.

### The Zeeman effect

The interaction energy of a magnetic moment  $\boldsymbol{\mu}$  with an external magnetic field  $\mathbf{B}$  is given by

$$E_{\text{mF}} = -\boldsymbol{\mu} \cdot \mathbf{B} = g m_{\text{F}} |\mathbf{B}| \quad (3.3)$$

where  $m_{\text{F}}$  is the angular momentum projection quantum number on the direction of the magnetic field,  $g$  is the so-called  $g$ -factor of the magnetic sub level and  $\mu_{\text{B}}$  is the Bohr magneton. In the weak field limit, e.g., the interaction energy with the external magnetic field is much weaker than the hyperfine interaction between the nuclear magnetic moment and the electronic magnetic moment the total angular momentum  $\mathbf{F} = \mathbf{I} + \mathbf{J}$  is a conserved quantum number, where  $\mathbf{I}$  is the nuclear angular momentum and  $\mathbf{J}$  the total electronic angular momentum. In this case the interaction Hamiltonian is given by

$$H_{\text{B}} = \mu_{\text{B}} g \frac{F_z}{\hbar} B_z \quad (3.4)$$

and the  $g$ -factor of the magnetic sub level is given by

$$g_{\text{F}} = g_{\text{J}} \frac{F(F+1) - I(I+1) + J(J+1)}{2F(F+1)} + g_{\text{I}} \frac{F(F+1) + I(I+1) - J(J+1)}{2F(F+1)} \quad (3.5)$$

where  $g_{\text{J}}$  and  $g_{\text{I}}$  are the  $g$ -factors of the electronic and the nuclear state. Since the  $^{199}\text{Hg}$  ground state level has  $\mathbf{J} = 0$ ,  $\mathbf{F} = \mathbf{I}$  ( $I = 1/2$ ) there is no hyperfine splitting in the electronic ground state. The  $g$ -factor of the  $6^1S_0$  state in  $^{199}\text{Hg}$  (calculated according to (3.5)) is

$$g_{6^1S_0, ^{199}\text{Hg, theo.}} = g_{\text{I}} = \frac{2\mu_{\text{Hg}}}{\mu_{\text{B}}} = 0.000\,551\,027\,71(98). \quad (3.6)$$

Here the diamagnetic shielding of the  $^{199}\text{Hg}$  nucleus by the electron shell is not taken into account. This correction is about 1.6% and is essential for the  $^{199}\text{Hg}$  co-magnetometer as it uses  $^{199}\text{Hg}$  atoms and not  $^{199}\text{Hg}$  nuclei. Therefore only measured values of either the gyromagnetic ratio or the  $g$ -factor of an atomic level will be used for the further calculation

Isotope	Electronic state	$F$	$m_F$	Energy shift Hz $\mu\text{T}^{-1}$	g factor
$^{199}\text{Hg}$	$6^1S_0$	1/2	$\pm 1/2$	$\pm 3.795\,059(6)$	0.000 542 296 7(18)
$^{201}\text{Hg}$	$6^1S_0$	1/2	$\pm 1/2$	$\mp 1.400\,904(6)$	-0.000 200 182 8(3)
$^{201}\text{Hg}$	$6^1S_0$	1/2	$\pm 3/2$	$\mp 4.202\,711(19)$	-0.000 200 182 8(3)

Table 3.5: Linear Zeeman shift of the magnetic sub-levels of the  $6^1S_0$  ground state in the odd mercury isotopes. The shift for each magnetic sub-level is given relative to the zero field position in frequency units as a function of the external magnetic field. Furthermore the g factor of the hyperfine level is given.

in this chapter. These values are listed for the  $6^1S_0$  state in Table 3.6. The g-factor for the  $^{199}\text{Hg}$  atom ground state is (see Table 3.2) as can be calculated from the measured gyromagnetic ratio [Cag61].

$$g_{1S_0,^{199}\text{Hg}} = g_{1,^{199}\text{Hg}} = \frac{2\mu_{\text{Hg}}}{\mu_B} = 0.000\,542\,296\,7(18). \quad (3.7)$$

The linear Zeeman effect of the ground state is responsible for the Larmor precession of the  $^{199}\text{Hg}$  atoms that is used to measure the magnetic field in the nEDM. It is given for the odd mercury isotopes in Table 3.5. The Larmor frequency of the  $^{199}\text{Hg}$  atoms is

$$\omega_L = \gamma_{\text{Hg}}\mathbf{B}, \quad (3.8)$$

where  $\gamma_{\text{Hg}}/2\pi = 7.590\,118(13)$  Hz  $\mu\text{T}^{-1}$  is the gyromagnetic ratio of the  $^{199}\text{Hg}$  atom ground state.

The  $g_J$ -factor for the  $^3P_1$  excited state was determined experimentally in Ref. [Dod61]

$$g_{3P_1} = 1.486\,31(8), \quad (3.9)$$

as the weighted mean from measurements in even and odd Hg isotopes. The  $^{199}\text{Hg}$   $6^3P_1$  state with  $J = 1$  is split into the two hyperfine levels  $F = 1/2$  and  $F = 3/2$  with  $g$ -factors given by

$$g_{3P_1,F=1/2,^{199}\text{Hg}} = -\frac{1}{3}g_{1,^{199}\text{Hg}} + \frac{4}{3}g_J, \quad (3.10)$$

and

$$g_{3P_1,F=3/2,^{199}\text{Hg}} = \frac{1}{3}g_{1,^{199}\text{Hg}} + \frac{2}{3}g_J. \quad (3.11)$$

The numerical values of the  $g$ -factors for the  $^3P_1$  excited state are given in Table 3.6 for the even and odd Hg isotopes.

The Zeeman shift of the excited  $6^3P_1$  state is about three orders of magnitude larger compared to the ground state as can be seen by comparing the  $g$ -factors given in Table 3.5 and Table 3.6. It thus dominates the shift of the atomic transition lines. The shift is

Isotope	$F$	g factor
$^{199}\text{Hg}$	1/2	1.978 06(11)
$^{199}\text{Hg}$	3/2	0.989 13(5)
$^{201}\text{Hg}$	1/2	-0.989 40(5)
$^{201}\text{Hg}$	3/2	0.395 48(2)
$^{201}\text{Hg}$	5/2	0.593 32(3)
even	1	1.486 31(8)

Table 3.6: The g-factors of the different hyperfine structure levels of the  $6^3P_1$  excited state calculated according to (3.5) in the different mercury isotopes. The measured factor  $g_{J,6^3P_1} = 1.486\,31(8)$  [Dod61] was assumed for the calculation.

calculated from the energy shift of the involved magnetic sublevels. The  $^{199}\text{Hg}$   $F = 1/2$  line is shifted by 14 kHz by the  $1\,\mu\text{T}$  magnetic field in the nEDM experiment. This is negligible on the current sensitivity level of the  $^{199}\text{Hg}$  co-magnetometer as far as a possible vector light shift effect is concerned, as discussed in subsection 4.1.2. But the line shift is exploited in the SD-DAVLL setup to frequency stabilize the UV laser system to the line center of the  $^{199}\text{Hg}$   $F = 1/2$  transition as described in Subsection 3.5. The external magnetic field lifts the degeneracy between transitions induced by left or right circularly polarized light components. Neglecting the ground state Zeeman effect the  $F = 1/2$  line is split into two and the  $F = 3/2$  is split into four transitions, two for left and two for right circularly polarized light. The frequency shift away from the zero field position is shown in Figure 3.3 for the  $^{199}\text{Hg}$  as a function of external magnetic field. This sets the scale for the magnetic field that has to be applied in the SD-DAVLL setup. A relative shift of 10 MHz for the  $F = 1/2$   $\sigma^\pm$  transitions requires a magnetic field of  $\approx 360\,\mu\text{T}$ .

### The DC-Stark effect

Besides the influence of the magnetic field described by the Zeeman effect atomic energy levels are also shifted by external DC electric fields. This effect is known as the DC-Stark effect. In the case that the Zeeman interaction energy is much larger than the DC-Stark effect the quantization axis is given by the direction of the magnetic field and the DC-Stark shift can be treated as a small perturbation of the atomic sub levels characterized by their total angular momentum  $F$  and the projection quantum number  $m_F$ . The shift can be expressed in the following way as given in Ref. [HR00].

$$\begin{aligned}
W(F, m_F) = & -\frac{1}{2}\alpha_0 E^2 \\
& - \alpha_2 \frac{[3m_F^2 - F(F+1)][3X(X-1) - 4F(F+1)J(J+1)](3E_z^2 - E^2)}{(2F+3)(2F+2)2F(2F-1)2J(2J-1)},
\end{aligned} \tag{3.12}$$

where  $X = F(F+1) + J(J+1) - I(I+1)$  and  $E_z$  represents the projection of the electric field on the direction of the magnetic field. There is an energy shift due to the so-called

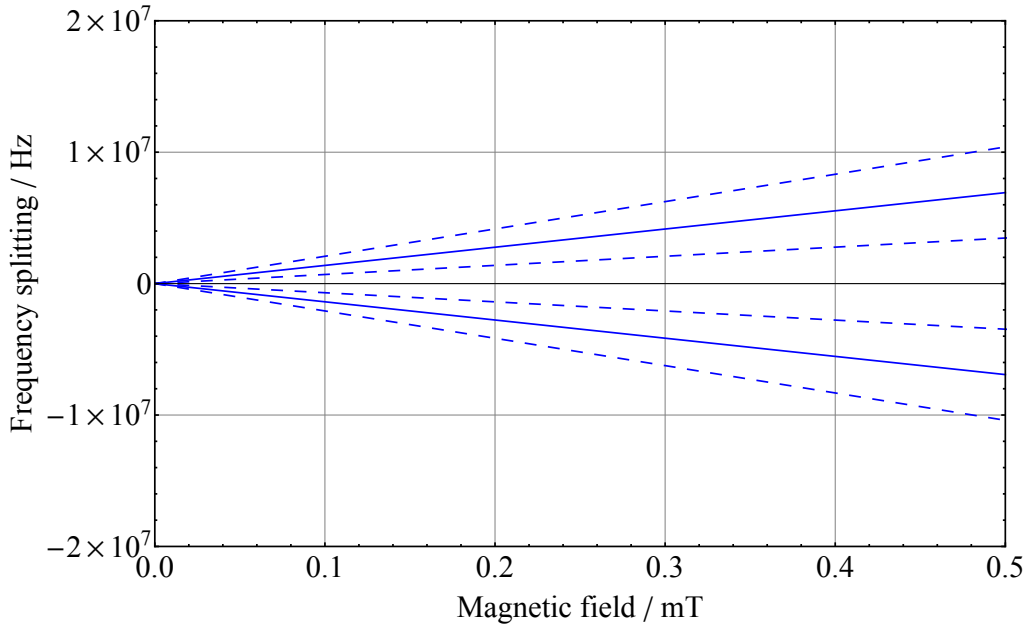


Figure 3.3: Zeeman effect of the hyperfine structure of  $^{199}\text{Hg}$ . The effect is shown for the magnetic sublevels of the  $F = 1/2$  (—) and the  $F = 3/2$  line (---) as a function of the external magnetic field. The effect is given as the energy equivalent frequency shift of the atomic levels relative to their zero field position. The  $F = 1/2$  line is split in two, the  $F = 3/2$  line in four components.

scalar polarizability  $\alpha_0$  independent of the electric field direction and a tensor polarizability  $\alpha_2$  part that depends on the electric field direction. For the  $6^1S_0$  ground state ( $J=0$  and  $I=1/2$ ) the tensor part vanishes and only the scalar component remains. Thus the Larmor precession frequency of the  $^{199}\text{Hg}$  atoms is not influenced to first order. Similarly the  $F = 1/2$  hyperfine component of the  $6^3P_1$  is not affected by a tensor like energy shift. The difference of the scalar polarizabilities for the two levels of the  $F = 1/2$  transition was measured in Ref. [HR00] and is given by

$$\alpha_{6^3P_1} - \alpha_{6^1S_0} = 3.95(7) \times 10^{-24} \text{ cm}^3 \quad (3.13)$$

For the  $^{199}\text{Hg}$   $F = 1/2$  line this translate into a shift of the line center position of

$$\Delta\nu_{E^2} = -3.32(6) \text{ kHz}/(\text{kV}/\text{cm})^2. \quad (3.14)$$

For the anticipated  $12 \text{ kV cm}^{-1}$  electric field in the nEDM experiment the frequency shift is thus  $-478 \text{ kHz}$  and can be as high as  $-922 \text{ kHz}$  for the maximal possible electric field of  $16.7 \text{ kV cm}^{-1}$  ( $200 \text{ kV}/12 \text{ cm}$ ). Comparing this with Figure 4.4 one sees that such a line shift does not produce a vector light shift of concern for the nEDM/n2EDM experiment. For the  $6^3P_1$  state the contribution related to  $\alpha_2$  is finite and splits the magnetic sublevels according to  $|m_F|$ . The frequency shift due to the tensor polarizability  $\alpha_2$  was measured



to be [KL72]

$$\alpha_2 = 1.578(3) \text{ kHz}/(\text{kV}/\text{cm})^2. \quad (3.15)$$

For the maximum electric field of  $16.7 \text{ kV cm}^{-1}$  along the direction of the magnetic field this results in

$$\delta\nu = \frac{1}{2}\alpha_2 E^2 = 219 \text{ kHz} \begin{cases} +1 & |m_F| = 1/2 \\ -1 & |m_F| = 3/2 \end{cases} \quad (3.16)$$

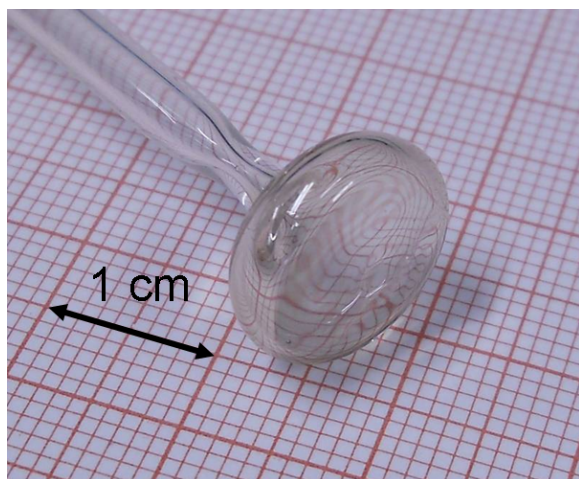
which is about a quarter of the line shift due to the scalar polarizability and thus of no concern.

### 3.3 The $^{204}\text{Hg}$ discharge bulbs

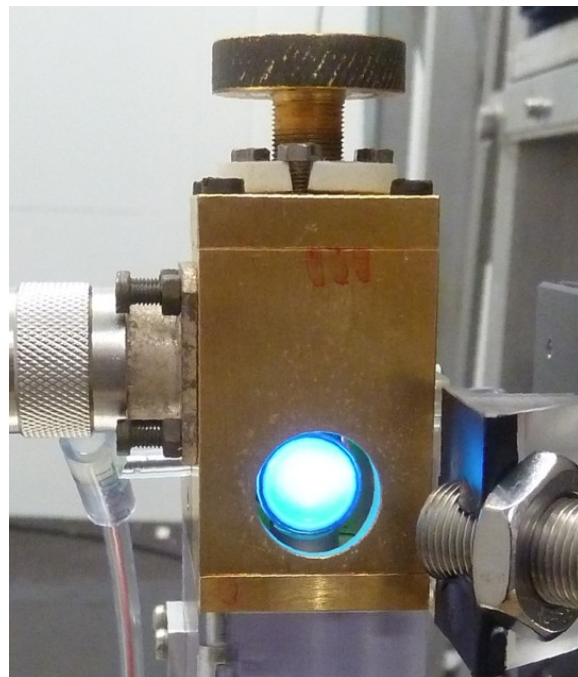
As mentioned in Section 3.1  $^{199}\text{Hg}$  is one of the rare cases where the nuclear spin can be manipulated by optical means. This is possible with a light source whose optical spectrum overlaps with the optical transitions in  $^{199}\text{Hg}$ . Since the end of the 19<sup>th</sup> century low pressure (buffer gas pressure  $< 10 \text{ mbar}$ ) mercury discharge lamps have served as a source of the  $253.7 \text{ nm}$  resonance light. A discharge bulb as used in the nEDM experiment is shown in Figure 3.4a. The bulbs are produced by the Fribourg Atomic Physics Group. The bulb, mouth blown from a quartz glass tube, has a flat head (diameter  $\approx 10 \text{ mm}$ ) and an extension tail. The bulbs are first evacuated, then filled with argon buffer gas and a small amount of metallic mercury before being sealed. The mercury in the bulb is enriched to 90 % in  $^{204}\text{Hg}$ . An electrode-less RF discharge is ignited in the bulb which is mounted inside a temperature stabilized microwave cavity running at  $2.4 \text{ GHz}$ . Mercury atoms are excited in the plasma and relax to the electronic ground state by emission of the  $253.7 \text{ nm}$  line. The emission line of  $^{204}\text{Hg}$  overlaps within the Doppler width ( $\approx 1 \text{ GHz}$ ) with the  $^{199}\text{Hg}$   $F = 1/2$  absorption line but does not suffer from hyperfine splitting (see Table 3.4). Therefore a  $^{204}\text{Hg}$  bulb is a convenient light source to manipulate the nuclear spin of  $^{199}\text{Hg}$  atoms.

But there are severe disadvantages to the  $^{204}\text{Hg}$  bulbs that makes their replacement desirable:

1. The optical line center in  $^{204}\text{Hg}$  is shifted by  $+96(18) \text{ MHz}$  relative to the line center of the  $^{199}\text{Hg}$   $F = 1/2$  line (see Table 3.4). This off-resonance light can induce a systematic frequency shift (vector light shift) in the  $^{199}\text{Hg}$  co-magnetometer which is discussed in detail in Subsection 4.1.2.
2. The emission lines are Doppler-broadened, effectively reducing the interaction cross-sections of the light beam and the mercury atoms.
3. The spectral emission profile can strongly deviate from a simple Doppler-broadened line shape due to radiation trapping. This effect reduces the absorption cross-section between atoms and the light emitted from the bulb drastically. The probability for a



(a) The bulb is mouth blown from a quartz glass tube transparent to 253.7 nm light. The tail serves as mercury reservoir and to hold the bulb inside the microwave cavity. The RF discharge is maintained mainly in the head area of the bulb.



(b) Photograph of an ignited  $^{204}\text{Hg}$  discharge bulb in a temperature stabilized RF cavity as used in the nEDM setup. A UV sensitive photodiode in front of the RF cavity is used to register fluctuations of the light output.

Figure 3.4: Photograph of a  $^{204}\text{Hg}$  discharge bulb as used in the nEDM setup.

photon to escape from the plasma discharge region is given by  $(1 - e^{-n\sigma d})$  where  $n$  is the atomic number density,  $\sigma$  the frequency dependent absorption cross-section and  $d$  the distance to the plasma surface. Therefore photons emitted on resonance with the atomic transition line have a very low probability to escape from a high density plasma region without re-absorption. Photons emitted with frequencies in the wings of the atomic transition line have a much higher probability to escape from the bulb. Consequently the emission profile normally resembles a double-hump structure with a minimum at the atomic transition line center. This effect is called line reversal and is strongly influenced by the bulb's temperature as the optical density changes with the Hg vapor pressure.

Since this effect also determines the efficiency of low pressure fluorescence-lamps (by determining how many UV photons hit the fluorescent material on the tube's wall) a wide range of Monte-Carlo simulations of Ar-Hg discharge tubes under various conditions have been performed by various authors. Figure 3.5 shows as an example the frequency distribution of photons that reach the inner surface of a 12.5 mm diameter discharge tube filled with mercury of natural isotopic composition and 400 mbar Ar buffer gas. The figure is taken from Ref. [BR03] but has been reduced to the coldest

spot temperature values of 20 °C and 40 °C as this is the relevant working range of the discharge bulbs in the nEDM experiment. In this case the line reversal is visible already at 20 °C. Data for temperatures up to 100 °C are given in Ref. [BR03].

4. Self-absorption depends on the geometry of the bulb and the buffer gas pressure, two parameters that are not well under control. Thus different bulbs can emit significantly different light spectra at the same operation temperature.
5. Emission lines of residual isotopes are present in the bulb's light spectrum. Light from the residual isotopes suffers less self-absorption in the lamp head due to the lower optical density and is thus emitted by the bulb with higher intensity than expected only from the mercury isotope ratio.
6. To avoid spectral misshaping, the bulbs have to be run at sub-room-temperature. This lowers the density of the Hg atoms in the gas phase and thus limits the light output to several microwatt for the bulbs in use. The cooling is limited by water condensation from the air on the bulb's surface.
7. The large area discharge bulbs have a low spatial coherence. Thus their light cannot be focused to small diameter light beams with low divergence. This is needed to efficiently transport light with optical fibers.

To qualitatively understand these effects it is interesting to measure the isotopic composition of the mercury in the  $^{204}\text{Hg}$  discharge bulbs. Figure 3.6a shows a setup to record a transmission spectrum of the  $^{204}\text{Hg}$  discharge bulbs. The transmission of a laser beam through the tail of the bulb is monitored while the laser light is frequency scanned over the absorption lines of the mercury isotopes. Details on the laser system can be found in Section 3.4. Figure 3.6b shows the recorded transmission spectrum for one bulb at room temperature. The two most prominent peaks can be assigned to the  $^{204}\text{Hg}$  and  $^{202}\text{Hg}$  isotopes. Fitting the transmission line shape as described in Section 3.1 confirms the high enrichment in  $^{204}\text{Hg}$  (88.8 % atom number fraction) but also reveals that a significant spectral contamination from  $^{202}\text{Hg}$  (10.5 % atom number fraction) has to be expected in the light emitted by the  $^{204}\text{Hg}$  discharge bulbs. A direct measurement of the  $^{204}\text{Hg}$  bulb emission spectrum was not intended although Zeeman absorption spectroscopy was recently performed on the 253.7 nm line as a nice alternative to high-cost, high-resolution UV spectrometers [ZRD08].

Summarizing one can say that the light frequency spectrum emitted by the discharge bulbs depend strongly on their running conditions. Thus the replacement by a well controllable laser light source is highly desirable.

### 3.4 The UV laser system

A commercial UV laser system (Toptica FHG pro, hereafter FHG) has been purchased to replace the  $^{204}\text{Hg}$  discharge bulbs (see Section 3.3) in the nEDM experiment. This section will discuss the laser system, describe its general performance parameters and demonstrate in which respects it is superior to the discharge bulbs used so far.

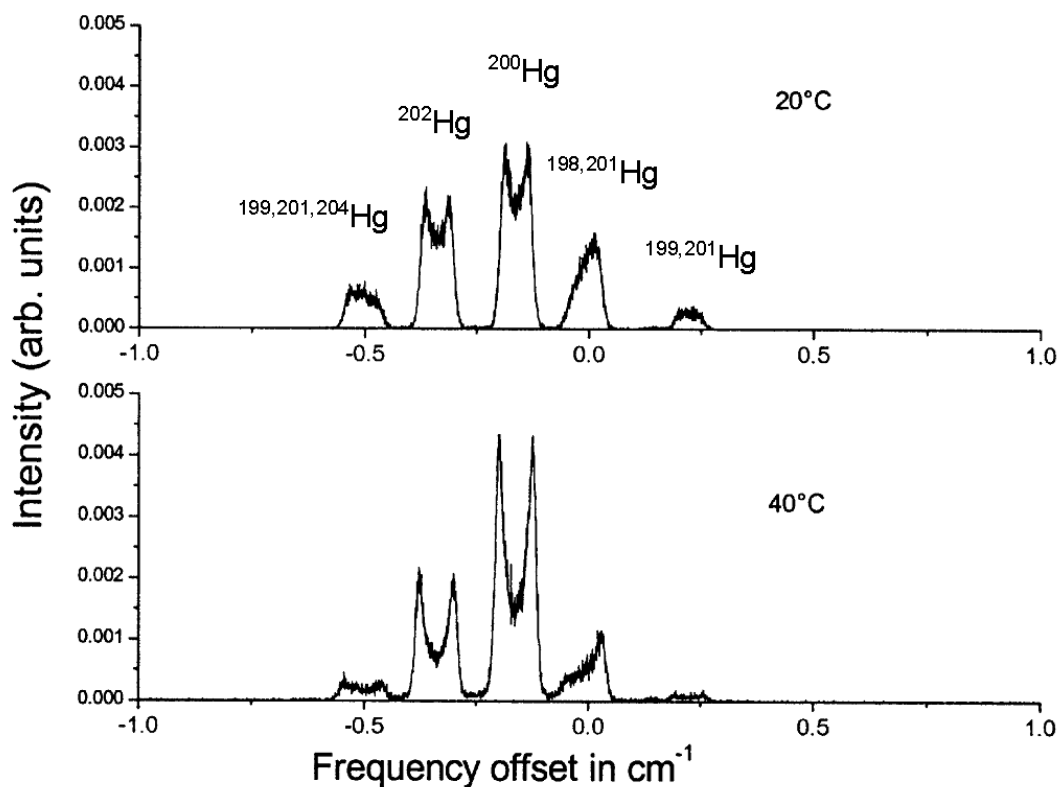
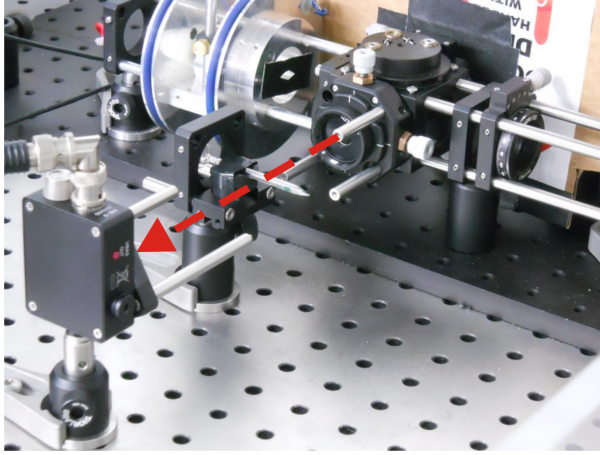
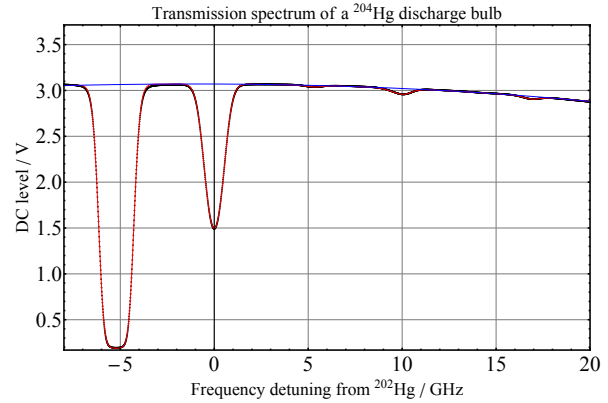


Figure 3.5: Monte-Carlo simulation of the emission spectrum of an Ar-Hg discharge tube of 12.5 mm diameter for two different temperatures and filled with Hg of natural isotopic composition. This result is taken from Ref. [BR03]. The line shape strongly deviates from a Doppler-broadened emission profile. Since the height of the nEDM discharge bulbs head is much smaller than its diameter the shown spectra can only indicate the qualitative behavior. On the other side the bulbs are filled with highly enriched  $^{204}\text{Hg}$  such that the effect is enhanced for the  $^{204}\text{Hg}$  line. The strong suppression of photons with frequencies at the atomic line center drastically reduces the ensemble averaged light absorption cross-section.



(a) Photograph of the optical setup. The UV laser light beam (indicated in red) passes through the tail of the  $^{204}\text{Hg}$  bulb and is detected on a UV photodiode.



(b) Transmission spectrum of  $^{204}\text{Hg}$  bulb # 24 as a function of frequency detuning relative to the transition in  $^{202}\text{Hg}$ . The two prominent peaks at 0 GHz and  $\approx 5$  GHz are due to  $^{202}\text{Hg}$  and  $^{204}\text{Hg}$ . Measured data points are shown in black. A fit of the absorption lines with (3.1) is also given (—).

Figure 3.6: Determination of the isotopic composition of the mercury in the  $^{204}\text{Hg}$  discharge bulb.

Since there are no high power laser diodes available at 253.7 nm the UV light has to be generated by frequency doubling in non-linear crystals. For a detailed theoretical description of the frequency doubling in non-linear crystals the reader is referred to one of the standard textbooks on non-linear optics, such as, e.g., Chapter 5.8 in [Dem08a]. As the frequency doubling is performed twice, the system is called a fourth-harmonic generator (FHG). The optical path of the laser system is shown in Figure 3.7. A picture of the open FHG system in operation is given in Figure 3.8. Components in slanted font are shown in Figure 3.7.

The FHG starts out with an external cavity diode laser (ECDL, *DL pro*) providing 45 mW of infrared light (IR) at the fundamental wavelength  $\lambda_{\text{IR}} = 1014.8$  nm. This master laser seeds a *tapered amplifier* (TA) from which it is separated by a  $-65$  dB Faraday isolator (transmission losses 30%, *optical isolator 1*). The pair of *folding mirrors 1* serves to optimize the coupling of the seed beam into the TA chip. The TA typically runs at a current of  $\approx 3$  A and amplifies the 34 mW input light to 560 mW after a second  $-65$  dB Faraday isolator (transmission losses 30%, *optical isolator 2*). The IR light is coupled with a double pair of *folding mirrors (2 and 3)* into a bow-tie enhancement cavity with a quality factor  $Q \approx 80$ . The proper spatial mode matching is achieved with the *mode matching optics 1* in front of the cavity. The light path in the cavity runs through a lithiumtriborate (*LBO*) crystal mounted on a height adjustable pitch-tilt-table. Together with the folding mirrors and the cavity mirror mounts one can align the non-linear crystal relative to the light beam to achieve the necessary phase matching for optimized frequency conversion.

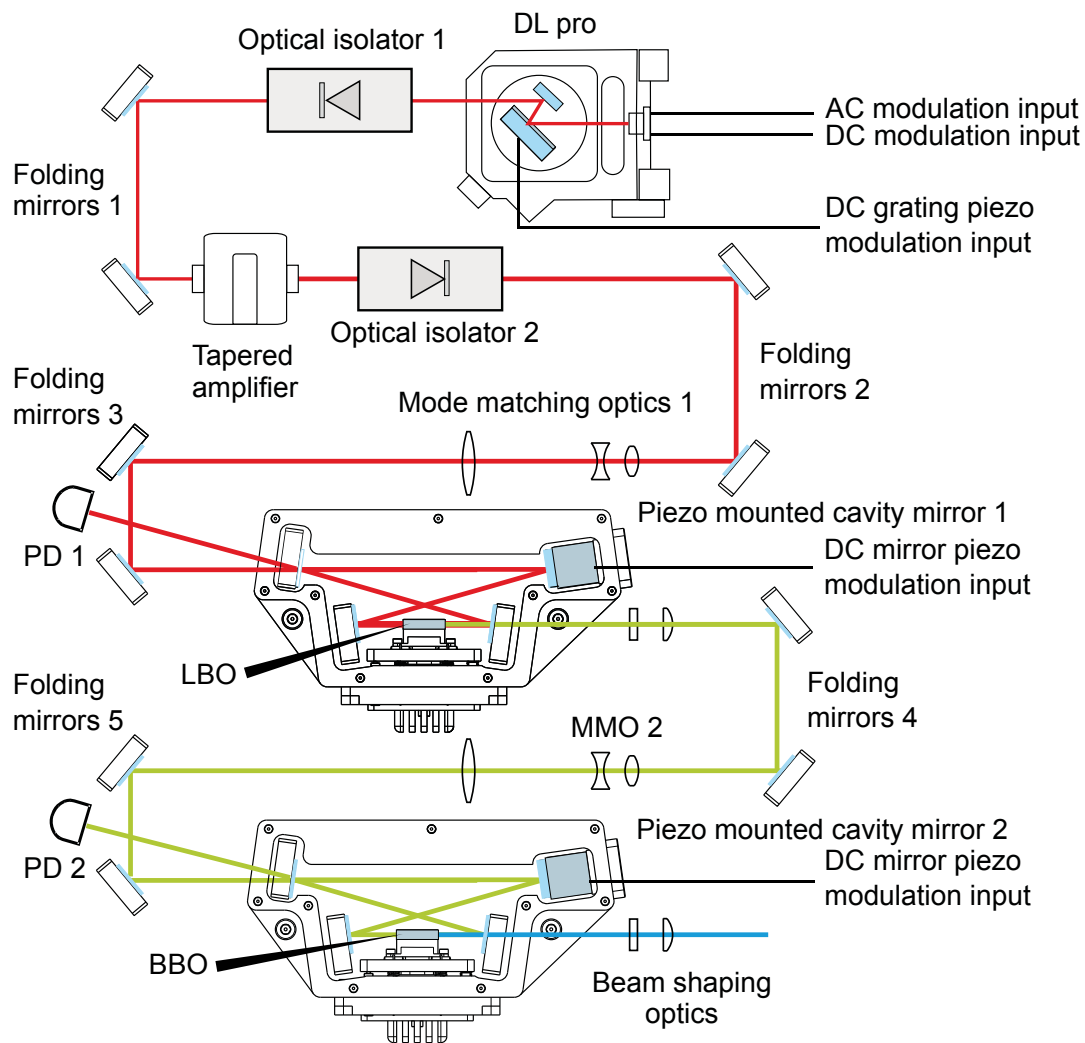
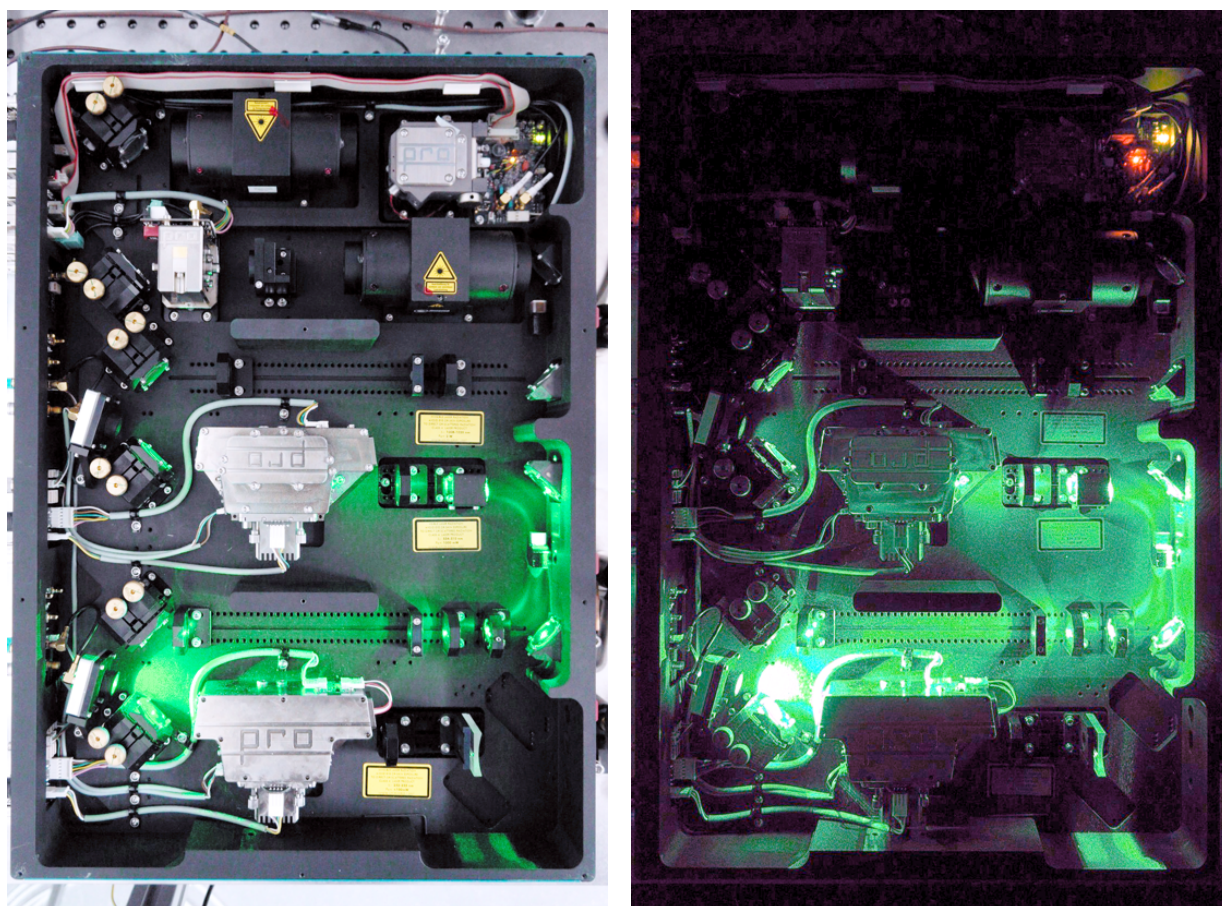


Figure 3.7: Scheme of the light path inside the Toptica FHG pro system. For a detailed discussion of the single components see the text. The picture is taken from Ref. [TOP] with modifications by the author.





(a) Photograph of the open FHG. The master laser head sits at the top right side of the system. To its left and below one can see the optical isolators. The resonator cavities are sealed to improve the stability of the system.

(b) Photograph of the open FHG. The IR and the UV are invisible to the camera.

Figure 3.8: Photograph of the open FHG during operation. During normal operation the system cover is closed to reduce dust settling in the system.

Most of the time it is sufficient to tune the two folding mirrors directly in front of the cavity and the crystal table to optimize the output power of the green light. The cavity mirror themselves are extremely sensitive and have only to be used for major readjustments. The output power of green light at 507.4 nm can be as high as 250 mW for an IR light input power of 560 mW. The crystal is actively temperature stabilized to 37.2 °C.

The green light is folded via a second double pair of *folding mirrors (4 and 5)* into the second enhancement cavity (basically a copy of the first one). The non-linear frequency-doubling element in this second cavity is a  $\beta$ -barium borate (BBO) crystal. The UV output power at 253.7 nm was as high as 27 mW when the system was delivered. However, a broken piezo actuator (used to keep the cavity on resonance with the input light) forced us to exchange a mirror-piezo combination. After the realignment a maximum UV output power of 20 mW was achieved. The BBO crystal is temperature stabilized to 25.0 °C. The UV beam passes *beam shaping optics* to compensate the strong astigmatism of the crystal to produce an approximate circular light beam. As the full UV output power is not always needed in the nEDM setup the TA normally runs with reduced current to give a UV power level between 5 mW and 10 mW. This reduces the light-induced damage in the BBO crystal and thus allows for longer maintenance intervals between the necessary realignments of the non-linear crystal (on the order of one week).

Both enhancement cavities are locked to their input light wavelength using the Pound-Drever-Hall (PDH) locking scheme [DHK<sup>+</sup>83]. The master laser diode current can be modulated on an *AC-coupled* and on a *DC-coupled input* channel. The AC-coupled channel is used to modulate the diode current at 5 MHz producing the symmetric frequency sidebands on the fundamental laser beam that are needed for the PDH lock. Fast photodiodes (*PD 1* and *PD 2*) in front of each enhancement cavity pick up the heterodyne signal of the carrier and the side band light. After demodulation, the frequency dependent error signal is used for feedback control. The error signal of the first enhancement cavity is split into two paths for a so-called bias-T lock. One part of the signal is directly fed back to the DC modulation input of the master laser diode current. This is a very fast feedback circuit that stabilizes the laser wavelength to the resonance wavelength of the first enhancement cavity on short time scales (microseconds to milliseconds). The second part of the signal is sent to a conventional PID controller that acts back on the *piezo mounted cavity mirror*. This intrinsically slower feedback circuit (limited by the mechanical resonance frequency of the piezo-mirror combination) stabilizes the cavity to the master laser wavelength on longer time scales (milliseconds to seconds). The second cavity can be length-stabilized without any further frequency modulator because the transmission function of the first enhancement cavity is sufficiently broad that IR light of the side band frequency can enter the cavity and can be frequency converted. Thus also the green light at 507 nm has 5 MHz sidebands that are used to keep the second cavity on resonance with the wavelength of the green light.

All electronic modules used to control the crystal temperatures, the master laser diode current, the master laser diode temperature, the master laser grating piezo and to lock the enhancement cavities are combined in a double staged 19" rack. In addition the rack houses a FPGA-based module used to frequency stabilize the master laser to the atomic



transitions in mercury. Here the PID error signal is fed back to the DC-coupled modulation input of the DL grating. The laser system has a mode-hop-free tuning range of more than 30 GHz at a scan rate of about 0.1 Hz. A transmission spectrum through a  $^{199}\text{Hg}$  enriched vapor is shown in Figure 3.2. The mode-hop-free tuning range<sup>4</sup> expands over the transition lines in all stable Hg isotopes.

## 3.5 The laser frequency lock

### 3.5.1 Light frequency accuracy requirements for nEDM/n2EDM

To make the new UV laser system useful for the  $^{199}\text{Hg}$  co-magnetometer in nEDM the UV light has to be frequency-stabilized (frequency locked). For the absorptive detection scheme with circularly polarized light (discussed in detail in the Subsection 4.1.1), the laser has to be frequency stabilized close to the center of the  $^{199}\text{Hg } 6^1S_0 \rightarrow 6^3P_1$   $F = 1/2$  or  $F = 3/2$  line to maximize the absorption cross-section. To suppress the vector light shift effect (discussed in Subsection 4.1.2) in  $^{199}\text{Hg}$  the optimal light frequency is shifted from the  $^{199}\text{Hg } 6^1S_0 \rightarrow 6^3P_1$  line center, e.g.,  $\approx -6$  MHz for the  $F = 1/2$  line. For the detection of the paramagnetic rotation effect, the laser has to be frequency stabilized between the two hyperfine components in  $^{199}\text{Hg}$  to maximize the effect with minimal light absorption. Alternatively one could frequency stabilize the laser to the maximum of the paramagnetic rotation effect close to the resonance center, but at these positions the absorption of light is still strong. For elliptically polarized light (e.g., a contamination of the linearly polarized light with circularly polarized light) the measured effect will be a combination of absorption and paramagnetic rotation.

Here the more restrictive requirements on the frequency accuracy for the absorptive measurement scheme for n2EDM are discussed. In Section 2.4 a magnetometric sensitivity goal of the  $^{199}\text{Hg}$  co-magnetometer of 10 fT per cycle was put forward. In a 1  $\mu\text{T}$  field this corresponds to a relative accuracy of  $1 \times 10^{-8}$ . From the statistical point of view, the minimum signal-to-noise density ratio (SNDR, normalized to unity bandwidth) required to achieve this sensitivity is  $(a_s/\rho)^* = 8400$  for a transverse spin relaxation time  $\tau = 100$  s and a measurement time  $T = 150$  s (see Section 2.4).

As shown in Section 5.2 a normalized signal amplitude  $(a_s/I_1) \approx 12.5\%$  can be achieved in the nEDM setup at  $A \approx 40\%$  light absorption. The shot noise of the detected photon flux is given by

$$\rho_N = \sqrt{2\dot{N}}, \quad (3.17)$$

where  $\dot{N}$  is the photon detection rate. Assuming shot noise only,  $\rho = \rho_N$ , the minimum

---

<sup>4</sup>The mode-hop-free tuning range describes the frequency range that a laser can be continuously frequency scanned without spontaneous jump to a different longitudinal operation mode.

photon detection rate is given by

$$\dot{N} = \frac{2(1-A)}{a_s^2} ((a_s/\rho)^*)^2 = 5.9 \times 10^9 \text{ s}^{-1}. \quad (3.18)$$

This corresponds to  $0.005 \mu\text{W}$  of detected UV photons. The maximum useful UV power is given by the light-induced depolarization of  $^{199}\text{Hg}$  and the maximally acceptable vector light shift effect. As derived later in (5.33) the depolarization of spin-polarized  $^{199}\text{Hg}$  atoms by light in the nEDM geometry is

$$\left\langle \frac{1}{T_{1,\text{light}}} \right\rangle_{V_{\text{chamber}}} = P_0 8.6 \times 10^{-4} \text{ s}^{-1} \mu\text{W}^{-1} \quad (3.19)$$

which limits the maximum light power to  $\leq 11.6 \mu\text{W}$ . The relative vector light shift (VLS) effect on the  $1 \mu\text{T}$  field is given in Figure 4.4 for  $5 \mu\text{W}$  and a misalignment of  $1 \text{ mrad}$  in the nEDM geometry. Under these conditions the residual VLS effect amounts to  $6 \text{ ppb}$  for laser light on resonance with the  $^{199}\text{Hg } 6^1S_0 \rightarrow 6^3P_1 F = 1/2$  transition. The relative VLS is smaller than  $10 \text{ ppb}$  for a laser frequency detuning of  $-22 \text{ MHz}$  to  $6 \text{ MHz}$  around the resonance. Therefore the frequency error signal has to have a width on the order of  $1 \text{ MHz}$  to be able to suppress the VLS effect to a negligible level.

### 3.5.2 The sub-Doppler dichroic atomic vapor laser lock

For the  $^{199}\text{Hg}$  co-magnetometer in n2EDM experiment the fractional UV laser frequency uncertainty has to be  $\approx 1 \times 10^{-9}$ . A suitable error signal for the frequency stabilization can be derived by suppressing the Doppler-broadening of atomic transitions. There exists a wide range of so-called sub-Doppler spectroscopy techniques and methods. A good overview of the field can be found in, e.g., Refs. [Dem08a, Dem08b]. A huge range of techniques has been developed in the last decades to frequency stabilize all different kinds of lasers used in research and industry far beyond the demands for the  $^{199}\text{Hg}$  co-magnetometer. Artificial wavelength and frequency references, e.g., ultra low expansion (ULE) cavities can be used to provide sub-Hz laser line width for diode lasers (fractional frequency uncertainty  $\approx 1 \times 10^{-15}$ ) [AMK<sup>+</sup>08, SMHS06, LHN<sup>+</sup>07]. These narrow bandwidth lasers are used for the spectroscopy of optical clock transitions or in the measurement of the hydrogen energy levels. Sometimes the ULE cavities are themselves locked to an atomic transition of similar line width to provide long term accuracy of the frequency. With the development of the frequency comb technology in 1998/1999 [RHUH99, Hän06] absolute measurements of optical frequencies became possible.

For the frequency stabilization in the  $^{199}\text{Hg}$  co-magnetometer for nEDM/n2EDM the idea of Sub-Doppler Dichroic Atomic Vapor Laser Lock (SD-DAVLL)<sup>5</sup>, as demonstrated for the first time in 2002/2003 for  $^{85,87}\text{Rb}$  and Na [PFL<sup>+</sup>03, WGZZ02], was extended to

---

<sup>5</sup>Dichroism is used here in the sense of different absorption rates for different *polarization* states of light. The second meaning, as used, e.g., in connection with dichroic beamsplitters or dichroic mirrors, is the splitting of a light beam according to the *wavelength* of the light.

the deep ultraviolet regime. At least one other group also successfully took this approach at the same time to frequency stabilize a FHG system for the use in a magneto-optical trap setup for mercury [LYQ<sup>+</sup>13]. The SD-DAVLL concept combines the two techniques of saturation absorption spectroscopy (SAS) and magnetically induced dichroism to obtain a dispersion-like error signal around the atomic resonance for the frequency stabilization of the laser.

### Dichroic Atomic Vapor Laser Lock

The signals involved in the DAVLL are explained in Figure 3.9. Because of the first order Zeeman effect (described in Subsection 3.2) an external magnetic field shifts the magnetic sublevels of atoms (and so the corresponding absorption lines) away from the resonance line center position in zero magnetic field. Consequently the left ( $\sigma^+$ ) and right ( $\sigma^-$ ) circularly polarized sub-components of a linearly polarized light beam propagating along the direction of the external magnetic field are absorbed at different rates when passing through the vapor. The different absorption can be detected if the light beam is passed through a  $\lambda/4$  plate and a polarizing beam splitter to separate the  $\sigma^\pm$  sub-components of the light before detection. The difference between the two absorption signals provides a dispersion-like error signal symmetric around the unshifted line center without any additional frequency modulation of the UV light. The DAVLL method can be applied to Doppler-broadened resonance lines with a locking range typically on the order of gigahertz [CLH<sup>+</sup>98] or to the sub-Doppler regime with locking ranges on the order of the natural line width of the transition.

### Saturation absorption spectroscopy

To resolve the natural line width  $\Gamma_0/2\pi$  of an atomic transition it is necessary to suppress the Doppler broadening due to the thermal motion. This can be done by probing the change in level population caused by an high intensity pump beam with a second low intensity and counter-propagating probe beam. The light intensity at which the population difference is reduced to half of its thermal equilibrium value is given by the saturation intensity [Dem08b]

$$I_{\text{sat}} = \frac{h\nu\Gamma_0}{2\sigma_0}, \quad (3.20)$$

where  $\sigma_0$  is the (non-Doppler-broadened) resonance absorption cross-section of the transition and  $\Gamma_0$  the excited state decay rate. The light absorption cross-section on the  $6^1S_0 \rightarrow 6^3P_1 F = 1/2$  line is only one third of the absorption cross-section in the even isotopes due to hyperfine splitting:  $\sigma_0(^{199}\text{Hg } F = 1/2) = 1/3 \sigma_0(\text{even Hg})$  (see Table 3.3). Thus the saturation intensity of the  $6^1S_0 \rightarrow 6^3P_1 F = 1/2$  transition is  $I_{\text{sat}, 199\text{Hg}, F=1/2} = 30.6 \text{ mW cm}^{-2}$ .

The SD-DAVLL setup described in detail below uses a strong pump beam and a back-reflected counter-propagating weak probe beam of the same light frequency  $\nu$ . Only atoms in the velocity class  $\mathbf{v}d\mathbf{v}$  which fulfill  $|(\nu - \mathbf{k} \cdot \mathbf{v}) - \nu_0| < \frac{\Gamma_0}{2\pi}$  can contribute significantly to

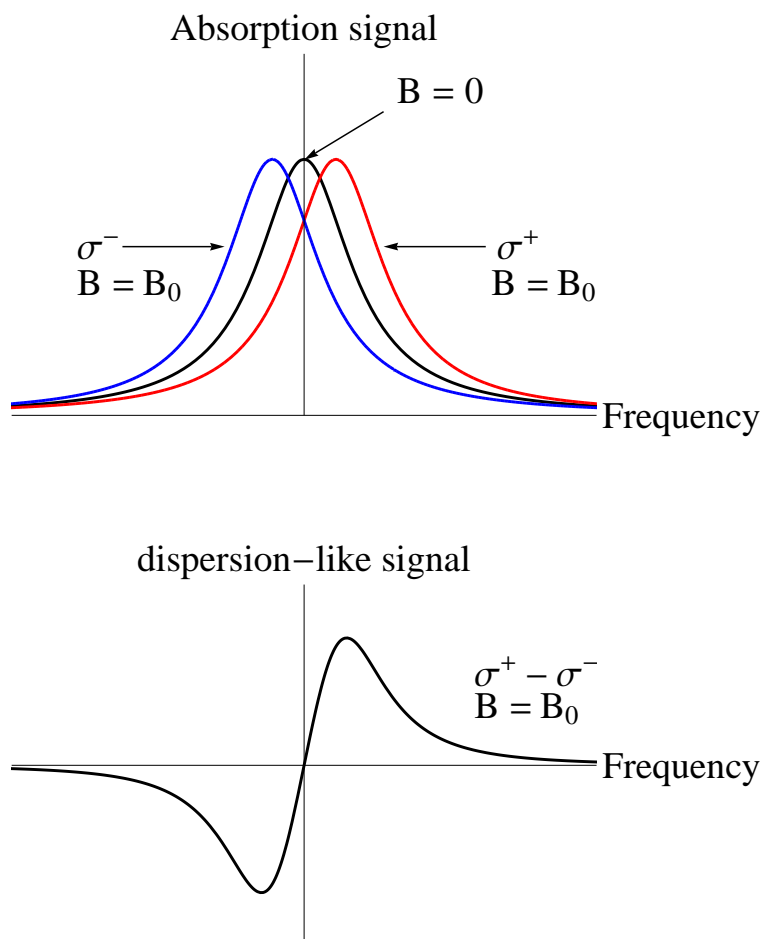


Figure 3.9: The basic signals involved in a DAVLL. Due to the Zeeman effect the magnetic sub-levels in an atom (and so the corresponding absorption lines) are shifted away from the resonance line center position. Consequently the right ( $\sigma^-$ ) and left ( $\sigma^+$ ) circularly polarized sub components of a linearly polarized light beam are absorbed at different rates when passing through the vapor. The difference between the two absorption signals provides a dispersion-like error signal symmetric around the un-shifted line center.

the light absorption and can therefore be saturated. Since the sign of  $\mathbf{k} \cdot \mathbf{v}$  is opposite for the pump and the probe beams in general two different velocity classes of atoms interact with the laser beams unless  $\mathbf{k} \cdot \mathbf{v} = 0$ . This is the case for atoms that only have velocity components perpendicular to the light beams. For the electronic configuration of the  $^{199}\text{Hg } F = 1/2$  line, the saturation of the transition by the pump beam leads to a reduced absorption of the probe beam (Lamb dip) and thus a small peak appears in the transmitted light intensity at the resonance frequency  $\nu_0$ . The exact shape of the Doppler-free line in general also depends on effects of optical pumping as discussed, e.g., in Ref. [SKWM94]. The detected width of the transition is given by the natural life time, the power broadening introduced by the pump and probe beam and other effects that reduce the excited state lifetime, e.g., rest gas collisions.

### The mercury SD-DAVLL setup

The SD-DAVLL setup for mercury is sketched in Figure 3.10 and a photograph is given in Figure 3.11. A variable fraction of the UV power available from the FHG system is split off the main light beam by using a  $\lambda/2$ -plate and a polarizing beam splitter cube (UV PBS). A pair of beam-steering mirrors allows the alignment of the light path. A second  $\lambda/2$  plate is used to maximize the transition of the UV light beam through a (nominally) non-polarizing beam splitter plate (UV BSP) as it was found experimentally that the UV BSP is not totally polarization insensitive. The high intensity pump beam passes through a 20 mm long spectroscopy cell installed between two coils in Helmholtz configuration (radius  $R = 40$  mm, 25 turns). The Helmholtz coils provide a longitudinal bias magnetic field along the light path with a calculated magnetic field of  $0.56 \text{ mT A}^{-1}$  at the center point. The calculated longitudinal field distribution along the light path is given for a coil current of 1 A in Figure 3.12.

The spectroscopy cells are filled with  $^{199}\text{Hg}$ -enriched mercury (details of the production procedure are given in App. E) and placed between two 1 mm apertures to block reflected light beams. The light transmission through the cell is  $\approx 73\%$  on the  $^{199}\text{Hg } F = 1/2$  resonance. A transmission spectrum of the cell is given in appendix E. To probe the atomic saturation the transmitted pump beam is reflected back onto itself for best spatial overlap. After passing the apertures again the probe beam is split a second time at the UV BSP. The  $\sigma^{+,-}$  components of the beam are converted into s- and p- linearly polarized components with a  $\lambda/4$  plate. The resulting s- and p- components are separated with a polarizing beam splitter. In this way the light components corresponding to  $\sigma^{+,-}$  polarization in the spectroscopy cell are detected separately on the two photodiodes of a differential detector. In addition to the detection signal of each photodiode the differential signal is available at an extra output channel. To balance the differential detector output, the light power in front of one photodiode can be adjusted by a neutral density filter (NDF). The three output signals are typically passed through a RC circuit that acts as a 10 kHz low-pass filter before being recorded or used for the frequency feedback.

A typical SD-DAVLL signal is shown in Figure 3.14 around the  $^{199}\text{Hg } F = 1/2$  resonance recorded in a 20 mm long spectroscopy cell filled with enriched  $^{199}\text{Hg}$ . The pump beam

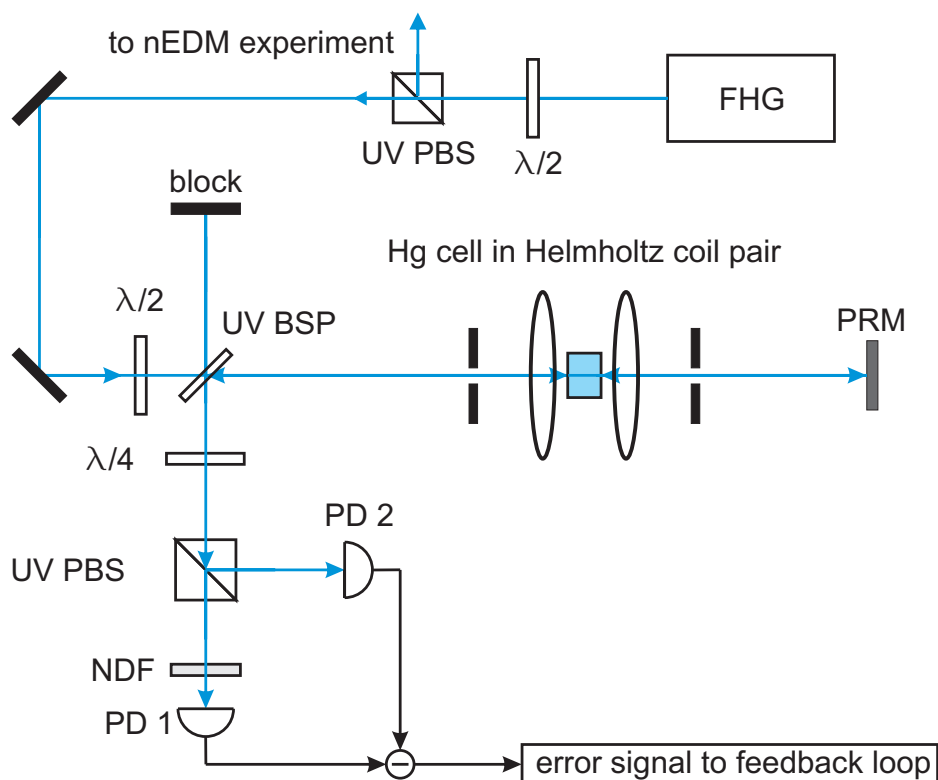


Figure 3.10: Sketch of the SD-DAVLL setup used for the Hg co-magnetometer. A detailed discussion of the light path is given in the text. The following abbreviations are used: FHG: Forth-harmonic generator,  $\lambda/2$ : half wave plate, UV PBS: UV polarizing beam splitter cube, UV BSP: non-polarizing beam splitter plate, PRM: partially reflecting mirror, NDF: neutral density filter, PD: photodiode.

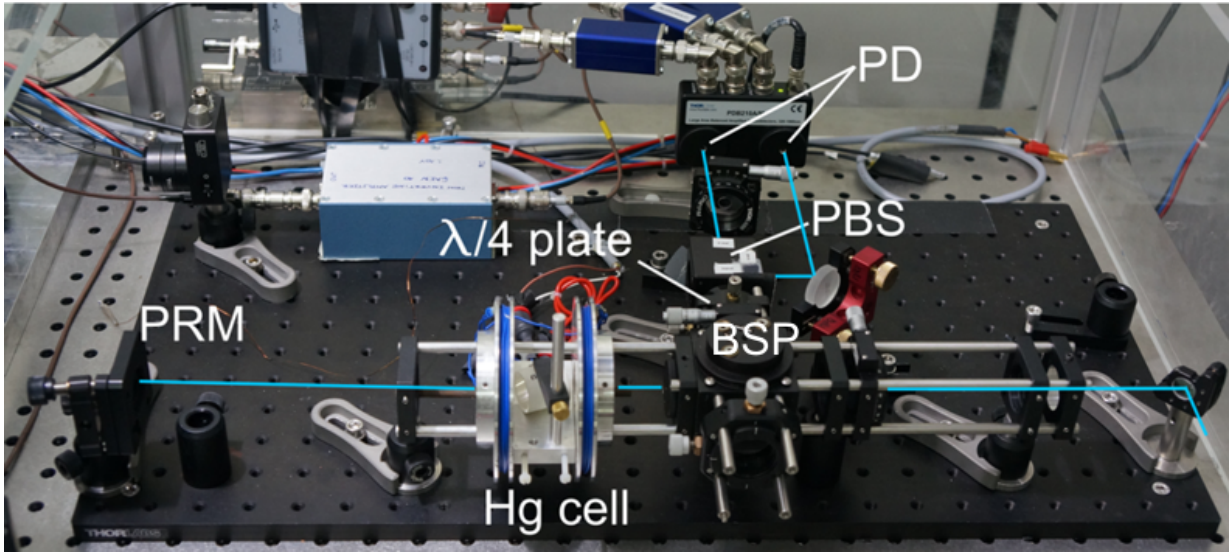


Figure 3.11: Picture of the SD-DAVLL setup. The cyan line indicates the light path. UV light enters the setup via the mirror at the lower right corner of the picture and travels to the left. The beam passes the 50/50 beam splitter plate (BSP). The pump beam is traversing the Hg spectroscopy cell and bounces back from a (partially) reflecting mirror to probe the saturation of the Hg atoms. The probe beam is split again at the BSP before traveling through a  $\lambda/4$  plate. The s- and p- polarized light components are separated by the polarizing beam splitter (PBS). Each component is detected on a photodiode (PD).

power was set to  $P_{\text{pump}} = 120(1) \mu\text{W}$  (measured at the front side of the spectroscopy cell with a calibrated power meter<sup>6</sup>). In this setup the probe beam power can be measured only in front of the polarizing beam splitter cube of the polarimeter as the probe beam is the back-reflected pump beam ( $P_{\text{probe}} = 11.3(1) \mu\text{W}$ ). The current in the Helmholtz coil pair was set to  $I_{\text{coil}} = 150 \text{ mA}$ . The extracted transition line width (FWHM) is  $\Gamma = 7.8 \text{ MHz}$ . This has to be compared to the natural line width (FWHM) of  $1.27 \text{ MHz}$ .

Four possible reasons for the increased line width have been considered:

1. Frequency fluctuations: If the UV laser shows frequency fluctuations on the time scale of the measurement time ( $\approx 1 \text{ ms}$ , frequency scan rate  $10 \text{ GHz s}^{-1}$ ) then the recorded signal will be broadened accordingly. The influence of air pressure changes on the laser frequency (e.g., due to the air conditioning system in the building) was observed. For the measurement of the SD-DAVLL signal the FHG was free running, i.e., the IR master laser was *wavelength* stabilized to the first resonator cavity. A change in air pressure changes the refractive index of the air in the resonator cavity and thus the corresponding laser *frequency*. A frequency shift of  $\approx 190 \text{ MHz mbar}^{-1}$  ( $47.5 \text{ MHz mbar}^{-1}$ ) or a relative change of  $1.9 \times 10^{-7} \text{ mbar}^{-1}$  has been observed for the UV light (IR light). The literature value for the relative change

<sup>6</sup>Thorlabs PM100D, sensor head S130VC

of the refractive index of air of standard composition and at STP and 15 °C (*standard air*) is  $2.7 \times 10^{-7} \text{ mbar}^{-1}$  [Cid96]. For reference air pressure fluctuations of  $1 \times 10^{-2} \text{ mbar}$  induce frequency fluctuations of 2 MHz for the UV light. The ambient air pressure in the laboratory could not be surveyed to this level. If the laser is frequency locked to an atomic transition these fluctuations are compensated for by the frequency feedback system.

2. Angular misalignment: If the pump and probe beams are not exactly counter-propagating there is a residual Doppler broadening  $\delta\nu_D = \nu_D\alpha$ , where  $\alpha$  is the angle of misalignment between pump and probe beam. In case of  $^{199}\text{Hg}$   $\nu_D \approx 1 \text{ GHz}$ . In the SD-DAVLL setup, the distance between the first 1 mm aperture and the reflecting mirror is  $L = 27 \text{ cm}$ . A maximum horizontal beam displacement of 1 mm after the  $L = 54 \text{ cm}$  long roundtrip corresponds to 1.9 mrad misalignment or an uncompensated Doppler contribution of 1.9 MHz.
3. Power broadening: Due to induced emission, the excited state lifetime is reduced and the transition is accordingly broadened. The expected power broadened FWHM is  $\Gamma_s = \Gamma_0\sqrt{1 + I/I_{\text{sat}}}$ . The extracted FWHM as a function of pump power in front of the spectroscopy cell is shown in Figure 3.15. For the conditions of Figure 3.14 the FWHM contribution due to power broadening is  $\approx 1.9 \text{ MHz}$ . From the fit of the expected intensity dependence an effective pump beam diameter  $d_{\text{beam,eff}} = 0.67(3) \text{ mm}$  is extracted for a flat top intensity profile by assuming the pump beam power  $P_{\text{pump}} = 120(1) \mu\text{W}$  and that there is no attenuation along the light path. Extrapolation to zero light power results in a  $FWHM = 4.5 \text{ MHz}$ .
4. Pressure broadening: The excited state lifetime can be reduced due to quenching collisions with rest gas. This possibility seems unlikely as the spectroscopy cell was pumped below  $p_{\text{rest}} = 1 \times 10^{-6} \text{ mbar}$  and baked for more than one day at 300 °C before it was filled with mercury. No pressure rise in the vacuum system was observed when sealing the spectroscopy cell.

To optimize the slope of the SD-DAVLL signal around the line center position, the SD-DAVLL signal as a function of the Helmholtz coil current was recorded for a set of specific but fixed pump light intensities. The measurement results are shown in Figure 3.13 for the  $^{199}\text{Hg } F = 1/2$  transition. The slope of the SD-DAVLL signal increases steeply with increasing current before reaching a maximum and then decreasing again for even stronger magnetic field. In the high magnetic field region, the Lamb dips for the  $\sigma^\pm$  components are shifted to far away from each other to produce a dispersion-like difference signal. The natural limit for the pump light intensity is the amount of additional power broadening that can be accepted. The SD-DAVLL technique has three advantages that make it particularly attractive:

- The laser can be frequency stabilized without an additional frequency modulation on the UV light.
- The technique can be applied to all Hg isotopes as can be seen from Figure 3.16 where the SD-DAVLL signal from a 2 mm thick spectroscopy cell filled with natural



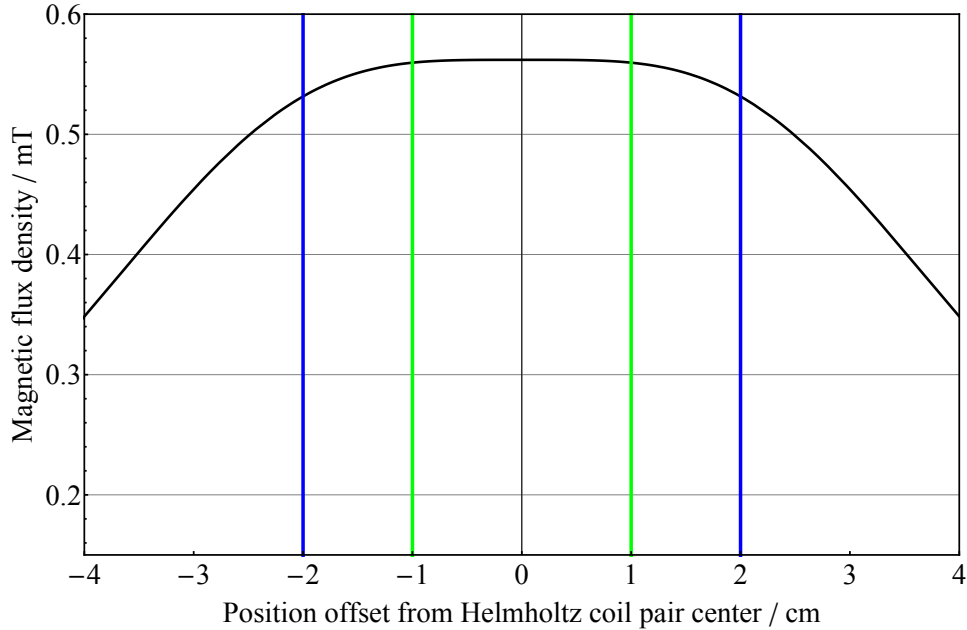


Figure 3.12: The calculated magnitude of the magnetic field created by the Helmholtz coil configuration (radius  $R = 40$  mm, 25 turns) used in the SD-DAVLL setup. The field value is given for positions on the symmetry axis relative to the center of the coil configuration for 1 A coil current. The green vertical lines indicate the edges of the 20 mm spectroscopy cell, while the blue vertical lines indicate the position of the coils.

Hg is shown. In addition a scan over the frequency range of all Hg isotopes is shown in Fig.3.17.

- Besides the field independent zero crossing at the center of the resonance line there are additional magnetic field-dependent lock points available in medium magnetic fields. The magnetic field has to split the transitions between the magnetic sub-levels by approximately their natural line width to optimize the signal slope. In this way a laser can easily be frequency stabilized to one of these additional lock points and its frequency can be tuned by magnetic field adjustment. The effect is shown in Figure 3.18 for the  $^{199}\text{Hg } 6^1S_0 \rightarrow 6^3P_1 F = 3/2$  transition.

Summarizing, one can say that the SD-DAVLL setup provides an error signal around the  $^{199}\text{Hg } F = 1/2$  resonance line that is very well suited to frequency stabilize the UV laser system with the required frequency accuracy (as discussed in detail in Subsection 3.5.1). Although there seems to be an additional contribution to the Doppler-free line width beyond the effects discussed above that contributes with 2.6 MHz to the measured linewidth.

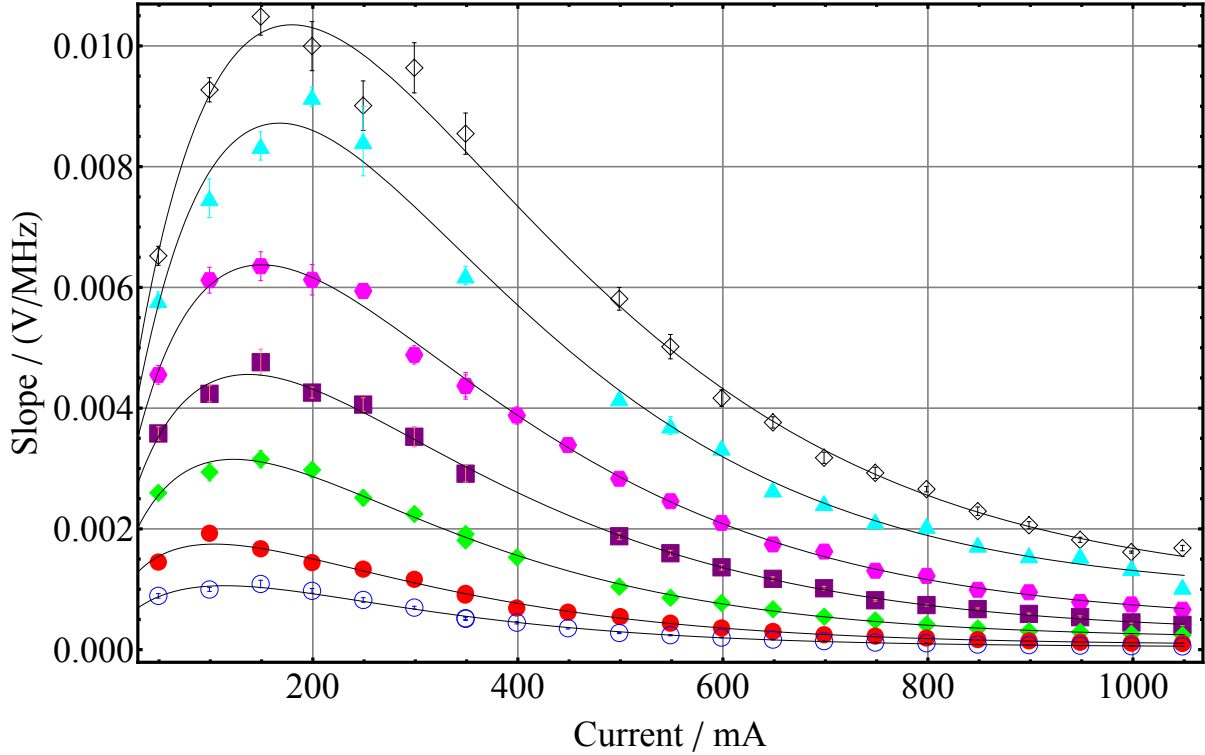


Figure 3.13: Slope of the SD-DAVLL signal at the center frequency as a function of the Helmholtz coil current for different values of the pump beam power. The pump beam power was set to  $42.5 \mu\text{W}$  ( $\circ$ ),  $57.5 \mu\text{W}$  ( $\bullet$ ),  $84.3 \mu\text{W}$  ( $\blacklozenge$ ),  $120 \mu\text{W}$  ( $\blacksquare$ ),  $160 \mu\text{W}$  ( $\blacklozenge$ ),  $222 \mu\text{W}$  ( $\blacktriangle$ ), and  $270 \mu\text{W}$  ( $\diamond$ ). The lines are guides to the eye.

### 3.6 UV grade optical fibers

The UV laser system has been installed in a laboratory about 50 m away from the nEDM experimental site. This laboratory provides better conditions in terms of temperature stability, cleanliness and accessibility compared to the experimental area around the thermally insulated house with the nEDM apparatus inside. However, the disadvantage is that there is no direct line-of-sight from the laboratory to the nEDM experiment. Therefore two solarization-resistant<sup>7</sup> UV grade multimode optical fibers<sup>8</sup> have been installed to transport the UV laser light from the optical table in the laboratory to the nEDM experiment. The optical fibers have core diameters of  $200 \mu\text{m}$  and  $600 \mu\text{m}$  and a length of 50 m each. The diameter of the laser beam in the precession chamber is three times larger for the  $600 \mu\text{m}$  fiber than for the  $200 \mu\text{m}$  fiber. The measured transmission of the new  $600 \mu\text{m}$  fiber was 4.2%. A second reason for the two optical fibers was the lack in experience with the solarization behavior of this type of fibers. For detailed fiber specifications see App. F.

<sup>7</sup>Solarization describes the decrease of light transmission due to UV exposure.

<sup>8</sup>Thorlabs UM22

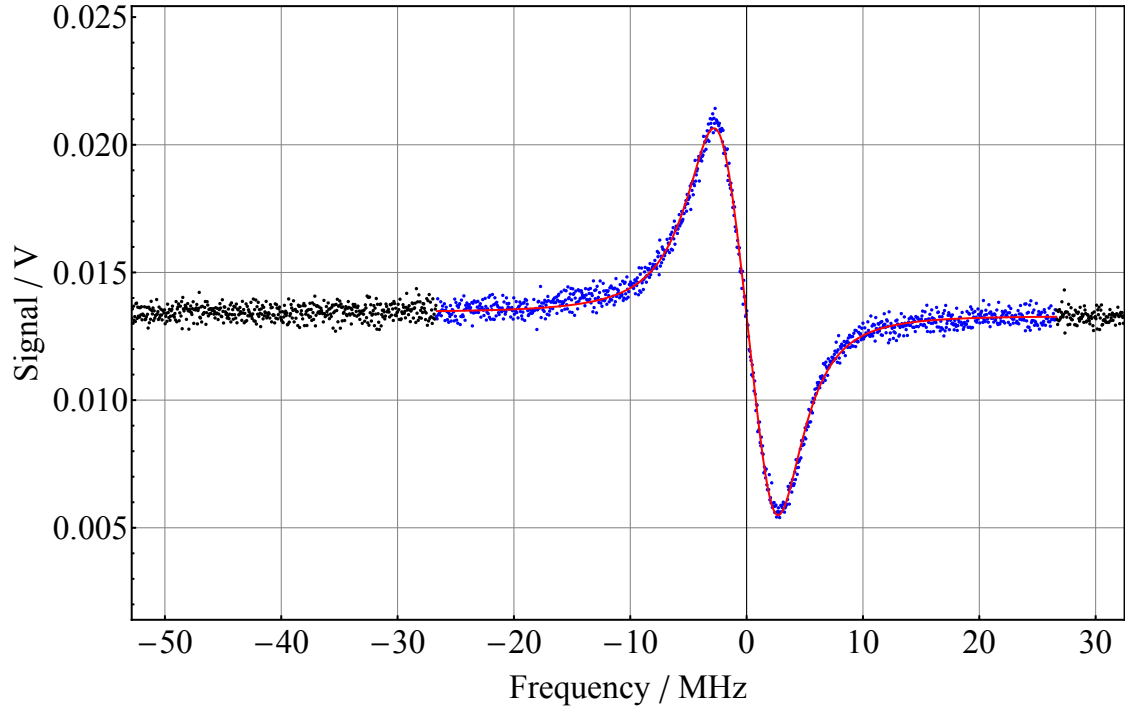


Figure 3.14: A typical SD-DAVLL signal around the  $^{199}\text{Hg } 6^1S_0 \rightarrow 6^3P_1 F = 1/2$  transition recorded in a 20 mm-long spectroscopy cell filled with  $^{199}\text{Hg}$ -enriched mercury. Black points indicate the background region in which a linear background function is fitted to the measured data. Blue points indicate the signal region where the difference of two Lorentzian lines is fitted on top of the background function. The red line represents the best fit. The frequency axis is given relative to the average of the fitted peak positions. The signal was recorded with  $P_{\text{pump}} = 120(1) \mu\text{W}$ ,  $P_{\text{probe}} = 11.3(1) \mu\text{W}$  and the current in the Helmholtz coil pair was set to  $I_{\text{coil}} = 150 \text{ mA}$ .

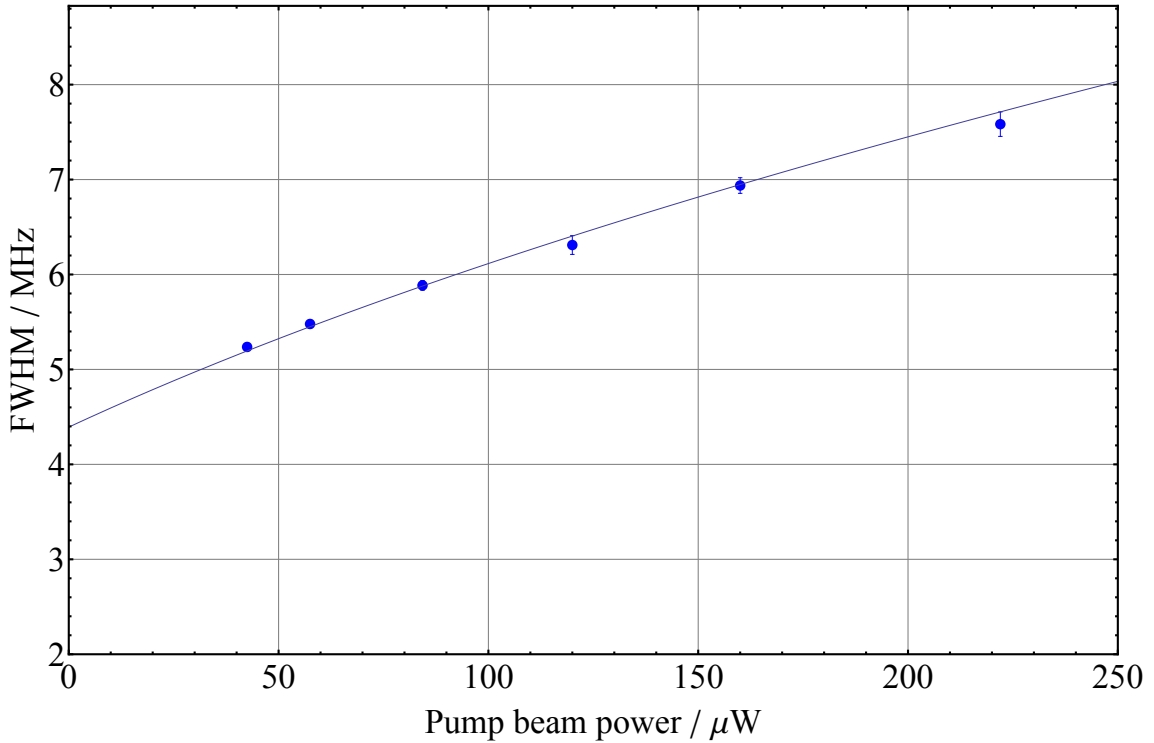


Figure 3.15: Full-width-half-maximum as a function of the pump beam power. The SD-DAVLL signal in Figure 3.14 was recorded with  $P_{\text{pump}} = 120(1) \mu\text{W}$ . Thus the additional contribution to the measured FWHM due to power broadening is  $\approx 1.9 \text{ MHz}$ .

The FHG delivers enough UV power to run the  $^{199}\text{Hg}$  co-magnetometer despite the high transmission losses of the optical fibers. The UV light is focused into the optical fiber and in the first experiments the amount of light was regulated by a feedback control system on the current of the tapered amplifier (TA)<sup>9</sup>. The end of the fiber is shown in Figure 3.19 as mounted at the nEDM experiment. The fiber end is mounted in a fiber dock with vertical and horizontal adjustments of the beam position with micrometer screws. To control the yaw and pitch angle the fiber dock is mounted on a yaw-pitch-platform with micrometer screws. In this way the beam position is optimized for small misalignment relative to the nEDM precession chamber. The position of a plano-convex lens ( $f = 25 \text{ mm}$ ), relative to the endface of the optical fiber, can be sufficiently well adjusted with a telescopic lens tube to produce a beam of low divergence in the precession chamber (optical fiber numerical

<sup>9</sup>A power stabilization scheme using an acousto-optical modulator (AOM) has been tested. The AOM has a working frequency of  $\pm 200 \text{ MHz}$ . To diffract light efficiently, the input angle has to be matched by aligning the AOM relative to the light beam. The FHG system shows some beam steering of the UV beam with frequency tuning. For the 22 GHz separation between the two hyperfine transitions in  $^{199}\text{Hg}$  the beam steering was too large to use the AOM without realignment for amplitude stabilization. Working only around one hyperfine transition an AOM was separately tested for amplitude stabilization and shown to work.

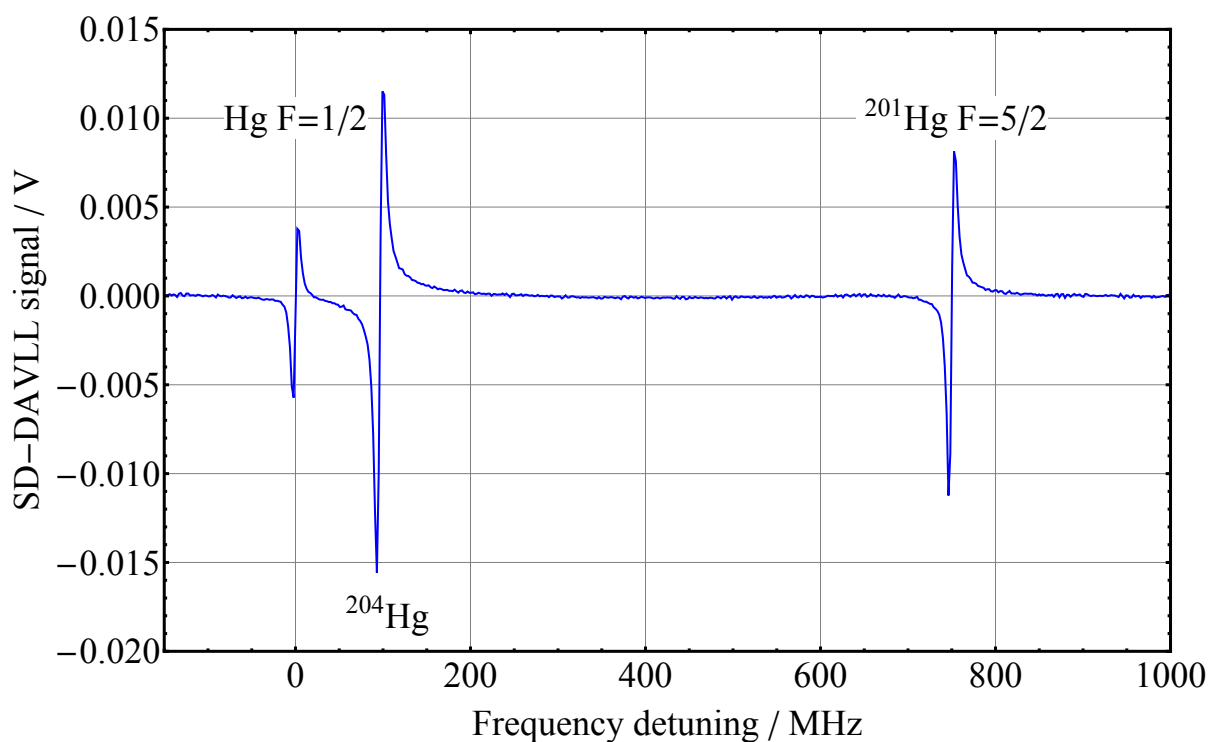


Figure 3.16: SD-DAVLL signal measured with a 2 mm thick spectroscopy cell filled with Hg of natural isotopic composition. The SD-DAVLL signal is obtained for all the lines overlapping within their Doppler-width. Here the SD-DAVLL signal is shown in the region of the  $^{199}\text{Hg}$   $F=1/2$ ,  $^{204}\text{Hg}$  and  $^{201}\text{Hg}$   $F=5/2$  line. For this plot the residual Doppler-background was subtracted. Unfortunately this cell suffers from the same darkening effect as shown in Figure E.1.

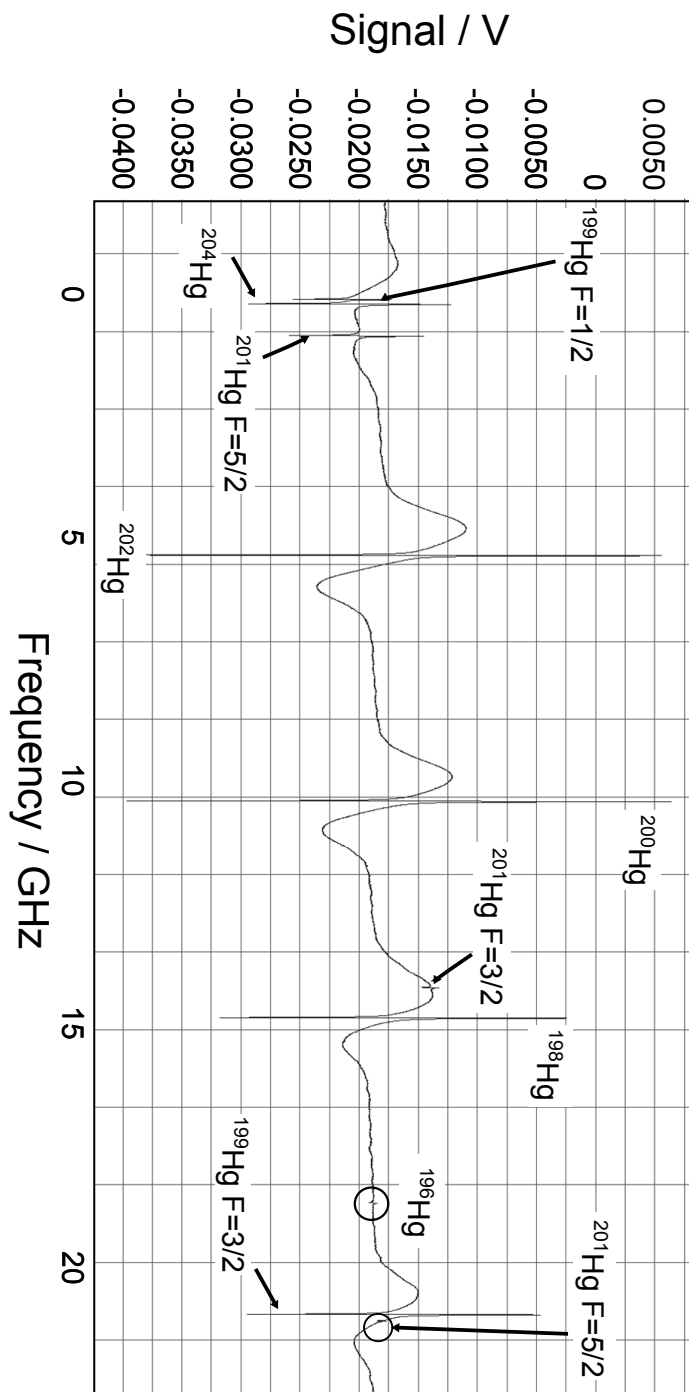


Figure 3.17: SD-DAVLL signal measured with a 2 mm thick spectroscopy cell filled with Hg of natural isotopic composition. The SD-DAVLL signal is obtained for all the transitions in the naturally abundant Hg isotopes. The  $^{196}\text{Hg}$  isotope has an abundance of 0.15%. The frequency axis is only a rough guide to the eye in this plot.

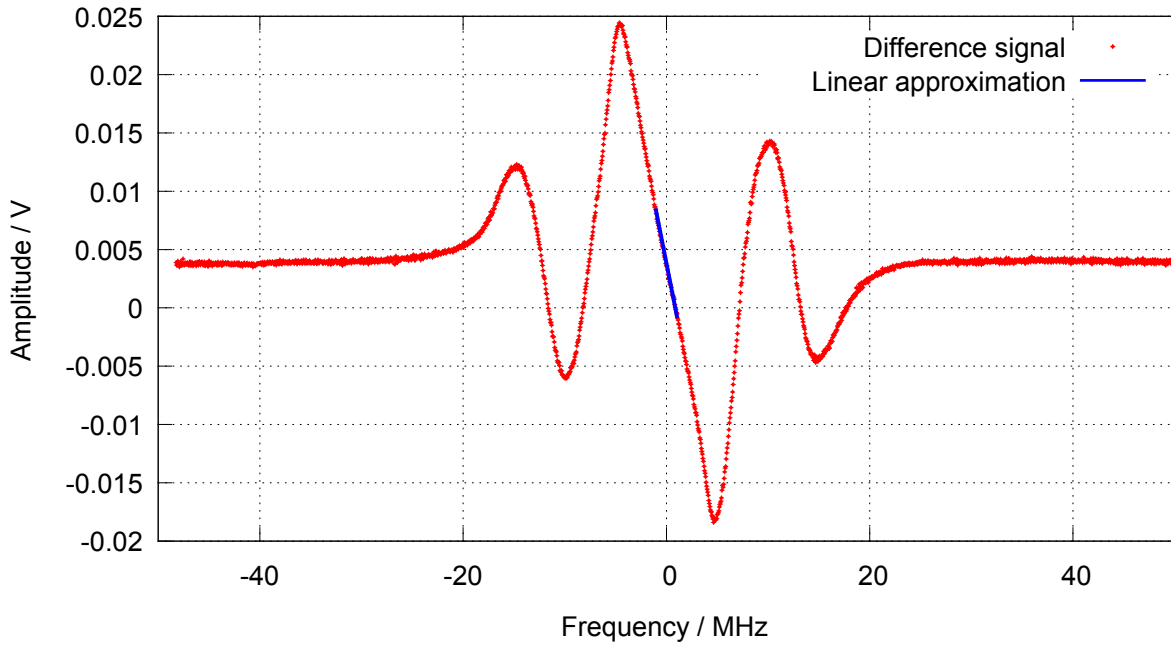


Figure 3.18: A SD-DAVLL signal recorded for the  $F = 3/2$  transition ( $\bullet$ ) in  $^{199}\text{Hg}$  with  $P_{\text{pump}} = 167(5) \mu\text{W}$ ,  $P_{\text{probe}} = 8.9(1) \mu\text{W}$ . The same 20 mm long spectroscopy cell filled with  $^{199}\text{Hg}$  enriched mercury was used as for the SD-DAVLL signal in Figure 3.14. The current in the Helmholtz coil pair (HPC) was set to  $I_{\text{coil}} = 948.5 \text{ mA}$ . A laser frequency stabilized to one of the zero crossings to the left and right side of the central lock point can be tuned by several MHz by changing the current in the HPC. The signal offset is due to a non perfect balanced detector. A linear fit to the central region of the signal is given ( $\text{---}$ ).

aperture  $NA=0.22$ ).

The UV beam is linearly polarized with a Glan-Taylor polarizer. A 50/50 non-polarizing beam splitter picks off a probe beam that is used for the intensity stabilization. A PID controller acts on the TA current to compensate for intensity variations picked up in the fiber. The non-deflected beam travels towards the vacuum tank. In the case of the absorptive measurement scheme, a  $\lambda/4$  plate is inserted into the light path. The alignment of the UV beam passing through the vacuum tank can be monitored with white paper strips that fluoresce in the UV beam as can be seen in Figure 3.20. A superposition of a picture at room light and a dark exposure is shown.

During the measurement it was found that mode interference is a major source of light amplitude noise. The light modes guided in a multimode fiber interfere on the photodetector and any relative phase shift, e.g. due to mechanical vibrations of the fiber, change the interference pattern and thus cause amplitude noise. A future setup should either use single-mode optical fibers that guide only the fundamental mode of the light field to avoid this effect or work with a direct line-of-sight access by bringing the UV laser system closer to the nEDM experiment. Recently, improvements of the solarization resistance of single-mode-optical-fibers have been reported by high-pressure hydrogen loading and subsequent exposure to UV light [Win]. But further investigations are necessary on the temporal stability of the light transmission through single mode optical fibers or on the light transport with automatically steered mirrors.



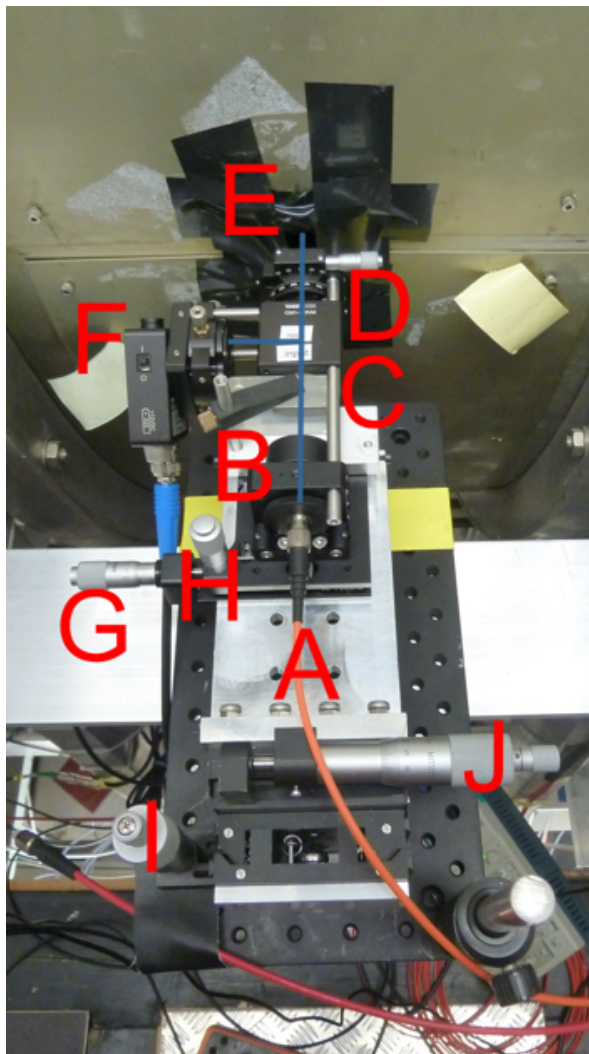


Figure 3.19: The mounting platform of the UV fiber end at the nEDM experiment. The fiber is screwed into a fiber coupler (A). The divergent light is refocused by a  $f = +25$  mm plano-convex lens (B) before passing a Glan-Taylor linear polarizer (C). A 50/50 non-polarizing beam splitter (D) picks off a monitor beam at right angle. The undeflected probe beam passes a  $\lambda/4$  plate (E) and goes to the vacuum tank. The monitor beam is refocused onto a photodiode (F). The measured light level is used to actively stabilize the light power by controlling the current of the tapered amplifier. The micrometer screws allow the adjustment of the yaw (G) and pitch (H) angles as well as the vertical (I) and horizontal (J) position of the light beam.

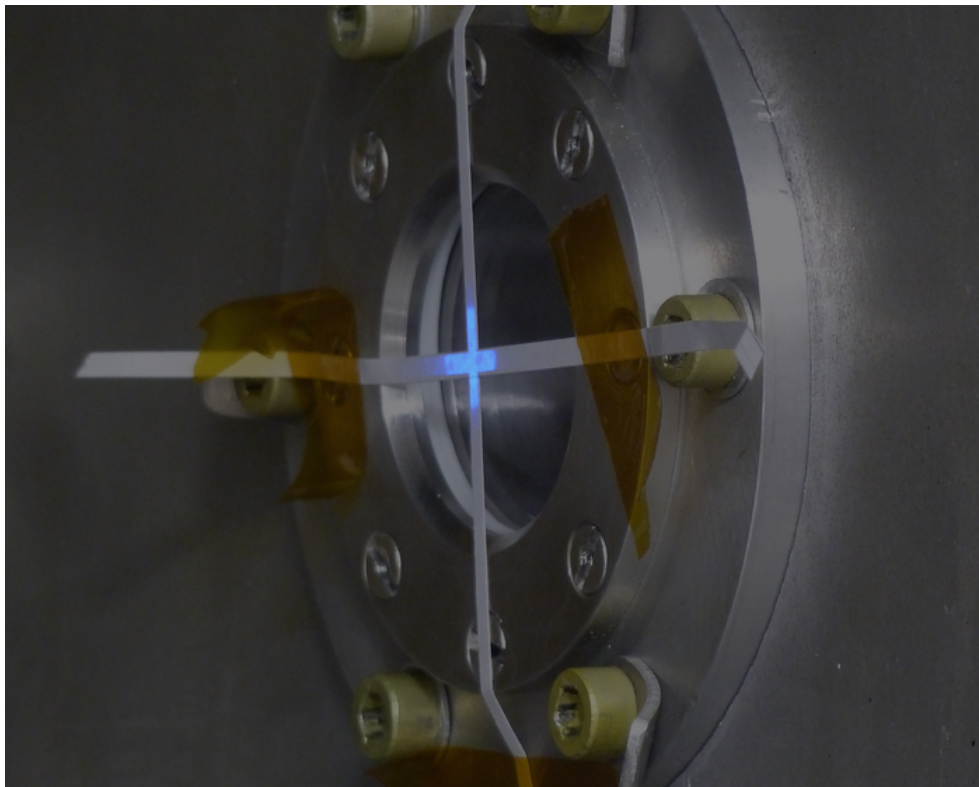


Figure 3.20: The UV beam in the nEDM vacuum tank can be aligned with the help of white paper strips. The picture is a superposition of a room light exposure and a dark exposure. The strips fluoresce under the illumination with UV light. The alignment strips are removed for the  $^{199}\text{Hg}$  co-magnetometer operation.

# Chapter 4

## The $^{199}\text{Hg}$ co-magnetometer signal

In this chapter a refined model of the  $^{199}\text{Hg}$  co-magnetometer signal is developed. This has become necessary since the model presented in Ref. [GHI<sup>+</sup>98] only holds for small signal amplitudes. With the use of laser light for the signal detection a significant increase in signal contrast was achieved compared to use of light from a  $^{204}\text{Hg}$  discharge bulb. Applying the old model to the data would lead to false conclusions. In a first step the fundamental interaction of a vapor of (spin polarized) mercury atoms with a weak light beam is summarized to explain the orientation dependent absorption and paramagnetic rotation. In a second step the results are used to describe the process of optical pumping that is used to produce spin-polarized  $^{199}\text{Hg}$  atoms in the nEDM setup. In the last section the new and extended model for the signal generation in the  $^{199}\text{Hg}$  co-magnetometer is presented. This extended model allows to derive an analytical expression for the atomic polarization of the  $^{199}\text{Hg}$  ensemble, in contrast to an exact model that is derived in Appendix D.

A sketch of a generic setup of a  $^{199}\text{Hg}$  co-magnetometer based on the absorption measurement or on the paramagnetic rotation measurement is shown in Figure 4.1.

### 4.1 The interaction of $^{199}\text{Hg}$ atoms with a weak light beam

In 1950 A. Kastler created a non-thermal equilibrium occupation of angular momentum (magnetic) sub-levels in sodium atoms in an external magnetic field by the use of circularly polarized resonance light [Kas50]. The detection scheme was based on the spatial intensity distribution of the detected fluorescence light after excitation. This technique solely relies on optical means to produce and probe the atomic polarization. It can be compared to the state preparation used by O. Stern and W. Gerlach [GS22]. They used an external magnetic field gradient to separate silver atoms in the two magnetic sub-levels of the electronic ground state to demonstrate the spatial quantization of the spin axis. Kastler called his technique "optical pumping".

The first one to point out the harmonic amplitude modulation of a circularly polarized light beam propagating through an ensemble of precessing polarized sodium atoms was

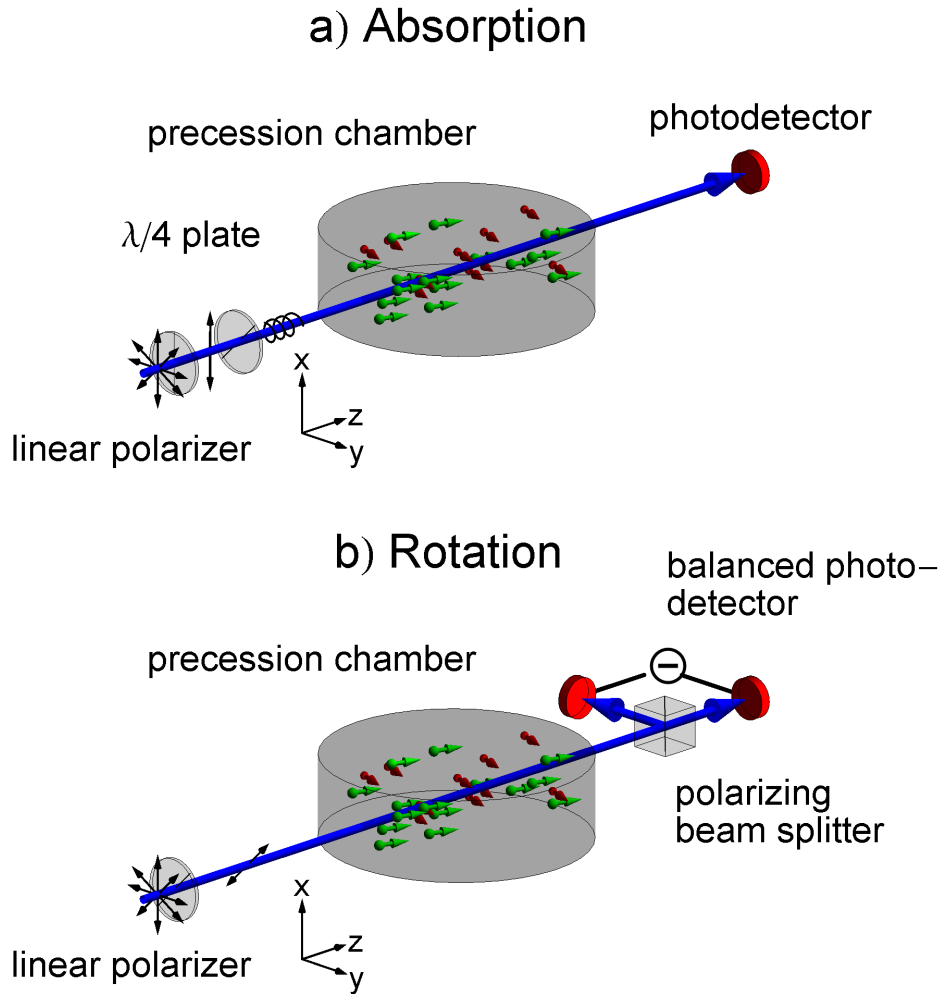


Figure 4.1: Comparison of the optical setups used to detect the Larmor precession of the  $^{199}\text{Hg}$  atoms (green) by the orientation dependent absorption of light (a) or the paramagnetic rotation effect (b). The  $^{199}\text{Hg}$  atoms are in the same volume as the ultra-cold neutrons (red). For method (a) the probe light is circularly polarized before entering the precession chamber, by passing it through a linear polarizer and a  $\lambda/4$  plate. The precessing  $^{199}\text{Hg}$  atoms act as a time dependent analyzer for the light's circular polarization. The intensity modulation is recorded on a photodetector. For method (b) the light enters the precession chamber with linear polarization at an angle of  $\pm 45^\circ$  relative to the analyzer plane. The precessing atoms imprint a polarization modulation on the transmitted light beam that is converted into an intensity modulation by a second linear polarizer in front of a balanced photodetector. The balanced detector configuration suppresses common mode noise, e.g., intensity fluctuations. The coordinate system is chosen such that the light beam travels along the z-axis. This is different from the general nEDM coordinate system.

H. Dehmelt in 1957 [Deh57]. A detailed density matrix formalism for the effect of polarized light on an ensemble of atoms was first worked out by J. Barrat and C. Cohen-Tannoudji in conjunction with their experiments on the optical pumping of the odd mercury isotopes  $^{199}\text{Hg}$  and  $^{201}\text{Hg}$ . This work demonstrated for the first time the orientation dependent light absorption for a diamagnetic atom as well as the shift of the atomic energy levels by the interaction with the light itself (light shift) [BCT61, Kas63]. A semi-classical operator formalism was worked out by W. Happer and B. Marthur in 1967, also taking into account the effect of the polarized atoms on the interacting light [HM67]. This approach is used to compare the absorptive measurement scheme and the detection of paramagnetic rotation to generate a magnetometry signal in the  $^{199}\text{Hg}$  co-magnetometer in the nEDM experiment. In the following all formulas are given in SI units while [HM67] uses the cgs system.

Here the interaction of  $^{199}\text{Hg}$  atoms, the most relevant case for the mercury co-magnetometer in the nEDM experiment, with light beams of different polarization states is discussed. Results for  $^{201}\text{Hg}$  are obtained in a similar way for the appropriate choice of the angular momenta. The results obtained for  $^{199}\text{Hg}$  can be applied to the even isotopes of mercury by considering only the contributions that are independent of nuclear spin. For the calculations it is assumed that an ensemble of  $^{199}\text{Hg}$  atoms with mass  $M$  in thermal equilibrium at temperature  $T$  is illuminated with light of frequency  $\nu$  (vacuum wavelength  $\lambda$ ). The resonance frequencies of the two hyperfine components of the  $^{199}\text{Hg}$   $6^1S_0 \rightarrow 6^3P_1$   $F = 1/2$  and  $F = 3/2$  transitions (see Figure 3.1) are denoted by  $\nu_{0,F}$ , where  $F = 1/2$  or  $3/2$ . The natural line width is given by  $\Gamma_0$  and the oscillator strength of the transition is denoted by  $f_{ge}$ . The nuclear spin (as well as the total angular momentum of the  $6^1S_0$  electronic ground state  $g$ ) is denoted by  $I$ , the total angular momentum of the excited electronic state  $e$  is denoted by  $F_e$ . The light intensity  $I_0 \ll I_{\text{sat}}$  where  $I_{\text{sat}}$  is given by (3.20). Within this semiclassical approach the interacting light is treated as a quasi-monochromatic wave with amplitude  $\frac{E_0}{2}$ <sup>1</sup>, wave vector  $\mathbf{k}$ , complex polarization unit vector  $\mathbf{e}$  and frequency  $\nu$ :

$$\mathbf{E}(\mathbf{r}, t) = \frac{E_0}{2} \mathbf{e} e^{i(\mathbf{k}\cdot\mathbf{r} - 2\pi\nu t)} + c.c. \quad (4.1)$$

The position vector is given by  $\mathbf{r}$ , the time variable by  $t$  and *c.c.* denotes the complex conjugate. The quantization of the light field is not taken into account but the atoms are treated as quantum mechanical objects. The light beam travels along the  $z$  direction ( $\mathbf{k} = k\mathbf{e}_z$ ), the vertical (horizontal) coordinate is denoted by  $x(y)$ . In this way  $(\hat{\mathbf{x}}, \hat{\mathbf{y}}, \hat{\mathbf{z}})$  form a right-handed coordinate system (see Figure 4.1). The complex polarization unit vectors  $\mathbf{e}$  are given by

$$\hat{e}_+ = \frac{1}{\sqrt{2}} \begin{pmatrix} 1 \\ i \\ 0 \end{pmatrix}, \quad \hat{e}_- = \frac{1}{\sqrt{2}} \begin{pmatrix} 1 \\ -i \\ 0 \end{pmatrix}, \quad \hat{e}_x = \begin{pmatrix} 1 \\ 0 \\ 0 \end{pmatrix} = \frac{1}{\sqrt{2}} (\hat{e}_+ + \hat{e}_-), \quad (4.2)$$

---

<sup>1</sup>Here the intensity of the plane wave is  $I_0 = \frac{|E_0|^2 c}{16\pi}$  in cgs units. In [Swa07] the amplitude is normalized such that  $I_0 = \frac{|E_0|^2 c}{8\pi}$  in cgs units. This difference of a factor of two has to be taken into account when comparing the two calculations.

for left and right circular polarized light and for vertical (x-direction) linearly polarized light. It can be seen that the linearly polarized light can be represented as the superposition of a left and right circularly polarized component. For the electric field of the light wave it is  $\mathbf{E}_X = E_0 \hat{e}_x$ .

The time evolution of the atom under the influence of the light field is governed by Schrödinger's equation

$$i\hbar(\partial\Psi/\partial t) = (H_0 + \delta H) \Psi \quad (4.3)$$

where  $\delta H$  is a small perturbation to the Hamiltonian  $H_0$  of the atoms in perfect vacuum. According to [HM67], the Hamiltonian of the interacting system can be given as

$$H = H_0 + \delta H = H_0 - i(\hbar/2) \delta\Gamma + \delta E \quad (4.4)$$

where  $\delta\Gamma$  is the light absorption rate and  $\delta E$  represents the shift of the atomic energy levels due to the interaction between the atoms and the light. These effects will be discussed in detail in the following subsections.

### 4.1.1 Light absorption

In the case of  $^{199}\text{Hg}$  atoms ( $6^1S_0$  ground state, no ground state electronic spin,  $I = \frac{1}{2}$ ) the light absorption rate can be separated into a scalar (nuclear spin independent) part  $\delta\Gamma_0$  and a vector (nuclear spin dependent) part  $\boldsymbol{\mu} \cdot \delta\boldsymbol{\Gamma}_1$

$$\delta\Gamma = \delta\Gamma_0 + \boldsymbol{\mu} \cdot \delta\boldsymbol{\Gamma}_1, \quad (4.5)$$

where  $\boldsymbol{\mu} = \gamma\mathbf{I}$  is the nuclear magnetic dipole moment and  $\gamma$  the gyromagnetic ratio. Because  $^{199}\text{Hg}$  has nuclear spin  $I = 1/2$  no higher order rank tensor interactions exist for the ground state (Wigner-Eckart-theorem).

The scalar part describes the absorption of unpolarized light while the vector part causes an orientation dependent absorption cross-section of the atom for circularly polarized light. This orientation dependence lies at the heart of the optical pumping of  $^{199}\text{Hg}$  atoms in the polarization cell and of the detection of the Larmor precession of the  $^{199}\text{Hg}$  atoms in the precession chamber via light absorption. For the transition between the ground state and the two hyperfine components of the first excited state (see Figure 3.1) the scalar absorption rate  $\delta\Gamma_0$  is given by [HM67]

$$\delta\Gamma_0 = \frac{1}{6\hbar} I_0 G \text{Im}Z \cdot \frac{2F_e + 1}{2I + 1} = \frac{1}{6\hbar} I_0 G \text{Im}Z \cdot \begin{cases} 1 & F_e = \frac{1}{2}, I = \frac{1}{2} \\ 2 & F_e = \frac{3}{2}, I = \frac{1}{2} \end{cases} \quad (4.6)$$

The vector absorption rate  $\delta\boldsymbol{\Gamma}_1$  can be expressed as [HM67]

$$\delta\boldsymbol{\Gamma}_1 = \frac{1}{8\hbar} I_0 \frac{1}{I\gamma} G \text{Im}Z \cdot \left[ \frac{\mathbf{e} \times \mathbf{e}^*}{i} \right] \cdot \frac{2F_e + 1}{(I + 1)(2I + 1)} \cdot [2 + I(I + 1) - F_e(F_e + 1)] \quad (4.7)$$

$$= \frac{1}{6\hbar} I_0 \frac{1}{I\gamma} G \text{Im}Z \cdot \left[ \frac{\mathbf{e} \times \mathbf{e}^*}{i} \right] \cdot \begin{cases} 1 & F_e = \frac{1}{2}, I = \frac{1}{2} \\ -1 & F_e = \frac{3}{2}, I = \frac{1}{2} \end{cases} \quad (4.8)$$

where  $\mathbf{e}$  and  $\mathbf{e}^*$  are the complex polarization vectors given in (4.2). The constant  $G$  is given by [HM67]

$$G = \frac{\lambda^2 e^2 f_{ge}}{2\pi^2 m_e c^2 \epsilon_0} \sqrt{\frac{M}{2RT}} \quad (4.9)$$

and takes the transition-specific, but angular momentum independent parameters into account. The complex Voigt-profile  $Z$ , a convolution of the natural Lorentzian line shape of the atomic transition and a Gaussian function takes the Doppler broadening into account:

$$Z = Z(M, T, \nu) = \frac{1}{\sqrt{\pi}} \int_{-\infty}^{\infty} \frac{e^{-u^2}}{u - \frac{c}{\nu} \sqrt{\frac{M}{2RT}} \left[ \nu - (\nu_0 + \nu_c) + i \left( \frac{\Gamma}{2} + \gamma_c \right) \right]} du \quad (4.10)$$

where  $\nu_c$  and  $\gamma_c$  take collisional line shifts and line broadening into account. The  $^{199}\text{Hg}$  co-magnetometer in the nEDM experiment works at very low mercury density in the precession chamber ( $n_{\text{Hg}} \approx 5 \times 10^{10} \text{ cm}^{-3}$  to  $1 \times 10^{13} \text{ cm}^{-3}$ ) and a low background helium pressure to stabilize the electric field (max.  $p_{\text{He}} = 1 \times 10^{-2}$  mbar). High precision values for the collisional line shift and line broadening at pressures below 1 bar are only available for  $N_2$  [JW03]. Taking the values from Ref. [JW03] for line shifts  $\Delta\nu_c = -2.54 \text{ MHz/Torr}$  and pressure broadening  $\Delta\Gamma_c = 9.01 \text{ MHz/Torr}$  one can estimate an order of magnitude for  $\nu_c \approx -20 \text{ kHz}$  and  $\Gamma_c \approx 72 \text{ kHz}$  for  $1 \times 10^{-2}$  mbar. Following this argument one can assume  $\nu_c \approx 0$  and  $\Gamma_c \approx 0$ . In the HgEDM experiment these corrections have to be taken into account as in that case mercury atoms in a buffer gas atmosphere of several hundreds of Torr are used [GSL<sup>+</sup>09].

From (4.8) one sees that the vector absorption rate is only present for light with a degree of circular polarization  $P_L$  if one takes into account that

$$\left[ \frac{\mathbf{e} \times \mathbf{e}^*}{i} \right] = \begin{pmatrix} 0 \\ 0 \\ -P_L \end{pmatrix} \text{ with } \begin{cases} P_L = +1 & \text{for 100 \% } \sigma^+ \text{ polarization} \\ P_L = 0 & \text{for 100 \% linear or no polarization} \\ P_L = -1 & \text{for 100 \% } \sigma^- \text{ polarization} \end{cases} \quad (4.11)$$

The absorption cross-section per atom is plotted for a monochromatic light source (like the new UV laser) in Figure 4.2 as a function of light frequency for (anti-)parallel alignment of light and atomic polarization vector. Perfect conditions of 100 % polarized  $^{199}\text{Hg}$  atoms and 100 % circularly polarized light are assumed. For the  $F = 1/2$  transition the absorption cross-section modulates between 0 % and 100 % of the maximum absorption cross-section. Atoms in the  $6^1S_0$ ,  $F = 1/2$ ,  $m_F = +\frac{1}{2}$  state are in a dark state for  $\sigma^+$  light due to angular momentum conservation. Only atoms in the  $6^1S_0$ ,  $F = 1/2$ ,  $m_F = -\frac{1}{2}$  state can absorb a  $\sigma^+$  photon and be excited to the  $6^3P_1$ ,  $F = 1/2$ ,  $m_F = +\frac{1}{2}$  state. For the  $F = 3/2$  transition the absorption cross-section for  $\sigma^+$  light modulates between 33 % and 100 % of the maximum absorption cross-section since the  $6^1S_0$ ,  $F = 1/2$ ,  $m_F = +\frac{1}{2}$  ground state is not a dark state of the  $F = 3/2$  transition. Atoms in this state can be excited by  $\sigma^+$  light to the  $6^3P_1$ ,  $F = 3/2$ ,  $m_F = +\frac{3}{2}$  level.

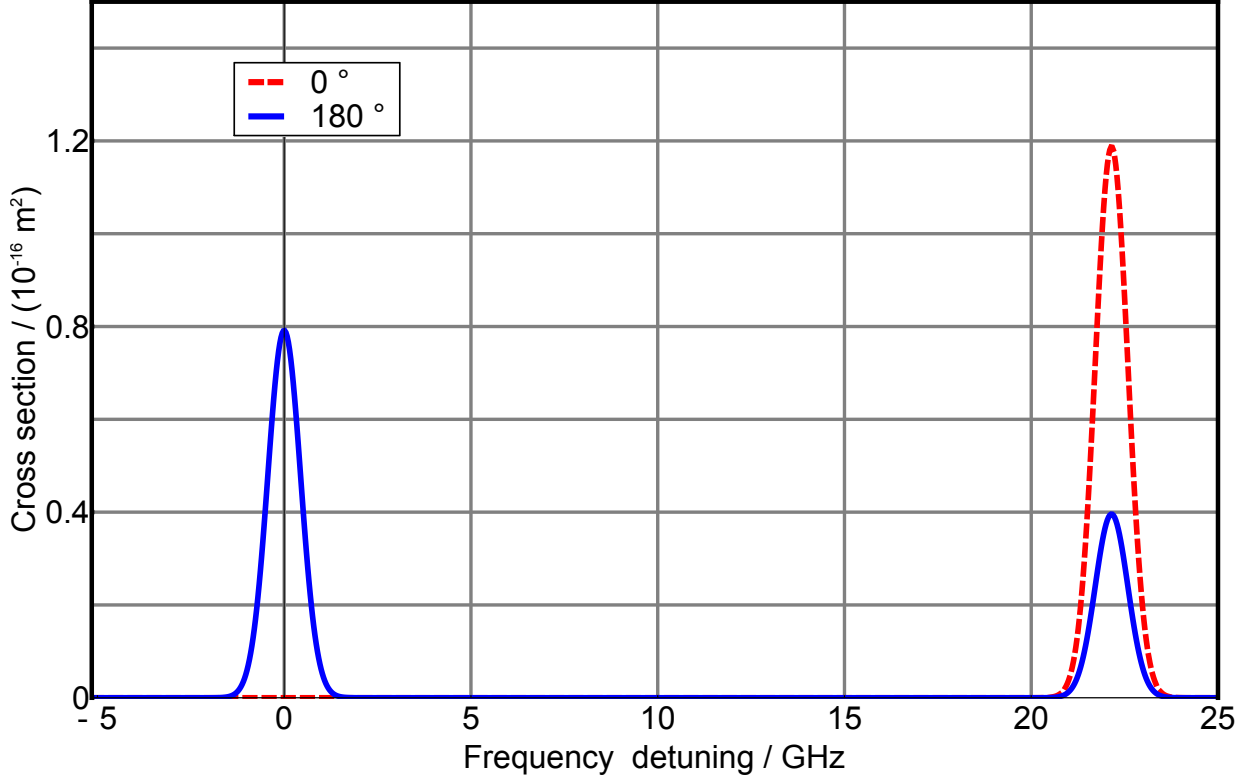


Figure 4.2: The absorption cross-section per atom for  $^{199}\text{Hg}$ . The frequency is given as a detuning from the  $^{199}\text{Hg}$   $F = 1/2$  line center. For a parallel alignment of the light polarization and atom polarization vector the cross-section is given by the red dashed line (---). A comparison with Figure 3.1 shows that the  $m_F = +1/2$  is a dark state of the  $F = 1/2$  transition but couples with relative factor of 1 to the  $m_F = +3/2$  sublevel of the  $F = 3/2$  transition. The blue solid line (—) represents the anti-parallel alignment. In this case the  $6^1S_0$ ,  $F = 1/2$ ,  $m_{-1/2}$  state couples to the  $6^3P_1$ ,  $F = 1/2$ ,  $m_{+1/2}$  state with maximum strength. But the coupling to the  $F = 3/2$ ,  $m_F = +1/2$  state is reduced to  $\frac{1}{3}$  of its maximum value.

The absorption cross-section for the  $F = 1/2$  and the  $F = 3/2$  lines modulate with a phase shift of  $180^\circ$ . This agrees with the rule that the sum over all hyperfine components of the cross-section has to be the same as for an even isotope, that does not show any modulation. The relative modulation depth is larger on the  $F = 1/2$  transition for the same amount of overall light absorption. Each absorption process contributes to the transverse spin relaxation of the  $^{199}\text{Hg}$  vapor. Therefore the  $F = 1/2$  transition is preferred over the  $F = 3/2$  transition since there is less depolarization by light at the same signal contrast.

To derive (4.6) and (4.8) a monochromatic light source was assumed. For the light of a  $^{204}\text{Hg}$  discharge bulb this assumption is not fulfilled as discussed in Section 3.3. To obtain the effective absorption cross-section  $\sigma_{\text{lamp}}$  between the light of a  $^{204}\text{Hg}$  discharge bulb and the ensemble of  $^{199}\text{Hg}$  atoms the absorption cross-section  $\sigma_{\text{laser}}$  shown in Figure 4.2 has to



be convoluted with the normalized spectral density of the  $^{204}\text{Hg}$  bulb  $\Phi_{\text{lamp}}(\nu)$ :

$$\sigma_{\text{lamp}} = \int \sigma_{\text{laser}}(\nu - \nu_0) \Phi_{\text{lamp}}(\nu) d\nu \quad (4.12)$$

For an ideal lamp (no self-absorption, no other isotopes, no isotope shift, same temperature as the  $^{199}\text{Hg}$  vapor) with Doppler-broadened line shape and the approximation of (4.10) by a Doppler-profile, the absorption cross-section (4.12) is given as the convolution of two Doppler-profiles:

$$\sigma_{\text{ideal lamp}} = \sigma_{\text{laser, peak}} \int_{-\infty}^{\infty} \frac{1}{\sqrt{2\pi}\Delta_D} e^{-\frac{(\nu-\nu_0)^2}{2\Delta_D^2}} d\nu = \frac{\sigma_{\text{laser, peak}}}{\sqrt{2}}. \quad (4.13)$$

Self-absorption, isotope-shift and light emitted by different isotopes will further reduce this effective cross-section for the  $^{204}\text{Hg}$  bulbs.

### 4.1.2 AC Light shifts

Near resonant light can shift the energy levels of the illuminated atoms. This effect is known as AC light shift. The energy shift term has a scalar part,  $\delta E_0$ , common to all magnetic sub-levels of a specific electronic configuration of the atom and independent of the light polarization. A second part,  $-\boldsymbol{\mu} \cdot \mathbf{B}_{\text{VLS}}$ , represents an energy shift proportional to the magnetic moment of the magnetic sub-levels in an effective magnetic field  $\mathbf{B}_{\text{VLS}}$  created by the light field (VLS - vector light shift)

$$\delta E = \delta E_0 - \boldsymbol{\mu} \cdot \mathbf{B}_{\text{VLS}}. \quad (4.14)$$

The scalar light shift can be expressed as [HM67]

$$\delta E_0 = -\frac{1}{12} I_0 G \text{Re}Z \cdot \frac{2F_e + 1}{2I + 1} = -\frac{1}{12} I_0 G \text{Re}Z \cdot \begin{cases} 1 & F_e = \frac{1}{2}, I = \frac{1}{2} \\ 2 & F_e = \frac{3}{2}, I = \frac{1}{2} \end{cases}. \quad (4.15)$$

where  $G$  and  $Z$  are given by (4.9) and (4.10). All levels are always lowered in their energy by the scalar light shift effect. For the vector light shift one finds [HM67]

$$\mathbf{B}_{\text{VLS}} = \frac{1}{16} I_0 \frac{1}{I\gamma} G \text{Re}Z \cdot \left[ \frac{\mathbf{e} \times \mathbf{e}^*}{i} \right] \cdot \frac{2F_e + 1}{(I + 1)(2I + 1)} \cdot [2 + I(I + 1) - F_e(F_e + 1)] \quad (4.16)$$

$$= \frac{1}{12} I_0 \frac{1}{I\gamma} G \text{Re}Z \cdot \left[ \frac{\mathbf{e} \times \mathbf{e}^*}{i} \right] \cdot \begin{cases} 1 & F_e = \frac{1}{2}, I = \frac{1}{2} \\ -1 & F_e = \frac{3}{2}, I = \frac{1}{2} \end{cases} \quad (4.17)$$

From (4.17) and (4.11) it follows that the VLS effect is only present for  $\sigma$  polarized light components and that the direction of the VLS field  $\mathbf{B}_{\text{VLS}}$  is parallel or anti-parallel to the direction of light propagation  $\mathbf{k}$ . The magnitude of the VLS field is proportional to the degree of circular polarization  $P_L$ , the light intensity  $I_0$  and is an antisymmetric (dispersive)

function  $f(\nu - \nu_0)$  of the light frequency  $\nu$  detuning from the atomic resonance  $\nu_0$ . The function  $f(\nu - \nu_0)$  absorbs all components of (4.17) not explicitly given

$$\mathbf{B}_{\text{VLS}} = |I_0| \mathbf{k} P_L f(\nu - \nu_0). \quad (4.18)$$

The induced change of the Larmor frequency can be calculated by assuming that the magnetic moments of the  $^{199}\text{Hg}$  atoms precess around the superposition  $\mathbf{B}$  of the main magnetic field  $\mathbf{B}_0$  and the VLS field  $\mathbf{B}_{\text{VLS}}$  (a pseudo-magnetic field)

$$\mathbf{B} = \mathbf{B}_0 + \mathbf{B}_{\text{VLS}}. \quad (4.19)$$

The Larmor precession frequency in this effective magnetic field is given by

$$\omega_{\text{Hg}} = \gamma_{\text{Hg}} \sqrt{(\mathbf{B}_0 + \mathbf{B}_{\text{VLS}})^2} = \gamma_{\text{Hg}} B_0 \sqrt{1 + 2 \cos \alpha \frac{B_{\text{VLS}}}{B_0} + \left(\frac{B_{\text{VLS}}}{B_0}\right)^2} = \quad (4.20)$$

$$= \gamma_{\text{Hg}} B_0 \left(1 + \cos \alpha \frac{B_{\text{VLS}}}{B_0} + \frac{1}{2} \sin^2 \alpha \left(\frac{B_{\text{VLS}}}{B_0}\right)^2 + \dots\right), \quad (4.21)$$

where  $\alpha$  is the angle between the main magnetic field  $\mathbf{B}_0$  and the VLS field  $\mathbf{B}_{\text{VLS}}$ . For  $\alpha = \frac{\pi}{2}$  the first order dependence on  $B_{\text{VLS}}$  vanishes and only the second order term remains. Any angle  $\alpha \neq \frac{\pi}{2}$  will produce a projection of the VLS field onto the main magnetic field. While the quadratic contribution is negligible even for the frequency accuracy demanded for n2EDM the linear contribution can be of concern for the nEDM measurement if the angular alignment is not well under control or if there is a large frequency detuning of the probe light from resonance as in the case of the  $^{204}\text{Hg}$  discharge bulbs.

Here the VLS effect for typical measurement conditions in the nEDM experiment at PSI is estimated. A light power of  $P = 5 \mu\text{W}$  and a misalignment of the light beam relative to the main magnetic field  $\mathbf{B}_0$  of  $\alpha = 1 \text{ mrad}$  is assumed. To estimate an upper limit, valid for all concentrations of mercury atoms in the precession chamber, the decrease of the light intensity along the light path or its modulation by the precessing atoms is not taken into account. Furthermore the change of the beam volume in the chamber due to the misalignment or due to beam divergence is neglected. These effects reduce the volume-averaged VLS field as the beam diameter increases and thus the local light intensity decreases. Compared to a beam propagation strictly perpendicular to the cylinder axis the volume effect is on the order of  $\cos \alpha^3 \approx 0.9999985$ . The VLS field has to be averaged over the volume of the precession chamber. The diameter of the probe beam is irrelevant but can be replaced by an effective beam cross-section that is only given by the precession chamber geometry ( $D_{\text{chamber}} = 470 \text{ mm}$ ,  $H_{\text{chamber}} = 120 \text{ mm}$ ). For a non-divergent beam with power  $P_{\text{beam}}$  (the intensity for a divergent beam becomes lower along the light path)

the effective chamber cross-section follows from

$$\langle B_{\text{VLS}} \rangle_{V_{\text{chamber}}} = \frac{1}{V_{\text{chamber}}} \int_{V_{\text{beam}}} B_{\text{VLS}} dV_{\text{beam}} = \quad (4.22)$$

$$= \frac{B_{\text{VLS}}}{I_{\text{beam}}} \frac{1}{V_{\text{chamber}}} \int_{V_{\text{beam}}} \frac{P_{\text{beam}}}{A_{\text{beam}}} dV_{\text{beam}} = \quad (4.23)$$

$$= \frac{B_{\text{VLS}}}{I_{\text{beam}}} \frac{P_{\text{beam}} D_{\text{chamber}}}{V_{\text{chamber}}} = B_{\text{VLS}} \frac{4A_{\text{beam}}}{D_{\text{chamber}} \pi H_{\text{chamber}}} \quad (4.24)$$

For the nEDM geometry it is

$$A_{\text{chamber}}^{\text{eff}} = \frac{D_{\text{chamber}} H_{\text{chamber}} \pi}{4} = 443 \text{ cm}^2, \quad (4.25)$$

independent of the actual light beam diameter. The VLS effect is proportional to the photon flux through the effective chamber cross-section. One can achieve the same result for the volume-average VLS field if a duty cycle is attributed to the VLS field which correspond to the volume ratio of light beam and precession chamber. The volume-averaged VLS field normalized to the main magnetic field  $B_0$  is given in Fig. 4.3 for a detuning range of  $\pm 2$  GHz. In Fig. 4.4 it is given for the frequency range covering the  $^{199}\text{Hg}$  and  $^{204}\text{Hg}$  lines of interest. For the running conditions given above the residual VLS for a laser beam on resonance with the  $^{199}\text{Hg}$   $F = 1/2$  transition is 6 ppb or 6 fT on the 1  $\mu\text{T}$  field. This VLS is still acceptable for n2EDM but can easily be decreased by reducing the amount of light.

### 4.1.3 Paramagnetic rotation

The effect of a dielectric medium on a plane electromagnetic wave propagating through it can be described by the complex index of refraction  $n$

$$n = n_r - i\kappa = \sqrt{\epsilon} = \sqrt{1 + \chi} \approx 1 + \frac{\chi}{2} \quad (4.26)$$

where  $\epsilon$  is the complex relative permittivity and  $\chi$  is the susceptibility tensor operator. A plane wave (frequency  $\nu$ , vacuum wave vector  $\mathbf{k} \parallel \mathbf{z}$ ) traveling along the z-direction is described by

$$\mathbf{E}_{\text{in}}(z, t) = \mathbf{E}_0 e^{i(2\pi\nu t - nkz)}. \quad (4.27)$$

The plane wave exiting from the medium of length  $l$  is given by

$$\mathbf{E}_{\text{out}} = e^{-i2\pi\nu l/c} \mathbf{E}_{\text{in}}(0, t) = e^{-i2\pi\nu(1 + \frac{\chi}{2})l/c} \mathbf{E}_{\text{in}}(0, t). \quad (4.28)$$

The real part of  $n$ ,  $n_r$ , describes the phase dispersion and the imaginary part,  $\kappa$ , describes the absorption of the wave in the medium as discussed in Subsection 4.1.1. The susceptibility tensor operator can be split in a scalar, spin independent and a vector, spin dependent part <sup>2</sup>

$$\chi = \chi_0 + \boldsymbol{\chi}_1. \quad (4.29)$$

---

<sup>2</sup>Here a operator notation applies:  $\chi \mathbf{E} = \chi_0 \mathbf{E} + \boldsymbol{\chi}_1 \mathbf{E}$ . For example  $\boldsymbol{\chi}_1 \mathbf{E} = \text{const}(\boldsymbol{\mu} \times \mathbf{E})$ .

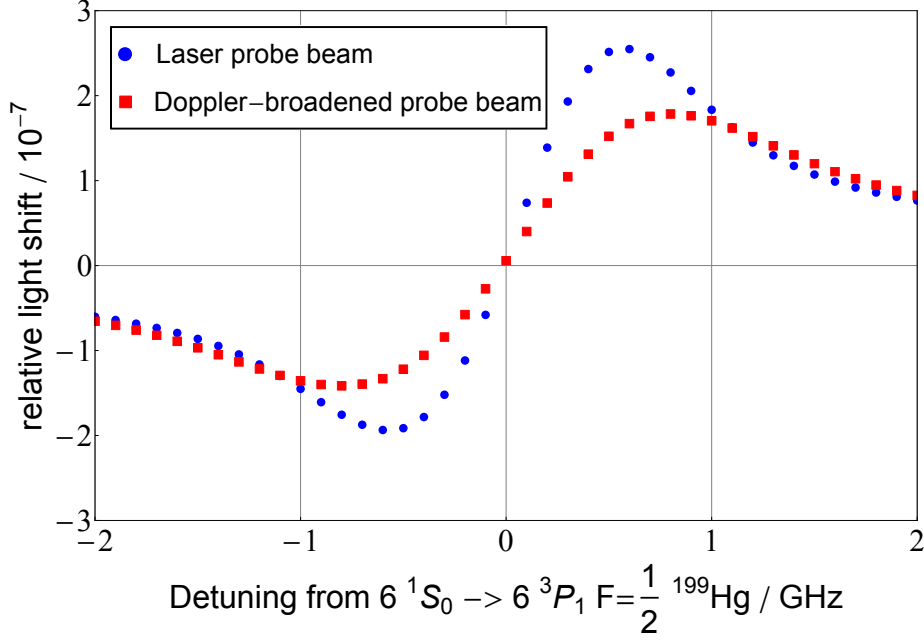


Figure 4.3: The volume-averaged vector light shift field normalized to the main magnetic field  $B_0$  for typical measurement conditions in the nEDM setup at PSI. A light power of  $5 \mu\text{W}$  and a misalignment of the light beam relative to the main magnetic field  $\mathbf{B}_0$  of 1 mrad is assumed. The UCN storage chamber has an effective cross-section of  $A_{\text{chamber}}^{\text{eff}} = 443 \text{ cm}^2$ .

In the case of  $^{199}\text{Hg}$  atoms the scalar part is given by [HM67]

$$\chi_0 = \frac{NGZ(2F_e + 1)}{3(2I + 1)} = \frac{NGZ}{3} \begin{cases} 1 & F_e = \frac{1}{2}, I = \frac{1}{2} \\ 2 & F_e = \frac{3}{2}, I = \frac{1}{2} \end{cases} \quad (4.30)$$

where  $N$  is the atomic number density and  $G$  and  $Z$  are given by (4.9) and (4.10). The spin dependent part of the susceptibility tensor operator is given by [HM67]

$$\chi_1 = -\frac{iNGZ(2F_e + 1)}{4\gamma I(I + 1)(2I + 1)} [2 + I(I + 1) - F_e(F_e + 1)] \boldsymbol{\mu} \times \quad (4.31)$$

$$= -\frac{iNGZ(2F_e + 1)}{4(I + 1)(2I + 1)} [2 + I(I + 1) - F_e(F_e + 1)] \frac{\mathbf{I}}{I} \times \quad (4.32)$$

$$= -\frac{iNGZ}{3} \begin{cases} 1 & \text{for } F_e = \frac{1}{2}, I = \frac{1}{2} \\ -1 & \text{for } F_e = \frac{3}{2}, I = \frac{1}{2} \end{cases} \frac{\mathbf{I}}{I} \times \quad (4.33)$$

$$= -i\tilde{\chi}_1 \frac{\mathbf{I}}{I} \times \quad (4.34)$$

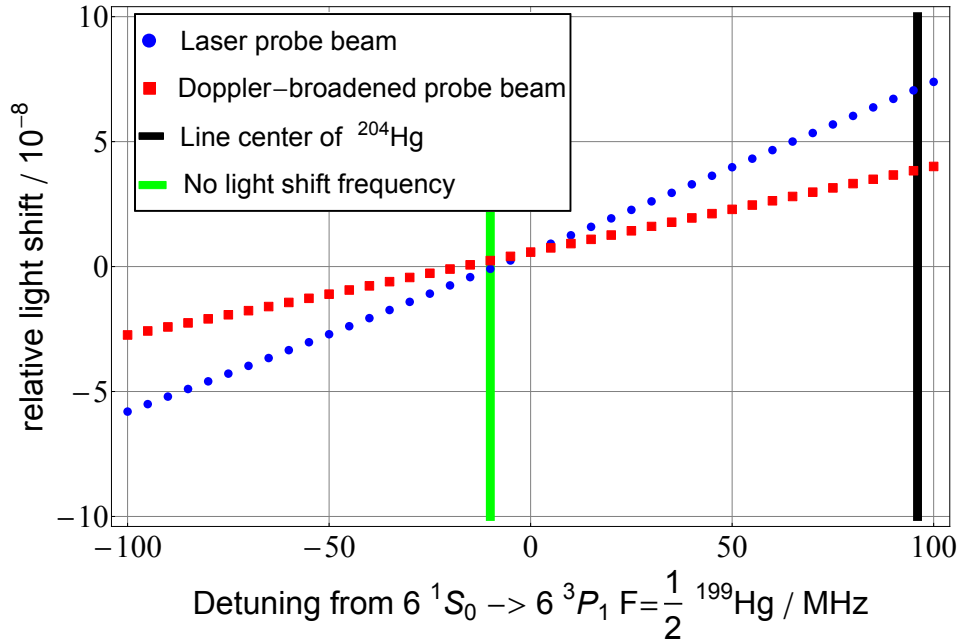


Figure 4.4: Detail of the data given in Fig. 4.3 around the absorption line center of the  $^{199}\text{Hg}$  line. The position of the line center of  $^{204}\text{Hg}$  is also indicated.

Note the nuclear spin dependence of (4.34). From (4.26) one gets

$$\mathbf{E}_{\text{out}} = e^{-i2\pi\nu l/c(1+\frac{\chi_0}{2}+\frac{\chi_1}{2})} \mathbf{E}_{\text{in}}(0, t) \quad (4.35)$$

where the exponential acts as an operator on  $\mathbf{E}_{\text{in}}$ . The effect of the medium is given as the additional complex phase  $-i2\pi\nu l/c(\frac{\chi_0}{2} + \frac{\chi_1}{2})$ . In the case that the spin  $\mathbf{I}$  is restricted to the y-z-plane (in the coordinate system defined after (4.1)) one finds

$$\hat{\mathbf{I}} = \begin{pmatrix} 0 \\ \sin(\omega t) \\ \cos(\omega t) \end{pmatrix}. \quad (4.36)$$

One can calculate the structure of (4.26) for  $\sigma^+$  and  $\sigma^-$  light propagating in the spin-polarized  $^{199}\text{Hg}$  vapor

$$(2 + \chi_0 - i\tilde{\chi}_1\hat{\mathbf{I}}\times) \mathbf{E}_+ = (2 + \chi_0 - \cos(\omega t)\tilde{\chi}_1) \mathbf{E}_+ + i\tilde{\chi}_1 \frac{E_0}{\sqrt{2}} \sin(\omega t) \begin{pmatrix} 0 \\ 0 \\ 1 \end{pmatrix} \quad (4.37)$$

$$(2 + \chi_0 - i\tilde{\chi}_1\hat{\mathbf{I}}\times) \mathbf{E}_- = (2 + \chi_0 + \cos(\omega t)\tilde{\chi}_1) \mathbf{E}_- + i\tilde{\chi}_1 \frac{E_0}{\sqrt{2}} \sin(\omega t) \begin{pmatrix} 0 \\ 0 \\ 1 \end{pmatrix} \quad (4.38)$$

where the electric field vectors are defined after (4.2). Since  $\chi_0, \tilde{\chi}_1 \ll 1$  the additional longitudinal electric field component is small and can be neglected. The corresponding electric field vector for  $\sigma^+$  and  $\sigma^-$  light at the end of the polarized vapor is given by

$$\mathbf{E}_+^{\text{out}} = e^{-\frac{i\pi\nu l}{c}(2+\chi)} \mathbf{E}_+(0, t) \approx e^{-\frac{i\pi\nu l}{c}(2+\chi_0)} e^{-\frac{i\pi\nu l}{c} \tilde{\chi}_1 \cos(\omega t)} \mathbf{E}_+(0, t) \quad (4.39)$$

$$\mathbf{E}_-^{\text{out}} = e^{-\frac{i\pi\nu l}{c}(2+\chi)} \mathbf{E}_-(0, t) \approx e^{-\frac{i\pi\nu l}{c}(2+\chi_0)} e^{+\frac{i\pi\nu l}{c} \tilde{\chi}_1 \cos(\omega t)} \mathbf{E}_-(0, t) \quad (4.40)$$

To determine the effect on linearly polarized light (vertical to the spin precession plane, x-direction) one combines (4.39) and (4.40) for the case of the superposition

$$\mathbf{E}_x = E_0 \hat{e}_x = \frac{1}{\sqrt{2}} (\hat{E}_+ + \hat{E}_-) \quad (4.41)$$

to get

$$\mathbf{E}_x^{\text{out}} = e^{-\frac{i\pi\nu l}{c}(2+\chi_0)} e^{-\frac{i\pi\nu l}{c} \tilde{\chi}_1 \cos(\omega t)} \frac{1}{\sqrt{2}} (\mathbf{E}_+ + e^{-2\frac{i\pi\nu l}{c} \tilde{\chi}_1 \cos(\omega t)} \mathbf{E}_-). \quad (4.42)$$

While  $\chi_0$  results in an undetectable common phase shift for both  $\sigma$  polarization components,  $\chi_1$  introduces a detectable differential phase shift  $\phi$  between both  $\sigma$  polarization components. A relative phase shift  $\phi$  causes a rotation of the polarization plane of linearly polarized light by the angle  $\Phi = \phi/2$ . For an atomic polarization degree  $P_a$  the light polarization angle is modulated at the Larmor frequency

$$\Phi = \frac{\phi}{2} = P_a \frac{l\pi\nu}{c} \text{Re}(\tilde{\chi}_1) \cos(\omega t) = \frac{l\pi\nu}{c} \text{Re}(\tilde{\chi}_1) \hat{\boldsymbol{\mu}}(t) \cdot \hat{\mathbf{k}} \quad (4.43)$$

where  $\cos(\omega t) = \hat{\boldsymbol{\mu}}(t) \cdot \hat{\mathbf{k}}$  is the time dependent projection of the magnetic moment unit vector on the unit vector of light propagation  $\hat{\mathbf{k}}$ .

As an example for the nEDM setup the rotation angle as a function of light frequency is shown in Figure 4.5 for a 100% spin-polarized  $^{199}\text{Hg}$  vapor with a number density of  $1.6 \times 10^{10} \text{ cm}^{-3}$  at 294 K and a light path of 50 cm. The light is assumed to be 100% linearly polarized. In the nEDM precession chamber (diameter  $D_{\text{chamber}} = 47 \text{ cm}$ ) this number density corresponds to an absorption value of 27% on the  $F = 1/2$  line. To suppress vector light shift effects due to residual circular polarization and to avoid signal amplitude variations one normally probes the optical rotation between the two  $6^1S_0 \rightarrow 6^3P_1$   $F = 1/2$  and  $F = 3/2$  transitions [SLG<sup>+</sup>13]. For the parameters given above the polarization rotation angle at a frequency between the two hyperfine transitions is  $\Phi \approx 10 \text{ mrad}$  in the nEDM setup.

For comparison a rotation angle of  $\Phi \approx 400 \text{ mrad}$  [Swa07] is achieved in the HgEDM experiment. Despite a  $\approx 21$  times longer light path in the nEDM setup (470 mm vs. 22 mm) the effect is a factor of 40 larger in the HgEDM experiment since the mercury vapor is 1000 times more dense in the HgEDM cells ( $N_{\text{HgEDM}} = 1.6 \times 10^{13} \text{ cm}^{-3}$  at 294 K).

Here a signal amplitude estimate for the detection of paramagnetic rotation in the nEDM setup is given. The optical rotation effect can be detected with first order sensitivity

in  $\phi$  with a linear polarizer under  $45^\circ$  relative to the incident plane of polarization:

$$I(t) = \frac{c}{16\pi} \frac{1}{2} \left| \mathbf{E}_x^{\text{out}}(t) \cdot \frac{1}{\sqrt{2}} \begin{pmatrix} 1 \\ 1 \\ 0 \end{pmatrix} \right|^2 = \frac{I_0}{2} (1 + \sin \phi) = \frac{I_0}{2} (1 + \sin 2\Phi) \quad (4.44)$$

The amplitude of the intensity modulation is  $\frac{\sin 2\Phi}{2} = 1\%$  for  $\Phi = 10$  mrad. To judge on possible enhancement factors for the optical rotation in the nEDM setup a comparison to the HgEDM setup and other magnetometers is useful. Here three aspects are discussed:

- **Increase the number density of polarized  $^{199}\text{Hg}$ :** As can be seen from Figure 5.15 the achievable atomic polarization decreases with the measured light absorption and thus the  $^{199}\text{Hg}$  number density. In this measurement the optical pumping of the  $^{199}\text{Hg}$  atoms was still performed with the  $^{204}\text{Hg}$  discharge bulbs. Unless optical pumping with the new laser system becomes much more efficient due to the larger photon flux available it will be difficult to increase the number density at the same polarization performance. Furthermore spin-relaxation by re-emitted photons has then to be taken into account.

The HgEDM experiment has two main advantages compared to the nEDM setup that allows it to run at much higher  $^{199}\text{Hg}$  densities. First of all, the spin-polarized  $^{199}\text{Hg}$  ensemble can be prepared without regards to a second spin-polarized species of easily absorbed UCN. This allows the use of a buffer gas atmosphere of 630 mbar CO. The CO non-radiatively quenches the excited  $6^3P_1$  state to suppress the re-emission of photons that cause depolarization at such a high density vapor. The second advantage in the HgEDM experiment is the use of sealed small volume cells. Thus the  $^{199}\text{Hg}$  atoms are polarized in the same volume as the spin precession takes place. In the nEDM experiment the spin-polarized  $^{199}\text{Hg}$  atoms are rapidly transferred into the precession chamber as the atoms travel on ballistic trajectories. This fast transfer is needed to minimize any dead time between filling the UCNs into the storage chamber and the beginning of the Ramsey cycle. Long waiting times, e.g., due to optical pumping directly in the precession chamber lead to a reduced number of counted UCN and thus decreased statistical sensitivity. A high buffer gas pressure results in a diffusive transport of the  $^{199}\text{Hg}$  atoms such that a fast transfer of the atoms from the polarization to the precession chamber is not possible. Furthermore the use a buffer gas in the nEDM experiment reduces the UCN lifetime drastically. The UCN are up-scattering to the non-UCN energy regime and rapidly lost from the storage chamber.

- **Increase the interaction light path:** By using a multi-pass cell geometry the optical rotation effect might be efficiently enhanced as has been shown recently, e.g., for Rb magnetometers [LVS<sup>+</sup>11]. In this experiment two mirrors are mounted inside a Rb vapor cell such that only the Rb vapor is between the mirror faces. In the nEDM setup the light beam has to pass the two windows in the precession chamber each time before reaching the mirrors that can only be installed outside of

the electric field region. This will reduce the amount of detected light by absorption and reflections on the windows. It is not yet clear if UCN- and HV-compatible anti-reflection coatings for the windows exist. To judge the feasibility of a multi-pass detection scheme residual window birefringence, absorption and reflection properties, UCN compatibility of coatings and HV compatibility have to be studied in detail.

- **Frequency stabilization at optical rotation maximum:** A third alternative to enhance the effect of paramagnetic rotation is to stabilize the UV laser frequency at one of the maxima of the effect in the vicinity of the line centers of the  $F = 1/2$  or  $F = 3/2$  lines. Here the achievable optical rotation is 100 mrad. But the vector-light-shift (VLS) effect and the paramagnetic rotation show the same frequency dependence as can be seen from (4.43) in combination with (4.34) and (4.17) and thus also the VLS effect is maximized. From Figure 4.3 one obtains for a  $5\ \mu\text{W}$  probe beam the maximum relative VLS effect of  $2.5 \times 10^{-7}$ . To realize this setup two goals have to be achieved. First of all the UV laser has to be frequency stabilized to the maximum of the effect. This could be done, e.g. by measuring the effect in a smaller cell of polarized  $^{199}\text{Hg}$  vapor and frequency modulation techniques. Furthermore the degree of linear light polarization *inside* the precession chamber has to be higher than 99%. Thus birefringence induced by components in the light beam (windows (in electric fields), wave plates,...) has to be controlled or compensated to the sub-percent level in the nEDM/n2EDM setup.

## 4.2 An extended model for the absorptive signal

To extract the characteristic parameters of the  $^{199}\text{Hg}$  co-magnetometer (light absorption, atomic polarization,...) from the measured data one has to employ a model that describes how the absorptive signal is generated. Here the absorptive measurement scheme is discussed. The first paragraph reproduces the signal model used so far (introduced in [GHI<sup>+</sup>98]) and discusses its weaknesses. In the second paragraph, an extended signal model that describes the observations with much higher accuracy is described.

### 4.2.1 Small signal model

A signal model for the  $^{199}\text{Hg}$  co-magnetometer was developed in [GHI<sup>+</sup>98] when the  $^{199}\text{Hg}$  co-magnetometer was introduced into the nEDM experiment. This model assumes an intensity modulation of the light beam transmitted through the precession chamber with amplitude  $a_s$ , small compared to the DC light level  $I_1$  as defined in Figure 2.9. The light level  $I_2$  is measured after the mercury is filled into the chamber. This model explicitly assumes that the measured intensity levels ( $I_1, I_2$ ) have no offsets due to non-absorbable light (e.g., from other Hg isotopes), that there is no spectral misshaping of the light from the  $^{204}\text{Hg}$  bulb as discussed in Section 3.3 and that no other mercury isotopes are present in the enriched  $^{199}\text{Hg}$ . After releasing the mercury into the precession chamber the light



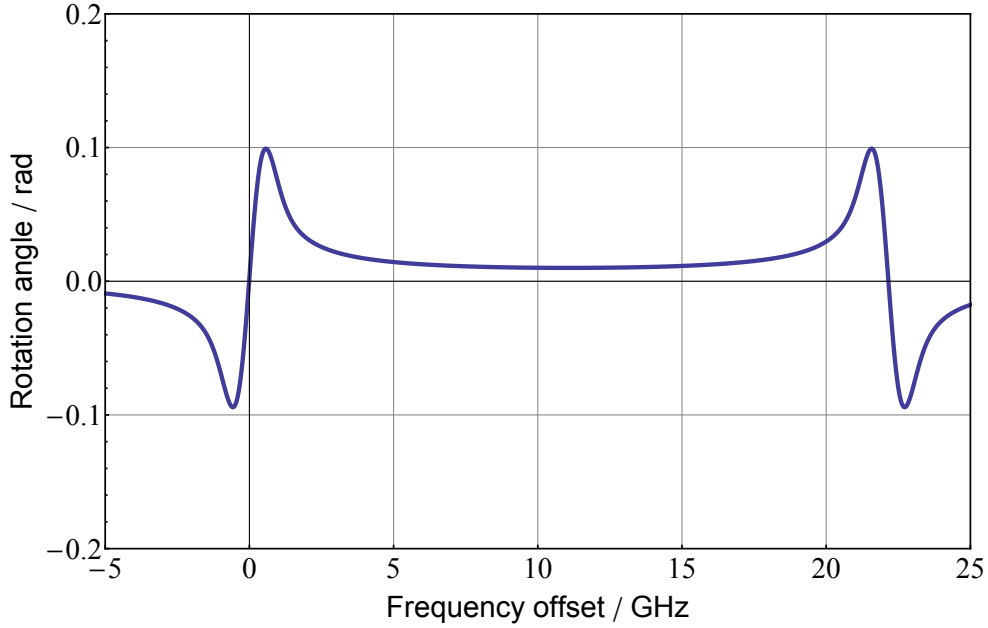


Figure 4.5: Frequency dependence of the paramagnetic rotation effect. The frequency is given as a detuning from the  $^{199}\text{Hg}$ ,  $F = 1/2$  line center. For the calculation a 100 % spin-polarized  $^{199}\text{Hg}$  vapor with a number density of  $1.6 \times 10^{10} \text{ cm}^{-3}$  at 294 K and a light path of 50 cm is assumed. The light is taken to be 100 % linearly polarized.

intensity is given by

$$I_2 = I_1 e^{-n_{\text{Hg}} \sigma l}. \quad (4.45)$$

The measured light absorption  $A$  is derived as

$$A = \frac{I_1 - I_2}{I_1} = 1 - e^{-n_{\text{Hg}} \sigma l}, \quad (4.46)$$

where  $n_{\text{Hg}}$  is the Hg density in the chamber,  $\sigma$  is the absorption cross-section and  $l$  is the diameter of the precession chamber. The AC signal amplitude is calculated by comparing the light absorption by a polarized and an unpolarized ensemble of Hg atoms

$$a_s = I_1 e^{-n_{\text{Hg}} \sigma (1-P)l} - I_1 e^{-n_{\text{Hg}} \sigma l} = I_1 e^{-n_{\text{Hg}} \sigma l} \left( \left( e^{-n_{\text{Hg}} \sigma l} \right)^{-P} - 1 \right) \quad (4.47)$$

where  $P$  is the atomic polarization. Substituting (4.46) in (4.47) gives the signal amplitude  $a_s$  as a function of  $A$  and  $P$

$$a_s = I_1 (1 - A) \left( (1 - A)^{-P} - 1 \right). \quad (4.48)$$

A value for the atomic polarization can be extracted by rearranging (4.47)

$$P = -\frac{\ln \left( 1 + \frac{a_s}{I_1 (1-A)} \right)}{\ln (1 - A)}. \quad (4.49)$$

With the approximation that  $a_s \ll I_1$  and  $A \ll 1$  the atomic polarization is given by [GHI<sup>+</sup>98]

$$P \approx \frac{a_s}{I_1 A \left(1 - \frac{A}{2}\right)}. \quad (4.50)$$

As discussed in Section 3.3 the  $^{204}\text{Hg}$  discharge bulbs have been found to not fulfill the assumptions for this model if they are run at temperatures of 40 °C. In addition the assumption of symmetric modulation around the  $I_2$  level is not valid for large absorption values  $A$ .

## 4.2.2 An extended model for the $^{199}\text{Hg}$ co-magnetometer signal

To be able to compare the  $^{204}\text{Hg}$  bulb and the UV laser  $^{199}\text{Hg}$  co-magnetometer one needs a model that is valid in both situations. The transmitted light intensity after the precession chamber is described by

$$I_2 = (I_1 - DC_{\text{offset}}) e^{-n_{199\text{Hg}}\sigma l(\beta - \frac{P}{\alpha})} + DC_{\text{offset}} \quad (4.51)$$

where  $\alpha$  is a correction factor that takes into account that the absorption cross-section between the  $^{199}\text{Hg}$  atoms and the light emitted by the  $^{204}\text{Hg}$  atoms in the bulb can be lowered due to spectral misshaping. The factor  $\beta$  takes light absorption by atoms other than  $^{199}\text{Hg}$  into account, as well as the possibly reduced effective light absorption cross-section as given by (4.12). The  $DC_{\text{offset}}$  term accounts for light that cannot be absorbed by the Hg atoms in the enriched  $^{199}\text{Hg}$  sample because it is emitted from isotopes different than the ones in the enriched  $^{199}\text{Hg}$  sample. The modulation signal amplitude  $a_s$  is assumed to be half the difference between the maximum and the minimum transmitted light intensity

$$a_s = \frac{I_2^{\text{max}} - I_2^{\text{min}}}{2} = \frac{(I_1 - DC_{\text{offset}})}{2} \left( e^{-n_{199\text{Hg}}\sigma l(\beta - \frac{P}{\alpha})} - e^{-n_{199\text{Hg}}\sigma l(\beta + \frac{P}{\alpha})} \right). \quad (4.52)$$

The measured absorption value has to be corrected for offset light

$$A^{\text{corr}} = \frac{I_1 - I_2}{I_1 - DC_{\text{offset}}} = 1 - e^{-n_{199\text{Hg}}\sigma l\beta}. \quad (4.53)$$

Substitution of (4.53) into (4.52) gives

$$a_s = \frac{I_1 - DC_{\text{offset}}}{2} e^{-n_{199\text{Hg}}\sigma l\beta} \left( e^{-n_{199\text{Hg}}\sigma l(-\frac{P}{\alpha})} - e^{-n_{199\text{Hg}}\sigma l(+\frac{P}{\alpha})} \right) \quad (4.54)$$

$$= (I_1 - DC_{\text{offset}}) e^{-n_{199\text{Hg}}\sigma l\beta} \sinh\left(\frac{P}{\alpha} n_{199\text{Hg}}\sigma l\right) \quad (4.55)$$

$$= (I_1 - DC_{\text{offset}}) \left(1 - \frac{I_1 - I_2}{I_1 - DC_{\text{offset}}}\right) \sinh\left(\frac{P}{\alpha} n_{199\text{Hg}}\sigma l\right). \quad (4.56)$$

The product  $n_{199\text{Hg}}\sigma l$  is directly measurable:

$$n_{199\text{Hg}}\sigma l = -\frac{1}{\beta} \ln \left( 1 - \frac{I_1 - I_2}{I_1 - DC_{\text{offset}}} \right). \quad (4.57)$$

The signal amplitude  $a_s$  is given by

$$a_s = (I_2 - DC_{\text{offset}}) \sinh \left( -\frac{P}{\alpha\beta} \ln \left( 1 - \frac{I_1 - I_2}{I_1 - DC_{\text{offset}}} \right) \right). \quad (4.58)$$

Rearranging (4.58) for the atomic polarization  $P$  gives

$$P = -\alpha\beta \frac{1}{\ln \left( 1 - \frac{I_1 - I_2}{I_1 - DC_{\text{offset}}} \right)} \operatorname{arcsinh} \left( \frac{a_s}{I_2 - DC_{\text{offset}}} \right). \quad (4.59)$$

In the case of  $DC_{\text{offset}} = 0$ ,  $\alpha = 1$  and  $\beta = 1$  the formula for the atomic polarization  $P$  simplifies to

$$P = -\frac{1}{\ln(1 - A)} \operatorname{arcsinh} \left( \frac{a_s}{I_2} \right) = -\frac{1}{\ln(1 - A)} \operatorname{arcsinh} \left( \frac{a_s}{I_1(1 - A)} \right). \quad (4.60)$$

For 100% atomic polarization,  $DC_{\text{offset}} = 0$ ,  $\alpha = 1$  and  $\beta = 1$ , the small amplitude model starts to deviate from the extended signal model for absorptions above 20%. The small amplitude model predicts a modulation from  $-I_1$  to  $I_1$  for 100% light absorption which is unphysical. The extended model oscillates between 0 and  $I_1$  for the same parameters. In the appendix D an exact signal model is developed to take the nonlinear character of the exponential light absorption into account. The normalized AC amplitudes predicted by the three models are compared for atomic polarizations of  $P = 25\%$ ,  $50\%$  and  $75\%$  in Figure 4.6. It is found that the degree of atomic polarization is systematically underestimated with the small amplitude model. For light absorption values  $A < 60\%$  and atomic polarization  $P = 75\%$ , the extended model deviates only slightly from the exact model. The extended model is used in this analysis as it provides an analytical expression for the atomic polarization  $P$  in terms of light absorption  $A$  and modulation amplitude  $a_s$  and the deviations are found to be small in the absorption  $A$  and signal amplitude  $a_s$  range of the nEDM experiment.

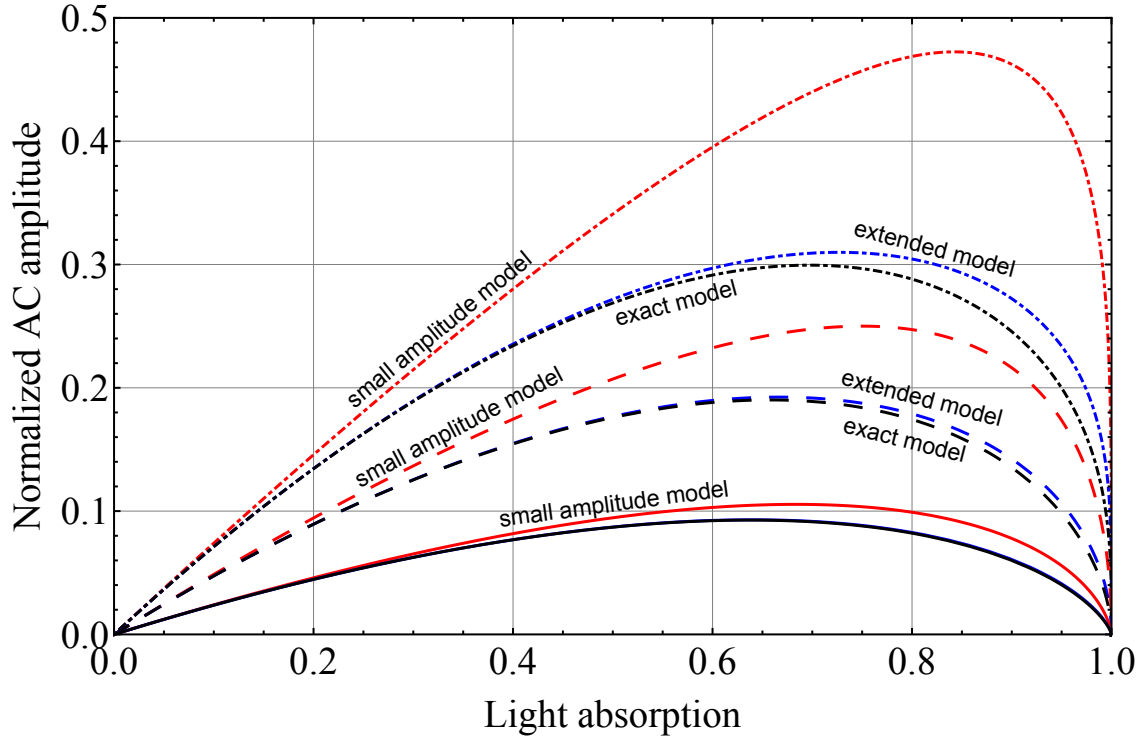


Figure 4.6: Comparison of the normalized modulation amplitude according to the small amplitude model (4.48) (red), the extended model (4.58) (blue) and the exact model (D.14) (black) for the case of  $P = 25\%$  (—),  $P = 50\%$  (---), and  $P = 75\%$  (-.-) atomic polarization,  $DC_{\text{offset}} = 0$ ,  $\alpha = 1$  and  $\beta = 1$ . In the low absorption limit the three models converge. The small amplitude model systematically predicts a larger signal amplitude which in turn leads to an underestimation of the atomic polarization  $P$ . The extended and the exact model only deviate significantly for light absorption  $A > 60\%$  and atomic polarization  $P > 75\%$ .

# Chapter 5

## Comparison of $^{204}\text{Hg}$ lamp and UV laser based $^{199}\text{Hg}$ co-magnetometry

The first section of this chapter presents the analysis procedure applied to the free induction decay signals that have been recorded with the UV laser light source and the  $^{204}\text{Hg}$  bulbs. A direct comparison of the achieved signal contrast is provided in the second section. The third section provides a comparison between the atomic polarization extracted with the small signal amplitude model and the extended signal model as developed in Chapter 4. In the fourth section the achieved signal-to-noise-density-ratio (SNDR) for the laser and lamp based Hg co-magnetometer is presented. Section five is used to show that the laser based  $^{199}\text{Hg}$  co-magnetometer provides the necessary SNDR to achieve the magnetometry requirements for the n2EDM experiment. Based on the atomic polarization extracted in the third section a new model is developed to describe the optical pumping process in the polarization chamber of the nEDM experiment in section six. The last section discusses the depolarization of the  $^{199}\text{Hg}$  atoms in the precession chamber of the nEDM experiment and motivates future investigations of the depolarization rate for different isotopic compositions of the Hg vapor.

### 5.1 Data analysis procedure

In this section the general data treatment used to obtain the results in the following sections is presented. The  $^{199}\text{Hg}$  co-magnetometer related part of the current data-acquisition system of the nEDM experiment is explained in detail in App. C. The AC signal component (see Figure 2.10) is digitized after a multiple-feedback bandpass filter (measured center frequency  $f_c=7.85\text{ Hz}$  and  $Q = 5.06$ ) by a 16-bit ADC at a sampling rate of 100 Hz. The DC component is digitized with a 12-bit ADC.

The AC part of the recorded free induction decay (FID) signal is first passed through a further digital finite impulse response (FIR) *zero-phase shift* bandpass filter (digital filter parameters: length  $n_{\text{df}} = 151$ , low cut-off frequency  $\nu_{1,\text{df}} = 7\text{ Hz}$ , high cut-off frequency  $\nu_{h,\text{df}} = 9\text{ Hz}$ ) to suppress the second harmonic component that was not suppressed by

the analog bandpass filter to below the noise level of the AC ADC. This second harmonic decays with double the decay rate as the fundamental signal. It can create a so-called *early-to-late* effect on the frequency extraction. At early times the second harmonic contribution would add signal components that can interfere with the frequency extraction for a single frequency fit. At later times these signal contributions are absent and can thus introduce systematic effect in the frequency extraction. To exclude filter charging effects of the analog and digitally filtered signal the first 4.5 s are removed from the time series of filtered data points. To exclude any filter charging effect of the analog filter at the end of the cycle a time window of 0.5 s that corresponds to approximately three times the length of the digital filter kernel is removed at the end of the filtered signal. To determine the initial FID signal parameters the filtered set of data points is fitted with the function given by

$$A_{\text{fit}}(t) = A_0 e^{-\frac{t}{\tau}} \sin(2\pi\nu t + \phi_0), \quad (5.1)$$

where  $A_0$  is the initial amplitude of the filtered FID signal,  $\tau$  the signal decay time,  $\nu$  the mean signal frequency and  $\phi_0$  the initial signal phase. To extract the phase evolution as a function of time the filtered FID signal is divided in subsets of 0.5 s and each subset of data points is refitted with fixed  $\tau$  but free  $A_0$ ,  $\nu$  and  $\phi(t)$ . In this way the phase evolution of the FID signal is extracted.

The Fourier transform (FT) of the FID signal is useful to investigate the higher harmonics of the signal and to search for additional noise sources that contribute at a constant frequency. The FT of an exponentially decaying FID signal  $A(t)$  ( $A(t < 0) = 0$ )

$$A(t) = A_0 e^{-\gamma t} \cos(2\pi\nu t + \phi_0), \quad (5.2)$$

is given by

$$A(\omega) = \frac{1}{\sqrt{2\pi}} \int_{-\infty}^{\infty} A(t) e^{-i\omega t} dt = \frac{1}{\sqrt{2\pi}} \int_0^{\infty} x_0 e^{-\gamma t} \cos(2\pi\nu t + \phi_0) e^{-i\omega t} dt \quad (5.3)$$

in angular frequency space. Using Euler's formula the power spectral density (PSD) is obtained

$$|A(\omega)| = \frac{x_0}{8\pi} \left| \frac{1}{i(\omega - \omega_0) + \gamma} + e^{-2i\phi_0} \frac{1}{i(\omega + \omega_0) + \gamma} \right|. \quad (5.4)$$

The PSD in frequency space is obtained by

$$|A(\nu)| = \frac{|A(\omega)|}{2\pi}. \quad (5.5)$$

For the special case  $\gamma \ll \omega_0$  the Lorentzian line profile for  $|A(\nu)|^2$  is recovered. While this approximation is very well fulfilled in the regime of optical frequencies, this is not always the case for the low frequency range the  $^{199}\text{Hg}$  co-magnetometer is working in. Thus (5.4) is used to fit the line shape of the peak at the fundamental frequency. Additional deviations

(phase shifts) are introduced by the analog bandpass filter that introduces a frequency dependent phase shift.

To determine the noise level in the vicinity of the mean precession frequency the power spectral density (PSD) of the FID signal has to be calculated. To reduce the influence of the main peak on the neighboring frequency bins (leaking) a so-called *window function* is applied to the FID signal (without the digital band pass filter) before calculating its FT. A wide range of different window functions has been developed to optimize the FT of a signal for different purposes, e.g. the separation of signal components with close-by frequencies or the recovery of a weak signal in the frequency wing of a much stronger signal. For a detailed review on digital filters the reader is referred to, e.g., Ref. [She05].

The windowed signal  $S_{n,\text{win}}$  is obtained by applying a *Hanning* window

$$Hann(n) = \begin{cases} a \left(1 - \cos\left(\frac{2\pi n}{N-1}\right)\right) & \text{for } 0 \leq n \leq N-1 \\ 0 & \text{else} \end{cases}, \quad (5.6)$$

to the FID signal  $S_n$  with total sample number  $N$  by multiplication

$$S_{n,\text{win}} = Hann(n) \cdot S_n. \quad (5.7)$$

The constant  $a = \sqrt{\frac{2}{3}} = \left(\frac{1}{N-1} \int_0^{N-1} Hann(n)^2 dn\right)^{-1/2} \approx 0.8165$  is chosen such that the PSD of white noise<sup>1</sup> is not altered by the application of the window function<sup>2</sup>. A comparison of the non-windowed and windowed PSD is shown in Figure 5.1. The non-windowed PSD reproduces the typical shape of the amplitude spectrum of an exponentially damped oscillation where the peak completely dominates the PSD. In the FT of the windowed FID signal the PSD reaches the noise level of the AC ADC for frequencies outside the interval of 5 Hz to 11 Hz. Within this interval the noise transmitted through the analog bandpass filter is visible. To determine the noise PSD at the position of the FID signal the transmission function of the analog bandpass filter (as described in App. C) is fitted to the windowed FFT data and evaluated at the peak position. The regions of the peaks at the fundamental and second harmonic frequency as well as around peaks from other noise sources are excluded from the background fit.

## 5.2 AC signal comparison: UV laser vs. $^{204}\text{Hg}$ bulb

To compare the achievable contrast of the  $^{199}\text{Hg}$  co-magnetometer signal recorded with the  $^{204}\text{Hg}$  bulb and the UV laser three measurement runs were performed with identical optical pumping setup ( $^{204}\text{Hg}$  bulb temperature 40 °C, RF generator excitation voltage 1.27 V) to polarize the  $^{199}\text{Hg}$  atoms. The number of Hg atoms, and thus the light absorption, was

<sup>1</sup>The term *white* noise refers to noise with a constant power spectral density independent of the frequency.

<sup>2</sup>Another common choice is  $a = 1/2$ . In this case  $Hann\left(\frac{N-1}{2}\right) = 1/2$ . Here this choice is inconvenient as the PSD of white noise is not reproduced.

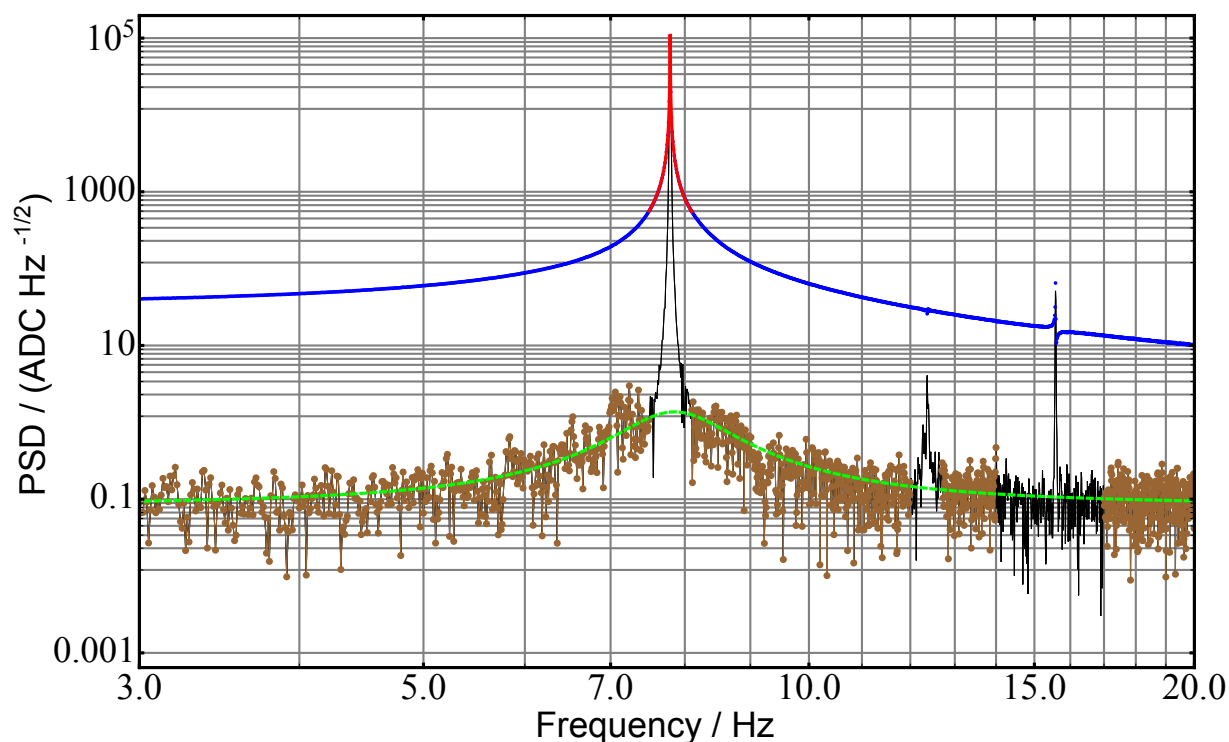


Figure 5.1: The power spectral density (PSD) can be calculated with and without windowing of the FID signal. While the PSD of the unwindowed FID signal (—) is completely dominated by the main peak around its center, one can extract the noise floor in the vicinity of the peak from the PSD of the windowed FID signal (—). A fit of (5.4) (—) reproduces the peak shape well. The transmission function of the analog bandpass filter is fitted to the windowed FID signal (excluding regions of well peaked frequency components (•)) to obtain an estimate of the PSD at the position of the main peak (—) (nEDM run 6494, cycle 123).



controlled by changing the temperature of the Hg source. This changes the dissociation rate of HgO at a fixed accumulation time. The three different detection light configurations are:

1. **Configuration A:** A  $^{204}\text{Hg}$  discharge bulb as shown in Figure 3.4b, temperature stabilized to  $40^\circ\text{C}$  as described in [Roc09] (nEDM run 6440).
2. **Configuration B:** Light from the UV laser system is delivered to the experiment in a  $600\ \mu\text{m}$  optical fiber as shown in Figure 3.19. The laser is frequency stabilized to the  $^{199}\text{Hg } 6^1S_0 \rightarrow 6^3P_1$   $F = 1/2$  line ( $F = 1/2$  line, nEDM run 6454, 6462, configuration B).
3. **Configuration C:** Light from the UV laser system is delivered to the experiment in a  $600\ \mu\text{m}$  optical fiber as shown in Figure 3.19. The laser is frequency stabilized to the  $^{199}\text{Hg } 6^1S_0 \rightarrow 6^3P_1$   $F = 3/2$  line ( $F = 3/2$  line, nEDM run 6461).

The time of optical pumping, i.e., the time for which the  $^{199}\text{Hg}$  atoms accumulate and are illuminated continuously in the polarization chamber was  $t_{\text{light,lamp}} = 140\ \text{s}$  in configuration A and  $t_{\text{light,laser}} = 212\ \text{s}$  in configurations B and C. A direct comparison of the lamp and laser results is only possible if the atomic polarization  $P$  has reached its equilibrium value  $P_{\text{equi}}$  within the shorter time interval  $t_{\text{light,lamp}}$ . Two arguments that this is indeed the case are presented in Section 5.3.

To become independent of different absolute light levels the AC signal amplitude  $a_s$  is normalized to the light level  $I_1$  without mercury atoms in the precession chamber. The value of  $a_s/I_1$  is given in Figure 5.2 as a function of the measured light absorption  $A$ . This comparison is useful since the ratio  $a_s/I_1$  has to have a maximum between  $A = 0$  and  $A = 1$ . For  $A = 0$  there are no atoms in the precession chamber that could contribute to the FID signal. On the other hand for  $A = 1$  no photons reach the detector and thus no FID signal can be recorded<sup>3</sup>. For configuration A a maximum value of  $(a_s/I_1)_{40^\circ\text{C}}^{\text{bulb}} = 2.5\ \%$  was found at  $A \approx 12\ \%$ . For configuration B a value of  $(a_s/I_1)_{F=1/2}^{\text{laser}} = 12.5\ \%$  at  $A \approx 43\ \%$  is found. In configuration C  $(a_s/I_1)_{F=3/2}^{\text{laser}} = 8.8\ \%$  was found at  $A \approx 57\ \%$ . The difference in contrast and in the position of the maximum between configurations B and C can be understood from Figure 4.2. In the best case (100% atomic polarization, 100% circular light polarization) the light absorption cross-section shows a modulation between 0% and 200% of the unpolarized light absorption cross-section for the  $F = 1/2$  line while the modulation is between 50% and 150% for the  $F = 3/2$  line. The polarization independent

---

<sup>3</sup>The current version of the nEDM DAQ only records the AC component of the FID signal during a measurement cycle. DC information is only provided before the beginning and after the measurement cycle. A even more reliable figure of merit would be the ratio of AC amplitude to the average number of detected photons. Up to now the amount of detected light can only be recalculated (with variable gain factors) by using the PMT gain calibration as a function of the applied HV. As the PMT HV is not written to file automatically and has to be set manually it can be subject to unrecorded changes. Thus different amount of photons can correspond to the same light level. This is especially the case with the discharge bulb since the achievable modulation amplitude depends on the running conditions. To make use of the full range of the 16-bit AC ADC the PMT HV was adjusted regularly resulting in variable gain factors. This problem should be avoided in a future DAQ system.

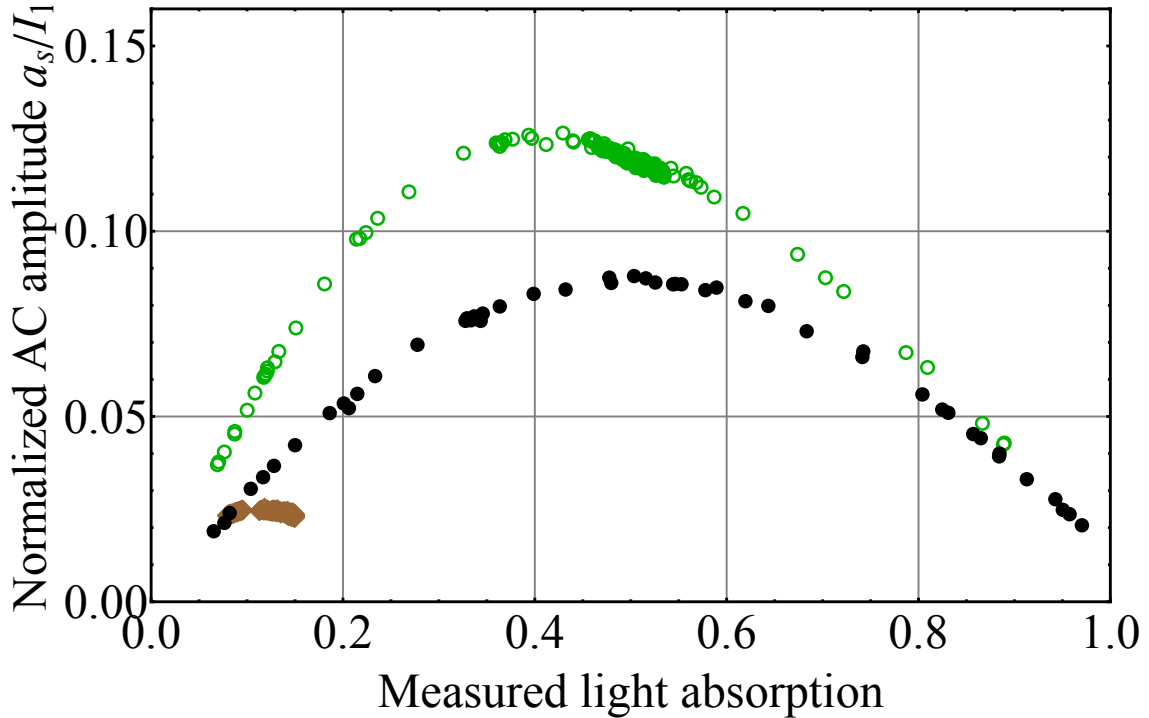


Figure 5.2: Normalized AC signal component for three different readout light configurations as a function of light absorption: UV laser system frequency stabilized to the  $^{199}\text{Hg}$   $F = 1/2$  transition ( $\circ$ ) or the  $^{199}\text{Hg}$   $F = 3/2$  transition ( $\bullet$ ) and the  $^{204}\text{Hg}$  discharge lamp ( $\blacklozenge$ ) temperature stabilized to  $40^\circ\text{C}$ .

part of the light absorption cross-section does not contribute to the AC signal component but reduces the overall light level. Therefore the maximum normalized AC signal is lower and shifted to larger light absorption values for the  $F = 3/2$  line. The five fold increase of normalized signal amplitude achieved with the UV laser frequency stabilized to the  $^{199}\text{Hg}$   $6^1S_0 \rightarrow 6^3P_1$   $F = 1/2$  line and the small light absorption that could be achieved in the  $^{204}\text{Hg}$  bulb configuration triggered the further investigation of the light spectrum emitted by the  $^{204}\text{Hg}$  bulb. The main reasons for the reduced modulation amplitude are listed in Section 3.3.

### 5.3 Small amplitude model vs. extended model

To optimize the normalized AC signal component a high degree of atomic polarization  $P$  is necessary. To study the influence of different parameters (optical pumping light power, Hg atomic density, ...) on the achievable  $P$  one has to extract a value for  $P$  with one of the signal models discussed in Subsection 4.2.1 and 4.2.2. To compare the results the atomic

polarization  $P$  was first extracted with the small amplitude model for the data sets shown in Figure 5.2. As the light absorption was not always small (4.49) was applied.

The atomic polarization  $P$  as a function of measured light absorption  $A$  is plotted in Figure 5.3. A cut of  $A < 0.8$  was applied to the data. To justify that the atomic equilibrium polarization was reached after  $t_{\text{light,lamp}} = 140$  s, data points from measurement configuration B with  $t_{\text{light,laser}} = 140$  s (nEDM run 6444) and  $t_{\text{light,laser}} = 122$  s (nEDM run 6453) are included in Figure 5.3. The measurement points for  $t_{\text{light,laser}} = 122$  s lie exactly in the trend of configuration B. The points for  $t_{\text{light,laser}} = 140$  s lie a bit lower. These points have been recorded only minutes after the  $^{204}\text{Hg}$  bulb for the optical pumping was switched on. Consequently it is not sure that the  $^{204}\text{Hg}$  bulb has reached its stable operation conditions but it supports the two measurement points for 122 s. The extracted atomic polarization values  $P$  in configuration A are in general more than a factor of two lower than for the configuration B and show a monotonic decrease with increasing light absorption  $A$  while in configuration B and C there is a plateau up to  $A \approx 12.5\%$ . A maximum value of  $P \approx 52\%$  is extracted for measurement configuration B while only  $P \approx 28\%$  is extracted for configuration A.

A direct comparison of the atomic polarization  $P$  extracted from the same raw data (nEDM run 6454) according to the small amplitude model (4.49) and the extended model (4.59) for configuration B is shown in Figure 5.4. The small amplitude model and the extended model are first compared without any correction for light absorption by Hg atoms other than  $^{199}\text{Hg}$ . The small difference in extracted polarization is due to the different characteristic functions  $\ln\left(1 + \frac{\alpha_s}{I_1(1-A)}\right)$  in (4.49) and  $\sinh\left(\frac{\alpha_s}{I_1(1-A)}\right)$  in (4.60). The small amplitude model assumes a symmetric amplitude modulation around the light level for the absorption by unpolarized atoms. Thus it always predicts a larger modulation amplitude than the extended model which assumes a modulation between the minimum and maximum transmitted light level. In turn the atomic polarization  $P$  extracted with the small amplitude model is always smaller than with the extended model. In a second step the measured light absorption  $A$  is corrected for the absorption by  $^{204}\text{Hg}$  and  $^{201}\text{Hg}$  according to the isotopic composition given in Figure B.1 ( $\alpha = 1$ ,  $\beta_{1/2} = 1.14$  (for the calculation see (B.1)),  $DC_{\text{offset}} = 0$ ). The light absorption by isotopes other than  $^{199}\text{Hg}$  causes a systematic underestimation of the  $^{199}\text{Hg}$  atomic polarization by the factor  $\beta_{1/2} = 1.14$ . These two points have to be taken into account when investigating the influence of system parameters on the achievable atomic polarization. The collaboration has switched to  $^{199}\text{Hg}$  from a different supplier (see Figure B.2) that has a lower relative content of  $^{204}\text{Hg}$  and  $^{201}\text{Hg}$  to reduce the necessary correction ( $\beta_{1/2} = 1.03$ , see (B.1)).

From Figure 5.4 one can see that the atomic polarization  $P$  reaches a plateau value for light absorption (as measured in configuration B) below  $A < 12.5\%$ ,  $P_{\text{plat}} \approx 62.5\%$ . This corresponds to an atomic density of  $1.25 \times 10^{11} \text{ cm}^{-3}$  or an absorption length  $n_{199}\sigma_{199} = 0.05 \text{ cm}^{-1}$  in the polarization chamber. During the campaign, measurement points have mainly been taken around the standard operation conditions of the  $^{199}\text{Hg}$  co-magnetometer  $A > 20\%$ . From two measurement runs performed at absorption values below  $12.5\%$  (light exposure times  $t = 176$  s (nEDM run 6445) and  $t = 208$  s (nEDM run 6454), 27 points in total) one can estimate the characteristic built-up time  $t_{\text{built-up}}$  of the atomic polarization

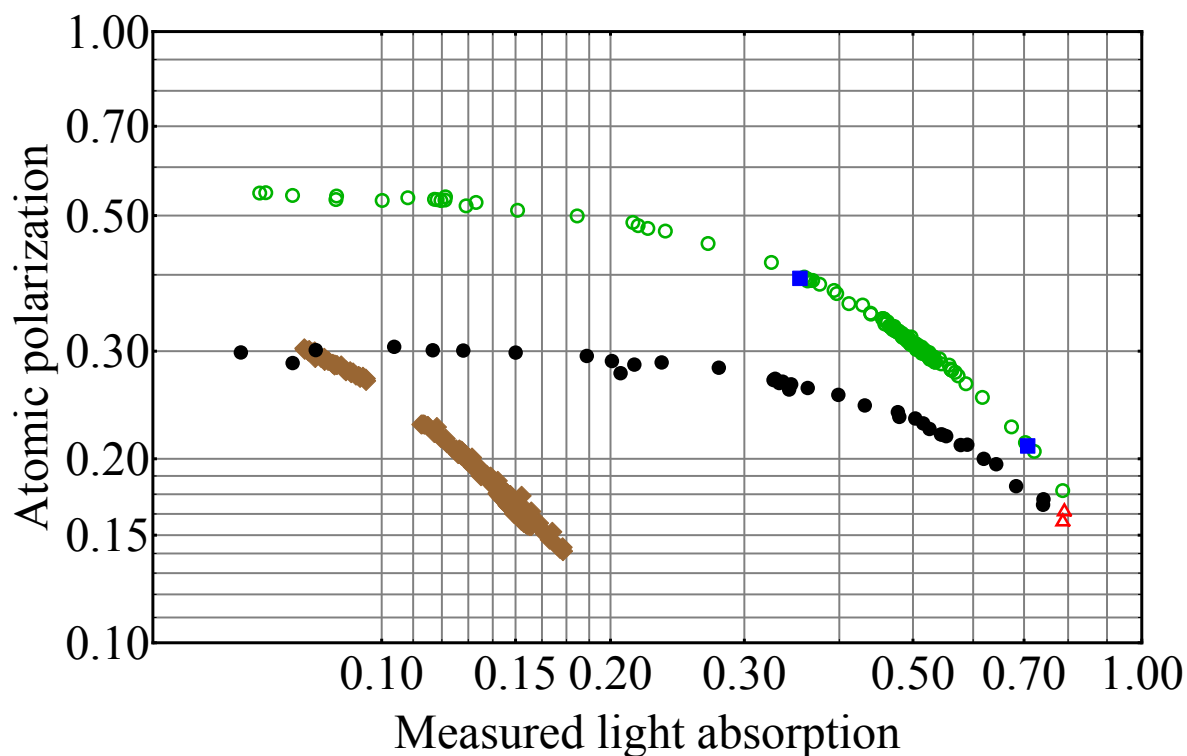


Figure 5.3: Atomic polarization for the data sets given in Figure 5.2 extracted with the small amplitude model (4.49). The three different readout light configurations are: UV laser frequency stabilized to the  $^{199}\text{Hg } F = 1/2$  transition (( $\circ$ , 212 s optical pumping time (opt)), ( $\triangle$ , 140 s opt), ( $\blacksquare$ , 122 s opt)) or the  $^{199}\text{Hg } F = 3/2$  transition ( $\bullet$ , 212 s opt) and the  $^{204}\text{Hg}$  discharge lamp ( $\blacklozenge$ , 140 s opt) temperature stabilized to  $40^\circ\text{C}$ .

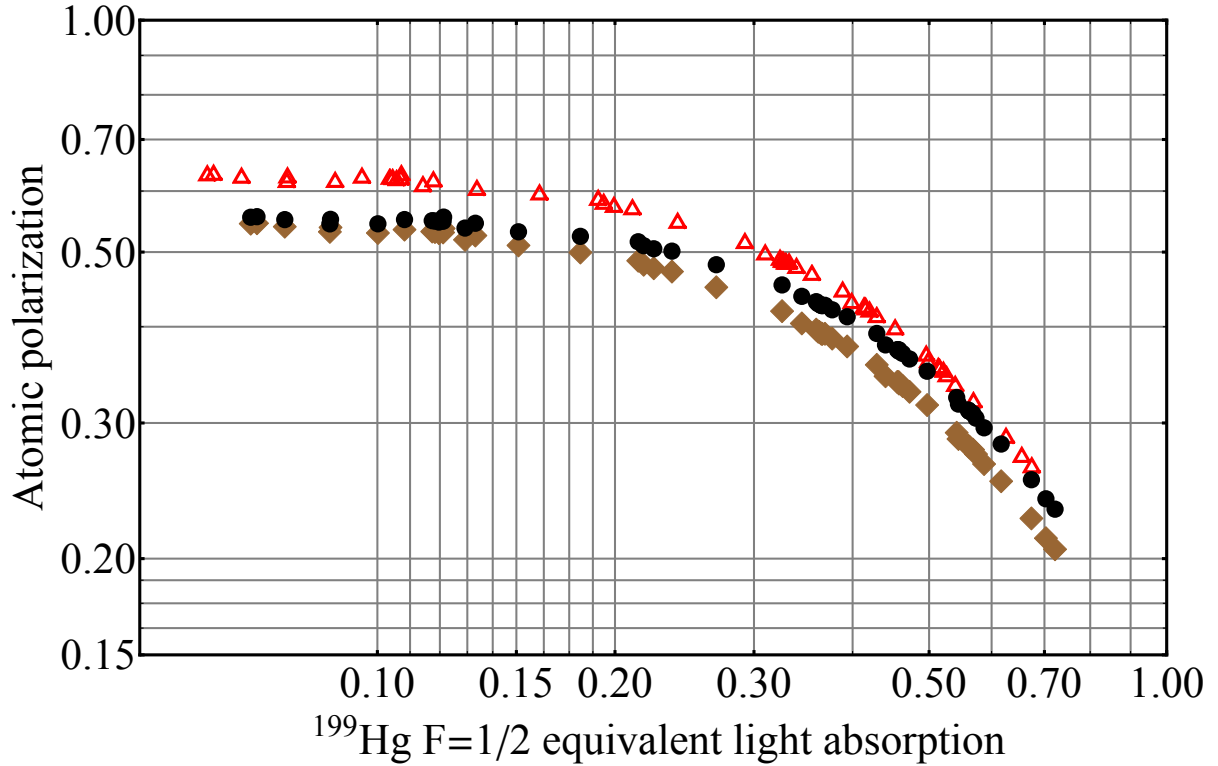


Figure 5.4: Comparison of the atomic polarization  $P$  extracted from the same raw data (nEDM run 6454) with the small amplitude model ( $\blacklozenge$ ) and the extended model without a correction for light absorption by non  $^{199}\text{Hg}$  atoms ( $\bullet$ ). The differences in  $P$  for low light absorption values are explained in the text. Taking the light absorption by non  $^{199}\text{Hg}$  atoms into account ( $\triangle$ ) shows that the atomic polarization  $P$  is underestimated by the small amplitude model by a factor  $\beta = 1.14$ .

in the polarization chamber. An exponential built-up function can be fitted to the atomic polarization  $P$  in the plateau region for different values of  $t_{\text{built-up}}$ . The plateau polarization  $P_{\text{plat}}$  is the free fit parameter. The result of such an evaluation is shown in Figure 5.5. The highest estimate for the built-up time,  $t_{\text{built-up}} < 77\text{ s}$ , is obtained when the built up function just touches the lowest measurement point for the  $t = 176\text{ s}$  and the highest point for the  $t = 208\text{ s}$  measurement. For  $t_{\text{light,lamp}} = 140\text{ s}$  this would result in an atomic polarization  $P = 84\% P_{\text{eq}}$  of the equilibrium polarization  $P_{\text{eq}}$ . For the more likely case of  $t_{\text{built-up}} < 50\text{ s}$  ( $\chi^2/\text{n.d.f} < 1.5$  (26 *n.d.f*), p-value  $\approx 5\%$ )  $P$  reaches 94% of  $P_{\text{eq}}$  in 140 s. The minimal value of  $\chi^2/\text{n.d.f} = 1.05$  is obtained for  $t_{\text{built-up}} = 30.6\text{ s}$ . In this case  $P$  reaches 99% of the equilibrium polarization in 140 s. Together with the measurements presented above one can conclude that the reduced light exposure time in measurement configuration A of Section 5.2 can maximally account for a 16% reduction of detected atomic polarization  $P$  but has most likely an influence of less than 5%.

To further characterize the  $^{204}\text{Hg}$  discharge bulbs the assumption that the atomic equilibrium polarization  $P_{\text{eq}}$  has been reached in all the measurement configurations defined in Section 5.2 before the  $^{199}\text{Hg}$  vapor is released into the precession chamber is used. One can adjust the parameters  $DC_{\text{offset}}$ ,  $\alpha$  and  $\beta$  of the extended model such that the atomic polarization extracted from measurement configuration A show the same scaling behavior as in measurement configuration B as a function of light absorption. For this purpose the dependance of the atomic polarization  $P$  on the measured light absorption (corrected for non- $^{199}\text{Hg}$  isotopes) is parametrized by the following function

$$P(A) = \frac{1}{F + B A + C A^2}, \quad (5.8)$$

where  $B$ ,  $C$  and  $F$  are free fit parameters and  $A$  is the  $^{199}\text{Hg}$   $F = 1/2$  equivalent light absorption. From the fit the atomic equilibrium polarization  $P_{\text{eq}} = 1/F$  can be extracted. The best fit of this function to the data set recorded with the UV laser setup frequency stabilized to the  $^{199}\text{Hg}$   $F = 1/2$  line is shown in Figure 5.6. Subsequently the parameters  $DC_{\text{offset}}$ ,  $\alpha$  and  $\beta$  of the extended model have been adjusted in the analysis of the  $^{204}\text{Hg}$  lamp detected data set to minimize the mean squared distance of the corrected data points to the interpolation function. Best agreement of the corrected lamp detected data set with the interpolation function is found for  $DC_{\text{offset}} = 5.14\text{ V}$ ,  $\alpha = 2.32$  and  $\beta = 0.67$ .

Compared to the average light level  $\bar{I}_1 = 8\text{ V}$  for the lamp based measurement run this means that more than 60% of the light emitted by the  $^{204}\text{Hg}$  bulbs at a temperature of  $40^\circ$  cannot be absorbed at all and produce a constant background light level on the photodetector. For an ideal lamp a factor of  $\alpha = \sqrt{2}$  would be expected due to the additional Doppler-broadening of the light spectrum as shown in (4.13), but  $\alpha = 1.64\sqrt{2}$  is found. This large correction factor indicates a strong spectral deformation of the emission line as discussed in Section 3.3 which leads to a reduced light absorption cross-section. In case that no other Hg isotopes were present in the vapor  $\beta = \frac{1}{\alpha} = 0.43$ . For the best fit  $\beta = 0.67$  which indicates that about 25% of the light emitted by the  $^{204}\text{Hg}$  bulbs is absorbed by non- $^{199}\text{Hg}$  atoms.

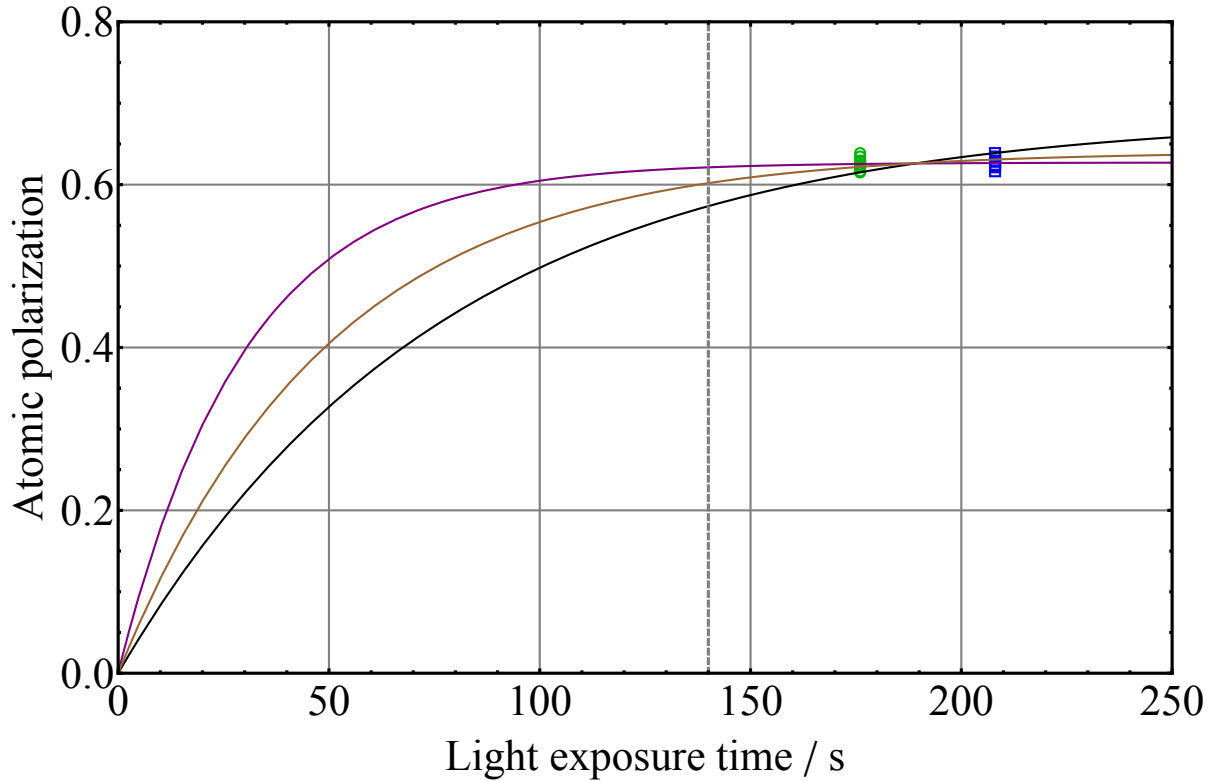


Figure 5.5: An upper limit on the characteristic build-up time  $t_{\text{build-up}}$  of the atomic polarization  $P$  in the polarization chamber is obtained by fitting exponential build-up functions to the  $P_{\text{eq}}$  values for different light exposure times. The average standard deviation of the two data sets is used for weighting in the fit. A reduced  $\chi^2/\text{n.d.f} < 1.5$  (26 *n.d.f*) is reached for  $t_{\text{build-up}} < 50$  s which corresponds to a p-value of 5%. The case that the exponential built up curve just touched the lowest hand highest measurement point in the two data sets is also given for  $t_{\text{build-up}} < 77$  s.

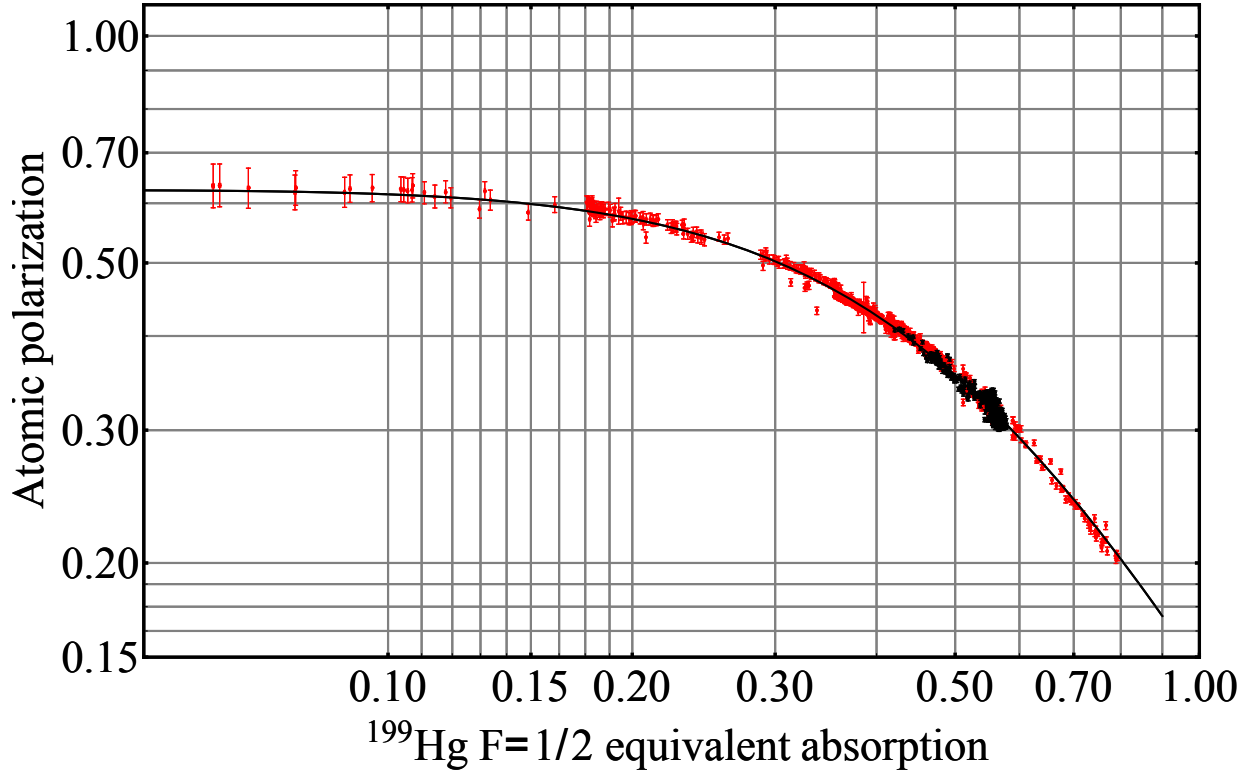


Figure 5.6: The parameters  $DC_{\text{offset}}$ ,  $\alpha$  and  $\beta$  of the extended model can be adjusted in the analysis of the  $^{204}\text{Hg}$  discharge bulb based measurements ( $\blacksquare$ ) such that the extracted atomic polarization shows the same scaling behavior as for the measurements performed with the laser frequency stabilized to the  $^{199}\text{Hg}$   $F = 1/2$  transition ( $\bullet$ ). The black line is the best fit of (5.8) to the measurement result for the laser. The model parameters that minimize the mean squared distance of the corrected lamp detected data set to the interpolation function are  $DC_{\text{offset}} = 5.14$  V,  $\alpha = 2.32$  and  $\beta = 0.67$ .



In summary one can conclude that the extended model provides a coherent analysis frame for the different measurement configurations. Only three well justified parameters in the extended model are needed to explain the differences in the  $^{204}\text{Hg}$  lamp based measurements and the UV laser based measurements.

## 5.4 Signal to Noise comparison

To achieve a high magnetometric sensitivity of the  $^{199}\text{Hg}$  co-magnetometer the signal-to-noise-density-ratio (SNDR) should be as high as possible. In Section 5.2 a five fold increase in signal contrast between the measurement performed with a  $^{204}\text{Hg}$  discharge bulb and the UV laser frequency stabilized to the  $^{199}\text{Hg}$   $F = 1/2$  line is presented. As the noise sources for the two detection light sources can be different one has to determine the SNDR explicitly for the  $^{199}\text{Hg}$  co-magnetometer with the discharge bulb as detection light source (nEDM run 6440) and the UV laser frequency stabilized to the  $^{199}\text{Hg}$   $F = 1/2$  transition (nEDM run 6494).

For the laser measurement the amount of light transmitted through the optical fiber was actively stabilized by regulating the current in the tapered amplifier of the UV laser system as described in Section 3.6. The PSD and the initial amplitude of the FID signal was determined as described in Section 5.1. Measurement cycles with unstable lamp conditions (drifting  $I_1$  level) or not frequency stabilized laser are removed from the analysis sample. The obtained SNDR for the  $^{204}\text{Hg}$  discharge bulb at  $40^\circ\text{C}$  is shown in Figure 5.7 over a time period of 17 h. For the UV laser system the obtained SNDR is shown in Figure 5.8 over a time period of more than 66 h (Friday afternoon till Monday morning). The average SNDR obtained with the UV laser is  $\overline{\text{SNDR}}_{\text{Laser}} = 7860 \pm 1380$  compared to  $\overline{\text{SNDR}}_{\text{Lamp}, 40^\circ\text{C}} = 1410 \pm 110$  achieved with the discharge bulb. Thus the increased signal contrast is directly transferred to the achieved SNDR and the magnetometric sensitivity. Histograms of the obtained SNDR are shown in Figure 5.9 for the lamp and in Figure 5.10 for the laser configuration. The frequency stabilization scheme of the laser failed around midnight on Feb 2 due to a continuous change in ambient air pressure, see Figure 5.11. The influence of the ambient air pressure on the laser system is described in Section 3.5.2. The PID controller for the frequency stabilization reached its pre-set (software) limits of its control output, which was chosen such as to keep the laser close to the resonance during Feb 2. The frequency stabilization scheme was reset per remote control several times during the rest of the week end.

In general the noise situation for the laser can still be improved such that an even higher signal-to-noise ratio can be achieved. The multimode optical fibers that have been used for these test experiments show amplitude noise pickup over the 50 m from the laser laboratory to the nEDM experimental site. Besides additional discrete peaks it was also found that the noise floor of the delivered light was increased well above the level measured in the laboratory for the same detected light power.

As a direct consequence of the results from the laser based measurements the  $^{204}\text{Hg}$  bulb temperature was reduced to  $30^\circ\text{C}$  until the UV laser system will be permanently installed.

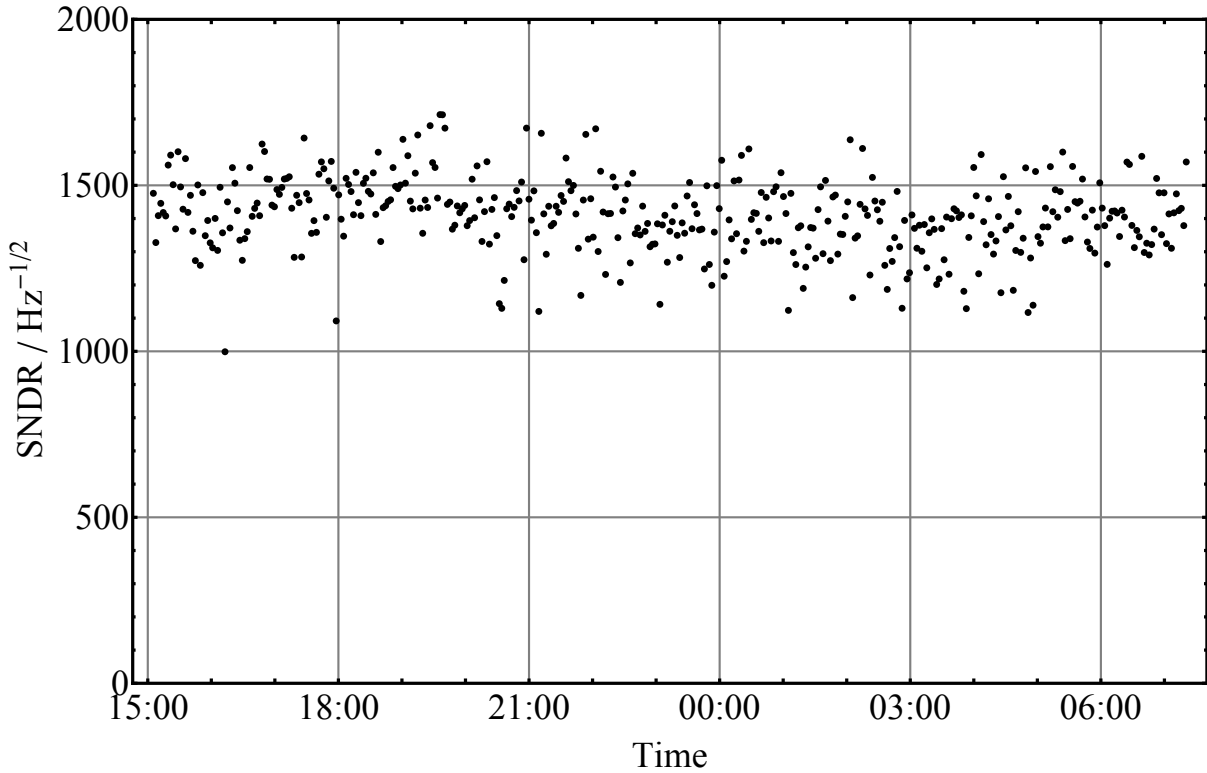


Figure 5.7: The achieved signal-to-noise-density ratio for the  $^{199}\text{Hg}$  magnetometer with a  $^{204}\text{Hg}$  discharge bulb at  $40^\circ\text{C}$  over a period of 17 h.

The signal contrast and the achievable absorption could be increased by more than a factor of two compared to the bulb at  $40^\circ\text{C}$ . This is shown in Figure 5.12. The signal-to-noise density ratio increased accordingly to  $\overline{\text{SNDR}}_{\text{Lamp}, 30^\circ\text{C}} = 3820(180)$  as can be seen in Figure 5.13 where a long term run (nEDM run 7529) around the optimal normalized signal amplitude was analyzed. This provides strong evidence for the hypothesis of the spectral misshaping of the light emitted by the  $^{204}\text{Hg}$  discharge bulbs.

## 5.5 Laser-based $^{199}\text{Hg}$ co-magnetometer sensitivity

The statistical sensitivity of the  $^{199}\text{Hg}$  co-magnetometer is given by

$$\delta B \geq \frac{\sqrt{12}}{\left(\frac{a_s}{\rho}\right) T^{3/2} \gamma_{\text{Hg}}} \sqrt{C} \quad (2.13)$$

Besides the  $\text{SNDR} \left(\frac{a_s}{\rho}\right)$  (the results are presented in Section 5.4) also the correction factor  $\sqrt{C}$  has to be taken into account. The data of nEDM run 6494 (presented in Section 5.4) was recorded at a sampling rate of 100 Hz for a total recording time of 100 s. After the

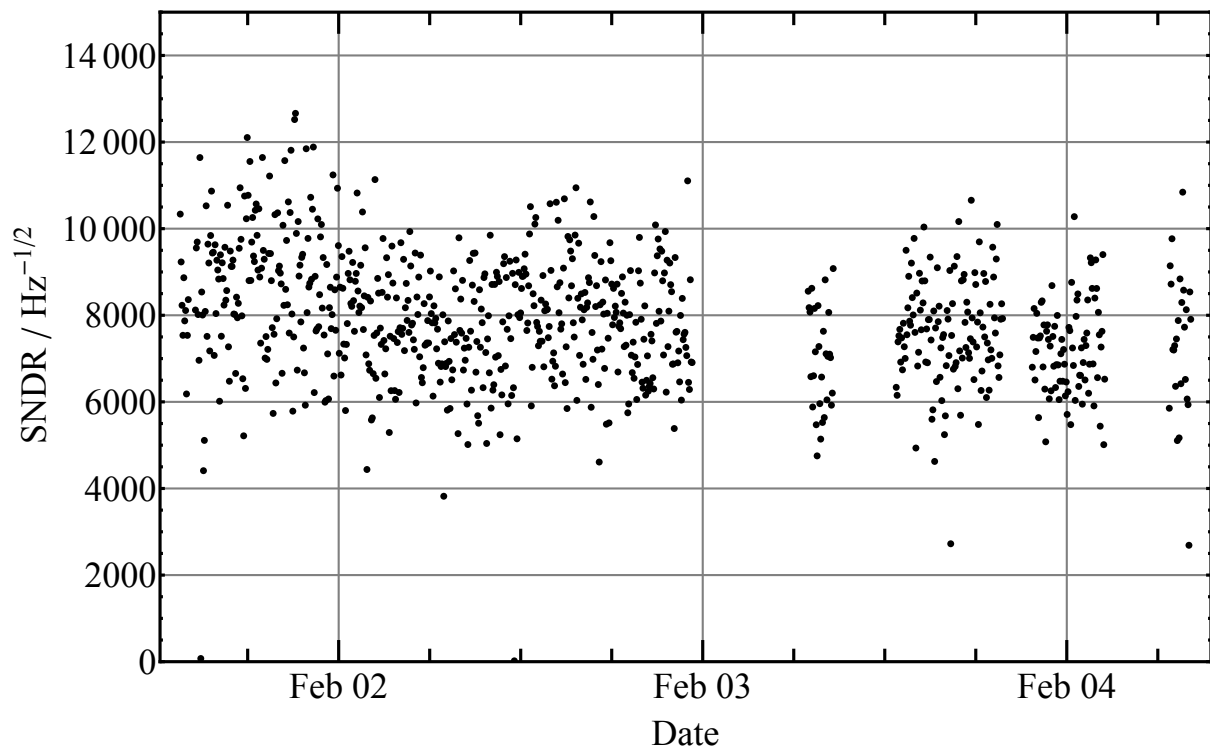


Figure 5.8: The achieved signal-to-noise-density ratio for the  $^{199}\text{Hg}$  magnetometer with the UV laser frequency stabilized to the  $^{199}\text{Hg}$   $F = 1/2$  line over a period of more than 66 h. The frequency stabilization failed several times during the weekend due to a strong weather change. The change in ambient air pressure (by about 30 mbar) caused the laser frequency to be shifted as described in Section 3.5.2 by about 600 MHz. The PID controller for the frequency stabilization reached its pre-set (software) limits of its control output, which was chosen such as to keep the laser close to the resonance during Feb 2. The limits were not removed for the weekend, thus the laser lost its frequency lock several times. The PID controller can easily compensate such large changes with increased output limits. This issue was solved.

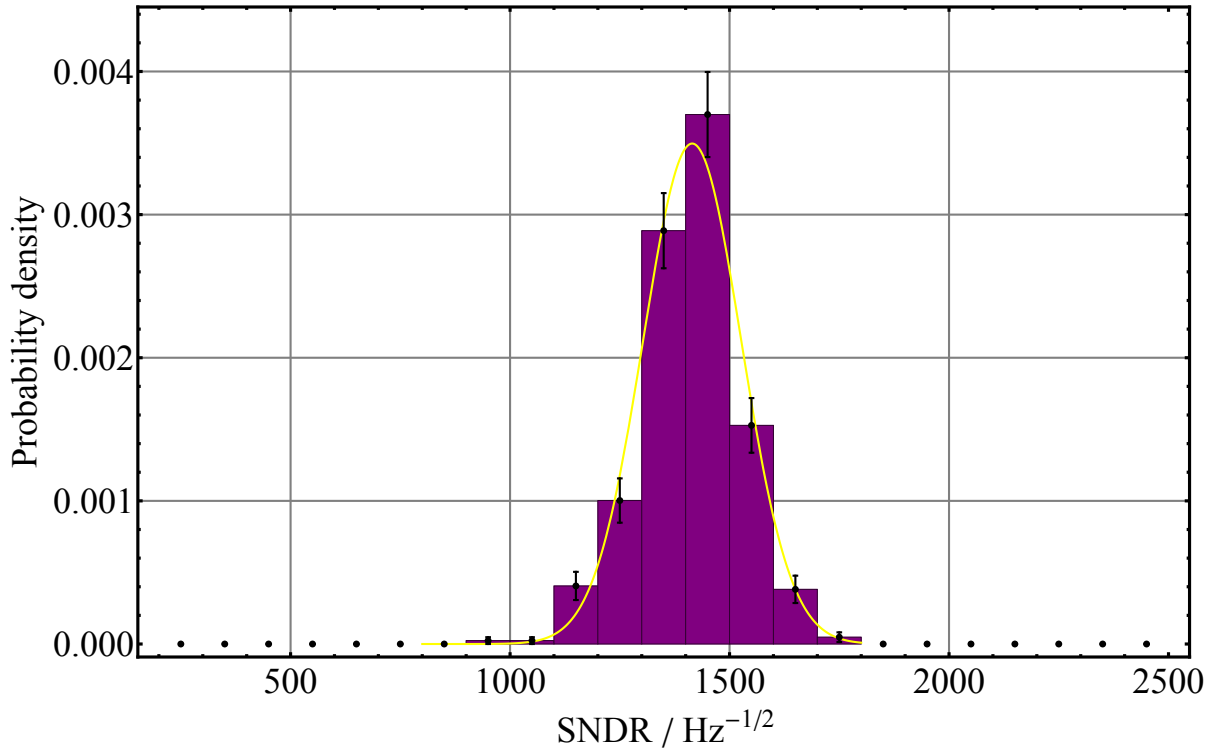


Figure 5.9: Histogram of the probability density of the obtained signal-to-noise-density ratios for the  $^{199}\text{Hg}$  co-magnetometer with the  $^{204}\text{Hg}$  discharge bulb setup (■) at  $40^\circ\text{C}$ . The error bars assume pure counting statistics. A Gaussian function is fitted to the data set (—) to obtain the mean and the width of the distribution. The  $\chi^2/\text{n.d.f} = 1.4$  (6 n.d.f).

signal cuts presented in Section 5.1 a total signal length of  $T = 95.5\text{ s}$  remains. The typical signal decay rate for that run was  $\beta = 1/\tau = 1/102\text{ s} = 0.0098\text{ s}^{-1}$ . For these conditions  $\sqrt{C} = 1.61$ . Evaluating (2.13) results in

$$\delta B_{95.5\text{ s}} \geq 16\text{ fT} \quad (5.9)$$

uncertainty of the magnetic field measurement. Figure 5.14 shows the magnetic field uncertainty that can be obtained as a function of measurement time  $T$ . The result is compared with the case without any signal decay and with the case of a further increase of the SNDR by a factor of two.

For the anticipated measurement time of  $T = 150\text{ s}$  in the nEDM/n2EDM experiment the calculated uncertainty on the magnetic field is

$$\delta B_{150\text{ s}} \geq 10.7\text{ fT} \quad (5.10)$$

This shows that the laser based  $^{199}\text{Hg}$  co-magnetometer satisfies the sensitivity requirements for the next generation experiment n2EDM, as put forward in Section 2.5. As

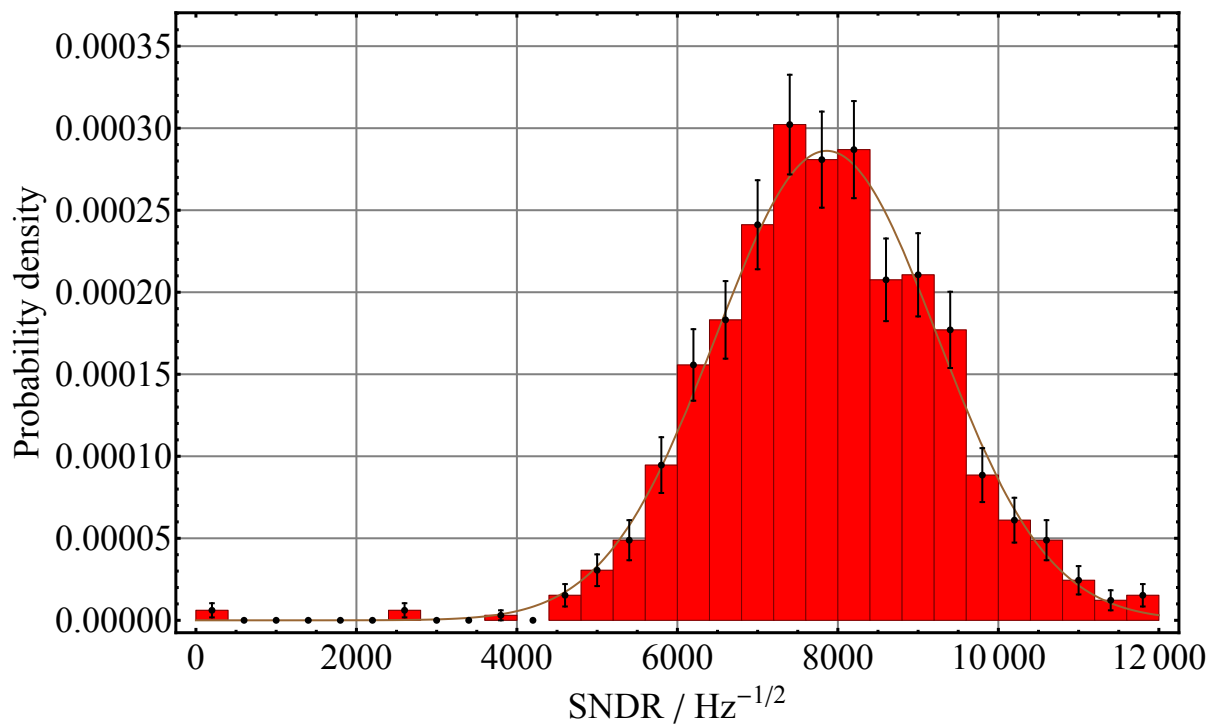


Figure 5.10: Histogram of the probability density of the obtained signal-to-noise-density ratios for the  $^{199}\text{Hg}$  co-magnetometer with the UV laser system (■). The error bars assume pure counting statistics. A Gaussian function is fitted to each data set (—) to obtain the mean and the width of the distribution. The  $\chi^2/\text{n.d.f} = 0.78$  (18 n.d.f).

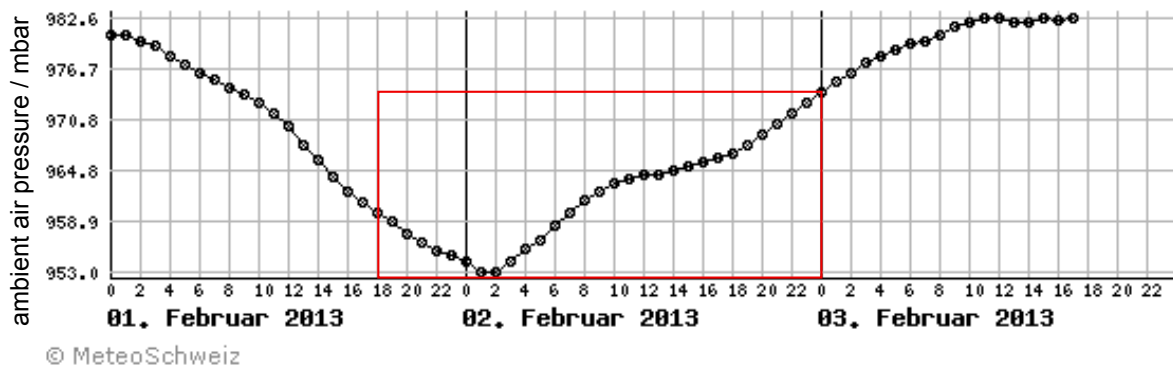


Figure 5.11: Ambient air pressure at PSI for Feb 1 and Feb 2 2013.

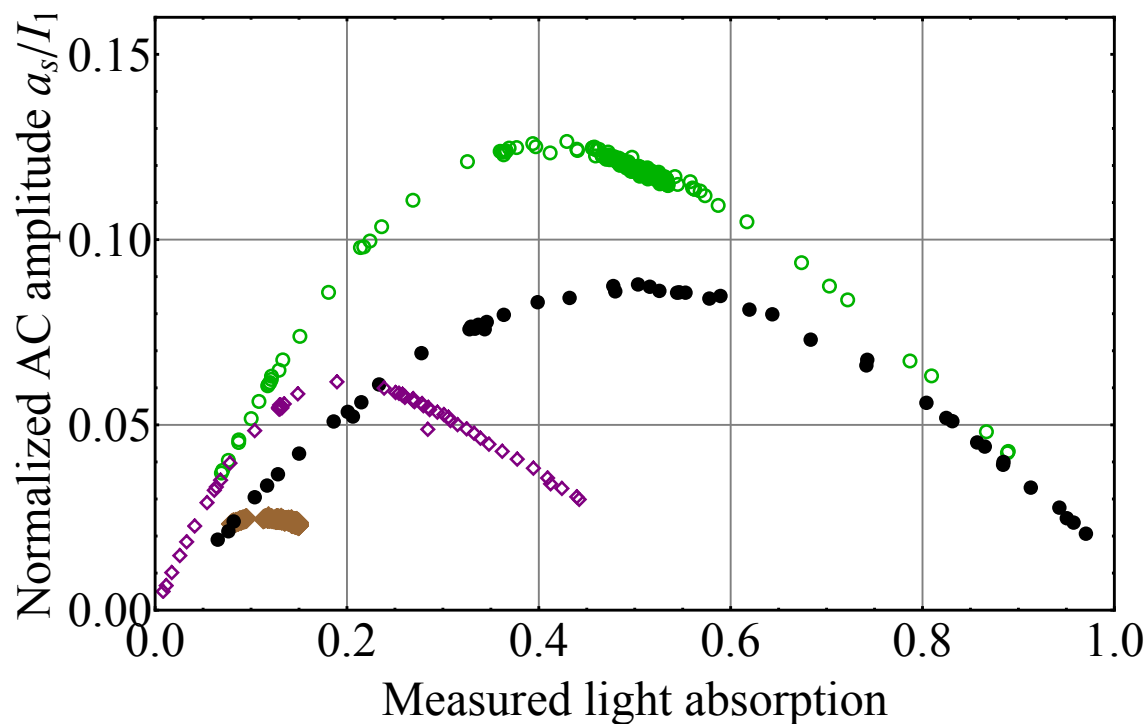


Figure 5.12: Normalized AC signal component for three different readout light configurations as a function of light absorption: UV laser system frequency stabilized to the  $^{199}\text{Hg}$   $F = 1/2$  transition ( $\circ$ ) or the  $^{199}\text{Hg}$   $F = 3/2$  transition ( $\bullet$ ) and the  $^{204}\text{Hg}$  discharge lamp ( $\blacklozenge$ ) temperature stabilized to  $40^\circ\text{C}$ . In addition the results for the  $^{204}\text{Hg}$  discharge lamp ( $\diamond$ ) temperature stabilized to  $30^\circ\text{C}$  are given.

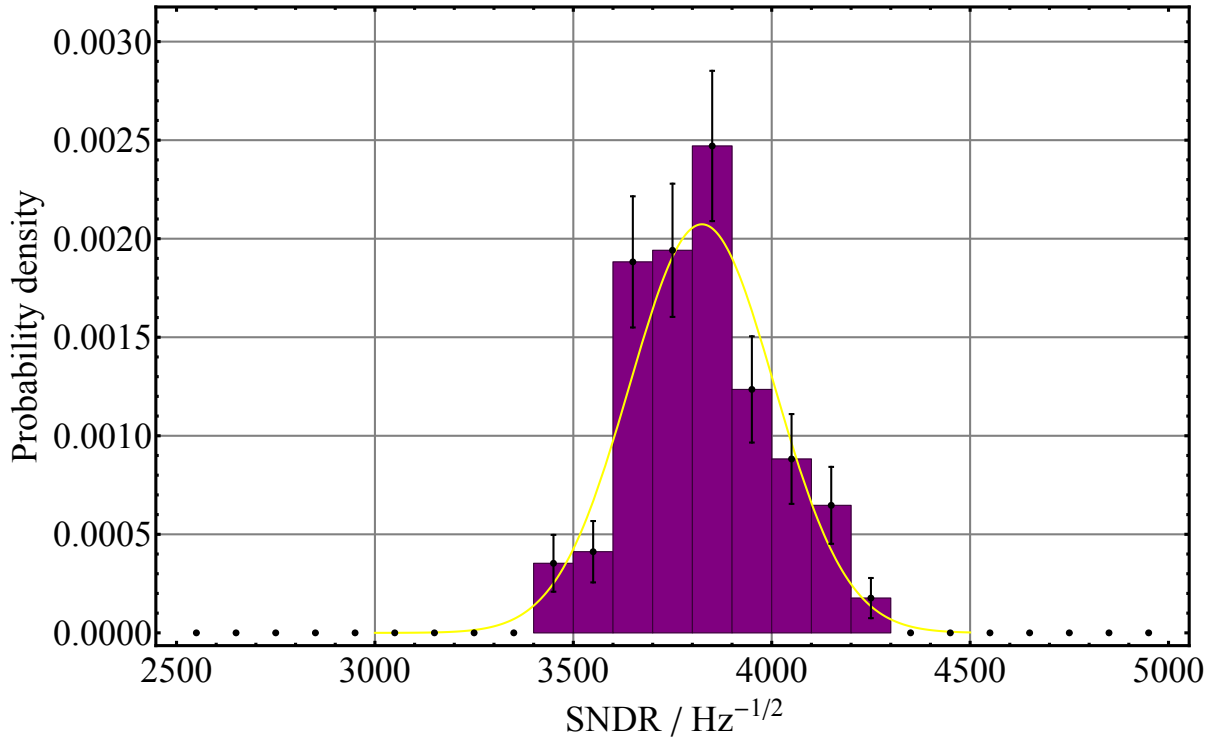


Figure 5.13: Histogram of the probability density of the obtained signal-to-noise-density ratios for the  $^{199}\text{Hg}$  co-magnetometer with the  $^{204}\text{Hg}$  discharge bulb setup (■) at  $30\text{ }^\circ\text{C}$ . The error bars assume pure counting statistics. A Gaussian function is fitted to the data set (—) to obtain the mean and the width of the distribution. The  $\chi^2/\text{n.d.f} = 1.9$  (6 n.d.f).

shown in Subsection 5.7.3 signal decay times of 150 s have been reached in the nEDM precession chamber for light absorption values around 40 %, where the signal contrast is maximized for the  $^{199}\text{Hg}$  co-magnetometer with UV laser light frequency stabilized on the  $^{199}\text{Hg}F = 1/2$  transition.

## 5.6 Optical pumping process of $^{199}\text{Hg}$ atoms in the nEDM setup

As can be seen from Figure 5.4 the atomic polarization  $P$  is not constant over the range of measured light absorption  $A$ . One way to increase the signal contrast of the  $^{199}\text{Hg}$  co-magnetometer is to increase the atomic polarization  $P$ . But in order to obtain a higher atomic polarization  $P$  one has to understand the limits of the optical pumping process in the polarization chamber, e.g., the relaxation mechanisms that take place. In this section the rate equations for the optical pumping process are derived, numerically integrated and compared to the measurement results.

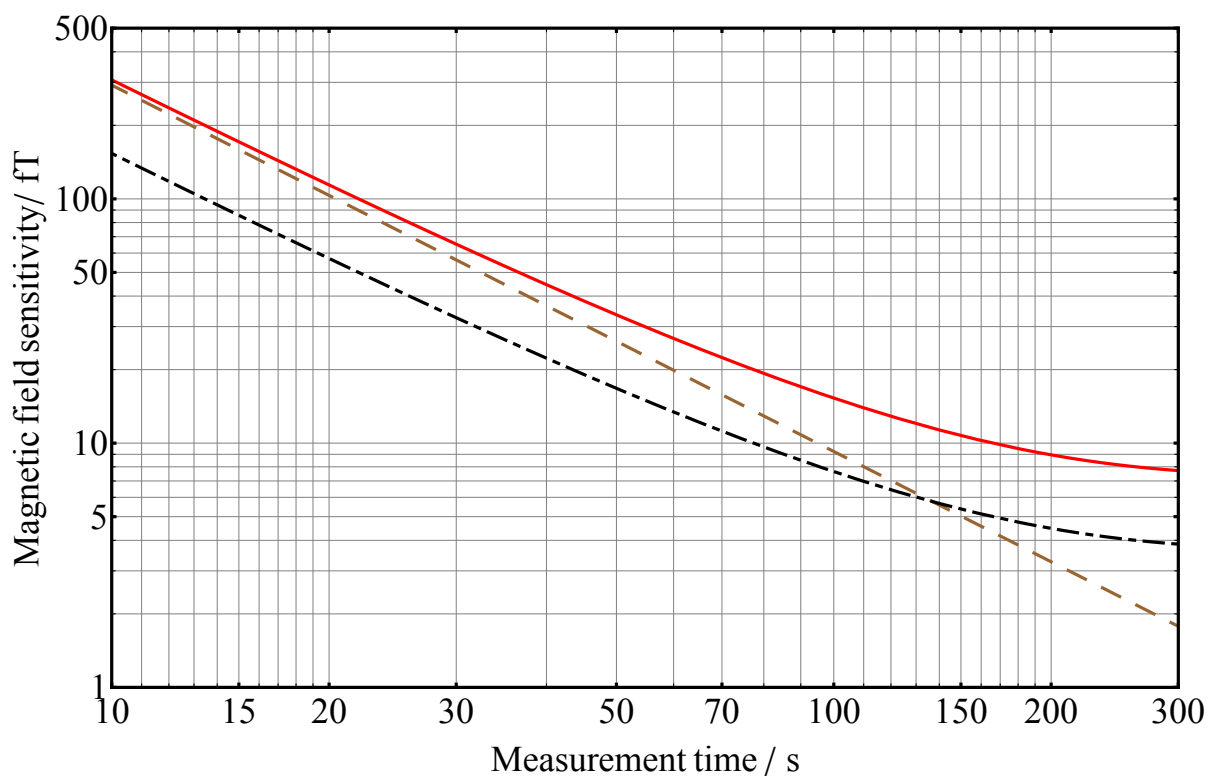


Figure 5.14: The uncertainty of the magnetic field measurement as a function of the total measurement time  $T$ . The laser-baser  $^{199}\text{Hg}$  co-magnetometer performance in January 2013 (—) is shown besides the prediction for an ideal, spin relaxation-free signal (---). The limit is also given for a two times increased SNDR (- - -).



Since the  $^{199}\text{Hg}$  atoms have total angular momentum  $F = 1/2$  in their electronic ground state, defined by the nuclear spin  $I = \frac{1}{2}$ , only spin orientation can occur. Higher order angular momentum distributions like alignment are not possible for these atoms (Wigner-Eckart-Theorem). In the nEDM setup as shown in Figure 2.5 the  $^{199}\text{Hg}$  atoms are spin-polarized in a cylindrical volume called the polarizing chamber below the main UCN precession chamber via optical pumping. Figure 2.8 concentrates on the components relevant for the optical pumping process in a schematic way. The  $^{199}\text{Hg}$  atoms are continuously delivered to the cylindrical polarization chamber ((f), length  $l_{\text{pol}} = 28.7$  cm, inner diameter  $d_{\text{pol}} = 7.3$  cm, overall volume  $V_{\text{pol}} = 1200$  cm<sup>3</sup>, particle mean free path  $\bar{l} = \frac{4V}{S} = \frac{2}{\frac{1}{l_{\text{pol}}} + \sqrt{\frac{\pi l_{\text{pol}}}{V_{\text{pol}}}}} = 6.5$  cm) from the  $^{199}\text{Hg}$  source (a) via a capillary tube. Two types of Hg sources can be used interchangeably in the nEDM experiment. One contains a droplet of liquid mercury that is temperature controlled around room temperature to adjust the vapor pressure above the metal. The second source contains a sample of HgO powder that is typically heated to a temperature of 230 °C to 300 °C to dissociate the HgO into Hg atoms and oxygen. In both cases Hg or HgO that is highly enriched in  $^{199}\text{Hg}$  (up to 91 at-%  $^{199}\text{Hg}$ ) is used. The Hg source is connected to the main vacuum system with a double valve system that allows to disconnect the Hg source, e.g., for refilling, without breaking the main experiment's vacuum.

So far a  $^{204}\text{Hg}$  discharge bulb (b) produces near resonant light that is focused with a lens (c) into the polarization chamber. The light acquires circular polarization by passing through a linear polarizer (d, e.g., a multilayer Brewster plate) and a  $\lambda/4$  plate (e) rotated by 45° to the linear polarizer axis. The circularly polarized light enters through the circular endface window at the bottom of the polarization chamber (which represents nearly the entire area of the light beam  $A_{\text{beam}}$ ) and propagates along the direction of the experiment's main magnetic field. The typical illumination time is the cycle length of a nEDM measurement ( $\approx 100$  s to 350 s). For the further discussion of the optical pumping it is assumed that the light has left circular ( $\sigma^+$ ) polarization and excites the atoms on the  $F = 1/2$  transition as depicted in Figure 3.1. From the level scheme one can see, that only atoms in the  $6^1S_0$ ,  $F = 1/2$ ,  $m_F = -1/2$  state can absorb the  $\sigma^+$  polarized light, the atoms in the  $m_F = +1/2$  form a so-called dark state of the transition. The excited state  $6^3P_1$ ,  $F = 1/2$ ,  $m_F = +1/2$  decays back into the electronic ground states  $m_F = -1/2$  and  $m_F = +1/2$  with a branching ratio of 2:1 given by the Clebsch-Gordan coefficients. Thus one needs on average three excitations of the atom in the  $m_F = -1/2$  electronic ground state to transfer (pump) it to the  $m_F = +1/2$  ground state.

The imbalance in the population of the magnetic sub levels can be expressed as the atomic polarization  $P$  of the atomic vapor

$$P = \frac{\langle N_+ \rangle - \langle N_- \rangle}{\langle N_+ \rangle + \langle N_- \rangle}, \quad (5.11)$$

where  $\langle N_{+,-} \rangle$  is the instantaneous ensemble averaged expectation value of the projection operator for the  $m_F = \pm 1/2$  sub level. For short  $N_{\pm} = \langle N_{+,-} \rangle$  will be used from here on. Spin-relaxation mechanisms (e.g., wall collisions, magnetic field inhomogeneities, ...) in-

duce mixing of the magnetic sub-levels and thus redistribute the atomic population among the sub-levels which reduces the atomic polarization. Without any spin relaxation all  $^{199}\text{Hg}$  atoms will finally end up in the  $m_F = +1/2$  ground state, forming a 100% polarized atomic vapor. The time evolution of the magnetic sub level population in  $^{199}\text{Hg}$  can be modeled by taking into account

- the absorption of circularly polarized light by a partly polarized vapor of  $^{199}\text{Hg}$  atoms,
- a relaxation mechanism between the two magnetic sub levels that takes place at the walls of the polarization chamber,
- and the constant proliferation of unpolarized  $^{199}\text{Hg}$  atoms from the Hg source.

The model for the optical pumping also has to reflect that some processes take place over the whole chamber volume. Optical pumping, which is not a spatially homogenous contribution and spin relaxation due to magnetic field inhomogeneities happen in the whole volume of the polarization chamber. Wall relaxation only takes place at the surfaces but can be taken into account with an ensemble averaged relaxation term, since the atoms travel mostly on undisturbed ballistic trajectories between the chamber walls.

In the cylindrical polarization cell as used in the nEDM setup the time evolution of the  $N_-$  state population due to optical pumping and dilution is given at a time  $t$  and at a distance  $x$  from the entrance window by the following differential equation

$$\frac{dN_-}{dt} = -\frac{1}{3}I_0 e^{-N(t)/V_{\text{pol}}\sigma_{\text{lamp}}(1+\beta-P(t))x} \sigma_{\text{lamp}} (1 - P(t)) N(t) + \frac{\dot{N}}{2}, \quad (5.12)$$

where  $N_-$  is the instantaneous population number of the  $m_F = -1/2$  sub level,  $N(t)$  is the overall number of  $^{199}\text{Hg}$  atoms,  $I_0$  is the local photon flux at the position of the atom,  $\sigma_{\text{lamp}} = 2.8 \times 10^{-13} \text{ cm}^2$  is the unpolarized absorption cross-section as defined in (4.6) for a Doppler-broadened light source (up to spectral modifications) and  $\dot{N}$  is the constant production rate of unpolarized  $^{199}\text{Hg}$  atoms from the  $^{199}\text{Hg}$  source. The factor  $\beta$  takes light absorption by other isotopes into account. Integration over the volume of the polarization chamber (under the assumption of a non divergent homogeneous light beam) results in

$$\left\langle \frac{dN_-(t)}{dt} \right\rangle_V = -\frac{1}{3}\Phi_0 \sigma_{\text{lamp}} (1 - (t)) \frac{N(t)}{V_{\text{pol}}} \int_0^{l_{\text{pol}}} e^{-N(t)/V_{\text{pol}}\sigma(1+\beta-P(t))x} dx + \frac{\dot{N}}{2} \quad (5.13)$$

$$= +\frac{1}{3}\Phi_0 \frac{(1 - P(t))}{(1 + \beta - P(t))} \left[ e^{-N(t)/V_{\text{pol}}\sigma(1+\beta-P(t))l_{\text{pol}}} - 1 \right] + \frac{\dot{N}}{2} \quad (5.14)$$

The differential equation is easier to interpret and to solve if it is entirely given in terms of atomic polarization  $P$  instead of magnetic sublevel population numbers. For a constant dilution with unpolarized  $^{199}\text{Hg}$  atoms it follows from (5.11) that

$$\frac{dP(t)}{dt} = \frac{d}{dt} \frac{N(t) - 2N_-(t)}{N(t)} = -2 \frac{1}{N(t)} \frac{dN_-(t)}{dt} + 2 \frac{N_-(t)}{N^2(t)} \frac{dN(t)}{dt} \quad (5.15)$$

Combining (5.12) and (5.15) one gets

$$\frac{dP(t)}{dt} = -\frac{2}{3}\Phi_0 \frac{1}{N(t)} e^{-N(t)/V_{\text{pol}}\sigma_{\text{lamp}}(1+\beta-P(t))l_{\text{pol}}} - \frac{P(t)}{t} \quad (5.16)$$

The effect of depolarizing wall collisions are taken into account by adding a time independent relaxation rate

$$\left(\frac{dP}{dt}\right)_{\text{wall}} = \Gamma_{\text{R}}P(t) \quad (5.17)$$

To reduce the spin relaxation special coatings, that have a lower depolarization probability per bounce than the wall material (glass or plexiglass) itself, are applied to the walls of the polarization chamber. Typically these coatings are Fomblin oil or paraffins or their fluorinated sibling. Depolarization probabilities as low as  $10^{-6}$  per bounce have been demonstrated recently for rubidium atoms and an alkene based wall coating [BKLB10]. Suitable anti-relaxation coating for the  $^{199}\text{Hg}$  co-magnetometer have been investigated within the nEDM collaboration. The results have been published in Ref. [CFH<sup>+</sup>13]. Details on the measurement setup and the applied techniques are also given in Ref. [Hor12].

Combining (5.16) and (5.17) the rate of change of the atomic polarization during the optical pumping process is given by

$$\frac{dP(t)}{dt} = -\frac{2}{3}\Phi_0 \frac{1}{N(t)} \frac{(1-P(t))}{(1+\beta-P(t))} e^{-N(t)\sigma_{\text{lamp}}(1+\beta-P(t))l_{\text{pol}}} - \frac{P(t)}{t} + \Gamma_{\text{R}}P(t). \quad (5.18)$$

This differential equation can be numerically integrated. The model of the optical pumping in the nEDM experiment is compared with experimental data in Figure 5.15. The atomic polarization  $P$  as a function of the  $^{199}\text{Hg}$   $F = 1/2$  equivalent light absorption  $A$ , which is a measure of the total number of  $^{199}\text{Hg}$  atoms in the polarization chamber at the end of the optical pumping cycle, is given for the measurements performed with the new laser system (configuration B in Section 5.3). The atomic polarization  $P$  was extracted from the recorded data according to the extended signal model presented in Subsection 4.2.2. The data was taken with a constant cycle length (time between two releases of polarized  $^{199}\text{Hg}$  atoms to the precession chamber) of  $t_{\text{laser, light}} = 212\text{ s}$  and the number of  $^{199}\text{Hg}$  atoms was controlled by changing the temperature of the HgO source. Equation (5.18) is integrated numerically using the MATHEMATICA function *NIntegrate* from 0 s to 212 s in steps of 1 s for a constant wall relaxation rate  $\Gamma_{\text{R}} = 0.017\text{ s}^{-1}$ . This value was measured 2 month after the data presented here has been taken, but represents from the experience over the last year a typical value. It is assumed that the polarization chamber contains no mercury at time  $t = 0$ . This is a good approximation as these atoms only present at maximum  $\frac{V_{\text{pol}}}{V_{\text{pol}}+V_{\text{chamber}}} = 5\%$  of the accumulated atoms. To determine the parameters  $\Phi_0$  and  $\beta$  in (5.18) that give the best agreement with the measured data the interpolation function

$$P(A) = \frac{1}{F + B A + C A^2}, \quad (5.19)$$

is first fitted to the atomic polarization values  $P$  extracted in Section 5.3, where  $A$  is the  $^{199}\text{Hg}$   $F=1/2$  equivalent light absorption and  $F, B, C$  are the free parameters of the fit<sup>4</sup>. Subsequently the parameters  $\Phi_0$  and  $\beta$  in (5.18) are adjusted to minimize the sum of squared distances of the modeled data points<sup>5</sup> to the best fit  $P(A)$ . A modification of the absorption cross-section for the  $^{204}\text{Hg}$  lamp light (as discussed in Section 3.3) was not taken into account in this simulation. From (5.16) it can be seen that only the product of photon flux and absorption cross-section dominates the time evolution of the polarization. Thus a spectral modification factor is not a free parameter. It was found that  $\Phi_0 = 4.65 \times 10^{12} \text{ s}^{-1} (3.6 \mu\text{W})$  and  $\beta = 1.11$  reproduce the data best. For these parameters and  $^{199}\text{Hg}$   $F = 1/2$  equivalent light absorption  $A < 0.7$  the simulated data points lie within  $\pm 3\%$  of the interpolation function.

This good agreement is a strong argument that the model takes the most relevant aspects of the optical pumping process in the polarization chamber into account. In Ref. [GHI<sup>+</sup>98] it is claimed that depolarization by re-emitted photons is the limiting factor for the achievable atomic polarization  $P$ . In this process the photons from the electronic de-excitation are emitted in random spatial directions and absorbed by neighboring  $^{199}\text{Hg}$  atoms in the dense  $^{199}\text{Hg}$  vapor. As the angular momentum transfer is not anymore well defined the  $^{199}\text{Hg}$  atoms depolarizes. Our result is in contradiction with this claim. The model described above reproduces the measured data without taking depolarization by re-emitted photons into account. A further argument against depolarization by light as the limiting process of the optical pumping can be derived from the integral instantaneous relaxation rate of  $^{199}\text{Hg}$  atoms just before the injection into the precession chamber. In the nEDM setup a  $^{199}\text{Hg}$   $F = 1/2$  equivalent absorption  $A = 0.4$  corresponds to  $5.7 \times 10^{14}$   $^{199}\text{Hg}$  atoms in the precession (and thus in the polarization) chamber. With a typical relaxation rate of  $\Gamma_R = 0.017 \text{ s}^{-1}$  and atomic polarization  $P = 0.4$  this gives an integral relaxation rate of  $3.9 \times 10^{12} \text{ s}^{-1}$  in the  $^{199}\text{Hg}$  vapor. Knowing that on average 3 photons are needed to transfer a  $^{199}\text{Hg}$  atom from the  $m_F = -1/2$  to the  $m_F = +1/2$  ground state a photon flux of  $1.2 \times 10^{13} \text{ s}^{-1}$  is necessary to counterbalance the spin relaxation. This photon flux corresponds to  $\approx 9.5 \mu\text{W}$  of UV light, which is a reasonable assumption for the photon flux from the bulb. Increasing the photon flux in the model by a factor of six (with otherwise unchanged parameters) predicts an increase of achievable atomic polarization up to  $P \approx 0.8$  even for  $A \approx 0.7$  as shown in Figure 5.16. This prediction has to be verified experimentally. Furthermore a suppression of  $^{204}\text{Hg}$  can increase the achievable  $^{199}\text{Hg}$  polarization by several percent. The light absorption by unpolarizable  $^{204}\text{Hg}$  is suppressed and more photons can be absorbed by  $^{199}\text{Hg}$  and contribute to the optical pumping.

---

<sup>4</sup>The interpolation function is the same as was used to investigate the spectral modification of the light emitted by the  $^{204}\text{Hg}$  bulbs as presented in Section 5.3

<sup>5</sup>The total number of  $^{199}\text{Hg}$  atoms for each modeled point was calculated by varying the  $^{199}\text{Hg}$  production rate according to  $\dot{N} = \dot{N}_0 \exp(\text{const } i)$  with equidistantly spaced values of  $i$ . To take into account the dominance of measurements points for  $A > 17\%$  only every second modeled point below  $A = 17\%$  was used in adjusting the parameters  $\Phi_0$  and  $\beta$ .

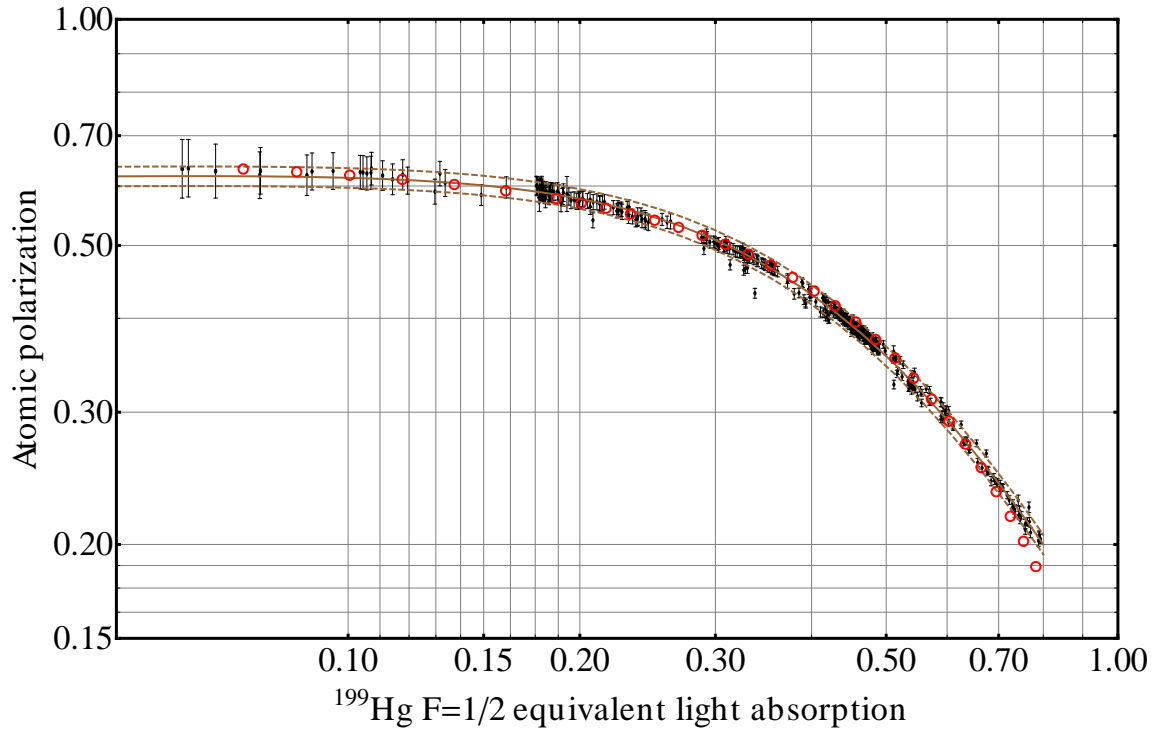


Figure 5.15: Comparison of the model for the optical pumping process in the polarization chamber with experimental data. The signal detection was performed with the laser light locked to the  $^{199}\text{Hg}$   $F = 1/2$  transition. The black points are the atomic polarization values  $P$  as extracted according to the model presented in Subsection 4.2.2. The best fit of (5.19) to the experimental data (—) and the  $\pm 3\%$  interval are shown (---). The results obtained by solving (5.18) with  $\Phi_0 = 4.65 \times 10^{12} \text{ s}^{-1}$  and  $\beta = 1.11$  lie within the  $\pm 3\%$  band for  $A < 0.7$  ( $\circ$ ).

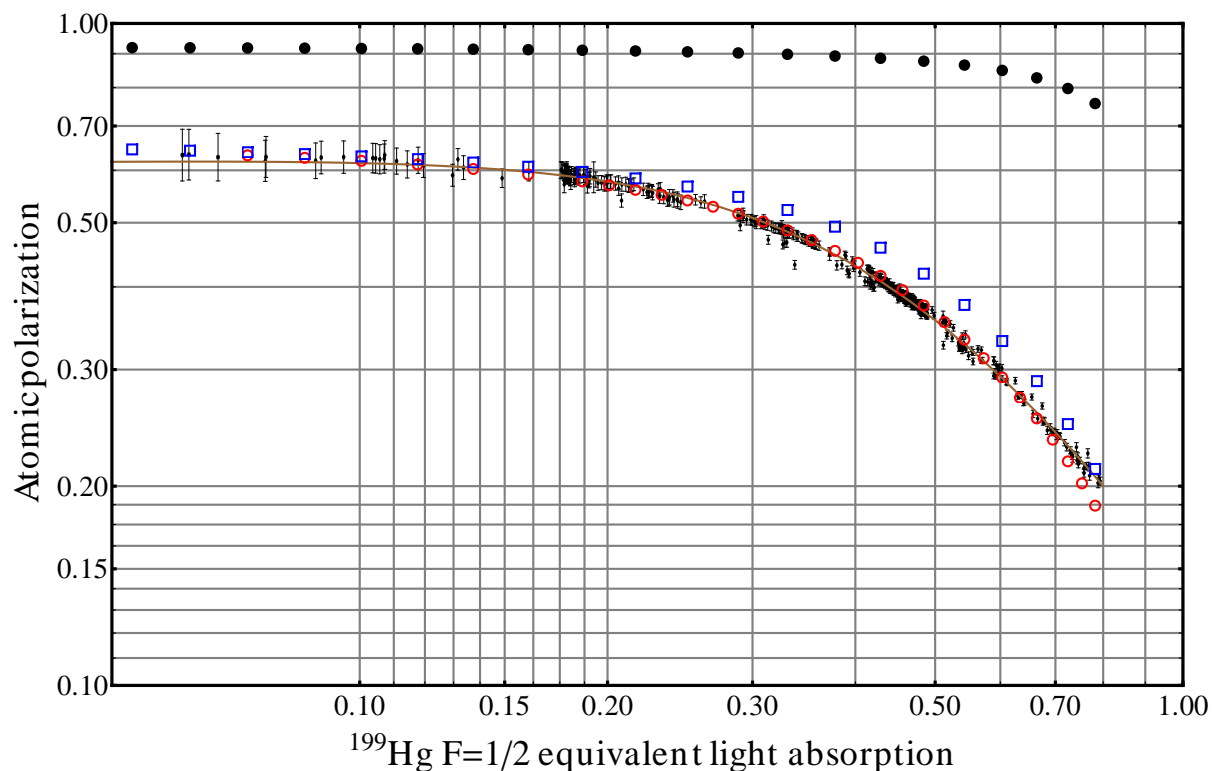


Figure 5.16: A prediction of achievable atomic polarization  $P$  for a different changes in the optical pumping system. The black points are the atomic polarization values  $P$  as extracted according to the model presented in Subsection 4.2.2. The best fit of (5.19) to the experimental data (—) is shown. Increasing the incident light power by a factor of six should result in  $P \approx 0.8$  for  $A \approx 0.7$  ( $\bullet$ ). The suppression of  $^{204}\text{Hg}$  in the  $^{199}\text{Hg}$  vapor can increase the achievable atomic polarization  $P$  by about 10% and the current light level ( $\square$ ).

## 5.7 The depolarization of mercury in the precession chamber

The atomic polarization of the  $^{199}\text{Hg}$  vapor after the application of the  $\frac{\pi}{2}$  pulse decays with a characteristic decay time, the so called transverse spin relaxation time  $\tau$ . This time constant is a combination of the transverse spin relaxation time  $T_2$  and the leakage time of  $^{199}\text{Hg}$  atoms out of the precession chamber  $T_{\text{leak}}$ . Under normal operation conditions of the  $^{199}\text{Hg}$  co-magnetometer  $T_{\text{leak}} \approx 1000$  s and can be neglected. The total observed transverse spin relaxation time is in general a combination of several spin relaxation mechanisms caused by different sources in the system. The individual sources contribute with different relaxation rates to the observed decay time. For an optimal performance of the  $^{199}\text{Hg}$  co-magnetometer the relaxation time should be as long as possible as can be seen from Figure A.2. A detailed understanding of the influence of different system parameters (number of Hg atoms, light flux, ...) can point the direction for performance improvements. Here the important contributions for the spin relaxation rate are separated into three major categories:

$$\frac{1}{T_2} = \frac{1}{T_{\text{mag}}} + \frac{1}{T_{\text{wall}}} + \frac{1}{T_{\text{light}}}, \quad (5.20)$$

where  $\frac{1}{T_{\text{mag}}}$  is the spin relaxation contribution from magnetic field inhomogeneities,  $\frac{1}{T_{\text{wall}}}$  describes depolarization processes that occur during collisions of the atoms with the wall of the precession chamber and  $\frac{1}{T_{\text{light}}}$  takes into account that the  $^{199}\text{Hg}$  atoms are depolarized during the optical detection process. All three relaxation contributions have to be kept small to achieve long spin coherence times on the order of hundreds of seconds.

### 5.7.1 Depolarization in inhomogeneous magnetic fields

In the case of the  $^{199}\text{Hg}$  co-magnetometer the spin relaxation contribution due to magnetic field inhomogeneities  $\mathbf{B}_{\text{inh.}}$  is given by [PR12]

$$\frac{1}{T_{\text{mag}}} = \frac{\Gamma_1}{2} + \int_0^\infty d\tau \langle \omega_z(0)\omega_z(\tau) \rangle, \quad (5.21)$$

where

$$\begin{aligned} \Gamma_1 = & \int_0^\infty d\tau \cos(\omega_0\tau) \langle \omega_x(0)\omega_x(\tau) + \omega_y(0)\omega_y(\tau) \rangle \\ & + \int_0^\infty d\tau \sin(\omega_0\tau) \langle \omega_y(0)\omega_x(\tau) - \omega_x(0)\omega_y(\tau) \rangle, \end{aligned} \quad (5.22)$$

is the the longitudinal spin relaxation rate and  $\langle \rangle$  represents the average over the atomic ensemble. Here  $\mathbf{B}_{\text{inh.}} = \mathbf{B}(\mathbf{r}) - \mathbf{B}_0$  is the local magnetic field inhomogeneity  $\omega = \gamma\mathbf{B}_{\text{inh.}}$  and  $\omega_0 = \gamma\mathbf{B}_0$ . The relaxation rate can be calculated as an auto correlation of the magnetic field inhomogeneities. To reach long spin relaxation times for the UCN as well as the  $^{199}\text{Hg}$

atoms it is necessary to establish a well controlled magnetic field. To avoid large local magnetic field gradients all components of the nEDM experiments that are in the vicinity of the spin polarized species are carefully selected and checked for magnetic impurities. This is done in a gradiometer setup of two Cs magnetometers. Details on the gradiometer setup can be found, e.g., in Ref. [Zen13].

### 5.7.2 Depolarization by light

The depolarization contribution from light absorption,  $T_{\text{light}}$ , is especially important for the absorptive detection of the spin precession as described in Subsection 4.1.1. From the sensitivity point of view it is desirable to have a high detection light level to achieve a low shot noise limit on the light beam (assuming that no technical noise is present). On the other hand the light absorption contributes to the depolarization of the atomic vapor. The excited electronic state has a three orders of magnitude different g-factor than the atomic ground state (see Section 3.2). During the lifetime of the excited state the total angular momentum precesses with the increased Larmor frequency and completely loses its phase relation to the atoms in the ground state. Furthermore the excited state decays statistically. Thus the desired polarization lifetime sets an ultimate limit on the light intensity for the absorptive measurement scheme.

The local depolarization contribution due to light absorption at a time  $t$  at a position  $\mathbf{r}$  in the precession chamber can be calculated in the following way:

$$\frac{1}{T_{\text{light}}(\mathbf{r}, t)} = \frac{1}{h\nu} I(\mathbf{r}, t) \sigma(\mathbf{r}, t), \quad (5.23)$$

where  $I(\mathbf{r}, t)$  is the local, instantaneous light intensity,  $h$  the Planck constant,  $\nu$  the frequency of the incident photons and  $\sigma(\mathbf{r}, t)$  is the instantaneous light absorption cross-section which depends on the polarization of the atom. In contrast to (5.12) where the factor  $\frac{1}{3}$  was introduced to take into account the branching ratio of the excited state, here the factor is 1 since each absorbed photon will leave an unpolarized atom. This atomic state can be described as a 50/50 superposition of the  $m_F = \pm 1/2$  sublevels with a relative phase. But the expectation value the spin projection operator along the main magnetic field direction is 0 and thus the atomic polarization is changed by one unit per absorbed photon.

In the case of the  $^{199}\text{Hg}$  co-magnetometer the cylindrical precession chamber of the nEDM setup is traversed perpendicularly to the cylinder axis by a circularly polarized light beam (see Figure 2.8). The light induced relaxation rate is given by

$$\frac{1}{T_{\text{light}}}(\mathbf{r}, t) = \frac{I_0}{h\nu} e^{-n\sigma_0(1+P_A \sin(\omega_L t))|\mathbf{r}|} \times \sigma_0 (1 + P_A \sin(\omega_L t)), \quad (5.24)$$

where  $I_0$  is the light intensity at the entrance window of the chamber,  $n$  is the density of the mercury atoms,  $\sigma_0$  the unpolarized absorption cross-section,  $P_A$  is the degree of atomic polarization of the ensemble and  $\omega_L$  is the Larmor frequency of the atoms in the given



magnetic field. The overall depolarization by light is given by the volume average over the precession chamber volume (indicated by  $\langle \rangle_{V_{\text{chamber}}}$ ). In case of the precessing  $^{199}\text{Hg}$  atoms one also has to average over one revolution of the Larmor precession.

In a first step the influence of the circularly polarized light beam incident on the  $^{199}\text{Hg}$  vapor (polarized along the magnetic field direction) before the  $\frac{\pi}{2}$  flip is applied will be discussed. In this case the atoms seem to be unpolarized to the circularly polarized beam, there is no time modulation and the light induced longitudinal relaxation contribution  $T_{1,\text{light}}$  is given by

$$\left\langle \frac{1}{T_{1,\text{light}}} \right\rangle_{V_{\text{chamber}}} = \frac{1}{V_{\text{chamber}}} \int \frac{I_0}{h\nu} e^{-n\sigma_0 \mathbf{k} \cdot \mathbf{r}} \times \sigma_0 dV_{\text{chamber}}, \quad (5.25)$$

where  $V_{\text{chamber}}$  is the volume of the precession chamber and  $\mathbf{k}$  the propagation direction of the probe light beam. For a non divergent light beam of area  $A_{\text{beam}}$  (5.24) evaluates to

$$\left\langle \frac{1}{T_{1,\text{light}}} \right\rangle_{V_{\text{chamber}}} = \frac{I_0}{h\nu} \frac{A_{\text{beam}}}{V_{\text{chamber}} n} \left(1 - e^{-n\sigma_0 D_{\text{chamber}}}\right) \quad (5.26)$$

$$= \frac{I_0}{h\nu} \frac{V_{\text{beam}}}{V_{\text{chamber}} D_{\text{chamber}} n} \left(1 - e^{-n\sigma_0 D_{\text{chamber}}}\right). \quad (5.27)$$

The factor in parentheses is giving the absorption  $A$  of the light beam by the atomic vapor and is thus directly measurable by comparing the light levels detected before and after filling the mercury vapor into the precession chamber. From

$$A = \left(1 - e^{-n\sigma_0 D_{\text{chamber}}}\right) \quad (5.28)$$

one can determine the product

$$n\sigma_0 D_{\text{chamber}} = -\log(1 - A). \quad (5.29)$$

Combining Eqn. 5.28 and Eqn. 5.29 in Eqn. 5.27 results in

$$\left\langle \frac{1}{T_{1,\text{light}}} \right\rangle_{V_{\text{chamber}}} = -\frac{I_0}{h\nu} \sigma_0 \frac{V_{\text{beam}}}{V_{\text{chamber}}} \frac{A}{\log(1 - A)} = \quad (5.30)$$

$$= -\frac{P_0}{h\nu} \sigma_0 \frac{1}{\frac{\pi D_{\text{chamber}} H_{\text{chamber}}}{4}} \frac{A}{\log(1 - A)} = \quad (5.31)$$

$$= -\frac{P_0}{h\nu} \sigma_0 \frac{1}{A_{\text{eff}}} \frac{A}{\log(1 - A)}. \quad (5.32)$$

In the nEDM experimental setup

$$\left\langle \frac{1}{T_{1,\text{light}}} \right\rangle_{V_{\text{chamber}}} = P_0 8.6 \times 10^{-4} \text{ s}^{-1} \mu\text{W}^{-1}, \quad (5.33)$$

for  $A = 45\%$ ,  $A_{\text{eff}} = 443 \text{ cm}^2$  on the  $6^1S_0 \rightarrow 6^3P_1$   $F = 1/2$  transition. This limits the maximum light power in(!) the precession chamber to  $\leq 11.6 \mu\text{W}$  for a relaxation time  $T_2 \geq 100 \text{ s}$ , without any other relaxation mechanism present.

For the transverse spin relaxation rate the situation is more complicated. The instantaneous local light intensity acquires a time modulation due to the precessing ensemble of  $^{199}\text{Hg}$  atoms. To calculate the time average of (5.24) the serial expansion of  $\exp(s)$  is used:

$$\frac{1}{T_{2,\text{light}}} = -\frac{I_0}{h\nu} \sigma_0 \frac{1}{nx\sigma_0} \sum_{s=0}^{\infty} \frac{[-n\sigma_0 (1 + P_A \sin(\omega_L t)) x]^{s+1}}{s!}. \quad (5.34)$$

The time average over one full revolution is given by

$$\left\langle \frac{1}{T_{2,\text{light}}} \right\rangle_T = -\frac{I_0}{h\nu} \frac{1}{nx} \frac{1}{2\pi} \int_0^{2\pi} \sum_{s=0}^{\infty} \frac{[-n\sigma_0 (1 + P_A \sin m) x]^{s+1}}{s!} dm = \quad (5.35)$$

$$= -\frac{I_0}{h\nu} \frac{1}{nx} \frac{1}{2} \sum_{s=0}^{\infty} \frac{[-n\sigma_0 x]^{s+1}}{s!} \left[ P_A^2 s {}_2F_1\left(\frac{1-s}{2}, 1 - \frac{s}{2}, 2, P_A^2\right) + 2 {}_2F_1\left(\frac{1-s}{2}, -\frac{s}{2}, 1, P_A^2\right) \right], \quad (5.36)$$

where  ${}_2F_1$  is the hypergeometric function

$${}_2F_1(a, b, c, z) = \sum_{n=0}^{\infty} \frac{(a)_n (b)_n}{(c)_n} \frac{z^n}{n!} \quad \text{with} \quad (5.37)$$

$$(q)_n = \begin{cases} 1 & n = 0 \\ q(q+1) \cdots (q+n-1) & n > 0. \end{cases} \quad \text{for } a, b, c. \quad (5.38)$$

With (5.29) it follows that

$$\left\langle \frac{1}{T_{2,\text{light}}} \right\rangle_T = \frac{I_0}{2h\nu} \sigma_0 \sum_{s=0}^{\infty} \frac{\left[ \frac{\log(1-A)x}{D_{\text{chamber}}} \right]^s}{s!} {}_2F_1\left(-\frac{s}{2}, -\frac{s+1}{2}, 1, P_A^2\right) = \quad (5.39)$$

$$= \frac{I_0}{h\nu} \sigma_0 \sum_{s=0}^{\infty} \frac{\left[ \frac{\log(1-A)x}{D_{\text{chamber}}} \right]^s}{s!} \left[ P_A^2 s {}_2F_1\left(\frac{1-s}{2}, 1 - \frac{s}{2}, 2, P_A^2\right) + \right. \quad (5.40)$$

$$\left. + 2 {}_2F_1\left(\frac{1-s}{2}, -\frac{s}{2}, 1, P_A^2\right) \right]. \quad (5.41)$$

The volume average can be calculated from (5.41)

$$\left\langle \frac{1}{T_{2,\text{light}}} \right\rangle_{V,T} = \frac{1}{V_{\text{chamber}}} \int_{V_{\text{chamber}}} \left\langle \frac{1}{T_{2,\text{light}}} \right\rangle_T dV_{\text{chamber}} = \quad (5.42)$$

$$= \frac{I_0}{2h\nu} \sigma_0 \frac{A_{\text{beam}} D_{\text{chamber}}}{V_{\text{chamber}} \log(1-A)} \sum_{s=0}^{\infty} \frac{\log(1-A)^{s+1}}{(s+1)!} \times \quad (5.43)$$

$$\times \left[ P_A^2 s {}_2F_1\left(\frac{1-s}{2}, 1 - \frac{s}{2}, 2, P_A^2\right) + 2 {}_2F_1\left(\frac{1-s}{2}, -\frac{s}{2}, 1, P_A^2\right) \right] \quad (5.44)$$

For the limiting case that the atomic polarization points perpendicular to the direction of light propagation,  $P_A = 0$ , the first term in (5.44) vanishes. Using

$${}_2F_1\left(\frac{1-s}{2}, -\frac{s}{2}, 1, 0\right) = 1 \quad (5.45)$$

one can see that (5.32) is obtained. The correction factor to (5.32) is between 0 and 1 and thus reduces the depolarization by light effect. This is qualitatively expected. In the coherently precessing ensemble of  $^{199}\text{Hg}$  atoms the absorption cross-section of an atom at position  $\mathbf{r}$  maximizes at a certain time  $t_m$ . But this happens also for all the other atoms in between the atomic position  $\mathbf{r}$  and the entrance window. At the time of maximal absorption cross-section the instantaneous photon flux is lowest, thus the absorption/depolarization rate is reduced. For normally achieved operation parameters (light absorption  $A = 0.45$ , atomic polarization  $P_A = 0.45$ , nEDM geometrical assumptions) (5.44) predicts a small correction for the transverse spin relaxation time

$$\left\langle \frac{1}{T_{2,\text{light}}} \right\rangle_{V_{\text{chamber}}} = 0.97 \left\langle \frac{1}{T_{1,\text{light}}} \right\rangle_{V_{\text{chamber}}} = P_0 8.4 \times 10^{-4} \text{ s}^{-1} \mu\text{W}^{-1}, \quad (5.46)$$

In case  $A = 0.6$  and  $P_A = 0.6$  operation conditions can be realized the correction factor is  $\approx 0.83$ .

From a measurement of the transverse spin relaxation rate as a function of detected light power at otherwise unchanged experimental conditions the photon flux *in* the precession chamber can be determined. Such a measurement is shown in Fig. 5.17. The light was detected with a large area photodiode (Hamamatsu S1337-21 and a FEMTO DLCPA-200 transimpedance amplifier) outside of the vacuum tank. The spectral sensitivity of the mounted photodiode (0.138(1) A W incl. entrance window) was determined relative to a calibrated power meter <sup>6</sup>. Comparing the scaling of the relaxation rate with the detected light intensity and the theoretically predicted scaling of (5.32) one can give a lower limit on the integral light losses at the exit window of the precession chamber and the vacuum tank. The measured relaxation rate dependence on the detected light intensity is  $\Gamma_{2,\text{light}} = 1.02(1) \times 10^{-3} \text{ s}^{-1} \mu\text{W}^{-1}$ . From this value it is found that not more than  $T = \frac{8.4 \times 10^{-4}}{1.02 \times 10^{-3}} = 82\%$  of the light inside the precession chamber is detected on the photodetector. This is a reasonable lower bound as the windows in the vacuum tank and the precession chamber are not anti-reflection coated. The expected transmission reduction due to surface reflection loss are  $0.92^2 = 0.85$ . In this estimate no absorption inside the window material or in the dPE-coating of the window in the precession chamber is taken into account.

### 5.7.3 Depolarization by wall collisions

A further very important contribution to the observed spin relaxation time in the nEDM precession chamber comes from atomic collisions with the walls of the precession chamber.

---

<sup>6</sup>Thorlabs PMD100 with SVC100 sensor head

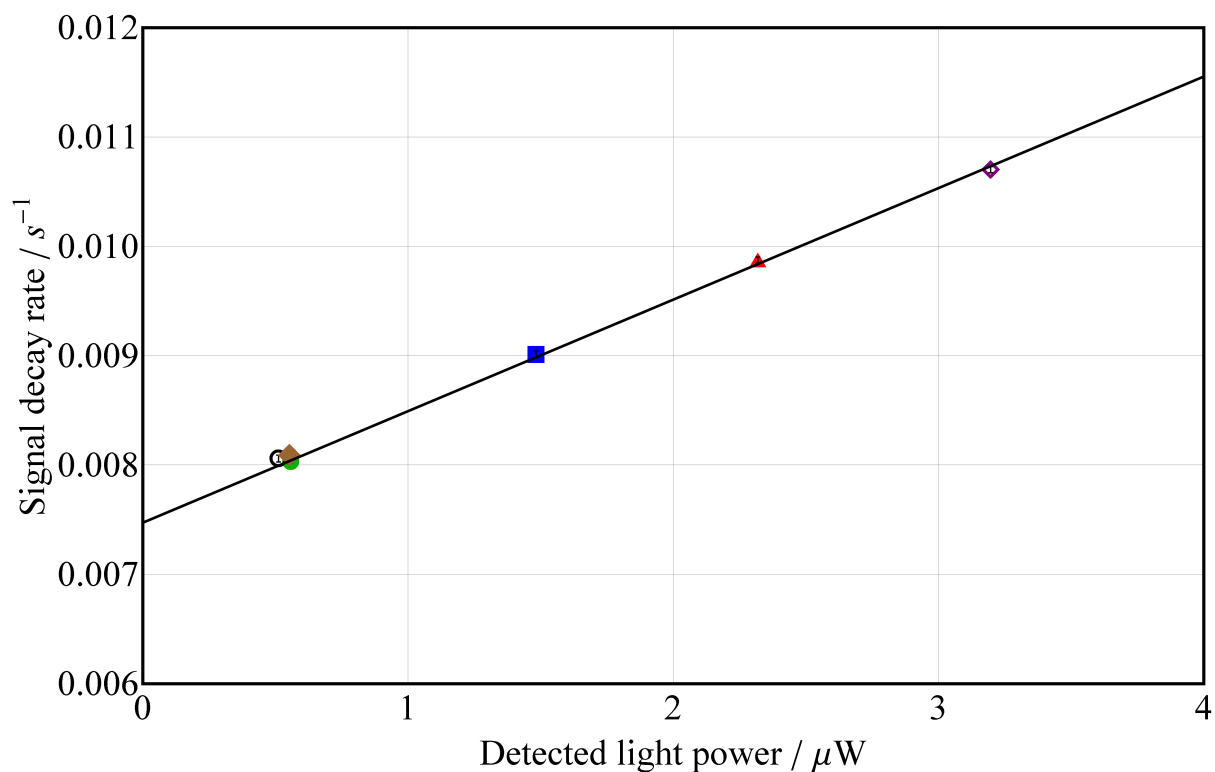


Figure 5.17: The transverse spin relaxation time was measured as a function of detected laser power. A linear model was fitted to the data and a light induced spin relaxation component of  $\Gamma_{2,\text{light}} = 1.02(1) \times 10^{-3} \text{ s}^{-1} \mu\text{W}^{-1}$  was determined. By comparison to the theoretically predicted scaling behavior it is possible to set a lower limit of the light losses between the precession chamber exit window and the photodetector. For details on the detector see the text.

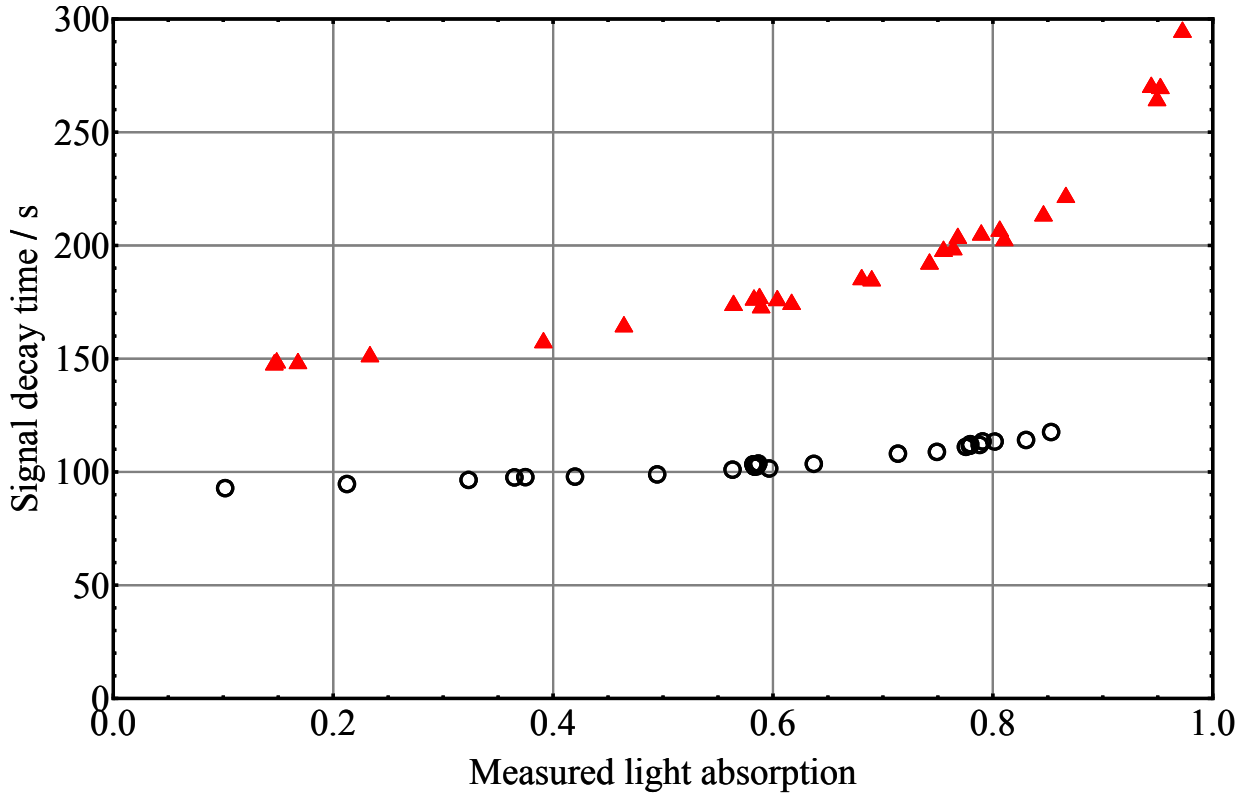


Figure 5.18: An oxygen discharge cleaning is regularly performed to improve the surface of the UCN precession chamber for the operation of the  $^{199}\text{Hg}$  co-magnetometer. Here the transverse spin relaxation time is given for a measurement run just before (run 6505, ○) and after a discharge cleaning (run 6506, ▲).

To improve the surface quality with respect to the spin relaxation time one regularly performs a so-called *discharge cleaning* of the precession chamber with oxygen as process gas [May98]. For this purpose the precession chamber is filled with  $\approx 1$  mbar of oxygen and the high voltage power supply is ramped up to the breakthrough voltage to ignite a plasma discharge. Via a feedback loop the current flowing between the two electrodes is stabilized to  $110\ \mu\text{A}$ . The discharge runs for typically four times 500 s with alternating HV polarity. The beneficial effect of such a discharge cleaning is shown in Figure 5.18. The spin relaxation time is increased from about 100 s to 150 s for low light absorption values. It is experimentally observed that the spin relaxation rate of the  $^{199}\text{Hg}$  atoms decreases with higher light absorption (and thus higher  $^{199}\text{Hg}$  density in the precession chamber). A model to describe this effect is developed in this section and compared to the depolarization by light as discussed in the previous section.

The  $^{199}\text{Hg}$  can be adsorbed at the surface of the precession chamber close to paramagnetic impurities or form short-lived paramagnetic molecules [RL04, BCC<sup>+</sup>13]. The  $^{199}\text{Hg}$  atoms depolarize in the local magnetic field gradient created by the impurity or due to the changed magnetic moment in the bound molecular state. An equilibrium coverage  $\theta$  of the

surface of the precession chamber by  $^{199}\text{Hg}$  atoms can be approximated by the Langmuir formula for constant temperature and low magnetic field

$$\theta = \frac{\alpha p}{1 + \alpha p}, \quad (5.47)$$

where  $p$  is the gas pressure and  $\alpha$  is a constant.  $^{199}\text{Hg}$  atoms adsorbed at the wall are preventing the  $^{199}\text{Hg}$  atoms in the gas volume from getting adsorbed themselves close to depolarizing impurities on the surface. Therefore the wall relaxation constant  $\frac{1}{T_{\text{wall}}} = \Gamma_{\text{R}}$  will be proportional to the unoccupied surface sites

$$\Gamma_{\text{R}} = \Gamma_{\text{R}}^0(1 - \theta(p)) = \Gamma_{\text{R}}^0 \left(1 - \frac{\alpha p}{1 + \alpha p}\right) = \Gamma_{\text{R}}^0 \frac{1}{1 + \alpha p} \quad (5.48)$$

Following the ideal gas law  $pV = Nk_{\text{B}}T$  (5.48) can be rewritten as

$$\Gamma_{\text{R}} = \frac{\Gamma_{\text{R}}^0}{1 + \alpha k_{\text{B}}T \frac{N}{V_{\text{chamber}}}}. \quad (5.49)$$

With (5.29) the wall relaxation constant can be given as a function of the measured light absorption

$$\Gamma_{\text{R}} = \frac{\Gamma_{\text{R}}^0}{1 - \frac{\alpha k_{\text{B}}T}{\sigma_0 D_{\text{chamber}}} \log(1 - A)} \quad (5.50)$$

Defining the parameter  $\alpha^* = \frac{\alpha k_{\text{B}}T}{\sigma_0 D_{\text{chamber}}}$  allows to rewrite (5.50) in the simple form

$$\Gamma_{\text{R}} = \frac{\Gamma_{\text{R}}^0}{1 - \alpha^* \log(1 - A)} \quad (5.51)$$

This shows that alternative to spin precession without probe light (*relaxation in the dark*), the contributions of spin relaxation by surface effects and by light induced depolarization can be separated by their individual scaling behavior as a function of the measured light absorption for a constant probe light intensity. A comparison of the two models (light induced relaxation or wall induced relaxation) is shown in Figure 5.19 for the data presented in Figure 5.18. The weights of each individual measurement point in the nonlinear fit procedure (*NonlinearModelFit* in MATHEMATICA) have been rescaled to achieve a  $\chi^2/n.d.f. = 1$  for the wall induced relaxation model. Subsequently the light induced relaxation model was fitted with the same weights. For the light induced model the  $\chi^2/n.d.f.$  is found to be larger by a factor 1.67 and 2.14. Combining both models has only as small effect on the goodness of fit. Thus one can conclude that the observed dependance of the transverse spin relaxation time on the measured amount of light absorption can be more likely explained by surface induced relaxation than by light induced effects.

These effects can be further investigated by adding Hg isotopes other than  $^{204}\text{Hg}$  or  $^{201}\text{Hg}$  to the  $^{199}\text{Hg}$  source. These isotopes are not detected with the laser, frequency

stabilized to the  $^{199}\text{Hg}$   $F = 1/2$  or  $F = 3/2$  line, since their isotope shift relative to the transition lines in  $^{199}\text{Hg}$  is much larger than the typical Doppler-width (1 GHz). Thus these isotopes do not disturb the magnetometry signal by additional absorption of light, but can maybe suppress wall induced transverse spin relaxation by occupying surface positions close to paramagnetic impurities. These isotopes would present an absorption background in case of the  $^{204}\text{Hg}$  discharge bulb based magnetometer.

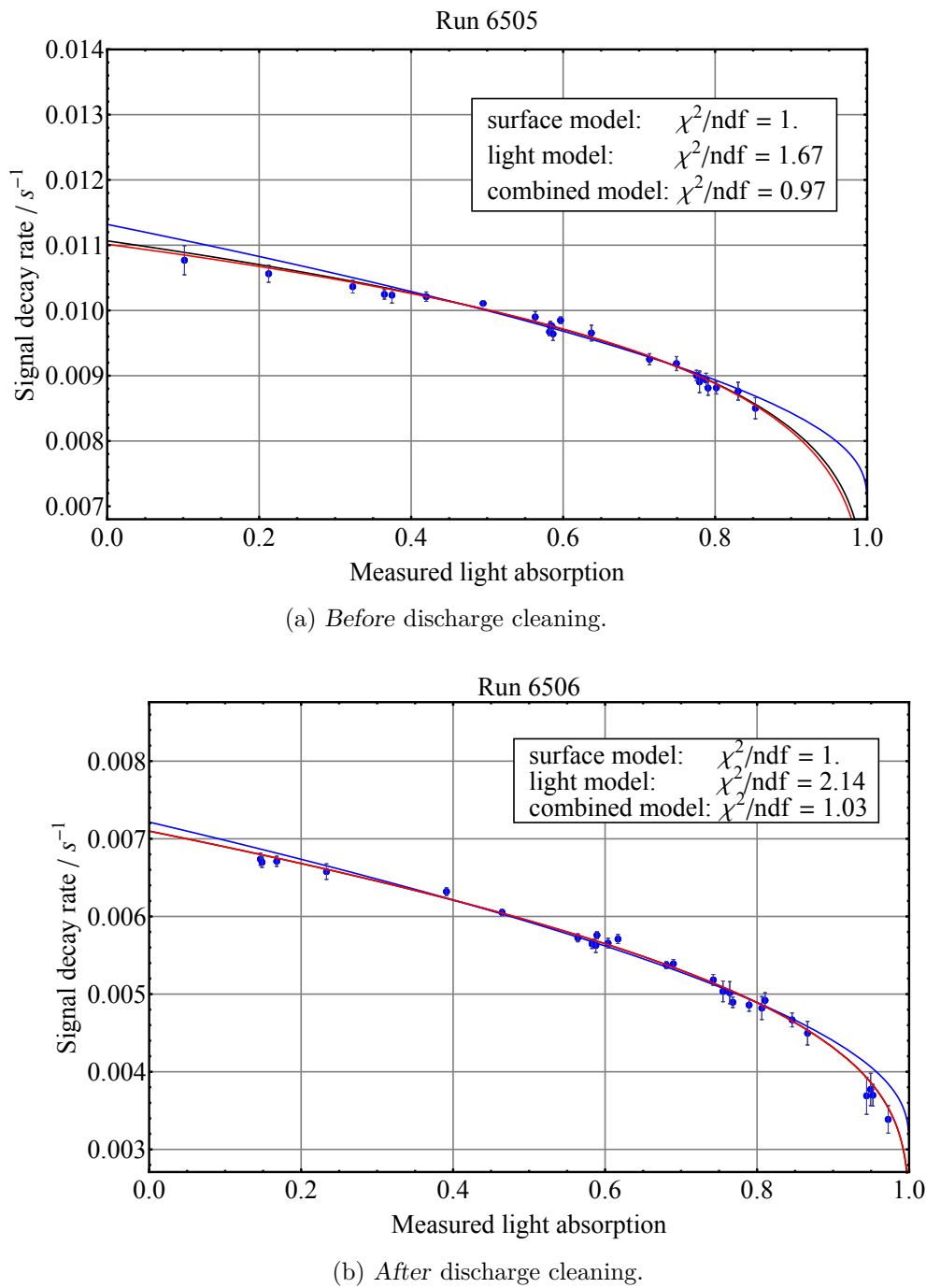


Figure 5.19: Comparison of light or wall induced transverse spin relaxation for the  $^{199}\text{Hg}$  co-magnetometer before and after an oxygen discharge cleaning of the precession chamber. The model of wall induced spin relaxation reproduces the measurement better than the model for light induced spin relaxation. Note the different scale on the y-axis.



# Conclusion and Outlook

Here a summary of the results presented in the previous chapters is provided and propositions for future measurements with the UV laser system are made that have not been possible with the  $^{204}\text{Hg}$  discharge bulbs used so far.

## Chapter 2: The nEDM experiment

A general introduction to the nEDM experiment is given in this chapter. Since the nEDM experiment uses Ramsey's method of separated oscillatory fields to detect a possible shift of the Larmor frequency of neutrons in parallel or anti-parallel configuration of electric and magnetic fields the technique is explained in detail. The use of the  $^{199}\text{Hg}$  co-magnetometer is motivated and its necessary sensitivity to magnetic field changes is derived. To reach the sensitivity goal of the nEDM (n2EDM) experiment it has to be  $\sigma(\delta B) < 100(10)\text{fT}$ . The minimum initial signal-to-noise-density ratio for a free induction decay signal, according to the Cramér-Rao lower bound, is  $\frac{\alpha_s}{\rho} > 840(8400)$  for the (possibly future) conditions of the nEDM (n2EDM) experiment.

## Chapter 3: The components of the $^{199}\text{Hg}$ co-magnetometer

Optically detected nuclear magnetic resonance (ODNMR) is the fundamental principle of the  $^{199}\text{Hg}$  co-magnetometer. The light sources used to spin polarize the  $^{199}\text{Hg}$  atoms and to detect the atomic polarization are presented. The properties of the  $^{204}\text{Hg}$  discharge bulbs used so far are discussed in detail. In particular the influence of the bulb temperature on the emitted light spectrum is discussed and identified as the major point to achieve an improvement of the signal-to-noise-ratio. It was found that the discharge bulbs do not emit a Doppler-broadened light spectrum but suffer from severe self-absorption (line-reversal) effects if operated at temperatures around  $40^\circ\text{C}$ . Furthermore light from other Hg isotopes contributes a constant background of light that cannot be absorbed by  $^{199}\text{Hg}$  atoms. At lower temperatures (with less self-absorption) the light output of the  $^{204}\text{Hg}$  discharge bulbs is limited to several microwatt. In contrast the purchased frequency quadrupled diode laser system (FHG) provides more than 20 mW UV light of narrow-bandwidth without spectral distortion. The laser light is frequency stabilized with a Sub-Doppler Dichroic Atomic Vapor Laser Lock (SD-DAVLL) system. The concept of SD-DAVLL and its advantages are discussed and the experimental setup to generate the SD-DAVLL signal is presented.

It is shown that this setup allows to frequency stabilize the UV laser system to sub-MHz accuracy without further frequency modulation in the UV range.

## Chapter 4: The $^{199}\text{Hg}$ co-magnetometer signal

Chapter 4 discusses the fundamental interaction of a weak light beam with the  $^{199}\text{Hg}$  atoms. The absorption of light, the light shift effect and the paramagnetic rotation are introduced. From the results the necessary frequency accuracy of the light to suppress the so-called vector light shift effect is derived on the one hand. This systematic effect can alter the Larmor precession frequency of the  $^{199}\text{Hg}$  atoms. On the other hand the results are used to develop two new models for the generation of the FID signal by absorption of light in the  $^{199}\text{Hg}$  magnetometer. This has become necessary to predict the correct signal amplitude as the laser-based  $^{199}\text{Hg}$  magnetometer signal does not fulfill the small signal amplitude approximation used so far. The new models also take into account the shortcomings of the  $^{204}\text{Hg}$  discharge bulb, which have been discussed in Chapter 3. Using the old model to extract the atomic polarization from the FID signal amplitude leads to a systematically underestimation of the degree of spin polarization of the  $^{199}\text{Hg}$  vapor. A wrongly determined atomic polarization leads to wrong conclusions about the performance limitations of the  $^{199}\text{Hg}$  co-magnetometer and disguises the way for future improvements.

## Chapter 5: Comparison of $^{199}\text{Hg}$ discharge bulb and UV laser-based $^{199}\text{Hg}$ co-magnetometry

In Chapter 5 the results of Chapter 4 are applied to a direct comparison measurement between the lamp and the laser-based  $^{199}\text{Hg}$  co-magnetometer. The general data analysis procedure for the recorded FID signals is presented. A more than five times larger signal contrast was obtained by use of the UV laser system compared to a  $^{204}\text{Hg}$  discharge bulb under then standard running conditions. This improvement can be explained by the properties of the discharge bulb as discussed in Chapters 3 and 4. It is found that the initial signal-to-noise-density-ratio of the laser-based magnetometer improved accordingly and is high enough to provide the magnetometer sensitivity goals defined in Chapter 2 for the next generation experiment n2EDM. The optical pumping process of the  $^{199}\text{Hg}$  atoms in the polarizer chamber is modeled and found to agree well with the experimental data. As a consequence it turns out that the achievable spin polarization is not limited by light induced depolarization but rather by the light intensity available from the  $^{204}\text{Hg}$  discharge bulbs. Furthermore a comparison between transverse spin relaxation by light absorption and by wall collisions is presented for the  $^{199}\text{Hg}$  atoms in the nEDM precession chamber. The surface relaxation model allows to investigate the sources of transverse spin relaxation. The new laser source allows to add even Hg isotopes (other than  $^{204}\text{Hg}$ ) to the  $^{199}\text{Hg}$  source to investigate possible surface effects without disturbing the generation of the FID signal of  $^{199}\text{Hg}$ .

# Appendix A

## The Cramér Rao lower bound

The Cramér Rao lower bound (CRLB) gives a lower limit on the variance  $\sigma^2$  of a parameter estimator  $\hat{\theta}$  extracted from a data set

$$\sigma^2(\hat{\theta}) \geq \frac{1}{I(\theta)} \quad (\text{A.1})$$

where  $I(\theta)$  is the Fisher information. For  $N$  parameters the Fisher information matrix has dimension  $N \times N$ .

Here the derivation of the CRLB for the frequency estimator of an exponentially damped sinusoidal function, as it is typical for the free induction decay (FID) signal of the Hg co-magnetometer, is discussed. This approach is according to Georg Bison.

The digitized FID signal is assumed to have the following form

$$C(A, \omega, \phi, \tau) = A \cos[\omega(n - n_0) dt + \phi] e^{-\frac{ndt}{\tau}} \quad (\text{A.2})$$

where  $A$  is the amplitude,  $\omega$  the angular frequency,  $\phi$  the phase and  $\tau$  the decay time of the signal. The sampling rate of the signal is given by  $sr = 1/dt$  with  $dt$  the time difference between two sample points. The index of the sample in  $n$ . The total number of samples is  $n_1$ , taken in the total observation time  $T$ . For the sake of mathematical simplicity a second  $\pi/2$  phase shifted signal

$$S(A, \omega, \phi, \tau) = A \sin[\omega(n - n_0) dt + \phi] e^{-\frac{ndt}{\tau}} \quad (\text{A.3})$$

is added with the same parameters as for the cos signal.

The Fisher information matrix has dimension  $4 \times 4$ . The elements of the combined variance matrix are

$$I_{j,k} = \frac{1}{\sigma_A^2} \sum_N \frac{\partial C}{\partial x_j} \frac{\partial C}{\partial x_k} + \frac{\partial S}{\partial x_j} \frac{\partial S}{\partial x_k}, \quad (\text{A.4})$$

where  $\sum_N$  extends over all sample points and  $\sigma_A^2$  is the signal amplitude noise. The matrix elements have been evaluated with MATHEMATICA 9. To achieve statistical

independence ( $I_{\omega,\phi} = 0$ ) between the estimator of the phase  $\phi$  and the angular frequency  $\omega$  the following substitution is made

$$n_0 \rightarrow \frac{-1 + e^{\frac{2dtn_1}{\tau}} + n_1 - e^{\frac{2dt}{\tau}} n_1}{\left(-1 + e^{\frac{2dt}{\tau}}\right) \left(-1 + e^{\frac{2dtn_1}{\tau}}\right)}. \quad (\text{A.5})$$

Then the elements of (A.4) are given by

$$I_{\omega,\omega} = \frac{A^2 dt^2 e^{\frac{2dt}{\tau}} n_1 \left( e^{-\frac{2dt(n_1-1)}{\tau}} + e^{\frac{2dt(n_1+1)}{\tau}} + 2e^{\frac{2dt}{\tau}} (n_1^2 - 1) - e^{\frac{4dt}{\tau}} n_1^2 - n_1^2 \right) \left( \coth\left(\frac{dtn_1}{\tau}\right) - 1 \right)}{2 \left(-1 + e^{\frac{2dt}{\tau}}\right)^3 \sigma_A^2} \quad (\text{A.6})$$

$$I_{A,A} = \frac{e^{-\frac{2dt(n_1-1)}{\tau}} \left(-1 + e^{\frac{2dtn_1}{\tau}}\right) n_1 \left(\coth\left(\frac{dt}{\tau}\right) - 1\right)}{2\sigma_A^2} \quad (\text{A.7})$$

$$I_{\phi,\phi} = \frac{A^2 e^{-\frac{2dt(n_1-1)}{\tau}} \left(-1 + e^{\frac{2dtn_1}{\tau}}\right) n_1 \left(\coth\left(\frac{dt}{\tau}\right) - 1\right)}{2\sigma_A^2} \quad (\text{A.8})$$

$$I_{\tau,\tau} = \frac{A^2 dt^2 e^{-\frac{2dt(n_1-1)}{\tau}} n_1 \left( e^{\frac{2dtn_1}{\tau}} + e^{\frac{2dt(n_1+1)}{\tau}} - e^{\frac{4dt}{\tau}} n_1^2 + e^{\frac{2dt}{\tau}} (2(n_1 - 1)n_1 - 1) - (n_1 - 1)^2 \right)}{\left(-1 + e^{\frac{2dt}{\tau}}\right)^3 \tau^4 \sigma_A^2} \quad (\text{A.9})$$

$$I_{\tau,\omega} = I_{\omega,\tau} = \frac{Adte^{-\frac{2dt(n_1-1)}{\tau}} n_1 \left( -e^{\frac{2dt}{\tau}} n_1 + n_1 + e^{\frac{2dtn_1}{\tau}} - 1 \right)}{\left(-1 + e^{\frac{2dt}{\tau}}\right)^2 \tau^2 \sigma_A^2} \quad (\text{A.10})$$

All other matrix elements are 0. The element of the inverse matrix  $I^{-1}$  related to the angular frequency parameter  $\omega$  is given by

$$I_{\omega,\omega}^{-1} = \frac{2e^{-\frac{2dt}{\tau}} \left(-1 + e^{\frac{2dt}{\tau}}\right)^3 \sigma_A^2}{A^2 dt^2 n_1 \left( -e^{\frac{4dt}{\tau}} n_1^2 - n_1^2 + e^{-\frac{2dt(n_1-1)}{\tau}} + e^{\frac{2dt(n_1+1)}{\tau}} + 2e^{\frac{2dt}{\tau}} (n_1^2 - 1) \right) \left( \coth\left(\frac{dtn_1}{\tau}\right) - 1 \right)} \quad (\text{A.11})$$

For the other elements  $I_{\omega,i}^{-1} = I_{i,\omega}^{-1} = 0$ . For a white amplitude noise spectrum the variance  $\sigma_A^2 = \rho^2 \frac{1}{2dt}$ , where  $\rho$  is the amplitude noise spectral density and  $\frac{1}{2dt}$  the measurement

bandwidth according to the Nyquist theorem. To calculate the variance for only one of the identical but phase shifted input signals one has to take into account

$$\sigma_A^2(1) = 2\sigma_A^2(2) \quad (\text{A.12})$$

where  $\sigma_A^2(1)$  is the amplitude variance of the single signal and  $\sigma_A^2(2)$  is the amplitude variance of the combined signal. Then

$$\sigma^2(\hat{\omega}) = 2I_{\omega,\omega}^{-1} = -\frac{\rho^2 sr^2 \left(e^{\frac{2}{sr\tau}} - 1\right)^3 e^{\frac{srT-4}{sr\tau}} \sinh\left(\frac{T}{\tau}\right)}{A^2 \left(sr^2 T^3 \cosh\left(\frac{2}{sr\tau}\right) - T \left(sr^2 T^2 + \cosh\left(\frac{2T}{\tau}\right) - 1\right)\right)}. \quad (\text{A.13})$$

For a constant signal amplitude ( $\tau \rightarrow \infty$ ) one obtains

$$\sigma^2(\hat{\omega}, \infty) = 2I_{\omega,\omega}^{-1}(\tau \rightarrow \infty) = \frac{12\rho^2 sr^2}{A^2 T (sr^2 T^2 - 1)} \quad (\text{A.14})$$

For a long enough measurement time ( $sr \times T \gg 1$ ) the limit is

$$\sigma^2(\hat{\omega}) = \frac{12\rho^2}{A^2 T^3}, \quad (\text{A.15})$$

which is independent of the sampling rate  $sr$ . This is the usual result for the CRLB for the frequency estimator of a single frequency constant amplitude sine signal. For a finite  $\tau$  one can write

$$\sigma^2(\hat{\omega}, \tau) = C\sigma^2(\hat{\omega}, \infty) \quad (\text{A.16})$$

where  $C > 1$  is a correction factor. In the limiting case of high sampling rate ( $sr \rightarrow \infty$ )  $C$  is given by

$$C = \frac{2T^3}{3\tau \left(-2T^2 + \tau^2 \cosh\left(\frac{2T}{\tau}\right) - \tau^2\right) \left(\coth\left(\frac{T}{\tau}\right) - 1\right)}. \quad (\text{A.17})$$

The dependence of  $C$  on the sampling rate is shown in Figure A.1 for  $T = 150$  s and  $\tau = 30$  s. For  $sr = 100$  Hz as currently used in the nEDM DAQ the approximation has a relative deviation from the exact expression of only  $2 \times 10^{-4}$ . Thus it is justified to apply the limit  $sr \rightarrow \infty$  in our case. Rewriting (A.17) as a function of the dimensionless parameter  $r = \tau/T$  one gets

$$C = \frac{e^{2/r} - 1}{3r^3 \cosh\left(\frac{2}{r}\right) - 3r(r^2 + 2)}. \quad (\text{A.18})$$

The correction factor  $C$  is given as a function of  $r$  in Figure A.2 in the limit  $sr \rightarrow \infty$ .

For the values assumed in Section 2.4 ( $T = 150$  s and  $\tau = 100$  s)  $r = 2/3$  and the correction factor on the frequency estimator error is given by

$$\sqrt{C} = 2.17 \quad (\text{A.19})$$

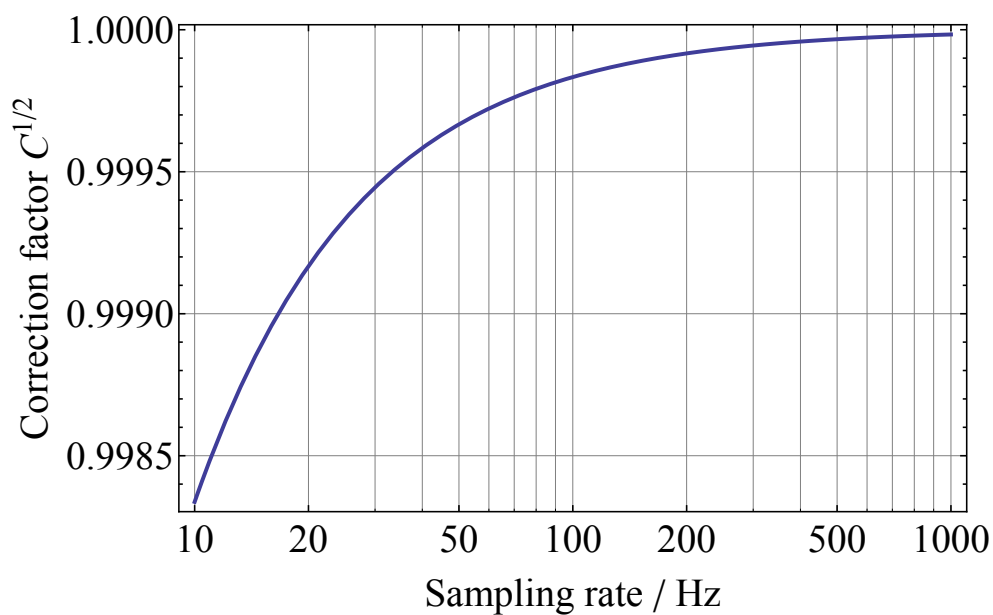


Figure A.1: The correction factor  $C$  as a function of the signal sampling rate. A total measurement time  $T = 150$  s and a signal decay time  $\tau = 100$  s is assumed.

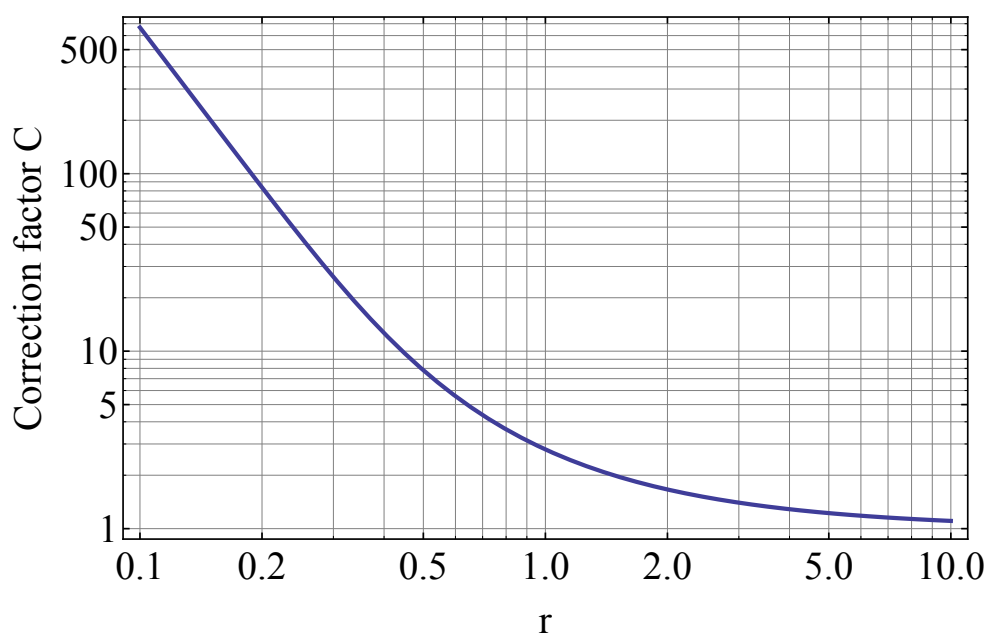


Figure A.2: The correction factor  $C$  as a function of the dimensionless parameter  $r = \tau/T$  in the limit of infinite sampling rate.

# Appendix B

## The isotopes of mercury

The Hg used in the  $^{199}\text{Hg}$  co-magnetometer is enriched in  $^{199}\text{Hg}$  to suppress light absorption by Hg isotopes other than the useful  $^{199}\text{Hg}$  isotope. The isotopic composition of the Hg used during the measurements presented in Chapter 5 is given in Figure B.1. The content of  $\approx 3\%$  of  $^{204}\text{Hg}$  and  $^{201}\text{Hg}$  in this sample presents an unwanted absorption background for both the lamp and the laser readout light. Trace Sciences supplies Hg enriched up to 91% in  $^{199}\text{Hg}$  with sub-percent residuals of  $^{204}\text{Hg}$  and  $^{201}\text{Hg}$ , see Figure B.2. This sample of enriched Hg is used in the  $^{199}\text{Hg}$  co-magnetometer. For the  $^{199}\text{Hg}$   $F = 1/2$  line, the correction factor  $\beta$  as defined in (4.51) is calculated from the absorption cross-section of an isotope at the frequency of the  $^{199}\text{Hg}$   $F = 1/2$  line and its abundance in the sample

$$\beta_{1/2} = \frac{n_{199} \times \sigma_{199}(\nu_{1/2}) + n_{204} \times \sigma_{204}(\nu_{1/2}) + n_{201} \sigma_{201}(\nu_{1/2})}{n_{199} \times \sigma_{199}(\nu_{1/2})}, \quad (\text{B.1})$$

where  $n_X$  is the relative fraction of the isotopes  $X$  in the Hg sample and the Doppler-broadened cross-section  $\sigma$  ( $T = 294\text{ K}$ ) is taken from (4.11). For the Hg sample from euriso-top  $\beta_{1/2} = 1.14$ , for the sample of Trace Sciences  $\beta_{1/2} = 1.03$ . In the analog way one gets for the  $^{199}\text{Hg}$   $F = 3/2$  line for the euriso-top sample  $\beta_{3/2} = 2.02$  and for the Trace Sciences sample  $\beta_{3/2} = 2.005$ .



## ANALYSIS CERTIFICATE

PRODUCT	<input type="text" value="MERCURY 199"/>																									
REFERENCE	<input type="text" value="MHG1990"/>																									
ANALYSIS N°	<input type="text" value="270"/>																									
LOT	<input type="text" value="J1851"/>																									
1 ISOTOPE	<input type="text" value="199Hg"/>	isotope weight <input type="text" value="41,9"/> MG element weight <input type="text" value="50,0"/> MG																								
2 CHEMICAL FORM	<input type="text" value="Hg O"/>	Compound weight <input type="text" value="54,0"/> MG																								
3 ISOTOPIC CONTENT	<input type="text" value="83,80"/> %																									
<table border="1"> <thead> <tr> <th>ISOTOPE</th> <th>196</th> <th>198</th> <th>199</th> <th>200</th> <th>201</th> <th>202</th> <th>204</th> </tr> </thead> <tbody> <tr> <td>Content %</td> <td>1,73</td> <td>1,06</td> <td>83,80</td> <td>2,75</td> <td>3,66</td> <td>3,40</td> <td>3,60</td> </tr> <tr> <td>Relative accuracy %</td> <td>+/-0,05</td> <td>+/-0,05</td> <td>+/-0,20</td> <td>+/-0,05</td> <td>+/-0,05</td> <td>+/-0,05</td> <td>+/-0,05</td> </tr> </tbody> </table>			ISOTOPE	196	198	199	200	201	202	204	Content %	1,73	1,06	83,80	2,75	3,66	3,40	3,60	Relative accuracy %	+/-0,05	+/-0,05	+/-0,20	+/-0,05	+/-0,05	+/-0,05	+/-0,05
ISOTOPE	196	198	199	200	201	202	204																			
Content %	1,73	1,06	83,80	2,75	3,66	3,40	3,60																			
Relative accuracy %	+/-0,05	+/-0,05	+/-0,20	+/-0,05	+/-0,05	+/-0,05	+/-0,05																			
4 CHEMICAL PURITY	<input type="text" value="99,9"/> %																									
5 ANALYTICAL METHOD :	<input type="text" value="ICP - MS"/>																									

RESPONSABLE QUALITE	DATE	VISA
F. ROBERT	10/10/2013	

PARC DES ALGORITHMES - BÂT. HOMÈRE ROUTE DE L'ORME - 91194 SAINT-AUBIN CEDEX - FRANCE - Tél : +33 (0)1 69 41 97 98 - Fax : +33 (0)1 69 41 93 52 - E-mail : eurisotop@eurisotop.com  
S.A.S AU CAPITAL DE 228 000 € - RCS CORBEIL ESSONNES B 380 479 055 - SIRET 380 479 055 00010 - CODE NAF 2014 Z - TVA Intracommunautaire - FR 56 380 479 055

Figure B.1: Isotopic composition of the <sup>199</sup>Hg enriched Hg used for the measurements presented in Chapter 5.



**CERTIFICATE OF ANALYSIS**

209701

Name of Preparation: **<sup>199</sup>Hg**
**TRACE** Trace Sciences International  
 Hg-199 Mercury (HgO oxide)  
 Enriched: 91.09% Lot: 209107
Country of Destination: **Switzerland**Compound weight: 27.0 mg  
Elemental weight: 25.0 mgConsignee: **Paul Scherrer Institut****CHARACTERISTICS OF ISOTOPE-ENRICHED PRODUCT****1. Weight of enriched isotope:**


<b>Compound weight:</b>	<b>27.0 mgs x 4</b>	<b>Elemental weight:</b>	<b>25.0 mgs x 4</b>
<b>Total Compound Mass</b>	<b>108 mgs</b>	<b>Total Elemental Mass</b>	<b>100 mgs</b>
<b>Form: HgO (Oxide)</b>			

**2. Isotopic composition:**

Isotope	196	198	<b>199</b>	200	201	202	204
Enrichment (%)	< 0.5	1.2	<b>91.09</b>	4.22	0.92	1.89	0.68

**3. Chemical Purity: 99.9% pure****4. Analytical method: ICP-MS**

Verified and signed by:

  
 Robyn Carter

Date: January 21, 2013

Please note this material is not approved for use in humans

Figure B.2: Isotopic composition of <sup>199</sup>Hg enriched HgO from Trace Sciences.



# Appendix C

## The DAQ system of the $^{199}\text{Hg}$ co-magnetometer

Here the hardware of the signal processing chain for the  $^{199}\text{Hg}$  co-magnetometry signal is described.

- **Current to voltage conversion:** The photo current signal from a photodiode or photomultiplier tube (PMT) is converted with a FEMTO DLPCA-200 transimpedance amplifier<sup>1</sup>. The amplification gain can be chosen to be  $10^n \text{V/A}$  where  $n = 3-11$ . The bandwidth of the amplifier depends on the choice of gain but is always above 1 kHz and thus of no concern for the  $^{199}\text{Hg}$  co-magnetometer signal. For the PMT<sup>2</sup> in use the maximally allowed anode current is  $10 \mu\text{A}$  and thus a gain of  $10^6 \text{V/A}$  is chosen to match the input range of the DC ADC. Depending on the detected light level the high voltage for the PMT base can be adjusted to make use of the full DC ADC range. For the large area photodiode<sup>3</sup> that was tested, transimpedance gain factors of  $1 \times 10^7 \text{V A}^{-1}$  or  $1 \times 10^8 \text{V A}^{-1}$  have been chosen.
- **Separation of DC and AC signal component:** The output voltage signal from the transimpedance amplifier is fed to an active, second-order, multiple feedback bandpass filter circuit to separate the DC and the AC signal components. The electronic scheme is shown in Figure C.1 and Figure C.2. The DC component is passed through an inverting multiple-feed back low pass filter with a corner frequency of  $160 \text{Hz}$ <sup>4</sup> to adapt the negative input signal from the PMT to the positive input range of the DC ADC. The AC signal component is separated by a double stage second order multiple feedback bandpass filter. Each stage has a measured center frequency of  $f_0 = 7.85 \text{Hz}$ , a measured quality factor of  $Q = 5.06$  and a calculated gain  $G(f_0) = -3$ <sup>5</sup>. The AC filter suppresses the higher order harmonic frequency

---

<sup>1</sup>For a detailed specification see: [www.femto.de](http://www.femto.de)

<sup>2</sup>Hamatsu RS6834

<sup>3</sup>Hamamatsu S1337-21

<sup>4</sup>Calculated from the parts specification in Figure C.1.

<sup>5</sup>Calculated from the parts specification in Figure C.1

components. The suppression of the second harmonic is not below the least significant bit (LSB) of the AC ADC and has to be filtered (or taken into account) in the data processing.

- **Digitization:** The DC component of the  $^{199}\text{Hg}$  magnetometry signal is directed via a multiplexer to a 1:2 voltage divider that adjusts the DC signal level to the input range of the 12-bit ADC (AD7476). The AC component is passed through a further amplifier whose gain can be adjusted by an adjustable voltage divider (potentiometer) to match the signal amplitude to the input range of the 16-bit AC ADC (AD7685).
- **Calibration:** To correctly record the DC and AC signal components the relative gain factor between the DC and the AC signal chain has to be determined. This is done by supplying an AC signal of known amplitude, frequency of 8 Hz and a known (negative) DC offset to the nEDM DAQ PMT input. The amplitude of the recorded sine signal is determined in ADC units by fitting a sinusoidal function. This allows one to calculate the conversion factor between ADC units and voltage. It is of great importance that the calibration procedure is repeated each time the relative AC gain is changed (e.g. due to increased signal amplitude with the laser light). Failure to do so will lead to wrongly extracted characteristic operation parameters, in particular in a mal-determination of atomic polarization, and can cause tedious and time consuming investigations<sup>6</sup>.

---

<sup>6</sup>Warning: It happened

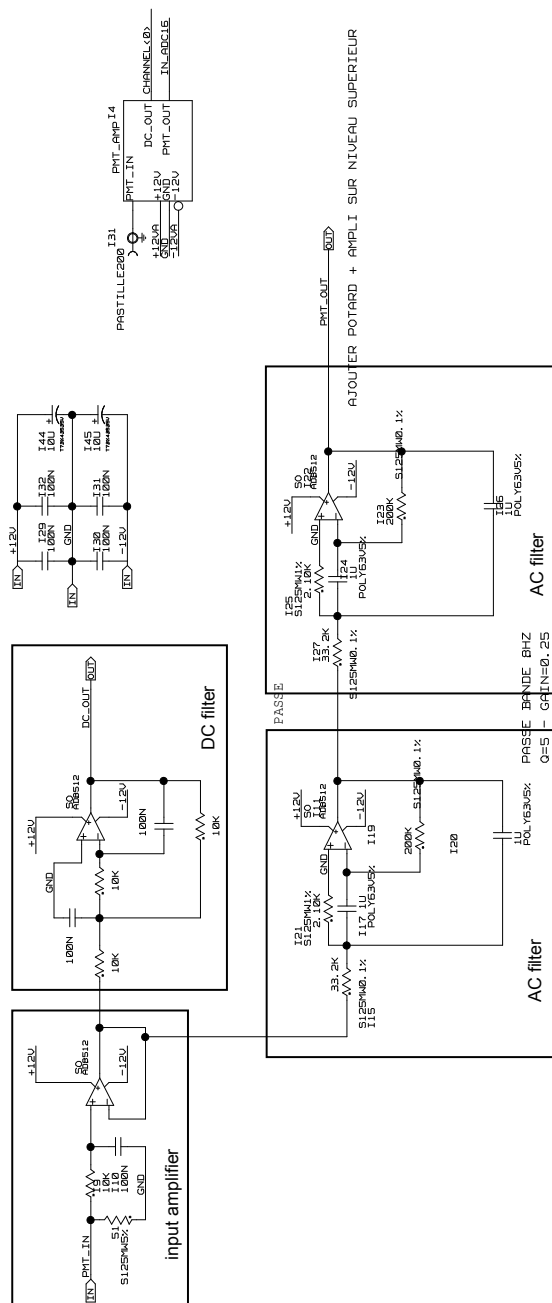


Figure C.1: This multiple feedback bandpass filter is integrated in the nEDM DAQ to separate the DC and AC components of the  $^{199}\text{Hg}$  co-magnetometer signal. The *prefilter*, a transimpedance amplifier, is currently not in use.

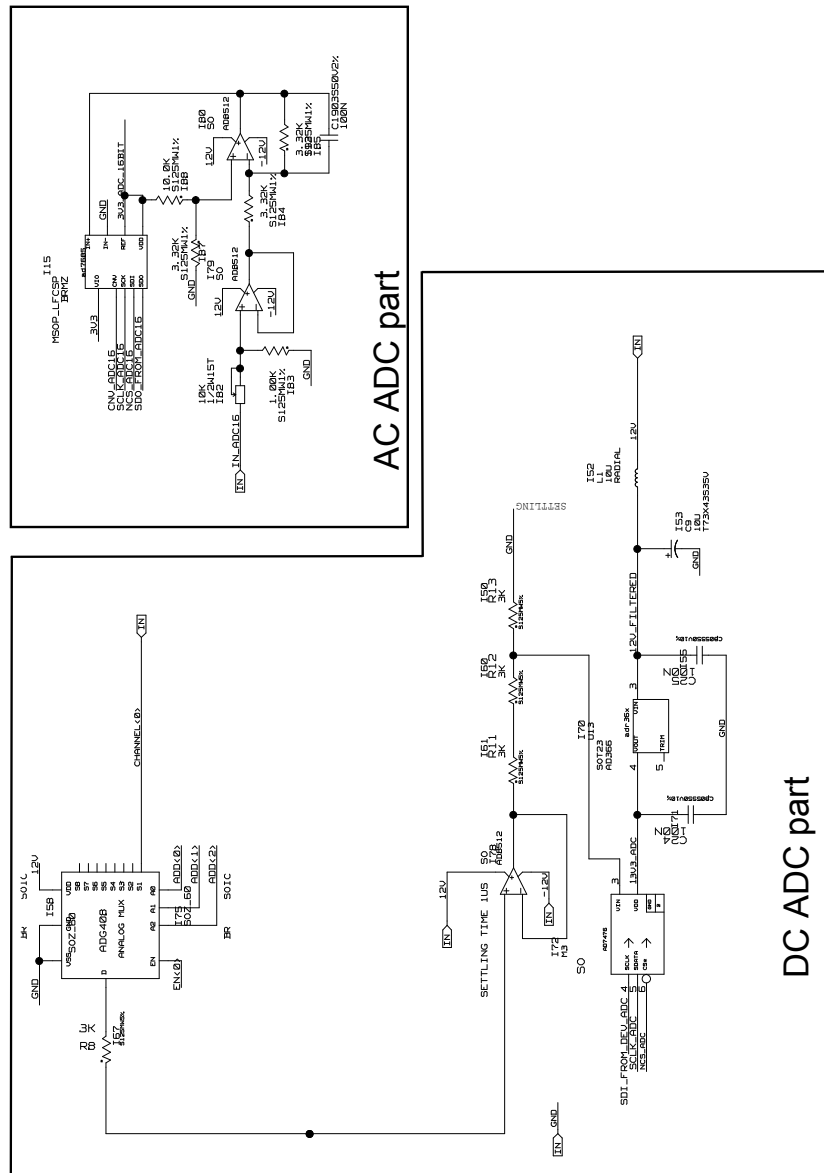


Figure C.2: The DC and AC components of the  $^{199}\text{Hg}$  magnetometer signal are digitized in these two electronic schemes. The adjustable voltage divider with the potentiometer to adjust the AC signal gain is highlighted.

# Appendix D

## The FID signal after a band pass filter

In this appendix the signal amplitude from a FID after an ideal band pass filter (BPF) is derived. It is assumed that only the signal components with frequency  $\omega$  are passed. Any DC and higher harmonics at  $m\omega$ ,  $m \in \mathbb{N}$  are cut by the BPF. Starting from (4.51) and taking the time modulation explicitly into account results in

$$I_2 = (I_1 - DC_{\text{offset}}) e^{-n_{199\text{Hg}}\sigma l(\beta - \frac{P}{\alpha} \cos(\omega t))} + DC_{\text{offset}}. \quad (\text{D.1})$$

The factor  $\alpha$  takes into account that a reduced effective absorption cross-section between the  $^{199}\text{Hg}$  atoms and the light from the  $^{204}\text{Hg}$  discharge lamp will lower the modulation amplitude. The factor  $\beta$  takes into account the additional possibility of light absorption by non- $^{199}\text{Hg}$  atoms. The  $DC_{\text{offset}}$  term takes light into account that cannot be absorbed by the  $^{199}\text{Hg}$  atoms because it is emitted by other isotopes than  $^{204}\text{Hg}$ . Splitting (D.1) in DC and AC signal components allows to expand the modulation term in a Taylor series as a function of the parameter  $n_{199\text{Hg}}\sigma l \frac{P}{\alpha}$

$$I_2 = DC_{\text{offset}} + (I_1 - DC_{\text{offset}}) e^{-n_{199\text{Hg}}\sigma l \beta} \sum_{m=0}^{\infty} \frac{[n_{199\text{Hg}}\sigma l \frac{P}{\alpha}]^m}{m!} \cos^m(\omega t) \quad (\text{D.2})$$

The power series can be split in odd and even powers of  $\cos^m(\omega t)$

$$\sum_{m=0}^{\infty} \frac{[n_{199\text{Hg}}\sigma l \frac{P}{\alpha}]^m}{m!} \cos^m(\omega t) = \quad (\text{D.3})$$

$$= \sum_{m=0}^{\infty} \frac{[n_{199\text{Hg}}\sigma l \frac{P}{\alpha}]^{2m+1}}{(2m+1)!} \cos^{2m+1}(\omega t) + \underbrace{\sum_{m=0}^{\infty} \frac{[n_{199\text{Hg}}\sigma l \frac{P}{\alpha}]^{2m}}{(2m)!} \cos^{2m}(\omega t)}_{\text{suppressed in BPF, see(D.5)}}. \quad (\text{D.4})$$

The powers  $\cos^m$  can be substituted by

$$\cos^m(x) = \begin{cases} \frac{2}{2^m} \sum_{k=0}^{m/2} \binom{m}{k} \cos((m-2k)x) & \text{for even } m \in \mathbb{N} \\ \frac{2}{2^m} \sum_{k=0}^{(m-1)/2} \binom{m}{k} \cos((m-2k)x) & \text{for odd } m \in \mathbb{N} \end{cases} \quad (\text{D.5})$$

From (D.5) it is obvious that only odd  $m$  in (D.4) will contribute to the signal after the BPF. Then (D.4) reads

$$\left( \sum_{m=0}^{\infty} \frac{[n_{199\text{Hg}} \sigma l \frac{P}{\alpha}]^m}{m!} \cos^m(\omega t) \right)_{\text{BPF}} = \quad (\text{D.6})$$

$$= \sum_{m=0}^{\infty} \frac{[n_{199\text{Hg}} \sigma l \frac{P}{\alpha}]^{2m+1}}{(2m+1)!} \frac{2}{2^{2m+1}} \sum_{k=0}^m \binom{2m+1}{k} \cos((2m+1-2k)\omega t). \quad (\text{D.7})$$

Furthermore the BPF will only transmit signal components at the fundamental frequency  $\omega$  thus only the term  $k = m$  in (D.7) can contribute

$$\left( \sum_{m=0}^{\infty} \frac{[n_{199\text{Hg}} \sigma l \frac{P}{\alpha}]^m}{m!} \cos^m(\omega t) \right)_{\text{BPF}} = \quad (\text{D.8})$$

$$= \sum_{m=0}^{\infty} \frac{[n_{199\text{Hg}} \sigma l \frac{P}{\alpha}]^{2m+1}}{(2m+1)!} \frac{1}{2^{2m}} \sum_{k=0}^m \binom{2m+1}{m} \cos(\omega t). \quad (\text{D.9})$$

Making use of the definition of the binomial coefficient

$$\binom{n}{k} = \frac{n!}{(n-k)!k!} \quad (\text{D.10})$$

one can write

$$\left( \sum_{m=0}^{\infty} \frac{[n_{199\text{Hg}} \sigma l \frac{P}{\alpha}]^m}{m!} \cos^m(\omega t) \right) = \sum_{m=0}^{\infty} \frac{[n_{199\text{Hg}} \sigma l \frac{P}{\alpha}]^{2m+1}}{(2m+1)!} \frac{1}{2^{2m}} \frac{(2m+1)!}{m!(m+1)!} \cos(\omega t). \quad (\text{D.11})$$

Using the identity

$$(2m+1)!! = \frac{(2m+1)!}{2^m m!} \quad (\text{D.12})$$

one arrives at <sup>1</sup>

$$\left( \sum_{m=0}^{\infty} \frac{[n_{199\text{Hg}} \sigma l \frac{P}{\alpha}]^m}{m!} \cos^m(\omega t) \right)_{\text{BPF}} = \sum_{m=0}^{\infty} \frac{[n_{199\text{Hg}} \sigma l \frac{P}{\alpha}]^{2m+1}}{(2m+1)!} \frac{(2m+1)!!}{2^m (m+1)!} \cos(\omega t). \quad (\text{D.13})$$

---


$${}^1n!! = \begin{cases} n \cdot (n-2) \cdot (n-4) \cdot \dots \cdot 2 & \text{for } n \text{ even,} \\ n \cdot (n-2) \cdot (n-4) \cdot \dots \cdot 1 & \text{for } n \text{ odd} \end{cases}$$



which is the exact expression in terms of a power series. The AC signal component is thus given by

$$a_s = (I_1 - DC_{\text{offset}}) e^{-n_{199\text{Hg}}\sigma l\beta} \sum_{m=0}^{\infty} \frac{[n_{199\text{Hg}}\sigma l\frac{P}{\alpha}]^{2m+1}}{(2m+1)!} \frac{(2m+1)!!}{2^m(m+1)!}. \quad (\text{D.14})$$

The exponential decay of the atomic polarization can be taken into account which gives

$$a_s = (I_1 - DC_{\text{offset}}) e^{-n_{199\text{Hg}}\sigma l\beta} \sum_{m=0}^{\infty} \frac{[n_{199\text{Hg}}\sigma l\frac{P}{\alpha}e^{-t/\tau}]^{2m+1}}{(2m+1)!} \frac{(2m+1)!!}{2^m(m+1)!}. \quad (\text{D.15})$$

The signal amplitude derived in (4.56) as half the difference of the maximal and minimal light intensity is obtained from (D.14) by replacing the factors  $[(2m+1)!!] / [2^m(m+1)!] \equiv 1$ . This approximation is equivalent to neglecting the fact that harmonic signal sidebands carry more and more power as the nonlinear modulation becomes stronger. There is no analytical way to solve (D.14) for the atomic polarization parameter  $P$  in general. A comparison of the three signal models is shown in Figure D.1 for polarization values of  $P = 1$  and  $P = 0.25$ . For this plot it is assumed that  $DC_{\text{offset}} = 0$ ,  $\alpha = 1$  and  $\beta = 1$ . It is again clear that the three models agree for low light absorption  $A$  and low atomic polarization  $P$ .

From (D.15) it is also seen that the AC signal amplitude is not strictly decaying with one time constant. Higher order terms of the series decay with fractions of the polarization decay time  $\frac{\tau}{2m+1}$ . To quantify this effect an ideal noiseless sine signal is simulated according to (D.15) ( $I_1 = 1$  V,  $DC_{\text{offset}} = 0$  V,  $\alpha = 1$ ,  $\beta = 1$ , up to order 10,  $n_{199\text{Hg}}\sigma lP = 0.64$ ) with polarization decay time  $\tau = 100$  s and a total length of 200 s. Subsequently the modeled data points are subdivided in 20 s long subsets. Each subset is fitted with (D.14) up to  $m = 3$  and a single exponential decay. The extracted signal decay time for each of the subsets is given in Fig.D.2. Clearly the polarization decay time  $\tau$  is underestimated from the single exponential fit. The results agree for long delay times because the higher order corrections become less relevant (or in other words the polarization decays and thus the modulation depth). This effect is experimentally observed in the nEDM setup when the polarization lifetime  $T_1$  in the precession chamber is determined by the *delayed  $\frac{\pi}{2}$  pulse* technique. In this measurement configuration the  $\frac{\pi}{2}$  is delayed after the  $^{199}\text{Hg}$  has been filled into the precession chamber. The polarization lifetime is then extracted from the initial FID amplitude as a function of the delay time.

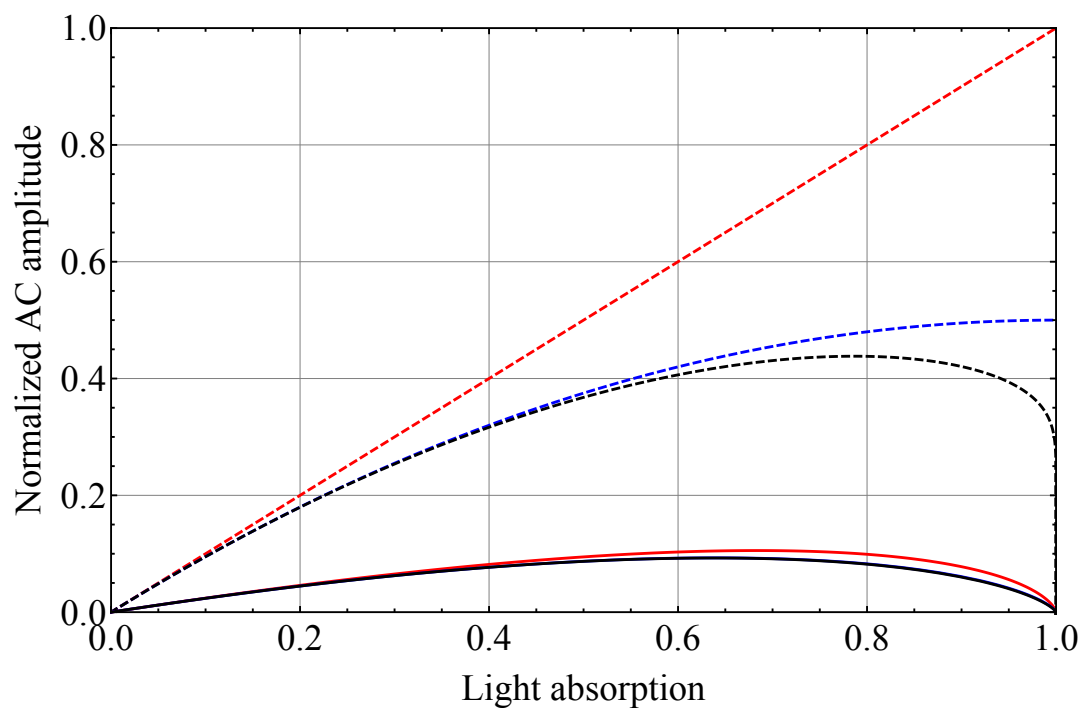


Figure D.1: Comparison of the signal amplitude predicted by the three different models as a function of light absorption. It is assumed that  $DC_{\text{offset}} = 0$ ,  $\alpha = 1$  and  $\beta = 1$ . The small amplitude signal according to (4.49) is given in red. The signal according to the extended model (4.59) is given in blue. The exact signal amplitude from (D.14) is given in black. Two degrees of atomic polarization have been assumed  $P = 1$  (---) and  $P = 0.25$  (—).

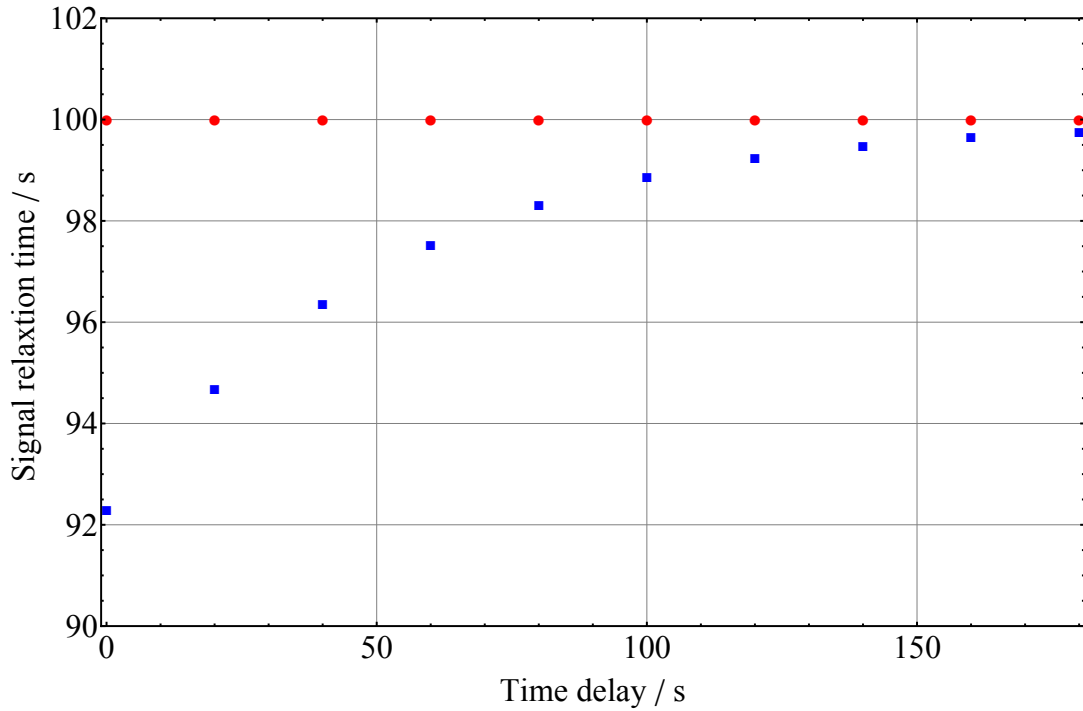


Figure D.2: The extracted decay time  $\tau$  of the FID signal as a function of the delay time after the signal start. An ideal noiseless sine signal is simulated according to (D.15) (details are given in the text). If only one single exponential decay constant is taken into account for the fit, the signal decay time  $\tau$  is underestimating the polarization decay time at the beginning of the signal (■). For longer waiting times the signal decay time converges to the polarization decay time since the contribution at the fundamental frequency that is nonlinearly generated by the third harmonic frequency according to (D.5) has decayed away with  $\tau/3$ . A fit according to (D.14) with  $m \leq 3$  reproduces the assumed polarization decay time of the model for all time delays (●).



# Appendix E

## Production of mercury spectroscopy cells

The quality and long term stability of the SD-DAVLL signals crucially depends on the high quality of the Hg spectroscopy cells. At the beginning commercially available spectroscopy cells<sup>1</sup> (made from SupraSil) of 1 mm or 2 mm optical path length have been used in the SD-DAVLL setup. Versions with Hg of natural isotopic composition or enriched in <sup>199</sup>Hg were purchased. It turned out, that these cells suffer from resonance-light induced deterioration, e.g., the cells turned opaque (dark spot on the inner glass surface) at the position of the UV beam within a time span of hours to a few days, see Figure E.1. Under the microscope no damage of the glass could be found. The effect only occurred for light on resonance with one of the Hg isotopes and the dark spot can be removed by heating the spectroscopy cell to about 100 °C with a hot-air gun. Therefore it seems likely that the excited Hg atoms suffer from a chemical reaction with some rest gas in the cell. The reaction product accumulates at the position of the beam spot and renders the cell opaque. To improve the long term stability of the SD-DAVLL signal (which is extremely important for nEDM runs without intervention) empty cylindrical Spectrosil spectroscopy cells<sup>2</sup> (optical path length ranging from 1 mm to 50 mm) were purchased with the intention to fill these with <sup>199</sup>Hg enriched mercury at sub-vapor pressure at room temperature.

During the first tests it was found that spectroscopy cells with long-term stable properties can be produced by gluing the stem of the spectroscopy cell (length about 60 mm) with Araldite Rapide into a stainless steel flange (6 mm outer diameter, 4 mm inner diameter steel pipe on a KF 16 flange). The intersection part was about 10 mm long. The stainless steel flange was connected to a turbo molecular pump and a HgO source and evacuated to  $\approx 1 \times 10^{-6}$  mbar. At the same time the spectroscopy cell body was put into a temperature controlled oven and heated to 350 °C to remove water from the cell body surface. Due to the poor thermal conductivity the glue joint never reached temperatures above 60 °C. A typical setup with a spectroscopy cell in the oven is shown in Figure E.2. After a day of

---

<sup>1</sup>e-optos

<sup>2</sup>Starna Scientific Ltd, UK or Starna Germany



Figure E.1: A commercial Hg spectroscopy cell with 1 mm optical path length. The dark spot was observed after several hours to few days of exposure to UV resonance light. It turned out to be a opaque layer on the inner surface of the glass could be removed by heating the cell to 100 °C. The cell is shown on its mounting support. A droplet of metallic Hg is visible at the bottom of the cell.

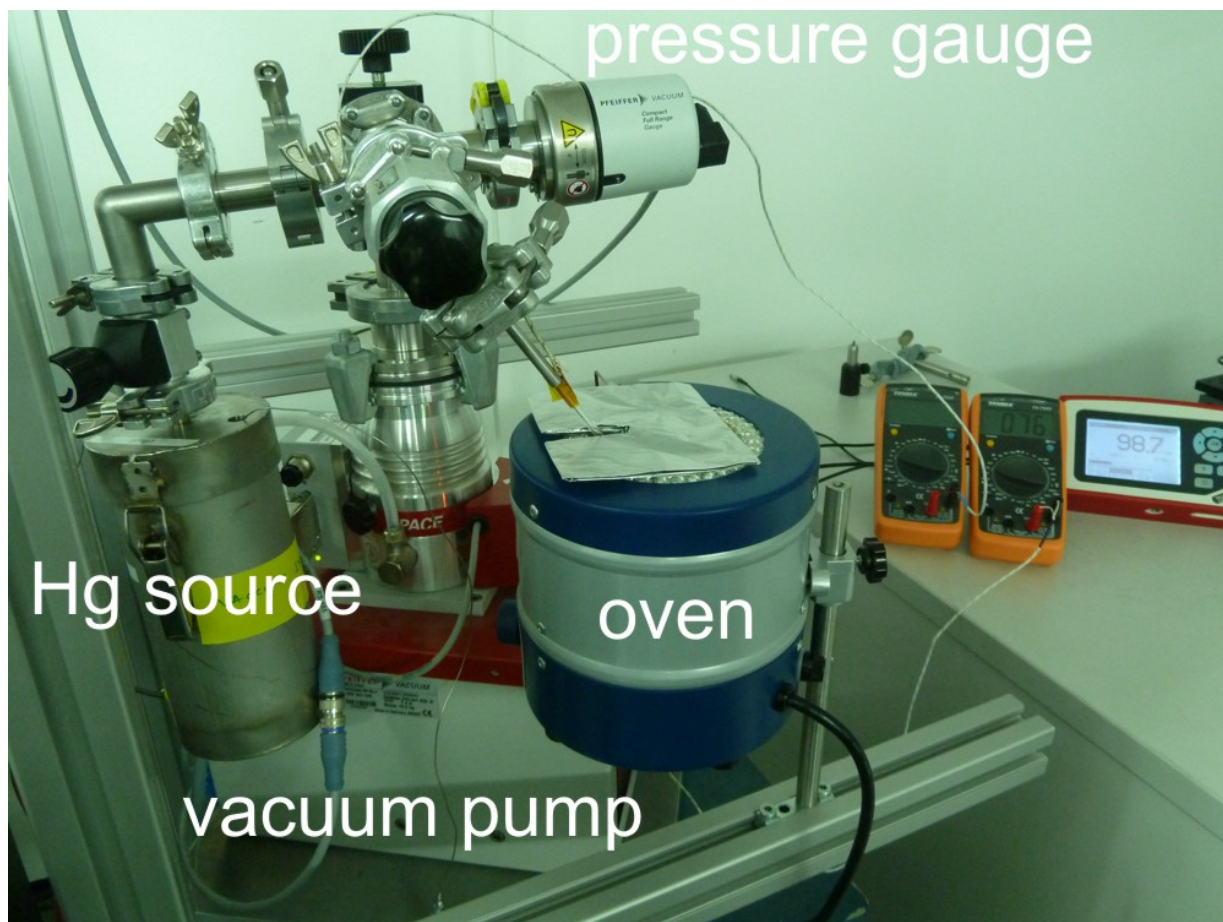


Figure E.2: The setup to bake out the Hg spectroscopy cells. The spectroscopy cell is attached to a turbo molecular vacuum pump and a HgO source. During the baking process the cell is heated in the temperature controlled oven and the pressure is measured with a pressure gauge. The oven can be lowered around the cell such that a UV laser beam can be shine through the spectroscopy cell from the left side of the picture. The temperature of the glue joint was surveyed with PT100 sensors. Note that the multimeter in the picture measure the temperature in  $^{\circ}\text{F}$ .

baking the cell under vacuum, the oven was turned off and the cell cooled down to room temperature. The set-up was installed next to the optical table with the UV laser system such that a UV beam could be steered through the cell and be detected on a power meter. This allowed to survey the amount of Hg inside the cell before sealing it with a propane-oxygen torch by frequency scanning the UV laser over the  $^{199}\text{Hg}$   $F = 1/2$  resonance line and recording the light transmission. This *online* measurement of the Hg content was important as a 5 mm long spectroscopy cell filled with 80%  $^{199}\text{Hg}$  enriched mercury at saturated vapor pressure at 298 K has as transmission of  $\approx 1 \times 10^{-5}$  ( $n_{\text{sat}} = 6.4 \times 10^{13} \text{ cm}^{-3}$ ). The normalized transmission spectrum of a 20 mm long spectroscopy cell filled with  $^{199}\text{Hg}$  enriched Hg is shown in Figure E.3. In general the shorter spectroscopy cells up to 20 mm

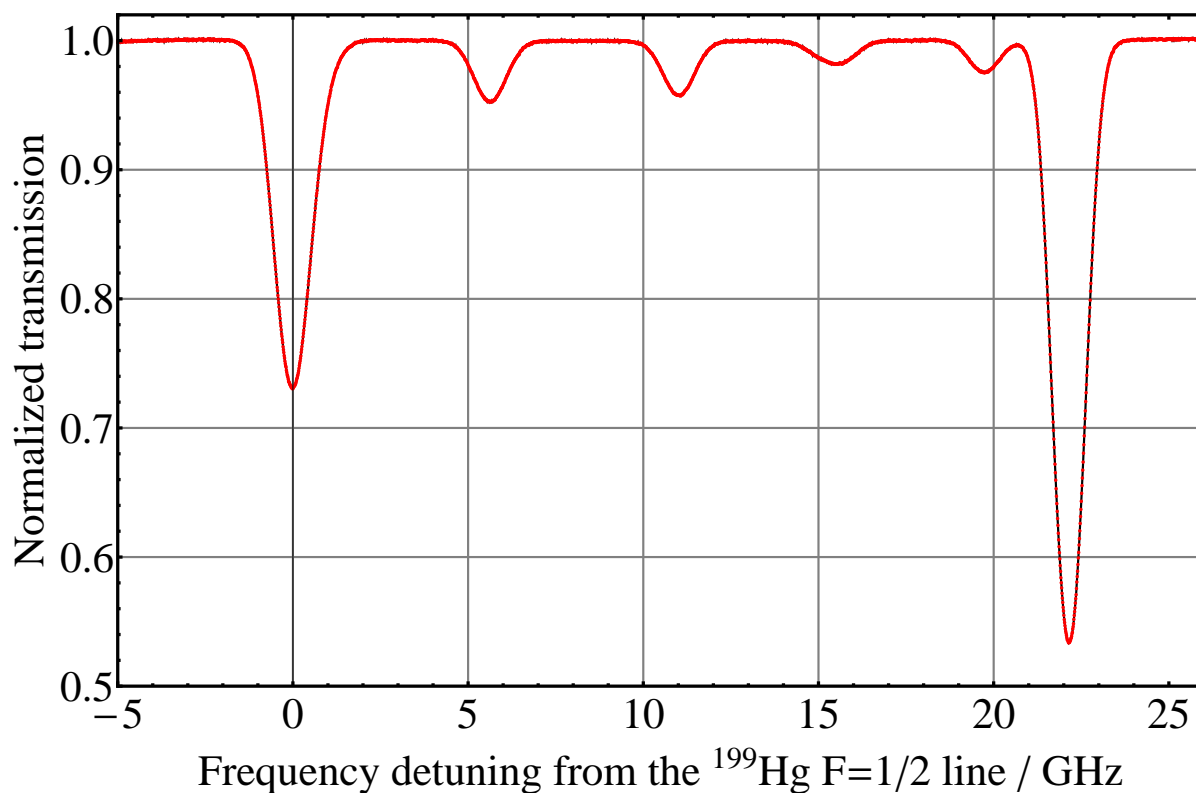


Figure E.3: The normalized transmission spectrum of a 20 mm spectroscopy cell filled with  $^{199}\text{Hg}$  enriched Hg. The mercury source was filled with the batch of isotopic composition given in Fig.B.1. The different isotopes can be identified from Figure 3.2. The transmission lines have been fitted with (3.1). The fit function is shown (—) besides the measurements points (•)



haven been found to be very convenient for the SD-DAVLL setup. The 20 mm long cell performs at the time of writing this for several months without any sign of deterioration.



## Appendix F

# Properties of solarization-resistant UV fibers

To transport the UV laser light from the laboratory to the nEDM experimental site solarization-resistant optical fibers have been used. Here we present the considerations that have been taken into account for the choice of the type of fiber. The transmission losses through an optical fiber increase towards the UV range due to Rayleigh scattering. Rayleigh scattering describes the elastic scattering of light from structures much smaller than the light's wavelength. In optical fibers the scattering centers can be, e.g., refractive index or impurity concentration fluctuations [Lin84]. The scattering cross-section scales like  $\sigma_{\text{scatt}} \propto \lambda^{-4}$ . In low loss telecommunication silica optical fibers the attenuation coefficient due to Rayleigh scattering is  $\approx 0.8 \text{ dB km}^{-1}$  for light with wavelength  $1 \mu\text{m}$  [ZGSS03]. This results in a lower estimate of the attenuation coefficient  $> 200 \text{ dB km}^{-1}$  for  $250 \text{ nm}$  light. The attenuation coefficient from the technical specifications [Tho] of the optical fibers used in this work (Thorlabs UM22 “Step Index Multimode Fiber: 0.22 NA”,  $200 \mu\text{m}$  and  $400 \mu\text{m}$  core diameter) is given in Figure F.1. The attenuation coefficient at  $250 \text{ nm}$  is  $\approx 250 \text{ dB km}^{-1}$ , in good agreement with the estimate. For a  $50 \text{ m}$  optical fiber the transmission (not taking coupling losses into account) is expected to be  $-12.5 \text{ dB}$  or  $5.6\%$ . Although the fibers are called *solarization-resistant* the transmission through the fibers drops after operation of some weeks. In this study several mW of UV light have been focused on the fiber end to compensate the high transmission losses. It is expected that light induced degradation of the fibers will be at a much smaller level in case the optical setup is brought closer to the nEDM setup. As the damping is exponential with fiber length shorter fibers will allow for highly reduced intensity at the fiber input.

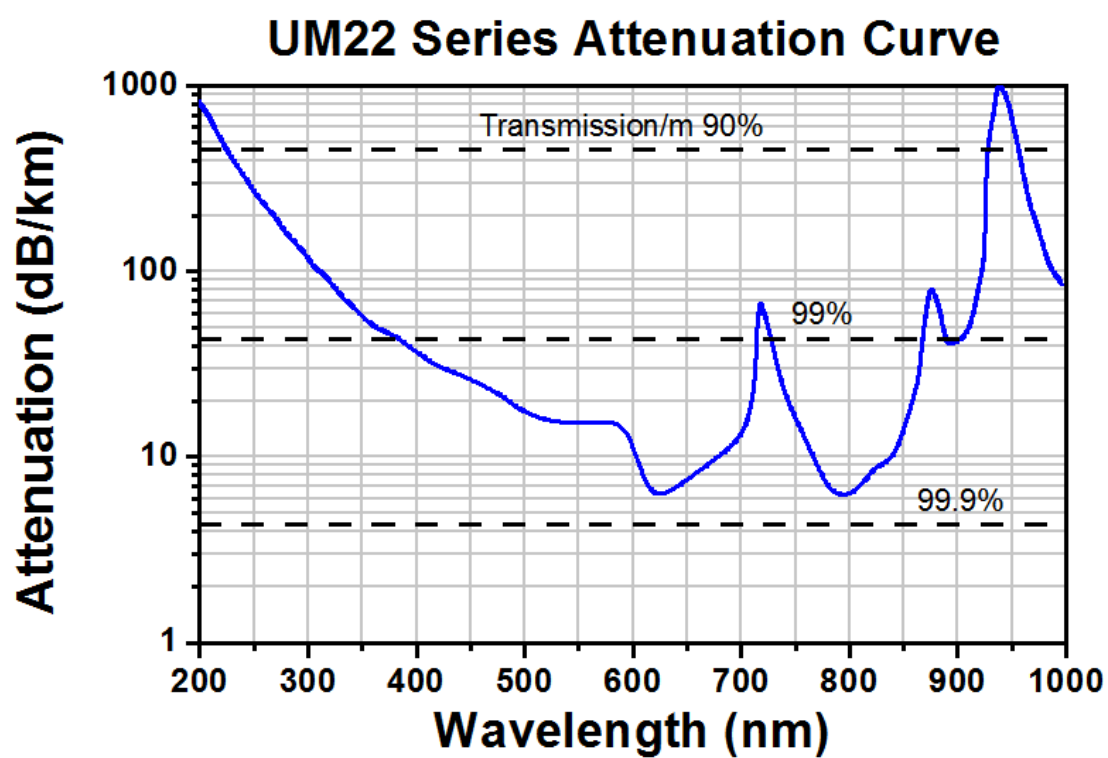


Figure F.1: Wavelength dependent light attenuation coefficient of the UV optical fibers used in this experiment. The plot is taken from the resellers technical specifications [Tho].

# Bibliography

- [AAAC<sup>+</sup>13] P.A.R. Ade, N. Aghanim, C. Armitage-Caplan, et al. Planck 2013 results. XVI. cosmological parameters. *Astronomy & Astrophysics*, 2013. (sumbitted). arXiv:1303.5076.
- [ABB<sup>+</sup>80] I.S. Altarev, Yu.V. Borisov, A.B. Brandin, et al. A search for the electric dipole moment of the neutron using ultracold neutrons. *Nuclear Physics A*, 341(2):269–283, 1980. doi:10.1016/0375-9474(80)90313-9.
- [ABB<sup>+</sup>81] I.S. Altarev, Yu.V. Borisov, N.V. Borovikova, et al. A new upper limit on the electric dipole moment of the neutron. *Physics Letters B*, 102(1):13–16, 1981. doi:10.1016/0370-2693(81)90202-1.
- [ABB<sup>+</sup>86] I.S. Altarev, Yu.V. Borisov, N.V. Borovikova, et al. Search for an electric dipole moment of the neutron. *JETP Letters*, 44(8):461, 1986.
- [ABB<sup>+</sup>92] I.S. Altarev, Yu.V. Borisov, N.V. Borovikova, et al. New measurement of the electric dipole moment of the neutron. *Physics Letters B*, 276(1–2):242–246, 1992. doi:10.1016/0370-2693(92)90571-K.
- [ABB<sup>+</sup>96] I.S. Altarev, Yu.V. Borisov, N.V. Borovikova, et al. Search for the Neutron Electric Dipole Moment. *Physics of Atomic Nuclei*, 59(7):1152–1170, 1996.
- [ABC<sup>+</sup>13] I. Altarev, D. H. Beck, S. Chesnevskaya, et al. A next generation measurement of the electric dipole moment of the neutron at the FRM II. *Il Nuovo Cimento C*, 35:122–127, 2013. doi:10.1393/ncc/i2012-11271-0.
- [Ac12] ATLAS-collaboration. Observation of a new particle in the search for the standard model higgs boson with the ATLAS detector at the LHC. *Physics Letters B*, 716(1):1–29, 2012. doi:10.1016/j.physletb.2012.08.020.
- [AMGP78] P. Ageron, W. Mampe, R. Golub, and J.M. Pendelbury. Measurement of the ultra cold neutron production rate in an external liquid helium source. *Physics Letters A*, 66(6):469–471, 1978. doi:10.1016/0375-9601(78)90399-7.
- [AMK<sup>+</sup>08] J. Alnis, A. Matveev, N. Kolachevsky, Th. Udem, and T. W. Hänsch. Sub-hertz linewidth diode lasers by stabilization to vibrationally and thermally

- compensated ultralow-expansion glass Fabry-Perot cavities. *Phys. Rev. A*, 77:053809, 2008. doi:10.1103/PhysRevA.77.053809.
- [BBB<sup>+</sup>09] G. W. Bennett, B. Bousquet, H. N. Brown, et al. Improved limit on the muon electric dipole moment. *Phys. Rev. D*, 80:052008, 2009. doi:10.1103/PhysRevD.80.052008.
- [BBB<sup>+</sup>11] C.A. Baker, G. Ban, K. Bodek, et al. The search for the neutron electric dipole moment at the Paul Scherrer Institute. *Physics Procedia*, 17(0):159–167, 2011. 2nd International Workshop on the Physics of fundamental Symmetries and Interactions - PSI2010. doi:10.1016/j.phpro.2011.06.032.
- [BBL<sup>+</sup>09] G. Ban, K. Bodek, T. Lefort, et al. UCN detection with <sup>6</sup>Li-doped glass scintillators. *Nuclear Instruments and Methods in Physics Research Section A: Accelerators, Spectrometers, Detectors and Associated Equipment*, 611(2–3):280–283, 2009. Particle Physics with Slow Neutrons. doi:10.1016/j.nima.2009.07.083.
- [BCC<sup>+</sup>13] C. A. Baker, Y. Chibane, M. Chouder, et al. Apparatus for measurement of the electric dipole moment of the neutron using a cohabiting atomic-mercury magnetometer. *ArXiv e-prints*, May 2013. arXiv:1305.7336.
- [BCT61] J.P. Barrat and C. Cohen-Tannoudji. Étude du pompage optique dans le formalisme de la matrice densité. *J. Phys. Radium*, 22(6):329–336, 1961. doi:10.1051/jphysrad:01961002206032900.
- [BDG<sup>+</sup>06] C. A. Baker, D. D. Doyle, P. Geltenbort, et al. Improved experimental limit on the electric dipole moment of the neutron. *Phys. Rev. Lett.*, 97:131801, 2006. doi:10.1103/PhysRevLett.97.131801.
- [BDH<sup>+</sup>08] K. Bodek, M. Daum, R. Henneck, et al. Storage of ultracold neutrons in high resistivity, non-magnetic materials with high fermi potential. *Nuclear Instruments and Methods in Physics Research Section A: Accelerators, Spectrometers, Detectors and Associated Equipment*, 597(2–3):222–226, 2008. doi:10.1016/j.nima.2008.09.018.
- [Bel55] J. S. Bell. Time reversal in field theory. *Proceedings of the Royal Society of London. Series A. Mathematical and Physical Sciences*, 231(1187):479–495, 1955. doi:10.1098/rspa.1955.0189.
- [BKLB10] M. V. Balabas, T. Karaulanov, M. P. Ledbetter, and D. Budker. Polarized alkali-metal vapor with minute-long transverse spin-relaxation time. *Phys. Rev. Lett.*, 105:070801, 2010. doi:10.1103/PhysRevLett.105.070801.
- [BMDR69] J. K. Baird, P. D. Miller, W. B. Dress, and Norman F. Ramsey. Improved upper limit to the electric dipole moment of the neutron. *Phys. Rev.*, 179:1285–1291, Mar 1969. doi:10.1103/PhysRev.179.1285.

- [BPR08] Pavel A. Bolokhov, Maxim Pospelov, and Michael Romalis. Electric dipole moments as probes of *CPT* invariance. *Phys. Rev. D*, 78:057702, 2008. doi:10.1103/PhysRevD.78.057702.
- [BR03] M. Baeva and D. Reiter. Monte Carlo simulation of radiation trapping in Hg-Ar fluorescent discharge lamps. *Plasma Chemistry and Plasma Processing*, 23(2):371–387, 2003. doi:10.1023/A:1022928320970.
- [Cag61] B. Cagnag. Orientation nucléaire par pompage optique des isotopes impairs du mercure. *Annales de Physique*, pages 467–526, 1961.
- [Cc12] CMS-collaboration. Observation of a new boson at a mass of 125 GeV with the CMS experiment at the LHC. *Physics Letters B*, 716(1):30–61, 2012. doi:10.1016/j.physletb.2012.08.021.
- [CCFT64] J. H. Christenson, J. W. Cronin, V. L. Fitch, and R. Turlay. Evidence for the  $2\pi$  decay of the  $K_2^0$  meson. *Phys. Rev. Lett.*, 13:138–140, 1964. doi:10.1103/PhysRevLett.13.138.
- [CFH<sup>+</sup>13] Z. Chowdhuri, M. Fertl, M. Horras, et al. Experimental study of  $^{199}\text{Hg}$  spin anti-relaxation coatings. *Applied Physics B*, pages 1–6, 2013. doi:10.1007/s00340-013-5598-8.
- [Cid96] Philip E. Ciddor. Refractive index of air: new equations for the visible and near infrared. *Appl. Opt.*, 35(9):1566–1573, Mar 1996. doi:10.1364/AO.35.001566.
- [CK84] Ling-Lie Chau and Wai-Yee Keung. Comments on the parametrization of the Kobayashi-Maskawa matrix. *Phys. Rev. Lett.*, 53:1802–1805, 1984. doi:10.1103/PhysRevLett.53.1802.
- [CLH<sup>+</sup>98] Kristan L. Corwin, Zheng-Tian Lu, Carter F. Hand, Ryan J. Epstein, and Carl E. Wieman. Frequency-stabilized diode laser with the zeeman shift in an atomic vapor. *Appl. Opt.*, 37(15):3295–3298, 1998. doi:10.1364/AO.37.003295.
- [DBMR68] W. B. Dress, J. K. Baird, P. D. Miller, and Norman F. Ramsey. Upper limit for the electric dipole moment of the neutron. *Phys. Rev.*, 170:1200–1206, Jun 1968. doi:10.1103/PhysRev.170.1200.
- [Deh57] H. G. Dehmelt. Modulation of a light beam by precessing absorbing atoms. *Phys. Rev.*, 105:1924–1925, 1957. doi:10.1103/PhysRev.105.1924.
- [Dem08a] W. Demtröder. *Laser Spectroscopy, Volume 1, Basic principles*. Springer-Verlag Berlin Heidelberg, 2008.

- [Dem08b] W. Demtröder. *Laser Spectroscopy, Volume 1, Experimental Techniques*. Springer-Verlag Berlin Heidelberg, 2008.
- [DHK<sup>+</sup>83] R.W.P. Drever, J.L. Hall, F.V. Kowalski, et al. Laser phase and frequency stabilization using an optical resonator. *Applied Physics B*, 31(2):97–105, 1983. doi:10.1007/BF00702605.
- [DMP<sup>+</sup>77] W. B. Dress, P. D. Miller, J. M. Pendlebury, Paul Perrin, and Norman F. Ramsey. Search for an electric dipole moment of the neutron. *Phys. Rev. D*, 15:9–21, Jan 1977. doi:10.1103/PhysRevD.15.9.
- [DMR73] W. B. Dress, P. D. Miller, and N. F. Ramsey. Improved upper limit for the electric dipole moment of the neutron. *Phys. Rev. D*, 7:3147–3149, Jun 1973. doi:10.1103/PhysRevD.7.3147.
- [Dod61] J.N. Dodd. The  $g_J$  Value of the  $6^3p_1$  Level in Mercury. *Proceedings of the Physical Society*, 78(1):65, 1961. URL: <http://stacks.iop.org/0370-1328/78/i=1/a=310>.
- [DS03] V. F. Dmitriev and R. A. Sen'kov. Schiff moment of the mercury nucleus and the proton dipole moment. *Phys. Rev. Lett.*, 91:212303, Nov 2003. doi:10.1103/PhysRevLett.91.212303.
- [DUB<sup>+</sup>01] S. A. Diddams, Th. Udem, J. C. Bergquist, et al. An optical clock based on a single trapped  $199\text{Hg}^+$  ion. *Science*, 293(5531):825–828, 2001. doi:10.1126/science.1061171.
- [Elm] Perkin Elmer.
- [ERMvK13] Jonathan Engel, Michael J. Ramsey-Musolf, and U. van Kolck. Electric Dipole Moments of Nucleons, Nuclei, and Atoms: The Standard Model and Beyond. *Prog.Part.Nucl.Phys.*, 71:21–74, 2013. arXiv:1303.2371, doi:10.1016/j.ppnp.2013.03.003.
- [FD12] V. V. Flambaum and V. A. Dzuba. Parity violation and electric dipole moments in atoms and molecules. *International Journal of Modern Physics E*, 21(11):1230010, 2012. arXiv:<http://www.worldscientific.com/doi/pdf/10.1142/S021830131230010X>, doi:10.1142/S021830131230010X.
- [Fer09] M. Fertl. Progress towards a new high density source of ultra cold neutrons at the Institut Laue-Langevin, Diplomarbeit, unpublished, 2009.
- [FG02] V. V. Flambaum and J. S. M. Ginges. Nuclear schiff moment and time-invariance violation in atoms. *Phys. Rev. A*, 65:032113, 2002. doi:10.1103/PhysRevA.65.032113.



- [FJK<sup>+</sup>09] V.V. Fedorov, M. Jentschel, I.A. Kuznetsov, et al. Perspectives for nEDM search by crystal diffraction. Test experiment and results. *Nuclear Physics A*, 827(1–4):538c–540c, 2009. PANIC08 - Proceedings of the 18th Particles and Nuclei International Conference. doi:10.1016/j.nuclphysa.2009.05.117.
- [FK85] V. V. Flambaum and I. B. Khriplovich. New bounds on the electric dipole moment of the electron and on T-odd electron-nucleon coupling. *JETP*, 62:872–875, 1985.
- [FM47] E. Fermi and L. Marshall. Interference phenomena of slow neutrons. *Phys. Rev.*, 71:666–677, May 1947. doi:10.1103/PhysRev.71.666.
- [Fra13] B. Franke. *Investigations of the Internal and External Magnetic Fields of the Neutron Electric Dipole Moment Experiment at the Paul Scherrer Institute*. PhD thesis, Eidgenössische Technische Hochschule Zürich, 2013.
- [FT57] Jerome I. Friedman and V. L. Telegdi. Nuclear emulsion evidence for parity nonconservation in the decay chain  $\pi^+ - \mu^+ - e^+$ . *Phys. Rev.*, 105:1681–1682, Mar 1957. doi:10.1103/PhysRev.105.1681.2.
- [GBS<sup>+</sup>06] S. Groeger, G. Bison, J.-L. Schenker, R. Wynands, and A. Weis. A high-sensitivity laser-pumped  $M_x$  magnetometer. *The European Physical Journal D - Atomic, Molecular, Optical and Plasma Physics*, 38(2):239–247, 2006. doi:10.1140/epjd/e2006-00037-y.
- [GGH<sup>+</sup>09] P. Geltenbort, L. Göttl, R. Henneck, et al. A compact, large-diameter adiabatic spinflipper for ultracold neutrons. *Nuclear Instruments and Methods in Physics Research Section A: Accelerators, Spectrometers, Detectors and Associated Equipment*, 608(1):132–138, 2009. doi:http://dx.doi.org/10.1016/j.nima.2009.06.038.
- [GHI<sup>+</sup>98] K. Green, P.G. Harris, P. Iaydjiev, et al. Performance of an atomic mercury magnetometer in the neutron EDM experiment. *Nuclear Instruments and Methods in Physics Research Section A: Accelerators, Spectrometers, Detectors and Associated Equipment*, 404:381–393, 1998. doi:10.1016/S0168-9002(97)01121-2.
- [GHK<sup>+</sup>10] C. Gemmel, W. Heil, S. Karpuk, et al. Ultra-sensitive magnetometry based on free precession of nuclear spins. *The European Physical Journal D*, 57:303–320, 2010. doi:10.1140/epjd/e2010-00044-5.
- [GLW57] Richard L. Garwin, Leon M. Lederman, and Marcel Weinrich. Observations of the failure of conservation of parity and charge conjugation in meson decays: the magnetic moment of the free muon. *Phys. Rev.*, 105:1415–1417, 1957. doi:10.1103/PhysRev.105.1415.

- [Göl12] L. Götl. *Characterization of the PSI ultra-cold neutron source*. PhD thesis, Eidgenössische Technische Hochschule Zürich, 2012. doi:10.3929/ethz-a-007313431.
- [GP75] R. Golub and J.M. Pendlebury. Super-thermal sources of ultra-cold neutrons. *Physics Letters A*, 53(2):133–135, 1975. doi:10.1016/0375-9601(75)90500-9.
- [GRL91] R. Golub, D. Richardson, and S.K. Lamoreaux. *Ultra-Cold Neutrons*. Adam Hilger, Bristol, Philadelphia and New York, 1991.
- [Gro12] Particle Data Group. Review of particle physics. *Phys. Rev. D*, 86:010001, 2012. doi:10.1103/PhysRevD.86.010001.
- [GS22] Walther Gerlach and Otto Stern. Der experimentelle Nachweis der Richtungsquantelung im Magnetfeld. *Zeitschrift für Physik*, 9:349–352, 1922. doi:10.1007/BF01326983.
- [GSL<sup>+</sup>09] W. C. Griffith, M. D. Swallows, T. H. Loftus, et al. Improved limit on the permanent electric dipole moment of <sup>199</sup>Hg. *Phys. Rev. Lett.*, 102:101601, 2009. doi:10.1103/PhysRevLett.102.101601.
- [GYO<sup>+</sup>84] M.B. Gavela, A. Yaouanc, L. Oliver, et al. Contribution of the triangle graphs to the neutron electric dipole moment. *Zeitschrift für Physik C Particles and Fields*, 23(3):251–261, 1984. doi:10.1007/BF01546193.
- [Hän06] Theodor W. Hänsch. Nobel lecture: Passion for precision. *Rev. Mod. Phys.*, 78:1297–1309, 11 2006. doi:10.1103/RevModPhys.78.1297.
- [Hay14] W. M. Haynes, editor. *Handbook of Chemistry and Physics 9*. CRC Press/Taylor and Francis, Boca Raton, FL, 2013–2014. 4th Edition (Internet Version 2014). URL: <http://www.hbcnetbase.com>.
- [HBG<sup>+</sup>99] P. G. Harris, C. A. Baker, K. Green, et al. New experimental limit on the electric dipole moment of the neutron. *Phys. Rev. Lett.*, 82:904–907, Feb 1999. doi:10.1103/PhysRevLett.82.904.
- [Hel14] V. Helaine. *tba*. PhD thesis, L’Universite de Caen Basse-Normandie, Caen, 2014.
- [HKS<sup>+</sup>11] J. J. Hudson, D. M. Kara, I. J. Smallman, et al. Improved measurement of the shape of the electron. *Nature*, 473(7348):493–U232, 2011. doi:10.1038/nature10104.
- [HM67] W. Happer and B. S. Mathur. Effective operator formalism in optical pumping. *Phys. Rev.*, 163:12–25, 1967. doi:10.1103/PhysRev.163.12.

- [HMP<sup>+</sup>08] H. Hachisu, K. Miyagishi, S. G. Porsev, et al. Trapping of neutral mercury atoms and prospects for optical lattice clocks. *Phys. Rev. Lett.*, 100:053001, 2008. doi:10.1103/PhysRevLett.100.053001.
- [Hor12] M. Horras. *A highly sensitive <sup>199</sup>Hg magnetometer for the nEDM experiment*. PhD thesis, Eidgenössische Technische Hochschule Zürich, 2012. doi:10.3929/ethz-a-007557385.
- [HR00] D. M. Harber and M. V. Romalis. Measurement of the scalar stark shift of the  $6^1S_0 \rightarrow 6^3P_1$  transition in hg. *Phys. Rev. A*, 63:013402, 2000. doi:10.1103/PhysRevA.63.013402.
- [Ito07] Takeyasu M. Ito. Plans for a neutron EDM experiment at SNS. *J. Phys. Conf. Ser.*, 69:012037, 2007. arXiv:nucl-ex/0702024, doi:10.1088/1742-6596/69/1/012037.
- [JW03] JP Jacobs and RB Warrington. Pressure shift and broadening of the 254-nm intercombination line of mercury by N-2. *Phys. Rev. A*, 68(3), September 2003. doi:10.1103/PhysRevA.68.032722.
- [Kas50] Kastler, Alfred. Quelques suggestions concernant la production optique et la détection optique d'une inégalité de population des niveaux de quantification spatiale des atomes. application à l'expérience de Stern et Gerlach et à la résonance magnétique. *J. Phys. Radium*, 11(6):255–265, 1950. doi:10.1051/jphysrad:01950001106025500.
- [Kas63] Alfred Kastler. Displacement of energy levels of atoms by light. *J. Opt. Soc. Am.*, 53(8):902–906, 1963. doi:10.1364/JOSA.53.000902.
- [KC10] Jihn E. Kim and Gianpaolo Carosi. Axions and the strong *CP* problem. *Rev. Mod. Phys.*, 82:557–601, 2010. doi:10.1103/RevModPhys.82.557.
- [KL72] R. D. Kaul and William S. Latshaw. Stark shift in the  $6s6p^3P_1$  state of mercury. *J. Opt. Soc. Am.*, 62(5):615–618, 1972. doi:10.1364/JOSA.62.000615.
- [KM73] Makoto Kobayashi and Toshihide Maskawa. CP-violation in the Renormalizable Theory of Weak Interaction. *Progress of Theoretical Physics*, 49(2):652–657, 1973. doi:10.1143/PTP.49.652.
- [Kon07] F.G. Kondev. Nuclear data sheets for A = 201. *Nuclear Data Sheets*, 108(2):365–454, 2007. doi:10.1016/j.nds.2007.01.004.
- [KSB<sup>+</sup>13] J. Karch, Y. Sobolev, M. Beck, et al. Performance of the solid deuterium ultra-cold neutron source at the pulsed reactor TRIGA Mainz. *ArXiv e-prints*, August 2013. arXiv:1308.4610.

- [KSW12] Daniel Kolbe, Martin Scheid, and Jochen Walz. Triple resonant four-wave mixing boosts the yield of continuous coherent vacuum ultraviolet generation. *Phys. Rev. Lett.*, 109:063901, 2012. doi:10.1103/PhysRevLett.109.063901.
- [Kuz08] M. Kuzniak. *The Neutron Electric Dipole Moment Experiment: Research and Development for the New Spectrometer*. PhD thesis, Jagiellonian University, Krakow, 2008.
- [KZ82] I.B. Khriplovich and A.R. Zhitnitsky. What is the value of the neutron electric dipole moment in the kobayashi-maskawa model? *Physics Letters B*, 109(6):490–492, 1982. doi:10.1016/0370-2693(82)91121-2.
- [Lau] B. Lauss. private communication.
- [LHN<sup>+</sup>07] A. D. Ludlow, X. Huang, M. Notcutt, et al. Compact, thermal-noise-limited optical cavity for diode laser stabilization at  $1 \times 10^{15}$ . *Opt. Lett.*, 32(6):641–643, 2007. doi:10.1364/OL.32.000641.
- [Lin84] M. E. Lines. Scattering losses in optic fiber materials. i. a new parametrization. *Journal of Applied Physics*, 55(11):4052–4057, 1984. doi:10.1063/1.332994.
- [Lüd57] Gerhart Lüders. Proof of the TCP theorem. *Annals of Physics*, 2(1):1–15, 1957. doi:10.1016/0003-4916(57)90032-5.
- [LVS<sup>+</sup>11] S. Li, P. Vachaspati, D. Sheng, N. Dural, and M. V. Romalis. Optical rotation in excess of 100 rad generated by rb vapor in a multipass cell. *Phys. Rev. A*, 84:061403, Dec 2011. doi:10.1103/PhysRevA.84.061403.
- [LYQ<sup>+</sup>13] Hongli Liu, Shiqi Yin, Jun Qian, Zhen Xu, and Yuzhu Wang. Optimization of doppler-free magnetically induced dichroic locking spectroscopy on the  $^1S_0$ – $^3P_1$  transition of a neutral mercury atom. *Journal of Physics B: Atomic, Molecular and Optical Physics*, 46(8):085005, 2013. URL: <http://stacks.iop.org/0953-4075/46/i=8/a=085005>.
- [MAH<sup>+</sup>12] Yasuhiro Masuda, Koichiro Asahi, Kichiji Hatanaka, et al. Neutron electric dipole moment measurement with a buffer gas comagnetometer. *Physics Letters A*, 376(16):1347–1351, 2012. doi:10.1016/j.physleta.2012.02.056.
- [May98] D.J.R. May. *A High Precision Comparison Of The Gyromagnetic Ratios Of The  $^{199}\text{Hg}$  Atom And The Neutron*. PhD thesis, University of Sussex, 1998.
- [MDBR67] P. D. Miller, W. B. Dress, J. K. Baird, and Norman F. Ramsey. Limit to the electric dipole moment of the neutron. *Phys. Rev. Lett.*, 19:381–384, Aug 1967. doi:10.1103/PhysRevLett.19.381.

- [MHJ<sup>+</sup>12] Yasuhiro Masuda, Kichiji Hatanaka, Sun-Chan Jeong, et al. Spallation ultracold neutron source of superfluid helium below 1k. *Phys. Rev. Lett.*, 108:134801, 2012. doi:10.1103/PhysRevLett.108.134801.
- [MMM<sup>+</sup>12] J. J. McFerran, D. V. Magalhaes, C. Mandache, et al. Laser locking to the  $^{199}\text{Hg } ^1S_0 \rightarrow ^3P_0$  clock transition with  $5.4 \times 10^{-15}$  fractional frequency instability. *Opt. Lett.*, 37(17):3477–3479, 2012. doi:10.1364/OL.37.003477.
- [MPO87] Ann-Marie Martensson-Pendrill and Per Oster. Calculations of atomic electric dipole moments. *Physica Scripta*, 36(3):444, 1987. URL: <http://stacks.iop.org/1402-4896/36/i=3/a=011>.
- [Nat] National Institute of Standards and Technology. Basic atomic spectroscopic data. Accessed 2013-11-13. URL: <http://physics.nist.gov/PhysRefData/Handbook/Tables/mercurytable1.htm>.
- [Nob] Nobel Foundation. Lists of Nobel prizes and laureates. Accessed 2013-11-13. URL: <http://www.nobelprize.org/>.
- [Noe18] E. Noether. Invariante Variationsprobleme. *Nachrichten von der Gesellschaft der Wissenschaften zu Göttingen, Mathematisch-Physikalische Klasse*, 1918:235–257, 1918. URL: <http://eudml.org/doc/59024>.
- [PAG<sup>+</sup>99] S. Perlmutter, G. Aldering, G. Goldhaber, et al. Measurements of  $\omega$  and  $\lambda$  from 42 high-redshift supernovae. *The Astrophysical Journal*, 517(2):565, 1999. URL: <http://stacks.iop.org/0004-637X/517/i=2/a=565>.
- [Pau57] W. Pauli. *Exclusion Principle, Lorentz group and reflection of space-time and charge*. W. Pauli, 1957. URL: [http://library.web.cern.ch/archives/Pauli\\_archive](http://library.web.cern.ch/archives/Pauli_archive).
- [PFL<sup>+</sup>03] T. Petelski, M. Fattori, G. Lamporesi, J. Stuhler, and G.M. Tino. Doppler-free spectroscopy using magnetically induced dichroism of atomic vapor: a new scheme for laser frequency locking. *Eur. Phys. J. D*, 22(2):279–283, 2003. doi:10.1140/epjd/e2002-00238-4.
- [PGF11] S. G. Porsev, J. S. M. Ginges, and V. V. Flambaum. Atomic electric dipole moment induced by the nuclear electric dipole moment: The magnetic moment effect. *Phys. Rev. A*, 83:042507, 2011. doi:10.1103/PhysRevA.83.042507.
- [Pie09] F.M. Piegsa. *Neutron Spin Precession in Samples of Polarised Nuclei and Neutron Spin Phase Imaging*. PhD thesis, Technische Universität München, 2009. URL: <http://nbn-resolving.de/urn/resolver.pl?urn:nbn:de:bvb:91-diss-20090713-804195-1-3>.

- [Pie11] E. Pierre. *Developpement et optimisation d'un systeme de polarisation de neutrons ultra froids dans le cadre d'une nouvelle mesure du moment dipolaire electrique du neutron*. PhD thesis, L'Universite de Caen Basse-Normandie, Caen, 2011. URL: <http://inspirehep.net/record/1187870>.
- [Pie13] Florian M. Piegsa. New concept for a neutron electric dipole moment search using a pulsed beam. *Phys. Rev. C*, 88:045502, Oct 2013. doi:10.1103/PhysRevC.88.045502.
- [PQ77] R. D. Peccei and Helen R. Quinn. *CP* conservation in the presence of pseudoparticles. *Phys. Rev. Lett.*, 38:1440–1443, 1977. doi:10.1103/PhysRevLett.38.1440.
- [PR50] E. M. Purcell and N. F. Ramsey. On the possibility of electric dipole moments for elementary particles and nuclei. *Phys. Rev.*, 78:807–807, 1950. doi:10.1103/PhysRev.78.807.
- [PR05] Maxim Pospelov and Adam Ritz. Electric dipole moments as probes of new physics. *Annals of Physics*, 318(1):119–169, 2005. Special Issue. doi:10.1016/j.aop.2005.04.002.
- [PR12] Guillaume Pignol and Stéphanie Roccia. Electric-dipole-moment searches: Reexamination of frequency shifts for particles in traps. *Phys. Rev. A*, 85:042105, April 2012. arXiv:1201.0699v1, doi:10.1103/PhysRevA.85.042105.
- [PSG<sup>+</sup>84] J.M. Pendlebury, K.F. Smith, R. Golub, et al. Search for a neutron electric dipole moment. *Physics Letters B*, 136(5–6):327–330, 1984. doi:10.1016/0370-2693(84)92013-6.
- [Ram50a] Norman F. Ramsey. A molecular beam resonance method with separated oscillating fields. *Phys. Rev.*, 78:695–699, 1950. doi:10.1103/PhysRev.78.695.
- [Ram50b] Norman F. Ramsey. A molecular beam resonance method with separated oscillating fields. *Phys. Rev.*, 78:695–699, 1950. doi:10.1103/PhysRev.78.695.
- [RCSD02] B. C. Regan, Eugene D. Commins, Christian J. Schmidt, and David DeMille. New limit on the electron electric dipole moment. *Phys. Rev. Lett.*, 88:071805, Feb 2002. doi:10.1103/PhysRevLett.88.071805.
- [RFC<sup>+</sup>98] Adam G. Riess, Alexei V. Filippenko, Peter Challis, et al. Observational evidence from supernovae for an accelerating universe and a cosmological constant. *The Astronomical Journal*, 116(3):1009, 1998. URL: <http://stacks.iop.org/1538-3881/116/i=3/a=1009>.

- [RHUH99] J. Reichert, R. Holzwarth, Th. Udem, and T.W. Hänsch. Measuring the frequency of light with mode-locked lasers. *Optics Communications*, 172(1–6):59–68, 1999. doi:10.1016/S0030-4018(99)00491-5.
- [Rio98] Antonio Riotto. Theories of baryogenesis. *lanl.arXiv.org*, pages 326–436, 1998. arXiv:hep-ph/9807454.
- [RL04] M. V. Romalis and L. Lin. Surface nuclear spin relaxation of  $^{199}\text{Hg}$ . *The Journal of Chemical Physics*, 120(3):1511–1515, 2004. doi:10.1063/1.1609396.
- [RM10] B Lee Roberts and William J Marciano, editors. *Lepton Dipole Moments*. World Scientific, 2010.
- [Roc09] S. Roccia. *La co-magnétométrie mercure pour la mesure du moment électrique dipolaire du neutron - Optimisation et application au test de l'invariance de Lorentz*. PhD thesis, Université Joseph Fourier, Grenoble I, 2009. URL: <http://tel.archives-ouvertes.fr/tel-00440287>.
- [SBE<sup>+</sup>11] A.P. Serebrov, S.T. Boldarev, A.N. Erykalov, et al. Supersource of ultracold neutrons at WWR-M reactor in PNPI and the research program on fundamental physics. *Physics Procedia*, 17(0):251–258, 2011. 2nd International Workshop on the Physics of fundamental Symmetries and Interactions - PSI2010. doi:10.1016/j.phpro.2011.06.044.
- [Sch63] Walter G. Schweitzer, Jr. Hyperfine structure and isotope shifts in the 2537-Å line of mercury by a new interferometric method. *J. Opt. Soc. Am.*, 53(9):1055–1071, 1963. doi:10.1364/JOSA.53.001055.
- [SCP<sup>+</sup>90] K.F. Smith, N. Crampin, J.M. Pendlebury, et al. A search for the electric dipole moment of the neutron. *Physics Letters B*, 234(1–2):191–196, 1990. doi:10.1016/0370-2693(90)92027-G.
- [Sea92] Varley F. Sears. Neutron scattering lengths and cross sections. *Neutron News*, 3(3):26–37, 1992. doi:10.1080/10448639208218770.
- [She05] B. A. Shenoi. *Introduction to Digital Signal Processing and Filter Design*. John Wiley & Sons, Inc., 2005. doi:10.1002/0471656372.fmatter.
- [Sin07] Balraj Singh. Nuclear data sheets for  $A = 199$ . *Nuclear Data Sheets*, 108(1):79–196, 2007. doi:10.1016/j.nds.2007.01.001.
- [SKWM94] O. Schmidt, K.-M. Knaak, R. Wynands, and D. Meschede. Cesium saturation spectroscopy revisited: How to reverse peaks and observe narrow resonances. *Applied Physics B*, 59(2):167–178, 1994. doi:10.1007/BF01081167.

- [SLB<sup>+</sup>10] Yu. Sobolev, Th. Lauer, Yu. Borisov, et al. Cubic boron nitride: A new prospective material for ultracold neutron application. *Nuclear Instruments and Methods in Physics Research Section A: Accelerators, Spectrometers, Detectors and Associated Equipment*, 614(3):461–467, 2010. doi:10.1016/j.nima.2009.12.035.
- [SLF<sup>+</sup>05] A.P. Serebrov, M.S. Lasakov, A.K. Fomin, et al. Superconducting UCN polarizer for a new EDM spectrometer. *Nuclear Instruments and Methods in Physics Research Section A: Accelerators, Spectrometers, Detectors and Associated Equipment*, 545(1–2):490–492, 2005. doi:10.1016/j.nima.2005.01.316.
- [SLG<sup>+</sup>13] M. D. Swallows, T. H. Loftus, W. C. Griffith, et al. Techniques used to search for a permanent electric dipole moment of the <sup>199</sup>Hg atom and the implications for CP violation. *Phys. Rev. A*, 87:012102, 2013. doi:10.1103/PhysRevA.87.012102.
- [SMHS06] H. Stoehr, F. Mensing, J. Helmcke, and U. Sterr. Diode laser with 1 Hz linewidth. *Opt. Lett.*, 31(6):736–738, 2006. doi:10.1364/OL.31.000736.
- [SN67] C. G. Shull and R. Nathans. Search for a neutron electric dipole moment by a scattering experiment. *Phys. Rev. Lett.*, 19:384–386, Aug 1967. doi:10.1103/PhysRevLett.19.384.
- [SNS<sup>+</sup>86] A. Steyerl, H. Nagel, F.-X. Schreiber, et al. A new source of cold and ultracold neutrons. *Physics Letters A*, 116(7):347–352, 1986. doi:10.1016/0375-9601(86)90587-6.
- [SPR57] J. H. Smith, E. M. Purcell, and N. F. Ramsey. Experimental limit to the electric dipole moment of the neutron. *Phys. Rev.*, 108:120–122, 1957. doi:10.1103/PhysRev.108.120.
- [Ste75] A. Steyerl. A “neutron turbine” as an efficient source of ultracold neutrons. *Nuclear Instruments and Methods*, 125(3):461–469, 1975. doi:10.1016/0029-554X(75)90265-7.
- [Swa07] M. Swallows. *A search for the permanent electric dipole moment of mercury-199*. PhD thesis, University of Washington, Seattle, 2007.
- [Tho] Thorlabs. Web catalogue, product details of UM22-600. Accessed 2013-10-06. URL: <http://www.thorlabs.de/thorproduct.cfm?partnumber=UM22-200>.
- [TOP] TOPTICA Photonics AG. Product description TA / FA-FHG pro. Accessed 2013-08-26. URL: [http://www.toptica.com/products/research\\_grade\\_diode\\_lasers/frequency\\_converted\\_diode\\_lasers/ta\\_fhg\\_pro\\_frequency\\_quadrupled\\_tunable\\_diode\\_laser.html](http://www.toptica.com/products/research_grade_diode_lasers/frequency_converted_diode_lasers/ta_fhg_pro_frequency_quadrupled_tunable_diode_laser.html).



- [vdG09] M.G.D. van der Grinten. CryoEDM: A cryogenic experiment to measure the neutron electric dipole moment. *Nuclear Instruments and Methods in Physics Research Section A: Accelerators, Spectrometers, Detectors and Associated Equipment*, 611(2–3):129–132, 2009. Particle Physics with Slow Neutrons. doi:10.1016/j.nima.2009.07.040.
- [WAH<sup>+</sup>57] C. S. Wu, E. Ambler, R. W. Hayward, D. D. Hoppes, and R. P. Hudson. Experimental test of parity conservation in beta decay. *Phys. Rev.*, 105:1413–1415, 1957. doi:10.1103/PhysRev.105.1413.
- [WG11] Fred E. Wietfeldt and Geoffrey L. Greene. *Colloquium: The neutron lifetime. Rev. Mod. Phys.*, 83:1173–1192, 2011. doi:10.1103/RevModPhys.83.1173.
- [WGZZ02] G. Wasik, W. Gawlik, J. Zachorowski, and W. Zawadzki. Laser frequency stabilization by Doppler-free magnetic dichroism. *Applied Physics B: Lasers and Optics*, 75:613–619, 2002. 10.1007/s00340-002-1041-2. URL: <http://dx.doi.org/10.1007/s00340-002-1041-2>.
- [WH06] M. Wohlmuther and G. Heidenreich. The spallation target of the ultra-cold neutron source UCN at PSI. *Nuclear Instruments and Methods in Physics Research Section A: Accelerators, Spectrometers, Detectors and Associated Equipment*, 564(1):51–56, 2006. doi:10.1016/j.nima.2006.03.040.
- [Win] D. Wineland. private communication.
- [Zen13] J. Zenner. *The search for the neutron electric dipole moment*. PhD thesis, Johannes Gutenberg Universität, Mainz, 2013. urn:nbn:de:hebis:77-35005. URL: <http://d-nb.info/1041244924/34>.
- [ZGSS03] Wang Zhi, Ren Guobin, Lou Shuqin, and Jian Shuisheng. Loss properties due to rayleigh scattering in different types of fiber. *Opt. Express*, 11(1):39–47, January 2003. doi:10.1364/OE.11.000039.
- [ZPI11] Oliver Zimmer, Florian M. Piegsa, and Sergey N. Ivanov. Superthermal source of ultracold neutrons for fundamental physics experiments. *Phys. Rev. Lett.*, 107:134801, 2011. doi:10.1103/PhysRevLett.107.134801.
- [ZRD08] N. Zorina, G. Revalde, and R. Disch. Deconvolution of the mercury 253.7 nm spectral line shape for the use in absorption spectroscopy. *Proc. SPIE*, 7142:71420J, 2008. doi:10.1117/12.815460.
- [Zwi33] F. Zwicky. Die Rotverschiebung von extragalaktischen Nebeln. *Helvetica Physica Acta*, 6:110–127, 1933.
- [Zwi37] F. Zwicky. On the masses of nebulae and of clusters of nebulae. *The Astrophysical Journal*, 86:217, 1937. doi:10.1086/143864.



# Acknowledgments

This thesis would not have been possible without the constant support by many people. I want to express my special gratitude to:

- **Klaus Kirch** for hiring me as a PhD student in the UCN group at PSI. Thank you for giving me the chance to define my PhD project and for the constant encouraging support over the four years.
- **Antoine Weis** for serving as co-examiner of this thesis and helpful discussions about the project.
- **Philipp Schmidt-Wellenburg** for friendship and scientific collaboration over more than seven years on our different UCN projects.
- **Jochen Krempel** for scientific collaboration and the good time we had in Grenoble and Baden.
- **Aliko Mtchedlishvili** for sharing the (often dark) laser laboratory and for discussions about theoretical aspects of modern particle physics.
- **Geza Zsigmond** for support with the SNF administration.
- **Bernhard Lauss** for many discussions about UCN physics and much beyond.
- **Georg Bison** for discussions about atomic physics and data analysis strategies.
- **Zema Chowdhuri** for proof reading and correcting countless abstracts, summaries and especially of this document here.
- **Florian Piegsa** for introducing me to Ramsey's method beyond nEDM.
- **Aldo Antognini** for discussions about laser physics and funny travels in the US.
- **Reinhold Henneck** for sharing his knowledge about the nEDM experiment.
- **Beatrice Franke** for sharing the office and having a good time over the last four years.
- **Andreas Knecht, Edgard Pierre, Lenny Göttl, Marlon Horras, Johannes Zenner, Beatrice Franke, Victor Helaine, Samer Afach, Pataguppi Prasanth, Dieter Ries and Sybille Komposch** for sharing the experience of being a PhD student.

Weiterhin möchte ich

- **Michi Meier** und **Fritz Burri** für die hervorragende technische Unterstützung meiner Projekte und ungezählte Diskussionen über Gott und die Welt beim morgentlichen Kaffee danken.
- **Anita Van Loon** für die tolle administrative und organisatorische Unterstützung danken.
- **Ben van den Brandt**, **Patrick Hautle** und **Paul Schurter** für die Unterstützung bei Experimenten an der BOA Strahllinie danken.

Meine Projekte haben vielfach von der Arbeit der technischen Dienste am PSI profitiert. Stellvertretend für alle Gruppen danke ich hier **Max Müller**, **Peter Rütimann** und **Ottmar Morath** für die Unterstützung durch die Versuchswerkstatt, die Vakuumgruppe und den Strahlenschutz am PSI.

Ich danke meinen WG-Mitbewohnern, insbesondere **Hans Regler**, **Sebastian Fritz**, **Matt Stark**, **Szymon Modelski** und **Andrea Huber** für die gute Zeit in Baden. Ich danke **Peggy Heunemann**, **Jochen Krempel**, **Jakoba Heidler**, **Simon Mariager**, **Lenny Göttl** und **Lizi Bomba** für die Freizeitaktivitäten.

Personen werden durch Persönlichkeiten im nahen Umfeld geprägt:

Ich danke **Barbara**, **Anneliese** und **Hans Haas** und der verstorbenen **Egert-Oma** für tatkräftige und moralische Begleitung in persönlich schwierigen Zeiten.

Ich danke meiner verstorbenen Großmutter **Zenta Sobek** für die immerwährende Unterstützung über mehr als 24 Jahre meines Lebens. Dieses Großprojekt durfte sie leider nicht mehr erleben.

Dank gebührt meiner Schwester **Kerstin Treppesch**, ihrem Mann **Martin** und dem neuen Sonnenschein der Familie, **Valentin**.

Zum Schluss möchte ich meiner Mutter **Elfriede Sobek** für die fortwährende Unterstützung danken.